University of Southampton
Faculty of Engineering, Science and Mathematics
School of Electronics and Computer Science

Channel-Coded Time-Hopping and Direct-Sequence UltraWideBand Systems

by

Raja Ali Riaz
BEng., MSc, MSc

A Doctoral thesis submitted in partial fulfilment of the requirements for the award of Doctor of Philosophy at the University of Southampton

09 September 2009

SUPERVISORS: *Professor Lajos Hanzo*
FREng, FIEEE, FIET, DSc, Chair of Telecommunications
and *Professor Sheng Chen*
MSc, PhD, FIEEE
School of Electronics and Computer Science
University of Southampton
Southampton SO17 1BJ
United Kingdom

𝔇edicated

to my mother, sister, brother
and to all those less fortunate people of my country for the betterment of whom I am expected to work after I complete my education in this university.

UNIVERSITY OF SOUTHAMPTON

ABSTRACT

FACULTY OF ENGINEERING, SCIENCE AND MATHEMATICS
SCHOOL OF ELECTRONICS AND COMPUTER SCIENCE

Doctor of Philosophy

Channel-Coded Time-Hopping and Direct-Sequence UltraWideBand Systems

by

Raja Ali Riaz

This thesis is aimed at providing detailed transceiver structures employing novel channel coding schemes for enhancing the achievable performance of UltraWideBand (UWB) systems. We commence by a rudimentary introduction to UWB systems, including a brief historical perspective of the field. Chapters 2 to 4 will then provide the designs of channel coded UWB systems with the aid of EXtrinsic Information Transfer (EXIT) charts in order to achieve near-capacity performances. Each chapter constitutes an evolutionary improvement of the previous chapter.

Chapter 2 deals with the UWB channel, which is one of the major factors differentiating UWB system from their narrow-band counterparts. This chapter starts with a brief review of the last two decades' advances in UWB channel estimation. Then the z-domain Discrete Time Transfer Function (DTTF) of UWB channels is derived based on the specifications presented in the preceding sections. This transfer function forms the basis of the proposed memory-efficient implementation of the equalizer advocated. Furthermore, the stability analysis and Mean Convergence Bound (MCB) of the UWB channel transfer function is presented. The UWB channel model is then used by all the following chapters, when developing enhanced UWB systems.

Chapter 3 starts with the implications of appropriate diversity order selection. Since it is possible to resolve the closely spaced multipath components of the channel, the system benefits from a high number of independent fading paths, which results in a high multipath diversity gain. Then we propose an EXIT chart aided iteratively detected Direct-Sequence (DS) Code Division Multiple Access (CDMA) system, which uses 2-stage concatenation of an inner and outer encoders, with their corresponding decoders exchanging extrinsic information for the sake of enhancing the attainable system performance. This system model constitutes the foundation for the following chapters, which will be further developed using different coding schemes with the aid of EXIT charts. A DS and a Time-Hopping (TH) Pulse Position Modulated (PPM) UWB systems are studied using EXIT charts and it is demonstrated that classic regular Forward Error Correction (FEC) encoders are unable to arbitrarily approach the system's capacity.

Hence Chapter 4 provides a solution for this problem by replacing the regular FEC codes with more sophisticated irregular FEC codes that are capable of approaching the system's capacity more closely. More specifically, we have used Irregular Variable Length Codes (IrVLC) in our design of a two-stage concatenated UWB TH Spread-Spectrum (SS) Impulse Radio (IR) system. We then progressed from the two-stage design philosophy to three-stage irregular concatenated UWB systems. Naturally, an improved performance is only achievable at the cost of an increased complexity and interleaver length. Hence, the second half of Chapter 4 addresses the above-mentioned complexity and interleaver delay problem by invoking sophisticated binary Self-Concatenated Convolutional Codes (SeCCC) using different puncturing rates. We commence with a rudimentary introduction of the binary SeCCC design, which is then used for developing a near-capacity TH UWB system. Finally, the achievable performance gains of different puncturing and coding rates are detailed.

Acknowledgements

First of all, after ALLAH Almighty, I would like to thank my supervisors, Professors Lajos Hanzo and Sheng Chen, for their invaluable guidance and inspiration during my work. I consider myself very fortunate to be a student of these learned men and have greatly benefitted from their vast experience, meticulous methods of research and their sincerity towards pursuit of knowledge.

Special thanks are due to Mr. Fasih Uddin Butt, Dr. Soon Xin Ng and Dr. Rob Maunder with whom I collaborated to produce research work that resulted in IEEE publications and that became part of my thesis. I also owe many personal thanks to all my colleagues of the Communications Group, particularly to Mr. Nasruminallah, Dr. Jos Akhtman, Dr. Osamah Alamri, Dr. Muhammad El-Hajjar and Dr Lie Liang Yang for their timely help, whenever I needed it.

I also wish to thank the COMSATS Institute of Information Technology for the financial support I received from them.

DECLARATION OF AUTHORSHIP

I, **Raja Ali Riaz**,

declare that the thesis entitled

Channel-Coded Time-Hopping and Direct-Sequence UltraWideBand Systems

and the work presented in the thesis are both my own, and have been generated by me as the result of my own original research. I confirm that:

- this work was done wholly or mainly while in candidature for a research degree at this University;
- where any part of this thesis has previously been submitted for a degree or any other qualification at this University or any other institution, this has been clearly stated;
- where I have consulted the published work of others, this is always clearly attributed;
- where I have quoted from the work of others, the source is always given. With the exception of such quotations, this thesis is entirely my own work;
- I have acknowledged all main sources of help;
- where the thesis is based on work done by myself jointly with others, I have made clear exactly what was done by others and what I have contributed myself;
- parts of this work have been published as: [1–9].

Signed: *R. A. Riaz*
Date: 09 September 2009

List of Publications

1. **R. A. Riaz**, M. F. U. Butt, S. Chen and L. Hanzo, "Generic z-domain discrete-time transfer function estimation for ultra-wideband systems", *IET Electronics Letters*, Vol. 44, pp. 1491–1492, December 2008.

2. **R. A. Riaz**, R. G. Maunder, M. F. U. Butt, S. X. Ng, S. Chen and L. Hanzo, "EXIT-Chart Aided 3-Stage Concatenated Ultra-WideBand Time-Hopping Spread-Spectrum Impulse Radio Design", accepted and to appear in IEEE Transactions on Vehicular Technology.

3. **Raja Ali Riaz**, Mohammed El-Hajjar, Qasim Z. Ahmed, Soon Xin Ng, Sheng Chen and Lajos Hanzo, "Convergence Analysis of Iteratively Detected Time Hopping and DS-CDMA Ultrawide Bandwidth Systems by EXIT Charts", in Proceeding of the IEEE Vehicular Technology Conference (VTC-2008 Spring), pp. 1127-1131, May 2008, Singapore.

4. **Raja A. Riaz**, Mohammed El-Hajjar, Qasim Z. Ahmed, Soon X. Ng, Sheng Chen and Lajos Hanzo, "EXIT Chart Aided Design of DS-CDMA UltraWideBand Systems Using Iterative Decoding", in Proceedings of the IEEE Vehicular Technology Conference (VTC-2008 Fall), pp. 1-5, September 2008, Calgary.

5. **R. A. Riaz**, R. G. Maunder, M. F. U. Butt, S. X. Ng, S. Chen and L. Hanzo,"Three-Stage Concatenated Ultra-Wide Bandwidth Time-Hopping Spread-Spectrum Impulse Radio using Iterative Detection", in Proceeding of the IEEE International Conference on Communications (ICC), pp. 1-6, June 2009, Dresden .

6. **R. A. Riaz**, M. F. U. Butt, S. X. Ng, S. Chen and L. Hanzo,"Optimized Irregular Variable Length Coding Design for Iteratively Decoded UltraWideBand Time-Hopping Spread-Spectrum Impulse Radio", in Proceedings of the IEEE Vehicular Technology Conference (VTC-2009 Spring), pp. 1-5, April 2009, Barcelona.

7. **R. A. Riaz**, M. F. U. Butt, S. X. Ng, S. Chen, and L. Hanzo,"Near-Capacity UWB Impulse Radio Using EXIT Chart Aided Self-Concatenated Codes", to appear in Proceedings of the IEEE Vehicular Technology Conference (VTC-2009 Fall), September 2009, Anchorage, Alaska, USA.

8. **R. A. Riaz**, M. F. U. Butt, S. X. Ng. S. Chen and L. Hanzo, "EXIT Chart Aided Design of Near-Capacity UWB Impulse Radio Using Self-Concatenated Codes", submitted in *IET Electronics Letters*.

9. M. F. U. Butt, **R. A. Riaz**, Ng, S. X. Ng and L. Hanzo, "Near-Capacity Iteratively Decoded Binary Self-Concatenated Code Design Using EXIT Charts", in Proceedings of the IEEE Global Telecommunications Conference (GLOBECOM), pp. 1–5, December 2008, New Orleans.

10. M. F. U. Butt, **R. A. Riaz**, Ng, S. X. Ng and L. Hanzo, "Distributed Self-Concatenated Coding for Low Complexity Power Efficient Cooperative Communication", to appear in Proceedings of the IEEE Vehicular Technology Conference (VTC-2009 Fall), September 2009, Anchorage, Alaska, USA.

11. M. F. U. Butt, **R. A. Riaz**, Ng, S. X. Ng and L. Hanzo, "Near-Capacity Iterative Decoding of Binary Self-Concatenated Codes with Soft Decision Demapping by Employing 3-D EXIT Charts", submitted in *IEEE Transactions on Wireless Communications*.

12. M. F. U. Butt, **R. A. Riaz**, Ng, S. X. Ng and L. Hanzo, "Distributed Self-Concatenated Coding for Cooperative Communication", submitted to *IEEE Transactions on Vehicular Technology*.

Contents

List of Symbols

General notation

- The superscript * is used to indicate complex conjugation. Therefore, a^* represents the complex conjugate of the variable a.
- The superscript ^{T} is used to indicate matrix transpose operation. Therefore, $\mathbf{a}^T$ represents the transpose of the matrix $\mathbf{a}$.
- The superscript † is used to indicate complex conjugate transpose operation. Therefore, $\mathbf{a}^\dagger$ represents the complex conjugate transpose of the matrix $\mathbf{a}$.
- The notation $\tilde{x}$ represents the estimate of x.

Special symbols

J: Number of source symbols.

T_F: Frame duration.

L: Number of frames.

$\phi(t)$: Signalling pulse shape.

T_{PP_n}: PPM-related shift in the pulse position.

R: Number of resolvable paths.

m_r: Nakagami fading parameter.

$\mathbf{A}$: Overall system matrix.

$\mathbf{n}$: Noise sequence.

$\mathbf{d}$: User data vector.

σ^2: Variance of the noise sequence.

N_s: Spreading factor.

Q: Number of VLC encoders.

$\Psi_a^o(\Upsilon^n)$: *A priori* LLR sub-frame.

$\Psi_p^o(\Upsilon^n)$: *A posteriori* LLR sub-frame.

$\Psi_p^o(\Upsilon)$: *A posteriori* LLR frame.

$\tilde{\Upsilon}$: Transmission frame estimate.

$\tilde{\Gamma}^n$: Source symbol frame component estimates.

$\{VLC^n\}_{n=1}^{Q}$: VLC codebooks.

ρ: Jamming factor.

T_s: Symbol interval.

S: Number of chips.

$\mathbf{h}^{(u)}$: UWB channel impulse response.

W: Samples during the chip interval.

N_u: Number of users.

Λ: Cluster arrival rate.

λ: Ray arrival rate.

Γ: Cluster decay factor.

γ: Ray decay factor.

T_b: Bit duration.

T_c: Chip duration.

h_u: Gain of the resolvable multipath component.

ϕ_u: Phase of the resolvable multipath component.

$\mathbf{R}_b$: Covarience matrix of information symbols.

$\mathbf{R}_n$: Covarience matrix of the noise.

N_o: AWGN power spectral density.

$\beta_{w,l}$: The wth ray-magnitude of the lth CIR-tap-cluster.

T_l: Delay of the lth cluster.

$\tau_{w,l}$: Delay of the wth ray relative to the lth cluster's arrival time T_l.

Θ_j: Magnitudes of the corresponding cluster components.

ξ_m: Statistically independent positive random variable having a Nakagami-m probability density function.

T_d: Sampling duration.

$\Psi^{\dagger}$: Power spectral density of the received UWB signal.

P: Transmitted signal power.

P_b: Probability of bit error.

P_J: Power of a single jamming tone.

P_{NJ}: Total power of noise jammer.

$\phi_n(t)$: PSWFs of order.

Ξ_n: Eigenvalues of $\phi_n(t)$.

Ω: Bandwidth.

Chapter 1

Introduction

According to Stanley Wang, Berkeley University [10] UWB Group: *"As opposed to traditional narrowband radios, Ultra-WideBand (UWB) is a wireless digital communication system exchanging data using short duration pulses. The complexity of the analog front-end in UWB is drastically reduced due to its intrinsic baseband transmission. Based on this simplification and the high spreading gain it possesses, UWB promises low-cost implementation with fine time resolution and high throughput at short distances without interfering with other existing wireless communication systems."*

UWB transmission techniques may be loosely defined as a family of wireless transmission schemes whose bandwidth (B) is more than 25 percent of the carrier frequency, or more than 1.5GHz [11, 12]. Alternatively, according to the Federal Communications Commission (FCC), UWB signals occupy a bandwidth of at least 500MHz in the 7.5GHz chunk of spectrum between 3.1GHz and 10.6GHz [13]. An UWB radio communicates using baseband pulses of very short duration, typically on the order of a nanosecond, thereby spreading the energy of the radio signal very 'thinly' (about a few μW per MHz) from near DC to a few GigaHertz. Because of the broad spectrum of this signal, which we typically associate with an appropriately shaped signalling impulse, this system is also referred to as Impulse Radio (IR) [12]. An interesting point to mention is that the most popular implementation of UWB systems is not a carrier-based system. More explicitly, it is a baseband system having a Power Spectral Density (PSD) that occupies frequencies stretching from near DC to a few Gigahertz [14]. The terminology of a carrierless system implies that it could be manufactured inexpensively. Furthermore, its baseband operation at low frequencies improves its capability of penetrating materials that tend to become more opaque at higher frequencies. Many properties of UWB systems are fundamentally different from those of RF communications. Again, instead of using a carrier frequency, as traditional systems, UWB systems transmit high-bandwidth carrierless radio impulses using extremely accurate timing [15].

1954	*Author:* De Rosa *et al.* [16] *Contribution:* The concept of a pulse generation system was introduced, where the occurance of a pulse was a random event.
1968	*Author:* Ross [17] *Contribution:* A time-domain solution was proposed for creating wideband radiating elements.
1973	*Author:* Ross [18] *Contribution:* The generation and reception of base-band signalling pulses was proposed. U. S. Patent
1978	*Authors:* Bennett and Ross *et al.* [19] *Contribution:* Introduction of the baseband pulse generation concept.
1980	*Author:* Harmuth [20] *Contribution:* The concept of synthetic aperture radar was introuduced, which was related to the UWB concept, because high bandwidth pulse position and pulse shape coding was used.
1990	The Defense Advanced Research Projects Agency (DARPA) and the Office of Secretary of Defense (OSD) assess the UWB technology, with the aid of the UWB Radar Review Panel, R6280, OSD.
1993	*Authors:* Kim, Didomenico, Jasper, Youmans and Koscica *et al.* [21] *Contribution:* A photoconductive switch coupled to an energy storage device was proposed for UWB high-power photon-triggered frequency-independent signal generation. U.S. Patent.
1993	*Author:* Scholtz *et al.* [22] *Contribution:* The features of a time-hopping modulation format employing impulse-based signalling were outlined.
2000	Federal Communications Commission, USA [13] Notice of Proposed Rule Making (NPRM) FCC 00-163, ET Docket 98-153, in the matter of revision of Part 15 of the commissions rules regarding UWB transmission systems.

Table 1.1: UWB advances part(1).

2002	*Authors:* Hamalainen, Hovinen, Tesi, Iinatti and Latva-Aho [23] *Contribution:* The evaluation of the level of interference imposed by different UWB signals on other radio systems, as well as the quantification of the performance degradation of UWB systems in the presence of narrowband interference and pulsed jamming.
2004	*Authors:* Yang and Giannakis [11] *Contribution:* A tutorial overview of UWB communications was presented along with different research aspects to be explored in the future.
2006	*Authors:* Molisch, Cassioli, Chong, Emami, Fort, Kannan, Karedal, Kunisch, Schantz, Siwiak and Win [24] *Contribution:* A comprehensive statistical model is proposed for UWB propagation channels that is valid for a frequency range spanning from 3 to 10 GHz.
2007	*Authors:* Bacci, Luise, Poor and Tulino [25] *Contribution:* A game-theoretic model for studying power control desgined for UWB wireless data networks operating in frequency-selective multipath environments was analyzed.
2009	*Authors:* Gezici and Poor [26] *Contribution:* The problem of position estimation in UWB systems employing various position estimation techniques was considered, with an emphasis on time-based approaches, which are particularly suitable for UWB positioning systems.

Table 1.2: UWB advances part(2).

Naturally, impulse radio signals are also subject to propagation impairments, even in benign propagation environments, which determine the achieveable Signal-to-Noise Ratio (SNR) and hence the attainable transmission rate. However, UWB systems benefit from a high diversity order, since owing to their high bandwidth, they have a high number of independently fading multipath components. Furthermore, they are capable of accommodating a high number of users even in multipath environments, as a benefit of their high bandwidth [11]. Hence UWB systems may revolutionize home media networking, facilitating the downloading of images from a digital camera to a computer, distributing HDTV signals from a single receiver to multiple TV sets around the house, connecting printers to computers, and potentially replacing any electronic signalling cables on the premises [27], except of course for main cables.

The idea of UWB dates back to the 1980s [28]. UWB impulses are transmitted in

sub-nanosecond intervals, which inherently leads to a high bandwidth and-as a benefit-to an accurate spatial resolution, which can be taken advantage of in positioning applications. The associated high signalling impulse rates facilitate high connection speeds over short distances. Since UWB signals occupy a broad spectrum, low transmission powers must be used in order to avoid interference with existing Radio Frequency (RF) systems. A common approach is to set the UWB power levels so low that the signals cannot be distinguished from external noise imposed by other systems operating at overlapping frequencies. However, the concepts have mainly been used in radar-based applications only, since the timing and synchronization requirements of UWB communications have been too challenging for creating cost-effective consumer products. Recent developments in semiconductor technology have brought the applications closer to realization and the regulatory steps taken in the US also indicate a trend towards accelerating research efforts. Tables 1.1 and 1.2 give an overview of past advances in the field of UWB communications.

1.1 Literature Survey of UWB Systems

UWB devices are limited to radiated power spectral densities that are potentially lower than the level of unwanted emissions allowed by other RF services [29]. Due to their low PSDs, UWB devices are categorized as unlicensed devices. However, they must adhere to PSD limits that are typically lower than those specified for the family of general Part 15 devices defined in [13]. Although they are unlicensed, some categories of UWB devices are limited to employment by personnel licensed in other (non-radio) professions [30, 31]. The main characteristics of UWB systems can be summarized as follows [32–34]:

- Ultra short duration pulses$\Longrightarrow$Ultra wideband signals;
- Extremely low power spectral density;
- High bandwidth in comparison to the center-frequency of the band used;
- Excellent immunity to interference from other radio systems;
- Coexistence with conventional radio systems;
- Time-hopping or frequency-hopping multiple access spread spectrum operation;
- Low duty cycle;
- Fine time resolution;
- The propagation environment has numerous independently fading resolvable multipath components;

- Low interference (similar to noise) and good interference rejection;
- Almost undetectable by malicious eavesdropping, hence it is inherently covert;
- Combined communication and positioning capabilities;

In the early evolution of UWB systems, the home appeared to be the natural environment for UWB applications. This is because of their limited coverage and their limited capabilities in handling bursty rather than periodic packet based traffic due to the relatively slow synchronization procedures available. In contrast to the example of 802.11 WLAN systems, the initial synchronization of UWB systems is typically three orders of magnitude slower [35]. This is problematic, when an arbitrary number of users attempt to acquire access to the channel in order to transfer small bursts of data, as in multi-user wireless Internet environments, for example. As opposed to the traffic models of Internet browsing, home applications usually require more static connections (e.g. downloading pictures from a digital camera or transferring a video signal), and in this application area UWB systems do well owing to their high throughput. Furthermore, the regulatory aspects and requirements of low interference with other systems are more easily tackled within the home than in outdoor applications [36–38].

1.2 UWB Transceiver

Since UWB communications rely on having an ultra-wide bandwidth, the first question that arises is, how high the transmission-rate can be and what type of modulation schemes should we use to approach this capacity? These issues will be discussed in the following sections.

1.2.1 Channel Capacity

In order to quantify the achieveable throughput, let us consider first the Additive White Gaussian Noise (AWGN) channel. The achieveable capacity is quantified by the well-known Shannon capacity formula of [39],

$$C = W log_2\big(1 + \frac{P_{av}}{W N_o}\big), \tag{1.1}$$

where W is the bandwidth, P_{av} is the average power and N_o is the noise spectral density. If we transmit at the thermal noise level within a 1 GHz bandwidth, the associated transmission power, P_{av}, is -84 dBm, given a 50 Ohm front-end Radio-Frequency (RF) amplifier load resistance [40]. The associated noise power spectral density, N_o, depends on the receiver amplifier's noise. Based on the measurement data collected by the Berkeley

Wireless Research Center (BWRC), the noise power integrated from 0 to 1GHz is about -56 dBm and it may be treated as AWGN. In this scenario, the channel capacity based on Equation 1.1 is about 2 Mbps.

As a matter of fact, the noise is coloured due to narrowband interferers, such as cellular phones, wireless TV channels, etc. When assuming that the transmitted power is evenly distributed over the entire band, the channel capacity is calculated as,

$$C = \int_W log_2\big(1 + \frac{P_{av}}{W \cdot N(f)}\big)df. \tag{1.2}$$

Furthermore, if the transmitter knows the channel's frequency-domain response, the channel capacity becomes higher according to information theory, which may be exploited using water-filling [41]. More explicitly, the idea is to assign more power to those frequency bands whose noise level is lower, while maintaining the same total transmission power. Then the channel capacity becomes:

$$C = \int_{-W}^{W} log(1 + S(f) \mid C(f) \mid^2)df, \tag{1.3}$$

where $C(f)$ is the channel response and $S(f)$ is the PSD. It was suggested in [11] that the UWB channel capacity based on the measured UWB channel response may be about 40 Mbps, as long as the transmitter is capable of cumulatively assigning the power over the different frequency bands according to water-filling. Naturally, the channel-response is time-invariant and hence accurate water-filling-based power control in impulse-radio based UWB communication is difficult to implement. Nonetheless, this water-filling method provides us with a capacity estimate.

1.2.2 Impulse Radio UWB Transmission

Probably the most important UWB modulation technique is constituted by Time Hopping (TH), hence deserves a detailed discussion. The seminal characterization of impulse-radio based UWB systems was provided by Scholtz and Win [12, 15, 22, 27].

As mentioned, this is a multiple access technique based on TH. Hence at any point in time N_u number of users share the same band. Each user emits a pulse-train of his own. These pulses are referred to as monocycles, since they look like a single cycle of a sine wave. The multiple access capability is provided with the aid of time hopping. A typical hopping format is based on Pulse Position Modulation (PPM), where the signal transmitted by the i^{th} transmitter is given by

$$g^{(i)} = \sum_l \phi_{tr}(t - lT_f - s_l^{(i)}T_c - \varrho d^{(i)}_{\lfloor \frac{l}{N_s} \rfloor}), \tag{1.4}$$

where ϕ_{tr} represents the transmitted monocycle waveform (basic pulse) that nominally begins at time zero based on the transmitter's clock and the quantities with superscript

i denote transmitter-dependent quantities, which will differ from the quantities for the $(i+1)^{th}$ transmitter. Hence the signal emitted by the i^{th} user's transmitter consists of a large number of monocycle waveforms, appropriately shifted to different times depending on the modulating signal, where the l^{th} monocycle nominally starts at time instant $(lT_f - s_l^{(i)}T_c - \varrho d^{(i)}_{\lfloor \frac{l}{N_s} \rfloor})$. Let us now consider the structure of each component of the time shift in more detail.

1.2.2.1 Uniform Pulse Train Spacing

A pulse train of the form $\sum_l \phi_{tr}(t - lT_f)$ consists of monocycle pulses spaced T_f seconds apart in time. The transmission frame time or pulse repetition time T_f typically may be a hundred to a thousand times the monocycle duration, with its largest value constrained by the stability of the available clocks. The result is a signal having a low duty cycle.

Consequently, we can imagine that in a frame there are thousands of compartments and the pulse emitted from the kth user's transmitter occupies one of the compartments, say, the 10^{th} compartment. Other users occupy the rest of the compartments. Now, if for all the frames, the pulse emitted by the i^{th} transmitter occupies the same compartment (the pulses will be uniformly spaced for a given transmitter), the system becomes vulnerable to catastrophic collisions, when a large number of pulses are received from two different users at the same time instances, similarly to ALOHA systems. In order to avoid this potential problem, the above-mentioned compartments of the users may be hopped according to a pseudo-random sequence.

1.2.2.2 Pseudo-random Time-Hopping

To eliminate catastrophic collisions owing to multiple access, each user's link (indexed by i) is assigned a distinct pulse shift pattern $s_l^{(i)}$, which we refer to as a time hopping code. These hopping codes $s_l^{(i)}$ are periodic pseudo-random codes with a period N_p, $s^{(i)}_{l+kN_p} = s_l^{(i)}$ for all integers l and k. Each pseudo-random code index is an integer in the range of

$$0 \leqslant s_l^{(i)} \leqslant N_h. \tag{1.5}$$

The pesudo-random time hopping code therefore provides an additional time shift for each signalling pulse in the pulse train, with the l^{th} monocycle undergoing an added shift of $s_l^{(i)}T_c$ seconds. Hence the added time shifts caused by the code are discrete times between 0 and N_hT_c.

A simple example will further clarify the concept. Say, for transmitter 1 ($i = 1$), the pseudo-random sequence is $\{1, 4, 7, 2, \dots\}$, in which case the pulse from transmitter 1 will occupy the 1^{st} compartment in the 1^{st} frame, 4^{th} compartment in the 2^{nd} frame, 7^{th} compartment in the 3 frame and so on. This way the position of the pulse will keep

on hopping from compartment to compartment, hence the terminology time hopping. We assume furthermore that

$$N_h T_c \leqslant T_f \tag{1.6}$$

and hence the ratio $\frac{N_h T_c}{T_f}$ indicates the fraction of the frame duration T_f over which time hopping is allowed. Since a short but nonetheless non-negligible time interval is required to read the output of a monocycle correlator and to reset the correlator, we assume that $\frac{N_h T_c}{T_f}$ is strictly less than 1. If $\frac{N_h T_c}{T_f}$ is too small, then the probabilistic event of encountering collisions remains significant. Conversely, given a sufficiently large value of $\frac{N_h T_c}{T_f}$ and well-designed codes, the multiple access interference encountered in many situations can be modeled as a Gaussian random process. This is an important issue, since different interference statistics require different receiver structures. Under the Gaussian distributed interference assumption, the optimal receiver structure takes a simple form. Hence $\frac{N_h T_c}{T_f}$ is kept close to 1.

The hopping code is periodic with a period of N_p, hence the waveform $\sum_l \phi_{tr}(t - lT_f - s_l^{(i)} T_c)$ is also periodic with a period of

$$T_p = N_p T_f. \tag{1.7}$$

Next we briefly discuss the data modulation.

1.2.2.3 Data Modulation

The input data sequence $d_l^{(i)}$ of transmitter i is a binary (0 or 1) symbol stream. We consider an oversampled modulation scheme associated with N_s monocycles transmitted per symbol, where the modulating data symbol changes only once every N_s hops. Upon assuming that a new data symbol is represented by the pulse index $l = 0$, the index of the data symbol modulating pulse l is $\lfloor \frac{l}{N_s} \rfloor$, where the notation $\lfloor \bullet \rfloor$ denotes the floor function. In this modulation method, when the input data symbol is a logical 0, no additional time shift is imposed on the monocycle, but a time shift of ϱ is imposed on a monocycle when the input symbol is a logical 1. Other forms of data modulation can also be employed to improve the performance of the synchronization loops, or the achieveable interference rejection capability, or, alternatively to reduce the implementation complexity, etc. Naturally, the data modulation further smoothens the PSD of the pseudo-random code based time-hopping modulation.

In short, we can say that we are sending N_s number of so-called transmission frames per data symbol, i.e. N_s number of monocycles per data symbol instead of a single pulse per symbol, so that the probability of correct reception increases. Hence, a single symbol has a duration of $T_s = N_s T_f$. For a fixed frame duration, i.e. pulse repetition time T_f, the binary symbol rate R_s determines the number N_s of monocycles that are modulated by a

given binary symbol, as formulated by

$$R_s = \frac{1}{T_s} = \frac{1}{N_s T_f}. \tag{1.8}$$

Let us now consider the characteristics of carrier-free UWB communications.

1.2.3 Carrier-free UWB

In the carrier-free UWB approach [11] the baseband pulse is directly fed to the antenna. In carrier-free UWB systems the information can either be transmitted using on/off keying [12] or PPM. Generally, a large number of pulses is used to convey a single information symbol. At the receiver, the pulses are coherently combined, resulting a substantial diversity gain. Instead of transmitting pulses at regular intervals, the pulse positions can be defined according to a user's specific positioning code. The advantage of this so-called dithering technique is that the transmitted signal appears noise-like in the spectral domain, hence the interference imposed on other systems operating in the same frequency band appears to be increased noise. Furthermore, different codes can be used to separate users, similarly to the multiple access philosophy of conventional Code-Division Multiple-Access (CDMA) systems.

The FCC plans to limit the UWB power levels to that allowed for unintentional emissions as specified in Part 15 of [13] and to restrict operation to frequency bands above 2 GHz.

1.2.4 Transmitted Pulse Shape

Dissimilarly to conventional narrow-band transmissions, where the baseband signal is typically modulated onto a radio frequency carrier, in IR no carrier frequency is used and the transmission scheme consists of a simple pulse generator. Moreover, the extremely short temporal duration of the pulses (fractions of a nanosecond) assures that we are using a wide bandwidth in the frequency domain that usually spans up to a few GHz. We can find numerous UWB signalling pulses in the literature [42], each referring to a particular application.

1.2.4.1 Gaussian Shape

The so-called Gaussian waveform is the most widely used signalling pulse shape. The zero-mean Gaussian function is described by:

$$G(x) = \frac{1}{\sqrt{2\pi\sigma^2}} e^{-\frac{x^2}{2\sigma^2}}, \tag{1.9}$$

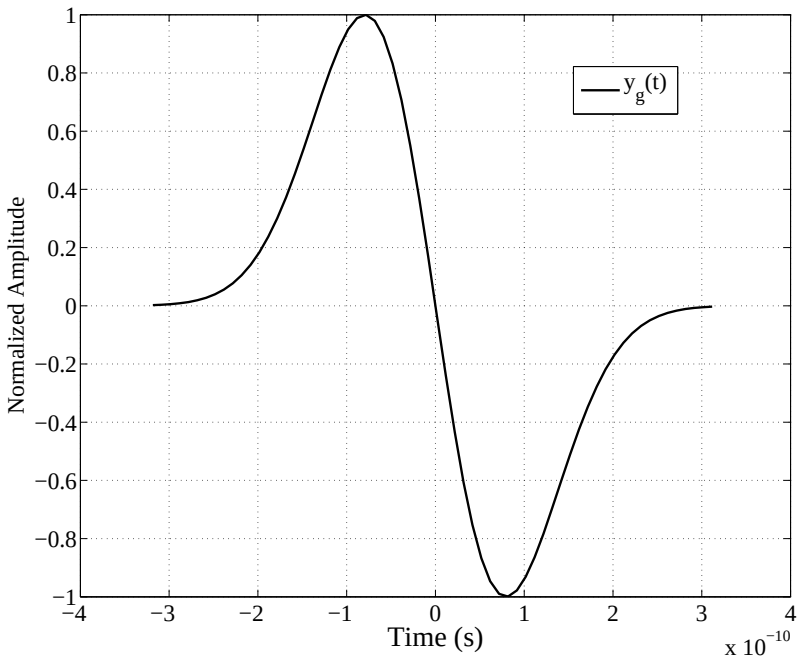

Figure 1.1: A Gaussian pulse shape in the time domain

where σ is the standard deviation. The basis of these Gaussian waveforms is a function represented by the following equation:

$$y_g(t) = Ke^{-(\frac{t}{\tau})^2} \tag{1.10}$$

where $-\infty < t < \infty$, τ is the time scaling factor and K_1 is a constant. Figures 1.1 shows the Time Domain (TD) shape of the Gaussian pulse its Fourier Transform is shown in Figure 1.2. We can find many other UWB signalling pulses in the literature which have different frequency domain representations [42].

1.2.5 Power Spectral Density

A periodic signal $w(t)$ having a time period of T_o may be formulated as

$$w_{T_o}(t) = \sum_{n=-\infty}^{\infty} g(t - nT_o), \tag{1.11}$$

where $g(t)$ is the signalling pulse. Equation 1.11 has a Fourier transform of

$$W_{T_o}(f) = \frac{1}{T_o} \sum_{n=-\infty}^{\infty} G\left(\frac{n}{T_o}\right)\delta\left(f - \frac{n}{T_o}\right). \tag{1.12}$$

The Fourier transform of a periodic signal is constituted by a line-spectrum, where the line frequencies are separated by $\frac{1}{T_o}$. Hence, when the duration of the period increases, the spectral resolution also increases. Therefore the beneficial effect of using a hopping code is to reduce the power spectral density from that of the line spectral density of $\frac{1}{T_f}$, where

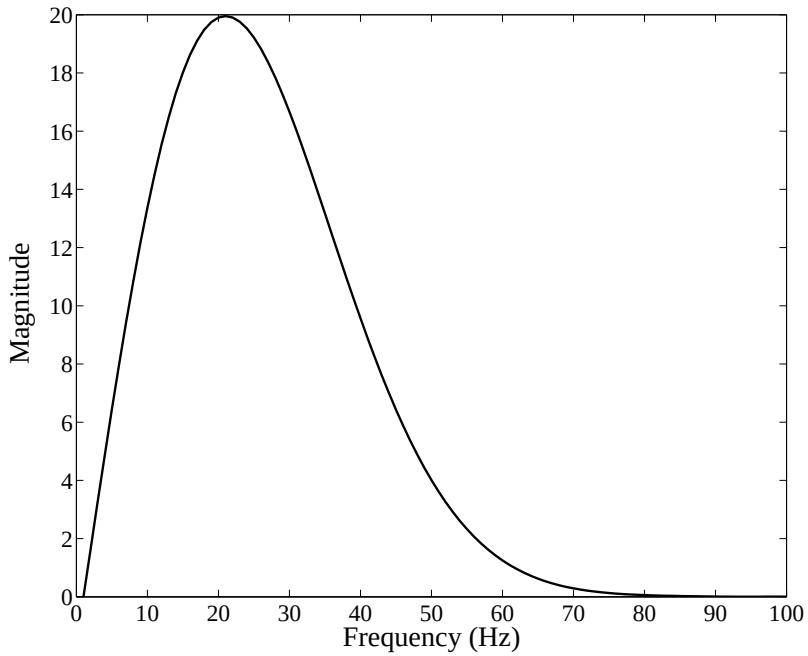

Figure 1.2: Fourier transform of the TD gaussian pulse

the FD lines are a distance of $\frac{1}{T_f}$ apart for the uniformly spaced line-spectrum down to a proportionally reduced spectral density having a finer line spacing of $\frac{1}{T_p}$, since we have $T_p > T_f$. Again, the power spectral density is regulated by the FCC. Therefore, one has to reduce the energy of any spikes in the frequency domain in order to satisfy the FCC regulations. This is another reason, why we introduce a pseudo random hopping-sequence in conjunction with PAM.

1.2.6 Receiver Model

The architecture of the system is constructed to ensure that the baseband signal processing output directly feeds into the antenna. Not discussed here are the issues of amplification, filtering and quantization, which are carried out at the analog front-end. Figure 1.3 potrays the entire receiver processing chain of the UWB communication system. An UWB signalling pulse is generated and transmitted by a pulse generator and a wideband antenna. The Gaussian-shaped time domain pulse may be employed [42] although other shapes might have different benefits depending on which type of antenna is used [42]. The benefit of the Gaussian-shaped time-domain pulse is that at a given signalling rate its frequency-domain spectrum is as compact as possible [42].The bandwidth of the signalling pulse may span from say 10MHz to a couple of GHz. The resultant wideband signal propagates through a multipath channel, which may distort the pulse shape, but the resultant independently fading signal replicas may be combined in order to achieve a diversity gain with the aid of Rake receivers.

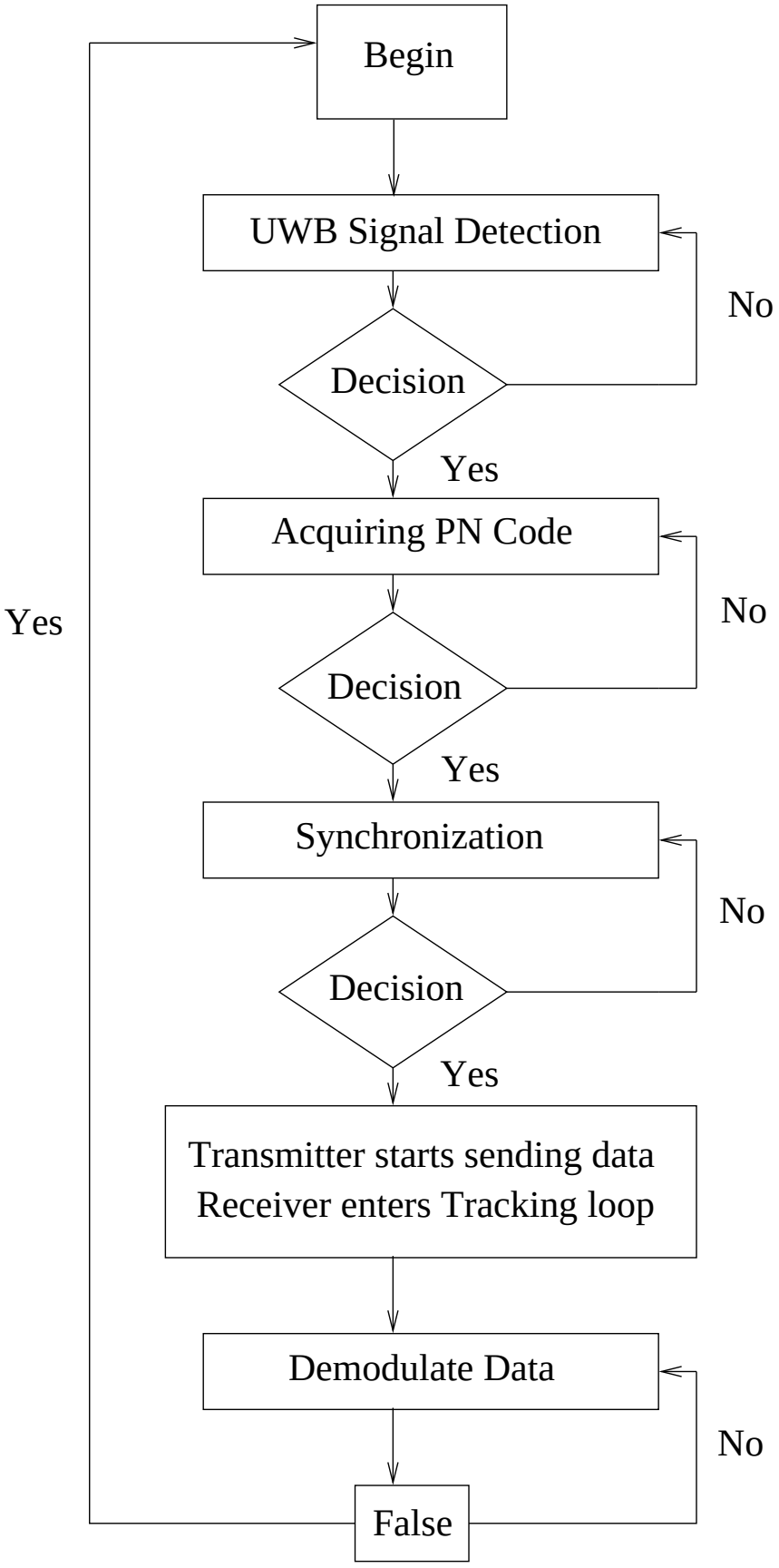

Figure 1.3: Flow-chart of the UWB receiver's operation

1.2.7 Demodulation

Since the UWB PSD spans a wide band, when it is transmitted through the propagation medium, even under benign channel conditions, the signalling pulses undergo linear distortion. Hence naturally, the received pulses are different from the transmitted pulses. When N_u user-links are active in a multiple-access system, then the received signal $r(t)$ can be modeled as

$$r(t) = \sum_{i=1}^{N_u} A_i s_{rec}^{(i)}(t - \tau_i) + n(t), \tag{1.13}$$

where A_i models the attenuation of the signal of user i over the propagation path to the receiver, while τ_i represents the time difference between the clocks of transmitter i and the receiver. The waveform $n(t)$ represents the AWGN Noise.

Let us now assume that the receiver is interested in determining the data sent by transmitter 1. If only a single signal is present, then we have

$$r(t) = A_1 s_{rec}^{(1)}(t - \tau_1) + n(t). \tag{1.14}$$

When appropriately synchronized, e.g. having learnt the value of τ_1 (or at least τ_1 mod $N_P T_f$), the receiver is ready to determine a sequence of signalling pulses, with the interval T_i containing the waveform of repeated pulses representing a specific data bit . When perfectly synchronized to the first user's signal, the receiver is then confronted with a standard hypothesis-testing problem formulated as

$$H(0) : r(t) = A_1 s^{(1)} w_{bit}(t - \varrho d) + n(t), \tag{1.15}$$

where the data d is either 0 or 1, and the observation takes place over the time interval of $t \in T_i$. The waveform during this time interval is given by

$$w_{bit}(t) = \sum_{l=jN_s}^{(j+1)N_s-1} w_{rec}(t - lT_f - c_l^{(1)} T_c - \tau_1). \tag{1.16}$$

Let us now introduce the so-called template signal of [12]

$$\begin{aligned} v_{bit}(t) &= w_{bit}(t) - w_{bit}(t - \varrho) \\ &= \sum_{l=jN_s}^{(j+1)N_s-1} v_{rec}(t - lT_f - c_l^{(1)} T_c - \tau_1) \end{aligned} \tag{1.17}$$

where the embedded single pulse template signal is

$$v_{bit}(t) = w_{rec}(t) - w_{rec}(t - \varrho). \tag{1.18}$$

Let us now consider a Pulse Position Modulated (PPM) scheme where $w_{rec}(t)$ is received for a transmitted logical 0 and $w_{rec}(t - \varrho)$ for a logical 1. Hence the signal-space has two legitimate signals, where $w_{rec}(t)$ and $w_{rec}(t - \varrho)$ are used as the basis functions. Hence

the optimal receiver, which turns out to be a simple correlation receiver for a single signal, simply multiplies the received signal by both $w_{rec}(t)$ as well as $w_{rec}(t-\varrho)$ and then evaluates the difference of the correlator outputs. Hence, the signal to be compared to the threshold 0 is

$$s = \int_{t=0}^{T} r(t) w_{rec}(t) dt - \int_{t=0}^{T} r(t) w_{rec}(t-\varrho) dt, \tag{1.19}$$

which can be written as

$$s = \int_{t=0}^{T} r(t)(w_{rec}(t) - w_{rec}(t-\varrho)) dt. \tag{1.20}$$

Hence, if we now multiply the received signal $r(t)$ by $v_{bit}(t) = w_{rec}(t) - w_{rec}(t-\varrho)$, then the receiver correlator's output becomes

$$s = \int_{t=0}^{T} r(t) v(t) dt. \tag{1.21}$$

Note however that $w_{rec}(t)$ and $w_{rec}(t-\varrho)$ are legitimate basis functions iff they are orthogonal, i.e. if $\varrho > w_{rec}(t)$ satisfied. However,it is not possible to satisfy this condition with the aid of finite-duration pulses. Hence in practice the functions no longer remain orthogonal. The optimal decision rule is

$$\underbrace{\sum_{l=0}^{N_s-1} \overbrace{\int_{\tau_1+lT_f}^{\tau_1+(l+1)T_f} r(t) v_{rec}(t - lT_f - c_l^{(1)} T_c - \tau_1) dt}^{pulse-correlator-output \triangleq \alpha_l}}_{test-statistic \triangleq \alpha} > 0 \tag{1.22}$$

when the transmitted bit is a logical 0. If the number of users is high and no multi-user detector is used, then it is reasonable to approximate the combined effect of the dehopped interfering signals by a Gaussian Process.

1.3 UWB Multiple Access Techniques

The most popular multiple access techniques in UWB communications are:

- **Direct Sequence Spread Spectrum**
- **Time Hopping**

1.3.1 Direct Sequence Spread Spectrum

In classic Direct Sequence Spread Spectrum (DSSS) based UWB systems [43–47], the signalling pulse transmissions are controlled by a pseudo random noise code, obeying an appropriate finite-bandwidth chip waveform generating an UWB signal. The v^{th} data bit

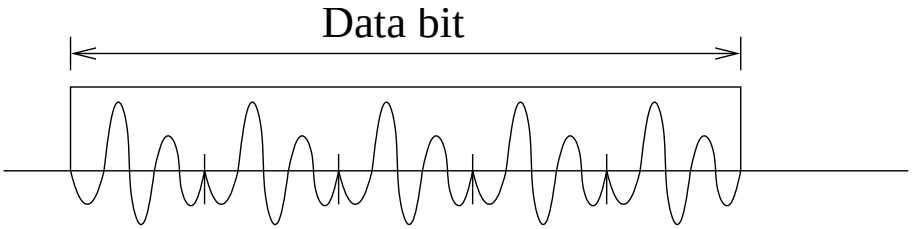

Figure 1.4: DS-UWB

of user u can be transmitted using Binary Pulse Amplitude Modulation (BPAM) and the corresponding transmitted signal $g^{(u)}(t)$ is formulated as:

$$g^{(u)}(t) = \sum_{v=0}^{\infty} \sum_{q=0}^{Q-1} \psi(t - vT_s - qT_c) s_q^{(u)} m_v^{(u)}, \tag{1.23}$$

where $\psi(t)$ is the chip waveform representing the UWB pulse, which controls the bandwidth of the UWB signal, $m_v^{(u)}$ corresponds to the data information of user u, T_c is the chip duration and $s_q^{(u)}$ is the q^{th} chip of the spreading code of user u. We assume that a block of data consisting of M bits is transmitted within the block duration of $0 < t \leq MT_b = T_s$, where T_b is the bit duration. The DSSS waveform $s^{(u)}(t)$ of user u consists of the aforementioned periodic sequences having a length of Q chips, which can be expressed as $s^{(u)}(t) = \sum_{q=0}^{Q-1} s_q^{(u)} \psi(t - qT_c)$, where $s_q^{(u)}$ assumes a value of +1 or -1. Figure 1.4 potrays the data bit of a DS-UWB signal.

1.3.2 Spreading Sequences

Below we briefly highlight the spreading sequences, which are widely employed.

1.3.2.1 m-Sequences

The family of m-sequences constitutes the largest set of codes that can be generated by a Linear Feedback Shift Register (LFSR) of a given length. Hence they are also referred to Maximal-Length Sequences (MLS). A m-sequence can be expressed as a ratio of finite-order polynomials as [48]

$$\begin{aligned} \mathbf{C(D)} &\triangleq \frac{\mathbf{P_g(D)}}{\mathbf{P_c(D)}} \\ &= \frac{\sum_{k=1}^{n} w_k D^k \left(e_{-k} D^{-k} + ... + e_{-1} D^{-1}\right)}{1 + \sum_{k=1}^{n} w_k D^k}, \end{aligned} \tag{1.24}$$

where $\mathbf{P_c(D)}$ is referred to as the characteristic polynomial of the LFSR sequence generator, which depends solely on the vector $w_1, ..., w_n$, describing the connection polynomial of the

LFSR and determines the main characteristics of the generated m-sequence. By contrast, the polynomial $\mathbf{P_g(D)}$ in the numerator depends on the initial condition of the LFSR, which is determined by the vector $e_{-n}, e_{-(n-1)}, ..., e_{-1}$, determining the phase shift of the sequence. The LFSR's connection vector w and the sequence vector e are related to each other by

$$\begin{aligned} e_i &= w_1 e_{i-1} + w_2 e_{i-2} + ... + w_n e_{i-n} \\ &= \sum_{k=1}^{n} w_k e_{i-k}. \end{aligned} \tag{1.25}$$

The period of the sequence generated by the aforementioned configuration will be $Q = 2^n - 1$. The Auto-CorreLation (ACL) of an m-sequence can be calculated as

$$\mathbf{R_{kk}(0)} = Q \tag{1.26}$$

$$\mathbf{R_{kk}(q)} = -1 \qquad for \quad q \neq 0. \tag{1.27}$$

These ACL properties are near-ideal for code acquisition or synchronization, where the perfectly aligned condition of $q = 0$ between the received and locally stored sequences has to be detected, as shown in Figure 1.5a. As an additional constraint, in multiuser communication a large set of spreading sequences exhibiting low Cross-CorreLation (CCL) values is needed. Unfortunately, the m-sequences do not satisfy this requirement, since some m-sequence pairs exhibit high CCL values [49].

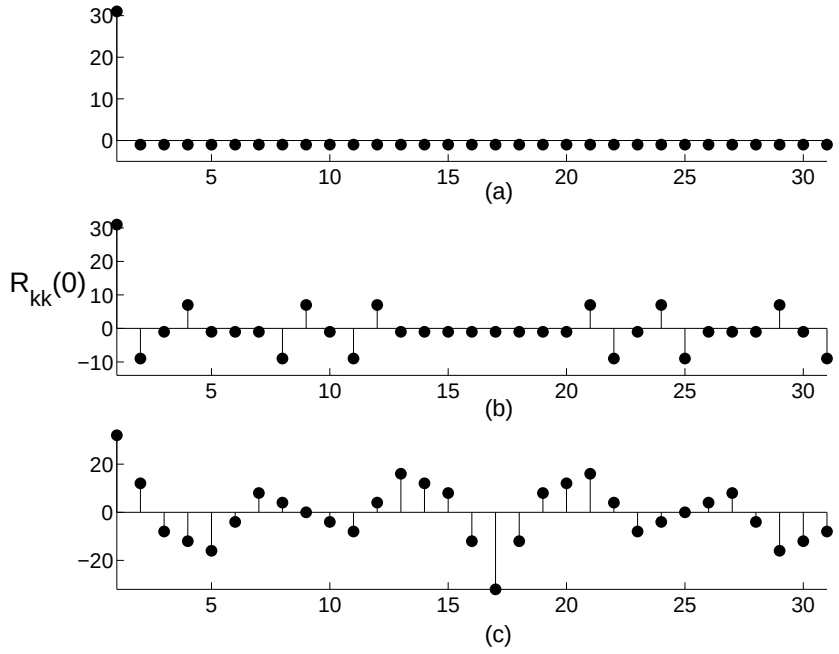

Figure 1.5: The ACLs of m (top), Gold (middle) and Walsh (bottom) spreading sequences of length $Q = 31$.

1.3.2.2 Gold Sequences

Gold Sequences (GS) are constructed from preferred pairs of m-sequences. The benefit of using Gold sequences is that there is a large number of codes in this family. The CCL between each pair of codes is the same and bounded over a set of codes available from a given generator. The family size of a Gold sequence set having a period of Q is $K = Q + 2$. The CCLs and out-of-phase ACLs i.e. asynchronous of Gold sequences have only three possible values, which are given by [49]

$$\mathbf{R_{kk}}(q) = \begin{cases} Q & \text{for } q = 0 \\ \{-1, -t(m), t(m) - 2\} & \text{for } q \neq 0, \end{cases} \tag{1.28}$$

$$\mathbf{R_{jk}}(q) = \{-1, -t(m), t(m) - 2\} \quad \forall q, j \neq k, \tag{1.29}$$

where

$$t(m) = \begin{cases} 2^{\frac{(m+1)}{2}} + 1 & m \text{ is odd} \\ 2^{\frac{(m+1)}{2}} + 1 & m \text{ is even.} \end{cases} \tag{1.30}$$

Figure 1.5b, potrays the ACL and CCL values evaluated from Equations (1.28) and (1.29).

1.3.2.3 Walsh-Hadamard Sequences

Walsh-Hadamard Sequences (WHS) are generated with the aid of Hadamard matrices for lengths of $Q = 2^n$ as follows [48]:

$$H_{2Q} = \begin{bmatrix} H_Q & H_Q \\ H_Q & \overline{H_Q} \end{bmatrix}, \tag{1.31}$$

where Q is a power of 2 and the bar denotes the binary complement of the bits in the matrix. The ACLs of WHSs are not particularly beneficial, as seen at the bottom of Figure 1.5 but their cross correlation is zero for synchronous sequences, which can be expressed as

$$\mathbf{R_{jk}}(q) = 0 \quad \forall q, j \neq k. \tag{1.32}$$

Let us now consider the basics of time hopping.

1.3.3 Time Hopping

The transmitted TH-UWB signal [50–55] conveying an M-ary symbol is generated by invoking L number of frames. Then the transmitted signal of the kth user can be expressed as:

$$u^{(k)}(t) = \sum_{m=0}^{\infty} \sum_{l=0}^{L} \varphi(t - mT_s - lT_f - s_m^{(k)}(l)T_h), \tag{1.33}$$

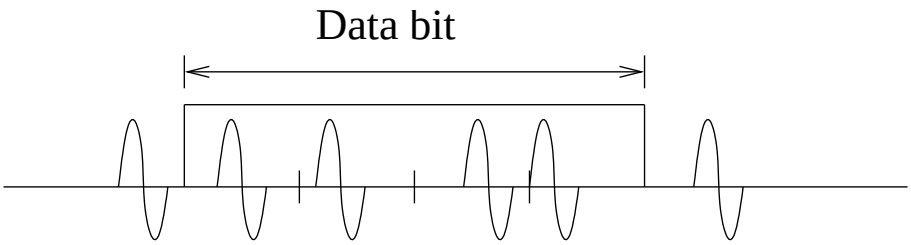

Figure 1.6: TH-UWB

where $\varphi(t)$ is the time domain UWB signalling pulse, $T_s = NT_f$ is the symbol duration, T_f is the frame duration, T_h denotes the time slot duration and $s_m^{(k)}(l)$ is TH code generated by the kth user's mth symbol:

$$\begin{aligned} \mathbf{S}_m^{(k)} &= \left[s_m^{(k)}(1), s_m^{(k)}(2), ..., s_m^{(k)}(L)\right] \\ &= \mathbf{X}^{(k)} \cdot \mathbf{1} \oplus \mathbf{t}_m^{(k)}, \end{aligned} \tag{1.34}$$

where $\mathbf{1}$ is the unit vector of length L and $\oplus$ denotes the modulo addition operation in the finite Galois Field (GF) having Q elements, $\mathbf{X}^{(k)}$ is the M-ary transmitted signal and $\mathbf{t_m^{(k)}}$ is the TH address code of user k given by:

$$\mathbf{t_m^{(k)}} = \left[t_m^{(k)}(1), t_m^{(k)}(2), ..., t_m^{(k)}(L)\right]. \tag{1.35}$$

Furthermore, each user k has a specific TH address code defined as above. Figure 1.6 potrays the data bit of a TH-UWB signal.

TH-UWB and Direct Sequence (DS) UWB have their own merits and disadvantages. The former has the advantages of low power-consumption owing to transmitting low-power baseband pulses and imposing a low signal-processing complexity as well as a beneficial multipath interference mitigation capability. By contrast, DS-UWB has a strong Multiuser Interference (MUI) mitigation capability because of assigning independent orthogonal codes to each user. Keeping the energy per bit constant for both systems, the peak to average power ratio and the power spectral density of the DS-UWB system are lower than those of the TH-UWB, because the energy per pulse is higher for the TH-UWB than for the DS-UWB arrangement. DS-UWB also imposes a reduced in-band interference on other systems operated in the frequency band of the UWB system.

1.4 Novel Contributions

This dissertation is based on the following publications and manuscript submissions [1–9], where the main novel contributions can be summarised as follows:

- Generic z-domain discrete-time transfer function estimation is proposed for ultra-wideband channels, which requires no channel sounding sequence transmission and

hence constitutes a blind technique. This is achieved by estimating the channel's impulse response based on the information signalling pulses and then equalising the effects of the channel by the corresponding inverse system. A complete inverse system is found and the corresponding recursive equation is provided for channel estimation [1].

- A generic Infinite Impulse Response (IIR) equalizer architecture is proposed for UWB systems, which halves the memory requirement of the conventional IIR equalizers. This is achieved by exploiting the aperiodically repeated clusters of negative-exponentially decaying segments of the Channel Impulse Response (CIR) and hence by providing a single common delay-line between the input and output of the equalizer. Furthermore, the stability of a general Linear Time-Invariant (LTI) UWB CIR model is investigated. The closed-form time-domain response of the so-called homogenous, non-homogenous and vectorial LTI system is developed. Furthermore, the normalized settling time of the step response is evaluated for diverse damping coefficients.

- The decoding convergence of both TH and DS-CDMA UWB systems communicating over multipath Nakagami channels is analyzed. The analysis is based on the novel semi-analytical tool of Extrinsic Information Transfer (EXIT) charts, where the UWB signal is constituted by serially concatenated pulse-position modulated TH and code-synchronous DS-CDMA. Our simulation results of the iteratively detected TH and DS-CDMA UWB schemes verify the accuracy of the EXIT chart analysis [5].

- A novel UWB DS-CDMA aided system designed for the IEEE 802.15.3a UWB channel specifications is proposed. Substantial performance improvements can be attained by serially concatenated channel encoding combined with a Unity Rate Code (URC). We compare the performance of the iterative decoding aided Correlation (Corr) and Minimum Mean Square Error (MMSE) detectors exchanging extrinsic information between the URC decoder as well as the outer Recursive Systematic Convolutional (RSC) decoder. Moreover, the iterative decoding convergence analysis of the proposed system is carried out with the aid of EXIT charts. As expected, the iteratively decoded fully-loaded system employing MMSE detection outperforms its counterpart employing the equivalent correlation detector [4].

- Furthermore, a serially concatenated and iteratively decoded Irregular Variable Length Coding (IrVLC) scheme is amalgamated with a unity-rate precoded TH-PPM aided Ultra-Wide Bandwidth UWB Spread-Spectrum (SS) IR design. The proposed design is capable of operating at low SNRs in Nakagami-m fading channels contaminated by Partial Band Noise Jamming (PBNJ) as a benefit of lossless IrVLC joint source and channel coding. Although this scheme may be readily used for lossless video or audio compression for example, we only used it in the thesis for lossless near-capacity data

transmission. A number of component Variable Length Coding (VLC) codebooks having different coding rates are utilized by the IrVLC scheme for encoding specific fractions of the input source symbol stream. EXIT charts are used to appropriately select these fractions in order to shape the inverted EXIT curve of the IrVLC and hence to accurately match that of the inner decoder, which allows us to achieve an infinitesimally low Bit Error Ratio (BER) at near-capacity SNR values [6].

- Finally a near-capacity TH-PPM based UWB IR system is proposed, which invokes iteratively detected Self-Concatenated Convolutional Codes (SeCCC) and employs the powerful design technique of EXIT charts. Orthogonal Prolate Spheroidal Wave Function (OPSWF) based signalling pulse shapes are used for the sake of minimizing the effects of both the MUI and Inter-Symbol Interference (ISI). RSC codes are employed as constituent codes combined with an interleaver for randomising the extrinsic information exchange between the constituent codes. Furthermore, a puncturer assists us in increasing the achievable bandwidth efficiency. Iterative decoding is invoked for exchanging extrinsic information between the hypothetical decoder components at the receiver end. The convergence behaviour of the decoder is analysed with the aid of bit-based EXIT charts [3, 7].

1.5 Outline of Thesis

Figure 1.7 gives an overview of the thesis chapters which is detailed below. In Section 1.1 we commenced by a rudimentary introduction to UWB systems, including a brief historical perspective of the field. Section 1.2 outlines the basic concepts of UWB transceivers in order to highlight the fundamental transmission and detection techniques. Chapters 2 to 4 will then provide detailed transceiver structures employing novel channel coding schemes for enhancing the achievable performance of UWB systems. Each chapter constitutes an evolutionary improvement of the previous chapter.

Chapter 2 deals with the UWB channel, which is one of the major factors differentiating UWB systems from their narrow-band counterparts. In Section 2.1 we commence with a brief review of the last two decades' advances in UWB channel estimation in Section 2.1. The z-domain transfer function of UWB channels is derived in Section 2.3 based on the specifications presented in the Section 2.2. This transfer function forms the basis of the proposed memory-efficient implementation of the equalizer advocated. Furthermore, the stability analysis and mean convergence bound of the UWB channel transfer function is finally presented in Section 2.5. The UWB channel model is then used by all the following chapters, when developing enhanced UWB systems.

Chapter 3 starts with the implications of appropriate diversity order selection in Sec-

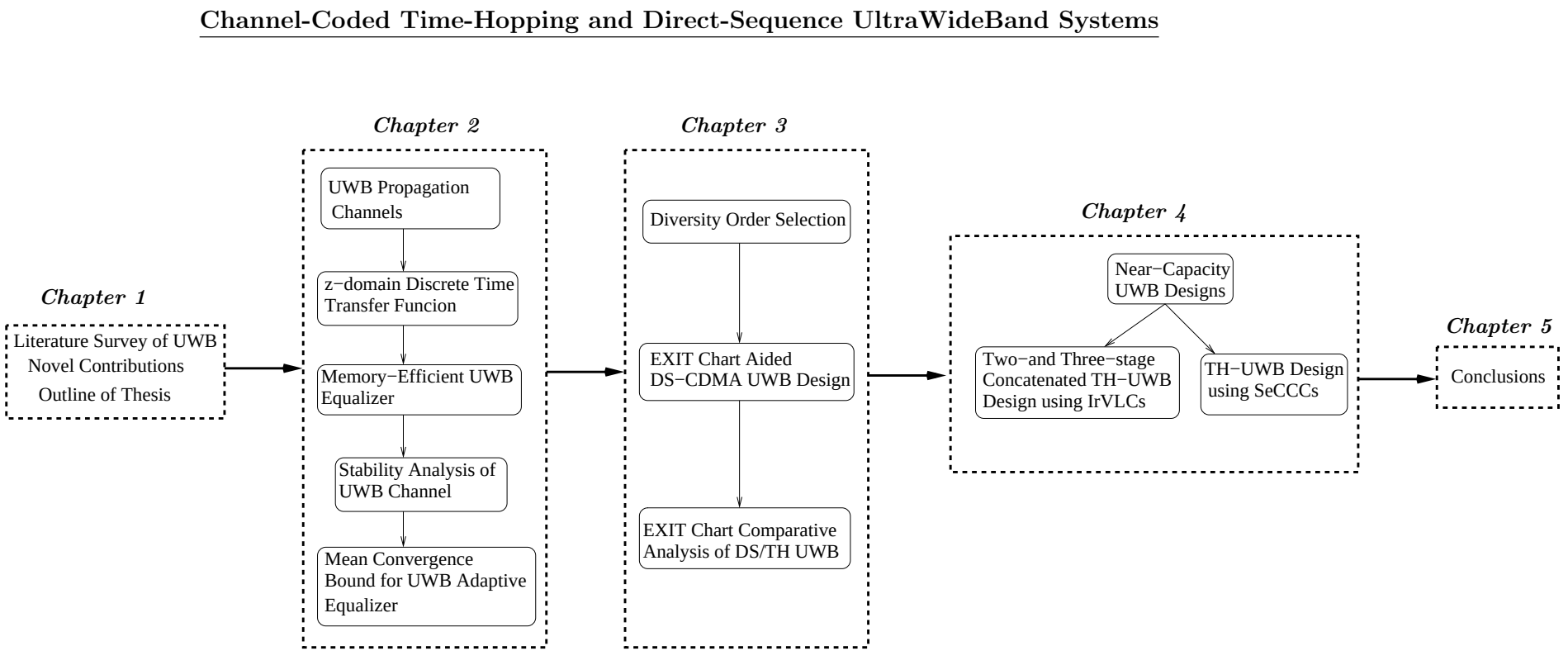

Figure 1.7: Outline of thesis.

tion 3.2. Since it is possible to resolve the closely spaced multipath components of the channel, the system benefits from a high number of independent fading paths, which results in a high multipath diversity gain. The system outlined in Section 3.3 uses a 2-stage serial concatenation of an inner and an outer encoders in conjunction with their corresponding decoders, which exchange extrinsic information for the sake of enhancing the attainable system performance. This system model constitutes the foundation for the following chapters, which will be further developed using different coding schemes with the aid of EXIT charts. Both DS and a TH-PPM UWB systems are studied using EXIT charts and it is demonstrated that classic so-called regular Forward Error Correction (FEC) encoders are unable to arbitrarily approach the system's capacity.

Hence Chapter 4 provides a solution for this problem by replacing the regular FEC codes with more sophisticated irregular FEC codes that are capable of approaching the system's capacity more closely. More specifically, we have used IrVLC [56, 57] in our designs of two-and three-stage concatenated UWB TH spread-spectrum impulse radio systems. To elaborate a little further, the irregular outer codec is comprised of a number of component codes, having a variety of coding rates. These different-rate component codes are invoked in order to generate specific fractions of the encoded bit sequence form specific input-bit segments, where the fractions may be specifically chosen in order to shape the EXIT function of the irregular outer code so that it matches that of the regular inner code. This facilitates the creation of an open EXIT chart tunnel and hence allows us to the achieve iterative decoding convergence to an infinitesimally low probability of error at channel Eb/No values that are close to the channel's capacity bound. In Section 4.3.2 we then progress from two-to three-stage irregular concatenated UWB systems. Naturally, an improved performance is only achievable at the cost of an increased complexity and interleaver length.

Hence Section 4.4 addresses the above-mentioned complexity and interleaver delay problem by invoking sophisticated binary self concatenated codes [58, 59] using different puncturing rates. In Section 4.4.1, we commence with a rudimentary introduction of a binary self concatenated code design, which is then used in Section 4.4.3 for developing a near-capacity TH UWB system. Furthermore, the achievable performance gains of different puncturing and coding rates are detailed in Section 4.4.3.1.

Finally, the main conclusions of the thesis and a range of furture research ideas are detailed in Chapter 5.

Chapter 2

UWB Channels

2.1 Introduction

The propagation of electromagnetic waves through walls and floors at carrier frequencies of 900 MHz, 1.8 GHz, 2.4 GHz, 5.85 GHz, 60 GHz has been studied by numerous researchers [60–62]. In many measurements, only the magnitude of the received signal was the quantity of interest. However, in UltraWideBand (UWB) communication systems, the received signal's phase or delay is also an equally important factor, because accurate phase information enables the receiver to coherently combine all UWB channel paths [63].

The propagation of UWB signals through various building materials has been reported in [24, 64]. Hashemi [65] has presented an excellent review and comparison of published results for different indoor penetration losses in the UWB frequency range. However, since the experimental conditions used were different, the statistically sound characterization of the indoor UWB propagation effects remains an open challenge. For example, in [65] significantly different measured values of 7 dB, 8.5-10 dB, 13 dB and 27 dB were cited for the insertion loss of concrete blocks. Moreover, in some cases, the relationship between the expected path loss and the operating frequency has not been satisfactorily addressed. Although the penetration-losses typically increase with frequency, in a ground floor experiment, de Toledo and Turkmani [66] reported average measured penetration losses of 14.2 dB, 13.4 dB, and 12.8 dB at 900 MHz, 1800 MHz, and 2300 MHz, respectively, which indicates a different trend. Zhang and Hwang [67] performed measurements in the frequency range of 900 MHz to 18 GHz. According to their investigations, the indoor penetration loss increases with frequency for a reinforced concrete wall, but this trend was not observed for plasterboard in [67].

Of special significance is a series of publications by Saleh and Valenzuela [68], Hashemi [72],

1987	*Authors:* A. Saleh and R. Valenzuela [68] *Contribution:* A statistical multipath model of the indoor radio channel is presented, which fits the measurements well and more importantly, appears to be extendable to other types of buildings.
1998	*Authors:* M. Z. Win and R. A. Scholtz [27] *Contribution:* Robustness of the UWB signal in multipath is quantified through cumulative distribution functions of the signal quality in various locations of the buildings considered.
1999	*Authors:* J. M. Cramer, R. A. Scholtz and M. Z. Win [69] *Contribution:* An iterative algorithm for the UWB channel's characterization is proposed and discussed.
2001	*Author:* J. R. Foerster [70] *Contribution:* Applied an analytical model to study the performance of an UWB system and characterized the associated performance trade-offs for different multilevel modulations as well as the benefits of RAKE reception.
2002	*Authors:* J. M. Cramer, R. A. Scholtz and M. Z. Win [71] *Contribution:* A comprehensive UWB propagation study, where the spatial and temporal components are decomposed into wave-fronts impinging on the receiver array.
2003	*Authors:* A. F. Molisch, J. R. Foerster and M. Pendergrass [64] *Contribution:* The modelling of ultrawideband wireless propagation channels encountered in Personal Area Networks (PAN) is detailed. The IEEE 802.15.3a standards task group has established a standard channel model to be used for the evaluation of the physical layer of PANs.
2006	*Authors:* A. F. Molisch, D. Cassioli, C. -C. Chong, S. Emami, A. Fort, B. Kannan, J. Karedal, J. Kunisch, H. G. Schantz, K. Siwiak and M. Z. Win [24] *Contribution:* A comprehensive ultrawideband propagation was proposed, which was also standardized.
2008	*Authors:* R. A. Riaz, M. F. U. Butt, S. Chen, and L. Hanzo [1] *Contribution:* A generic z-domain discrete-time transfer function estimation technique was proposed for UWB.

Table 2.1: UWB channels advancements.

Durgin and Rappaport [73] and Rappaport [74–76] on the characterization of radio channels. The primary objective of these researchers has been to develop models that provide a statistically reliable characterization of radio channels and hence assist us inadequately quantifying the achievable system performance. Naturally, a reliable statistical characterization requires extensive and accurate measurements. The accuracy of the resultant model inferred depends mainly on the accuracy of the measurements.

Table 2.1 gives an overview of the past two decades' progression in the field of UWB channel modelling and estimation. In [77], channel estimation techniques were proposed for assisting the receiver in recovering the transmitted UWB signal and hypothesising that an inverse system may be found for signal recovery. We found this complete inverse system and the corresponding recursive equation was provided for channel estimation [1]. More explicitly, a z-domain transfer function of UWB channels was developed for representing the inverse system used for channel estimation, which did not require any channel sounding. This transfer function forms the basis of the proposed memory-efficient implementation of the equalizer advocated. Furthermore, the stability analysis and mean convergence bound of the UWB channel transfer function is also presented.

The novelty and rationale [1] of this chapter can be summarised as follows:

1. *Generic z-domain discrete-time transfer function estimation is proposed for ultra-wideband channels, which requires no channel sounding sequence transmission and hence constitutes a blind technique. This is achieved by estimating the channel impulse response with the aid of the information signalling pulses and then equalising the effects of the channel by the corresponding inverse system [1].*

2. *Additionally, A generic Infinite Impulse Response (IIR) equalizer architecture is proposed for UWB systems, which halves the memory requirement of the conventional IIR equalizers. This is achieved by exploiting the aperiodically repeated clusters of negative-exponentially decaying segments of the Channel Impulse Response (CIR) and hence by pro-viding a single common delay-line between the input and output of the equalizer.*

3. *Finally, The stability of a general Linear Time-Invariant (LTI) UWB CIR model is investigated. The closed-form time-domain response of the so-called homogenous, non-homogenous and vectorial LTI system is developed. Furthermore, the normalized settling time of the step response is evaluated for diverse damping coefficients.*

The rest of the chapter is organised as follows. First, UWB propagation fundamentals are provided in Section 2.2. Then, the generic z-domain discrete time transfer function of UWB channels is derived in Section 2.3 along with a memory-efficient infinite impulse response UWB equalizer implementation, while in Section 2.5 we present a stability study

of a linear time invariant UWB channel model. In Section 2.6 the mean convergence bound of UWB Time Hopping (TH) Impulse Radio (IR) adaptive equalization is presented. Our conclusions are offered in Section 2.7, followed by a chapter summary in Section 2.8.

2.2 UWB Propagation Channels

Before delving into the derivation of the generic z-domain Discrete-Time Transfer Function (DTTF) of UWB systems, in this section we will detail some of the basic equations characterizing UWB channels. These equations will be helpful in deriving the DTTF of UWB systems, which are based on the comprehensive standardized UWB propagation channel model of [24, 64, 68, 78].

2.2.1 Power Delay Profile

The complex baseband CIR of the Saleh-Valenzuela (SV) model is given in general as [68]

$$h(t) = \sum_{l=0}^{L} \sum_{k=0}^{K} \alpha_{(k,l)} e^{(\psi_{(k,l)})} \delta(t - T_l - \tau_{k,l}), \tag{2.1}$$

where $\alpha_{(k,l)}$ is the tap weight of the kth component in the lth CIR cluster, T_l is the delay of the lth cluster, and $\tau_{k,l}$ is the delay of the kth MultiPath Component (MPC) relative to the lth's cluster arrival time T_l. The phases $\psi_{(k,l)}$ are uniformly distributed, i.e., for a bandpass system, the phase is assumed to be a uniformly distributed random variable from the range of $[0, 2\pi]$. The stylized model of the UWB CIR characterized by the variables Γ and γ representing the power decay time constants for the clusters and rays, respectively, is shown in Figure 2.1

2.2.2 The Cluster's Distribution

The number of clusters L was shown to be closely modelled by the Probability Density Function (PDF) [79]

$$P_L = \frac{(\overline{L})^L e^{-\overline{L}}}{L!}, \tag{2.2}$$

where the mean $\overline{L}$ unambiguously characterizes the distribution. Figure 2.2 shows the cluster's distribution versus the number of clusters L.

2.2.3 Ray Arrival Time Distribution

The ray arrival times may be modelled by a mixture of two Poisson processes as follows [80]:

$$p(\tau_k/\tau_{k-1,l}) = \beta\lambda_1 e^{[-\lambda_1(\tau_{k,l}-\tau_{k-1,l})]} + (1-\beta)\lambda_2, \tag{2.3}$$

where β is the mixture probability, while λ_1 and λ_2 are the ray arrival rates.

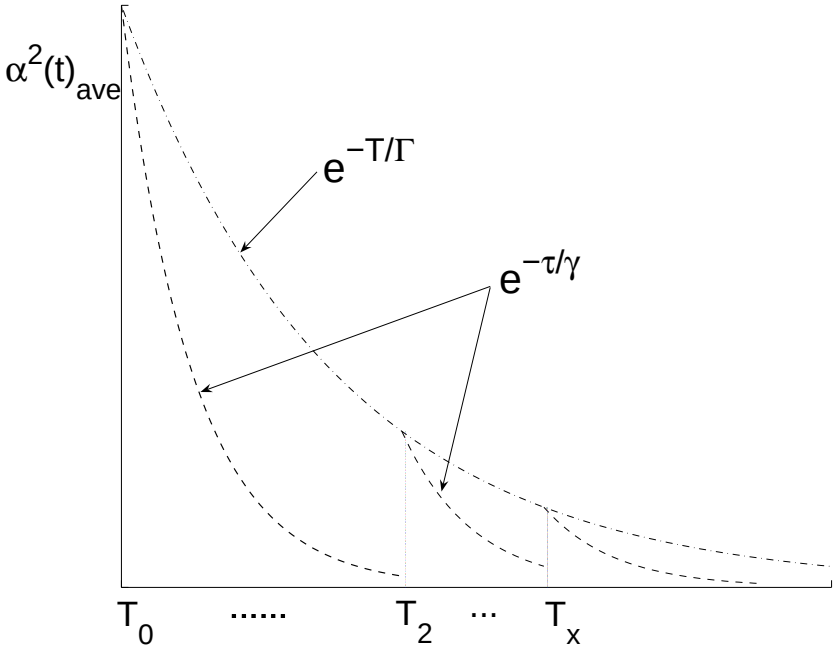

Figure 2.1: Stylized UWB CIR.

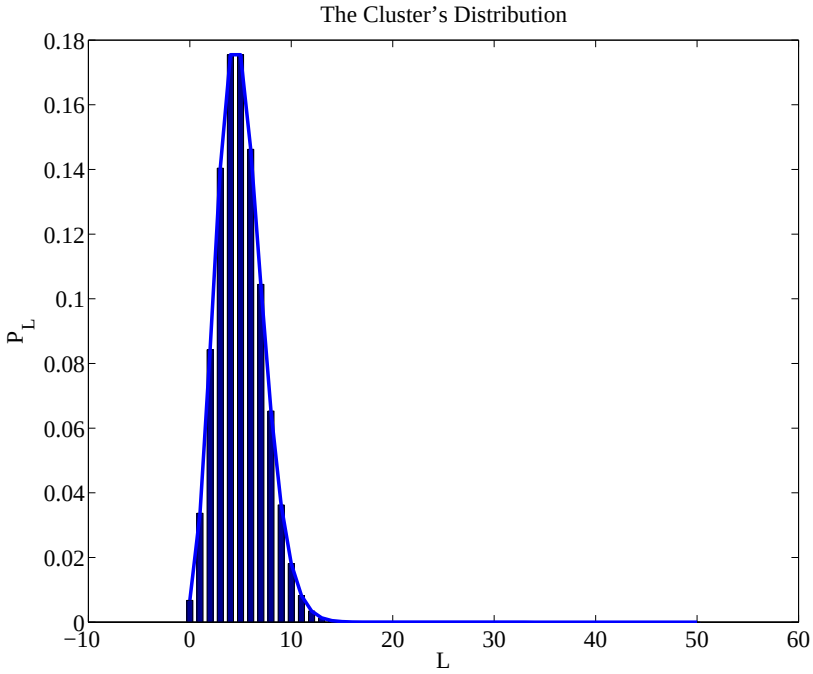

Figure 2.2: The distribution of the number of clusters.

2.2.4 Cluster Powers

The mean power of the different paths is a negative-exponentially decaying function, as formulated in [24]

$$E\{\mid \alpha_{(k,l)} \mid^2\} \propto \Omega_l e^{(\frac{-\tau_{k,l}}{\gamma_l})}, \tag{2.4}$$

where $\alpha_{(k,l)}$ is the power, Ω_l is the integrated energy of the lth cluster, γ_l is the intra-cluster decay time constant and $\tau_{k,l}$ is the ray arrival time within a cluster. The larger the delay, the higher the decay time constant of the cluster, resulting in more rapidly decaying clusters, as formulated in the relationship of

$$\gamma_l = k_\gamma T_l + \gamma_0, \tag{2.5}$$

where k_γ describes the increase of the decay constant with delay, which gives a good agreement with measurements [78]. The energy of the lth cluster, normalized to γ_l and averaged over an appropriately selected window in order to remove the effects of both shadowing and the small-scale fading, follows in general an exponential decay [24]

$$10log(\Omega_l) \propto 10log\big(e^{(\frac{-T_l}{\Gamma})}\big) + M_{cluster}, \tag{2.6}$$

where Ω_l is the integrated energy of the lth cluster, $M_{cluster}$ is a normally distributed variable with a standard deviation of $\sigma_{cluster}$, Γ is the cluster's power-decay time constant and T_l is cluster's arrival time. For the Non-Line Of Sight (NLOS) scenario of both office and industrial environments, the above description does not constitute a sufficiently accurate model for the PDP. It was shown in [24] that only a single cluster whose power first increases with the delay and then decreases again may be observed. The shape of the Power Delay Profile (PDP) may significantly influence the ranging and geolocation resolution accuracy of UWB systems, since ranging algorithms require the identification of the first (not the strongest) MPC. In this NLOS scenario the following functional fit gives a good description:

$$E\{\mid \alpha_{(k,l)} \mid^2\} \propto (1 - \chi \cdot e^{(\frac{-\tau_{k,l}}{\gamma_{rise}})}) \cdot e^{(\frac{-\tau_{k,l}}{\gamma_1})}, \tag{2.7}$$

where the parameter χ describes the attenuation of the first component, the parameter γ_{rise} determines how rapidly the PDP increases to its local maximum, while γ_1 determines the PDP decay at later times.

2.2.5 Path Loss

The path loss, which is frequency-dependent, is defined as [24]:

$$G(f,d) = \frac{1}{\Delta f} E\Big\{ \int_{f-\frac{\Delta f}{2}}^{f+\frac{\Delta f}{2}} \mid H(\tilde{f},d) \mid^2 d\tilde{f} \Big\}, \tag{2.8}$$

where $H(f,d)$ is the Frequency Domain Channel Transfer Function (FDCTF) between the Transmitter (TX) and Receiver (RX), including the antennas, measured between the TX

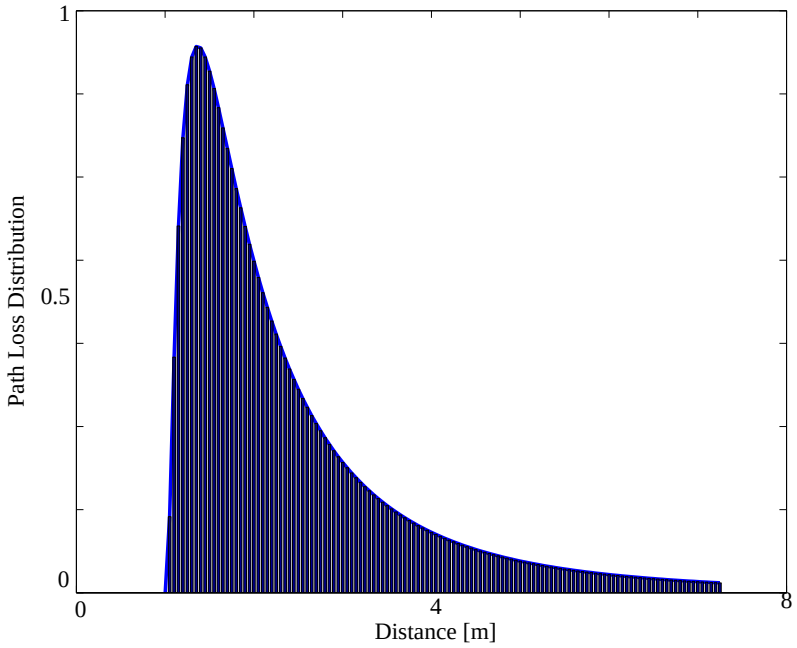

Figure 2.3: Path loss distribution.

antenna connector and the RX antenna connector. The expectation $E\{\cdot\}$ is taken over an appropriately selected window, averaging the effects of both the small-scale and large-scale fading. The frequency range Δf is chosen to be sufficiently narrow, so that the diffraction coefficients, dielectric constants, etc. can be considered constant within that bandwidth. The total path loss may be described by the classic distance-based inverse power law. The long-term random variations due to shadowing are lognormally distributed

$$G_{dB}(f,d) = G_0 - 10nlog_{10}\left(\frac{d}{d_0}\right), \tag{2.9}$$

where the reference distance d_0 is set to 1 meter and G_0 is the path loss at the reference distance. The distribution is depicted in Figure 2.3. The path-loss exponent n depends on whether or not a line-of-sight (LOS) connection exists between the TX and RX. Although in practice an improved path loss model may be constructed by a regime using several path-loss regression lines of different steepness [68], we employ a simple single-slope power decay law.

2.2.6 Small Scale Fading

The model describes the distribution of the small-scale amplitudes by the Nakagami PDF of [24]

$$pdf(y) = \frac{2}{\Gamma(m)}\left(\frac{m}{\Omega}\right)^m y^{2m-1} e^{\left(\frac{-m}{\Omega}y^2\right)}, \tag{2.10}$$

where $m \geq \frac{1}{2}$ is the Nakagami m-factor, $\Gamma(m)$ is the gamma function, and is the mean-square value of the amplitude. An approximate conversion of the Nakagami distribution to the Ricean distribution is possible according to the m-to-k factor conversion of [24]

$$K_r = \frac{\sqrt{m^2 - m}}{m - \sqrt{m^2 - m}}, \tag{2.11}$$

where K_r is the Rice factor.

Residential	LOS	NLOS
valid Range of d	7-20m	7-20m
$G_0[dB]$	-43.9	-48.7
$\overline{L}$	3	3.5
$\Lambda[1/ns]$	0.047	0.12
$\lambda_1, \lambda_2[1/ns], \beta$	1.54,0.15,0.095	1.77,0.15,0.045
$\Gamma[ns]$	22.61	26.27
k_γ	0	0
$\gamma_0[ns]$	12.53	17.50
$\sigma_{cluster}$	2.75	2.93
$m_0[dB]$	0.67	0.69
$\widehat{m}_0$	0.28	0.32
$\tilde{m}$	NA	NA

Table 2.2: Parameters for channel models CM1 AND CM2 (Residential) [24]

The m-parameter itself is an environment-dependent parameter, which may be modeled as a lognormally distributed random variable, whose logarithm has a mean of μ_m and standard of deviation σ_m. Both of these parameters may be delay-dependent and this relationship may be described as [24, 81]:

$$\mu_m(\tau) = m_0 - k_m\tau \tag{2.12}$$

$$\sigma_m(\tau) = \widehat{m}_0 - \widehat{k}_m\tau. \tag{2.13}$$

For the first CIR-tap of each cluster, the Nakagami factor is typically modeled differently [24, 64, 78]. It is assumed to be deterministic and independent of the delay, hence we have:

$$m = \tilde{m}_0. \tag{2.14}$$

Table 2.2 gives an example of the so-called residential channel models defined and detailed in [24]. Figures 2.4 and 2.5 show the Nakagami-m distribution for $m = 1$ and $m = 2.7$, respectively.

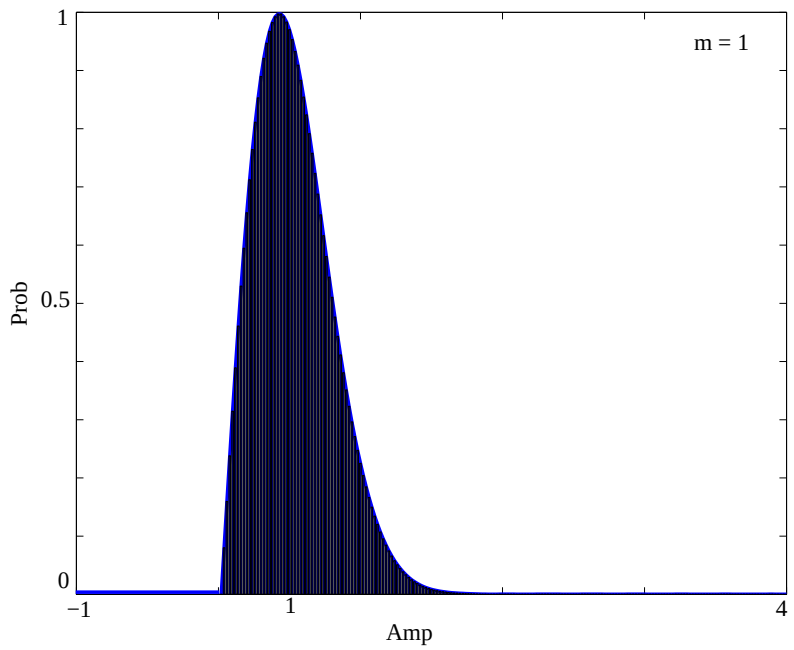

Figure 2.4: Nakagami-m distribution with m=1.

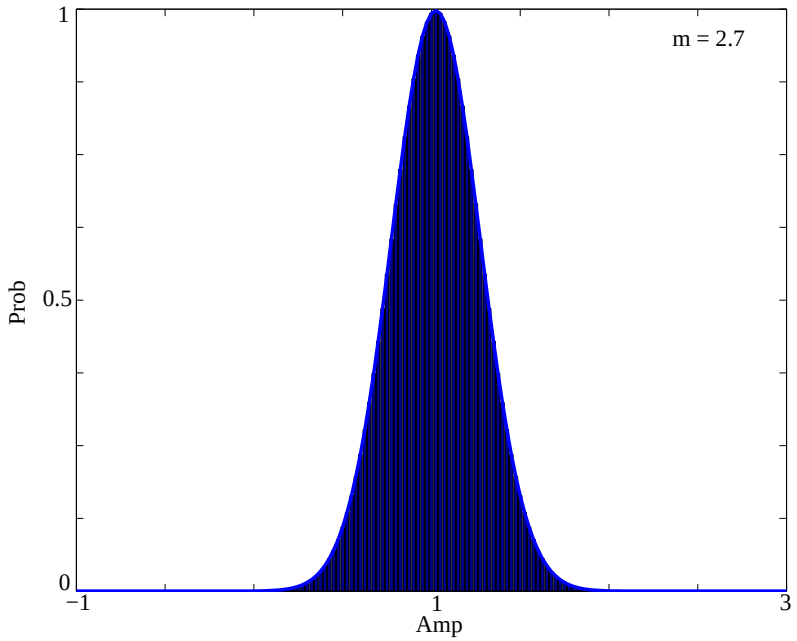

Figure 2.5: Nakagami-m distribution with m=2.7.

2.3 Z-Domain Discrete Time Transfer Function

In this section, we will use the UWB channels overview of Section 2.2 in order to present a generic z-domain DTTF estimation for UWB channels, which requires no channel sounding sequence transmission and hence constitutes a blind technique as discussed in Section 1.5. This is achieved by estimating the CIR with the aid of the information signalling pulses and then equalizing the effects of the channel by the corresponding inverse system. In [77], channel estimation techniques were proposed for assisting the receiver in recovering the transmitted UWB signal and hypothesising that an inverse system may be found for signal recovery. We found this complete inverse system and the corresponding recursive equation was provided for channel estimation [1].

The statistical channel model specified by the IEEE 802.15 standard is employed for link-budget design. The corresponding Wide Sense Stationary Uncorrelated Scattering (WSSUS) based CIR exhibiting clusters of similar-delay paths may be modelled as [24]

$$h_j(t) = \Theta_j \sum_{l=1}^{L} \sum_{w=1}^{W} \beta_{w,l}^{j} \delta(t - T_l^j - \tau_{w,l}^j), \tag{2.15}$$

where $h_j(t)$ is the jth CIR realisation, $\beta_{w,l}$ is the wth ray-magnitude of the lth CIR-tap-cluster, while T_l is the delay of the lth cluster. Moreover, $\tau_{w,l}$ is the delay of the wth ray relative to the lth cluster's arrival time T_l. Finally, Θ_j represents the magnitudes of the corresponding cluster components. When assuming perfect symbol synchronisation, Equation (2.15) may be simplified to

$$h(t) = \sum_{l=1}^{L} \beta_l \delta(t - \tau_l), \tag{2.16}$$

because as stated in [77], perfect symbol synchronisation removes the effects of cluster-overlapping. Furthermore, it was validated by Kolmogorov-Smirnov distribution-fitting of the model to measurement results at a significance level of 1% that the fading amplitudes can be modeled as Nakagami-m distributed [24]. Next we present a brief overview of Prolate Spheroidal Wave Function (PSWF), which will be used as signalling pulse in the subsequent sections.

2.3.1 Prolate Spheroidal Wave Function Fundamentals

As detailed in Section 1.2.4, the transmitted pulse shapes are of particular importance in UWB systems. Many transmitted pulse shapes have been outlined in [42], each referring to a particular application. The two main desired features of a transmitted pulse shape are [82]

1. The members of the pulse set should be orthogonal to each other in order to allow for their unique demodulation.

2. The pulse set should be robust with respect to the linear distortion caused by the channel.

Since PSWF have superior orthogonal properties compared to other singalling pulse functions [82–85], they constitute attractive candidates for detection and demodulation in typical UWB scenarios. Furthermore, the basis vectors of the PSWFs offer a unique solution for blind equalization [77] without using pilot-based channel sounding.

In mathematical terms, the family of PSWFs constitutes a set of functions derived by time-limiting and lowpass filtering a general basis function followed by a second time-limiting operation for all $\mid t \mid > \frac{T}{2}$. In an analogous manner, $F(f)$ is band-limited, so that it is zero outside the band $(-\Omega, \Omega)$. The PSWF is the solution of the equation [82, 83, 86]

$$\int_{\frac{-T}{2}}^{\frac{T}{2}} \phi_n(y) \frac{sin\Omega(t-y)}{\pi(t-y} dy = \lambda_n \phi_n(t), \tag{2.17}$$

for $\phi_n(t)$. Alternatively, PSWFs may also be defined as the solution of the differential equation [82, 83]

$$\frac{d}{dt}(1-t^2)\frac{d\phi_n(t)}{dt} + (\Xi_n - v^2 t^2)\phi_n(t) = 0, \tag{2.18}$$

for $\phi_n(t)$, which represents PSWFs of order n and Ξ_n are the eigenvalues of $\phi_n(t)$. The constant v is [86]

$$v = \frac{\Omega T}{2}, \tag{2.19}$$

where Ω is the bandwidth and T is the pulse duration. In Equation 2.17, λ_n characterizes the concentration of energy in the interval $[\frac{-T}{2}, \frac{T}{2}]$ with respect to the total energy, which is given by [82, 86]

$$\lambda_n = \frac{\int_{\frac{-T}{2}}^{\frac{T}{2}} \mid \phi_n(t) \mid^2 dt}{\int_{-\infty}^{\infty} \mid \phi_n(t) \mid^2 dt}, \tag{2.20}$$

whose values range from 0 to 1. Moreover, it can be shown that PSWFs exhibit the following orthogonality properties over the intervals of $[-\infty, \infty]$ and $[\frac{-T}{2}, \frac{T}{2}]$, respectively [83, 86]:

$$\int_{\frac{-T}{2}}^{\frac{T}{2}} \phi_m(t)\phi_n(t)dt = \begin{cases} \lambda_n, & m = n \\ 0, & m \neq n. \end{cases} \tag{2.21}$$

$$\int_{-\infty}^{\infty} \phi_m(t)\phi_n(t)dt = \begin{cases} 1, & m = n \\ 0, & m \neq n, \end{cases} \tag{2.22}$$

Maintaining orthogonality according to Equations 2.21 and 2.22 constitutes a necessary property for an UWB communication system to guarantee interference-free demodulation at the receiver. These orthogonal pulse sets are constituted by coded monocycles or coded baseband waveforms. Figures 2.6 and 2.7 potrays a fourth-order and fifth-order PSWF generator, respectively.

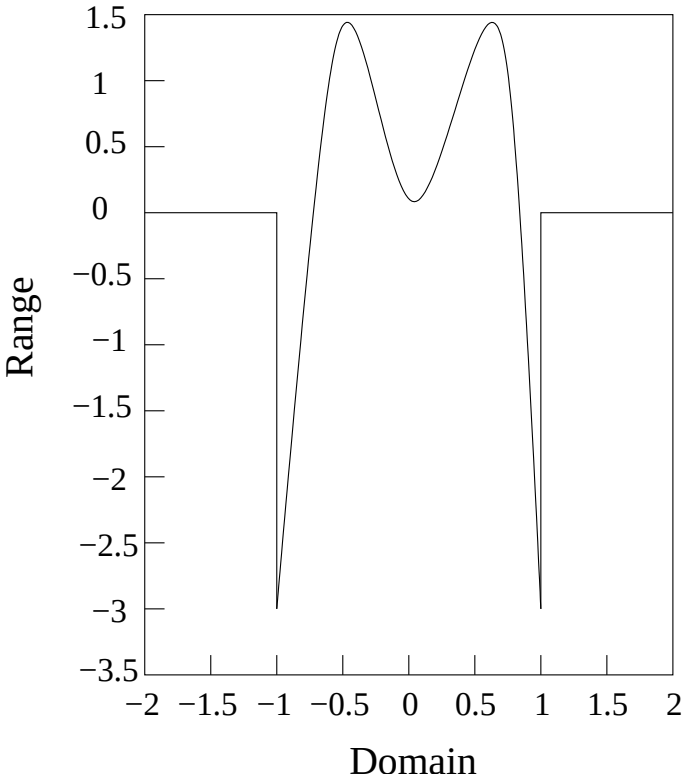

Figure 2.6: Fourth-order PSWF generator.

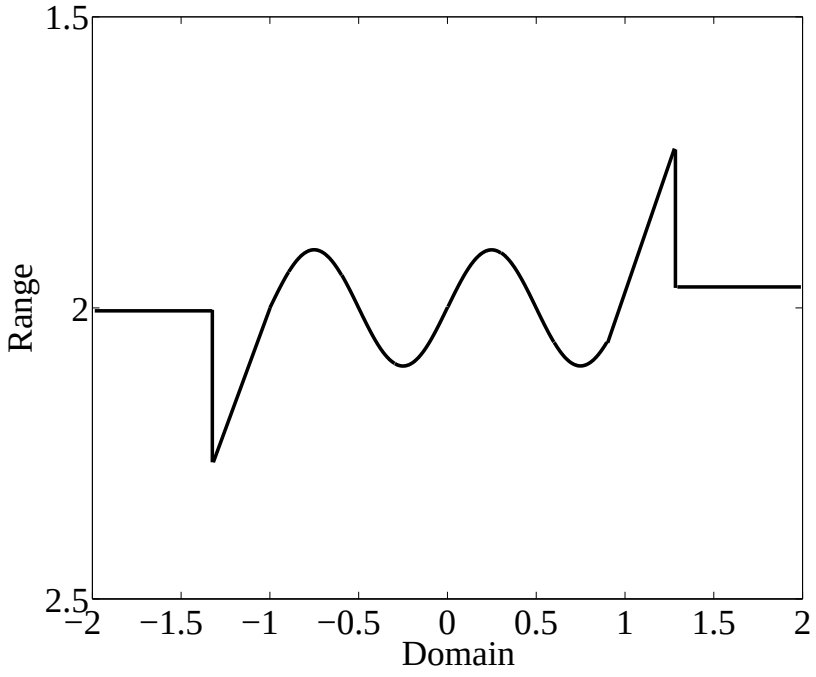

Figure 2.7: Fifth-order PSWF generator.

If we solve the differential Equation 2.18, we get [82, 83]

$$(1-t^2)\frac{d^2\phi_n(t)}{dt^2} - 2t\frac{d\phi_n(t)}{dt} + (\Xi_n - v^2t^2)\phi_n(t) = 0, \tag{2.23}$$

and consequently [82, 83]

$$\ddot{\phi}_n(t) = \frac{1}{1-t^2}\big[2t\dot{\phi}_n(t) - (\Xi_n - v^2t^2)\phi_n(t)\big]. \tag{2.24}$$

As seen in Equation 2.24, different orders of the pulses can be simply obtained by changing the values of Ξ_n; Hence, Equation 2.24 is the basis of the multipulse generator. Different values of Ξ_n have been calculated from Equation 2.24 and are shown in Table 2.3 [86]

0	1.12773
1	4.28712
2	8.22571
3	14.10020
4	22.05482
5	32.03526
6	44.02474
7	58.01837
8	74.01419
9	92.01130

Table 2.3: Eigenvalues of different pulse orders for $v = 2$

The noteworthy properties of Orthogonal Prolate Spheroidal Wave Function (OPSWF) shapes are as follows [86]:

- The pulses are double-orthogonal;
- The pulse bandwidth is almost the same for all values of n;
- The pulse duration is exactly the same for all values of n;
- The pulses have a nonzero DC component;
- Pulse duration and bandwidth can be controlled simultaneously;

If $\phi_n(t)$ is written in terms of the prolate angular function of the first kind [86], we have,

$$\begin{aligned}\phi_n(t) &= \phi_n(\Omega, T, t) \\ &= \frac{\big[2\lambda_n(v)T\big]^{\frac{1}{2}} Q^1_{0n}(v, \frac{2t}{T})}{\left(\int_{-1}^{1}\big[Q^1_{0n}(v,y)\big]^2 dy\right)^{\frac{1}{2}}},\end{aligned} \tag{2.25}$$

where it was shown that [86]

$$\left(\int_{-1}^{1} \left[Q_{0n}^{1}(v,y) \right]^2 dy \right)^{\frac{1}{2}} = \frac{2}{2n+1}, \tag{2.26}$$

where Q_{0n}^{1} is the prolate angular function of the first kind and λ_n is the fraction of energy of $\phi_n(t)$ that lies in the interval $[-1, 1]$. Further explanations of the fundamentals can be found in [86] and [87]. In the next section, we will derive the generic z-domain transfer function which will be used for UWB channel estimation, as discussed in Section 2.3.

2.3.2 Derivation of the Transfer Function

In [77], channel estimation techniques were proposed for assisting the receiver in recovering the transmitted UWB signal and hypothesising that an inverse system may be found for signal recovery. We found this complete inverse system and the corresponding recursive equation was provided for channel estimation in [1]. In this section, we will formally derive the z-domain transfer function of UWB channels representing the inverse system for channel estimation, which does not require any channel sounding, as discussed in Sections 1.5 and 2.3.

The UWB pulse transmission regime based upon PSWFs [87] is employed for transmitting the UWB-PSWF pulse $\phi_p(t)$ of width T, $t \in [\tau, \tau + T]$ over the UWB channel characterized by Equation 2.16. The received signal $r_p(t)$ is given by

$$r_p(t) = \phi_p(t) * h(t) + n(t), \tag{2.27}$$

where $*$ represents the convolution operation and $n(t)$ is the Additive White Gaussian Noise (AWGN) having a zero mean and a double-sided power spectral density of $N(s)$.

Moreover, when using the orthonormal basis of the Paley-Wiener space [83] for PSWFs in order to have an equivalent model for UWB CIR, Equation 2.16 can be expressed as

$$h(t) = \sum_{n=0}^{\infty} a_n \phi_n(t). \tag{2.28}$$

The s-transform of Equation 2.28 becomes

$$H(s) = \sum_{q=0}^{\infty} a_q \xi_q \Phi_q(s), \tag{2.29}$$

where ξ_q represents the specific fraction of energy in the interval $q = 0 \ldots \infty$. Taking the s-transform of Equation 2.16 and equating it with Equation 2.29, we obtain the value for β_l as a function of the UWB-PSWF pulse duration T and energy E, respectively [77]:

$$\beta_l = \sum_{m=0}^{\infty} \sqrt{\frac{E\xi_m}{T}} \xi_m \phi_m(\tau_l). \tag{2.30}$$

Substituting Equation 2.30 into the s-transformed version of Equation 2.16 yields

$$H(s) = \sum_{l=1}^{L} \sum_{m=0}^{\infty} \sqrt{\frac{E\xi_m}{T}} \xi_m \phi_m(\tau_l) e^{-s\tau_l}. \tag{2.31}$$

The Tustin Transformation (TT) [85] $\left\{z \to e^{sT_d}\right\}$ is a conformal mapping employing the sampling time T_d, in order to convert the s-domain Channel Transfer Function (CTF) $\{H(s)\}$ to the z-domain $\{H(z)\}$. Using the following approximation of the TT [85]

$$s = \frac{1}{T_d} ln(z) = \frac{2}{T_d} \left[\frac{z-1}{z+1} + \frac{1}{3} \left(\frac{z-1}{z+1} \right)^3 + \dots \right] \approx \frac{2}{T_d} \frac{1-z^{-1}}{1+z^{-1}}, \tag{2.32}$$

and substituting Equation 2.32 into Equation 2.31 in order to convert $H(s)$ to $H(z)$ yields

$$H(z) = H(s)\Big|_{s=\frac{2}{T_d}\frac{1-z^{-1}}{1+z^{-1}}} = \sum_{l=1}^{L} \sum_{m=0}^{\infty} \sqrt{\frac{E\xi_m}{T}} \xi_m \phi_m(\tau_l) e^{\frac{-2\tau_l}{T_d}\frac{1-z^{-1}}{1+z^{-1}}}. \tag{2.33}$$

When applying the power series expansion of

$$e^{\frac{-2\tau_l}{T_d}\frac{1-z^{-1}}{1+z^{-1}}} = \sum_{n=0}^{\infty} \frac{\left(\frac{-2\tau_l}{T_d}\frac{1-z^{-1}}{1+z^{-1}}\right)^n}{n} \approx 1 - \frac{2\tau_l}{T_d}\frac{1-z^{-1}}{1+z^{-1}}, \tag{2.34}$$

and exploiting that τ_l is in the range of nano-seconds, the higher-order components of the power series in Equation 2.34 can be neglected. Since τ_l is in the range of nano seconds for a range of practical channel models, as explained in [24]. Equation 2.34 holds for any value of τ_l between 3 to 7 ns. Then substituting Equation 2.34 into Equation 2.33 yields a general expression for the UWB-channel's z-domain DTTF having L number of CIR-tap clusters as follows:

$$H(z) = \sum_{l=1}^{L} \sum_{m=0}^{\infty} \sqrt{\frac{E\xi_m}{T}} \xi_m \phi_m(\tau_l) \left(1 - \frac{2\tau_l}{T_d}\frac{1-z^{-1}}{1+z^{-1}}\right), \tag{2.35}$$

where ξ_m is a statistically independent positive random variable having a Nakagami-m probability density function (PDF) with a unity fading parameter m for rays within a cluster, as given by [81]

$$p(\xi_m) = \left(\frac{2\xi_m}{\overline{\xi_m^2}}\right) e^{\left(\frac{-\xi_m^2}{\overline{\xi_m^2}}\right)}. \tag{2.36}$$

Next we detail an application example, in order to illustrate the accuracy of the derivation.

2.3.3 Application Example

In this section, we demonstrate the accuracy of our model of Section 2.3.2 using an $L = 2$-cluster scenario, where each cluster obeys a Nakagami-m distribution with a fading parameter of $m = 1$ for ξ_m in Equation 2.36. After a few algebraic steps we arrive from Equation 2.35 at the DTTF in the form of:

$$H^{\star}_{(L=2,m)}(z) = \mathbf{\Psi}^{\dagger} \left(\frac{1-z^{-1}}{1+z^{-1}}\right), \tag{2.37}$$

where we have

$$\mathbf{\Psi}^{\dagger} = \left[\left(\sqrt{\frac{E\xi_m}{T}} \xi_m \right) \left\{ (\phi_m(\tau_1) + \phi_m(\tau_2)) - (\frac{2}{T_d}(\tau_1 \phi_m(\tau_1) + \tau_2 \phi_m(\tau_2))) \right\} \right]. \tag{2.38}$$

Upon taking the inverse z-transform of Equation 2.37 over the stable region of convergence, the resultant recursive equation can be expressed as

$$h^{\star}_{(L=2,m)}(n) = \mathbf{\Psi}^{\dagger} 1^n u[-n-1] - \mathbf{\Psi}^{\dagger} 1^n u[-n-1]\delta[n-1]. \tag{2.39}$$

Finally, upon substituting $\mathbf{\Psi}^{\dagger}$ from Equation 2.38 into Equation 2.39, the resultant two-cluster Nakagami-m distributed CIR model becomes:

$$\begin{aligned} h^{\star}_{(L=2,m)}(n) = & \left[\left(\sqrt{\frac{E\xi_m}{T}} \xi_m \right) \left\{ (\phi_m(\tau_1) + \phi_m(\tau_2)) - (\frac{2}{T_d}(\tau_1 \phi_m(\tau_1) + \right. \right. \\ & \left. \left. \tau_2 \phi_m(\tau_2))) \right\} \right] 1^n u[-n-1] - \left[\left(\sqrt{\frac{E\xi_m}{T}} \xi_m \right) \left\{ (\phi_m(\tau_1) + \phi_m(\tau_2)) \right. \right. \\ & \left. \left. - (\frac{2}{T_d}(\tau_1 \phi_m(\tau_1) + \tau_2 \phi_m(\tau_2))) \right\} \right] 1^n u[-n-1]\delta[n-1]. \end{aligned} \tag{2.40}$$

The CIR of Equation 2.37 was restricted to retain only those multipath components, which are less than 12 dB below the maximum multipath component. The UWB-PSWF pulse duration was 0.15 ns, which was transmitted every 120 ns and the channel's inverse system was estimated for each new pulse. Finally, a threshold-detector was used to recover the transmitted data. The BER versus Signal-to-Noise Ratio (SNR) performance of the system considered is seen in Figure 2.8, demonstrating that using $W = 15$ taps in the proposed model approaches the full-complexity performance-evaluation curve of Equation 19 in [77].

This example fully supports the analysis of Section 2.3.2, suggested that the BER quantified in Figure 2.8 may be improved by increasing number of the taps in the inverse system. Hence the hypothesis claimed in [77] that an inverse system may be found for signal recovery was shown here to be valid [1]. Furthemore, this mathematical model of the inverse system of Section 2.3.2 may be used for the implementation of a memory-efficient IIR UWB equalizer, which does not require any channel sounding when using the orthogonal properties of PSWF pulse shapes, as detailed in Section 2.3.1. Next, we elaborate on the proposed memory-efficient equalizer architecture with the aid of the background of Sections 2.3.1 and 2.3.2.

2.4 Memory-Efficient IIR UWB Equalizer

This section will present the architecture of a memory efficient equalizer based on the z-domain transfer function and on the arguments presented in Section 2.3. The distinct

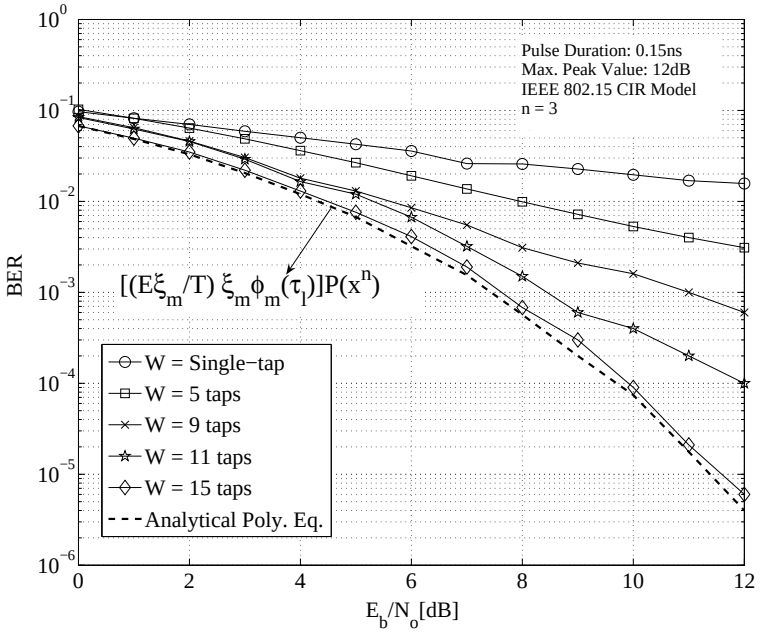

Figure 2.8: Accuracy of the proposed z-domain DTTF estimation of Equation 2.40 for L=2 and W=1, 5, 9, 11, 15 CIR taps

clusters of dense multipath components in UWB systems result in CIRs potentially spanning over hundreds of transmitted symbols, hence imposing excessive memory requirements on the equalizer's implementation. Again, in [1], a generic discrete-time z-domain transfer function estimation technique was proposed, hypothesizing that a memory efficient IIR UWB equalizer implementation may be found. Hence the novel contribution of this section is that this memory efficient UWB IIR equalizer is indeed found and the corresponding design is detailed. The proposed equalizer attains exactly the same BER performance as the conventional equalizer, despite requiring only half the memory, as demonstrated against the benchmarker designs provided in [1], [77].

2.4.1 Design Preliminaries

The UWB CIR is constituted by aperiodically repeated clusters of negative-exponentially decaying segments as seen in Figure 2.1, which gives a frequency response having a gradually tapering magnitude. This specific characteristic of the UWB CIR results in a memory-reduction for the receiver's IIR equalizer. A generic z-domain discrete-time transfer function derived for a UWB CIR [24] with L tap-clusters, each tap having Nakagami$-m$ distribution was given in [1]

$$H^{(L)}_{(UWB)}(z) = \sum_{m=0}^{\infty} \sqrt{\frac{E\xi_m}{T}}\xi_m \Phi(z)\left(1 - \frac{2}{T_d}\frac{1-\sum_{l=1}^{L}\tau_l z^{-l}}{1+\sum_{l=1}^{L} z^{-l}}\right), \tag{2.41}$$

where ξ_m is a statistically independent positive random variable having a Nakagami-m PDF with m=1 for rays within a cluster, $\Phi(z)$ is the z-transform of the UWB signalling-pulse of

duration T and energy E, τ_l is the cluster arrival time expressed in nano-seconds and T_d is the sampling duration with $T_d \gg \tau_l$. Introducing the Power Spectral Density (PSD) of the received UWB signal, which depends on both $\Phi(z)$ and on the tap-distribution determined by m

$$\Psi^{\dagger} = \sum_{m=0}^{\infty} \sqrt{\frac{E\xi_m}{T}} \xi_m \Phi(z), \tag{2.42}$$

in Equation 2.41 yields

$$H_{(UWB)}^{(L)}(z) = \Psi^{\dagger} - \frac{2\Psi^{\dagger}}{T_d} \left(\frac{1 - \tau_1 z^{-1} - \tau_2 z^{-2} \cdots - \tau_L z^{-L}}{1 + z^{-1} + z^{-2} \cdots + z^{-L}} \right). \tag{2.43}$$

We can assume any particular signalling pulse shape and find the corresponding time domain characteristics from [24]. Therefore, by employing any UWB signalling pulse shape having a linearly evolving phase-shift, corresponds to Equation 2.42, hence Equation 2.43 can be approximated as:

$$H_{(UWB)}^{(L)}(z) \approx \frac{2\Psi^{\dagger}}{T_d} \left(\frac{1 - \tau_1 z^{-1} - \tau_2 z^{-2} \cdots - \tau_L z^{-L}}{1 + z^{-1} + z^{-2} \cdots + z^{-L}} \right). \tag{2.44}$$

As $\frac{1}{T_d}$ is the sampling frequency, which is twice the bandwidth of the system and $\Psi^{\dagger}$ is the known PSD of the signalling-pulse, we introduce the product of these two constants as

$$\Psi^{\star} = \frac{2\Psi^{\dagger}}{T_d}. \tag{2.45}$$

Finally, upon substituting Equation 2.45 in Equation 2.44, after a few algebraic simplifications we arrive at:

$$H_{(UWB)}^{(L)}(z) = \frac{Y(z)}{X(z)} = \begin{cases} \frac{\Psi^{\star} - \sum_{\zeta=1}^{L} \Psi_{\zeta}^{\star} z^{-\zeta}}{1 + \sum_{\zeta=1}^{L} z^{-\zeta}} \\ \Psi_{\zeta}^{\star} = \Psi^{\dagger} \tau_{\zeta} \qquad \text{for } \zeta = 1, 2, ..., L, \end{cases} \tag{2.46}$$

which is the required transfer function of the UWB IIR equalizer.

2.4.2 Conventional IIR UWB Equalizer Design

This design hinges on the extension of Equation 2.46 into a difference equation. Upon solving Equation 2.46 for $Y(z)$ we obtain

$$H_{(UWB)}^{(L)}(z)\Big|_{IIR}^{(1)} : Y(z)\Big(1 + \sum_{\varphi=1}^{L} z^{-\varphi}\Big) = X(z)\Big(\Psi^{\star} - \sum_{\vartheta=1}^{L} \Psi_{\vartheta}^{\star} z^{-\vartheta}\Big). \tag{2.47}$$

Finally, taking the inverse z-transform of Equation 2.47 gives the causal recursive difference equation for the conventional IIR UWB equalizer design in the form of:

$$y[n] = \Psi^{\star} x[n] - \sum_{\nu=1}^{L} y[n - \nu] - \sum_{\omega=1}^{L} \Psi_{\omega}^{\star} x[n - \omega]. \tag{2.48}$$

The architecture modelling Equation 2.48 is shown in Figure 2.9.

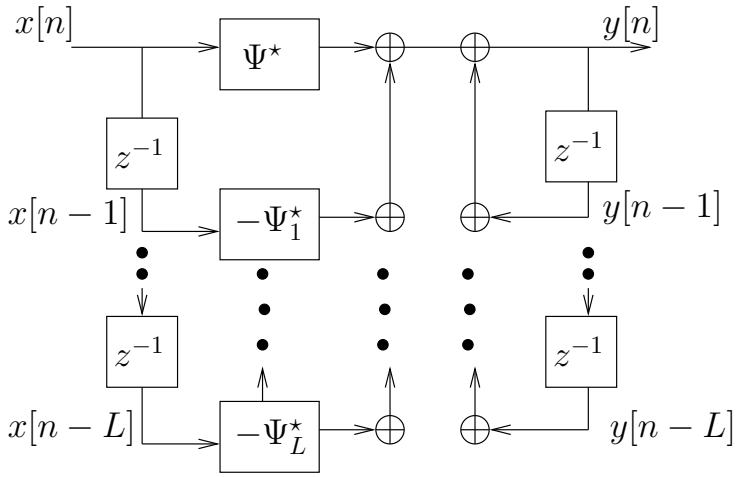

Figure 2.9: Conventional UWB IIR equalizer for L ray-clusters and Nakagami$-m$ distribution.

2.4.3 Memory Efficient IIR UWB Equalizer Design

The aim of this design is to combine the two delay-lines of Fig 2.9 into a single one, as Equation 2.48 cannot be implemented by a single delay-line. But this design requires two recursive difference equations for interpreting the input-output relationship of the equalizer in order to rely on a single delay-line, which halves the IIR equalizer's memory requirement. These equations should be causal so that the new memory-efficient equalizer design remains practically realizable. To achieve this objective, we solve Equation 2.46 again for $Y(z)$, which yields:

$$H^{(L)}_{(UWB)}(z)\Big|^{(2)}_{IIR} : Y(z) : V(z)\Big(\Psi^{\star} - \sum_{\Delta=1}^{L} \Psi^{\star}_{\Delta} z^{-\Delta}\Big), \tag{2.49}$$

where $V(z)$ is given by

$$V(z) = \frac{X(z)}{1 + \sum_{\Theta=1}^{L} z^{-\Theta}}. \tag{2.50}$$

Finally, solving Equation 2.50 for $X(z)$ and taking the inverse z-transform of Equations 2.49 and 2.50 we arrive at the required pair of causal recursive difference equations, which results in the halved-memory IIR UWB equalizer design as:

$$x[n] = \sum_{\alpha=0}^{L} v[n-\alpha], \tag{2.51}$$

$$y[n] = \Psi^{\star} v[n] - \sum_{\beta=1}^{L} \Psi^{\star}_{\beta} v[n-\beta]. \tag{2.52}$$

The architecture modelling Equations 2.51 and 2.52 is shown in Figure 2.10.

By contrasting Equations 2.48, 2.51 and 2.52 as well as Figures 2.9 and 2.10, it becomes evident that the proposed design requires a single delay-line, which halves the memory requirement of the conventional design. Both equalizer designs are characterized in the

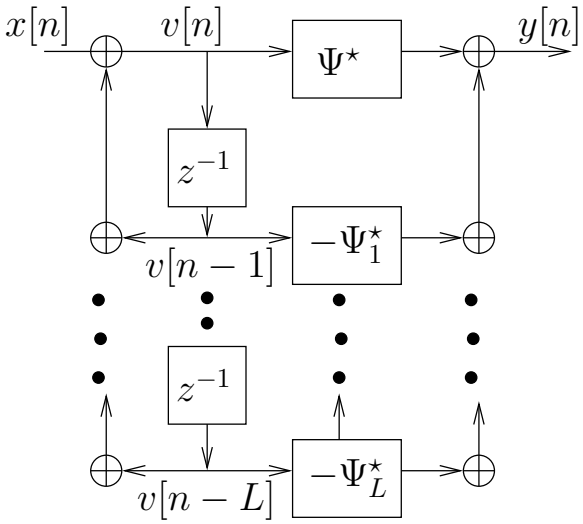

Figure 2.10: Memory-efficient UWB IIR equalizer with L ray-clusters and Nakagami$-m$ distribution.

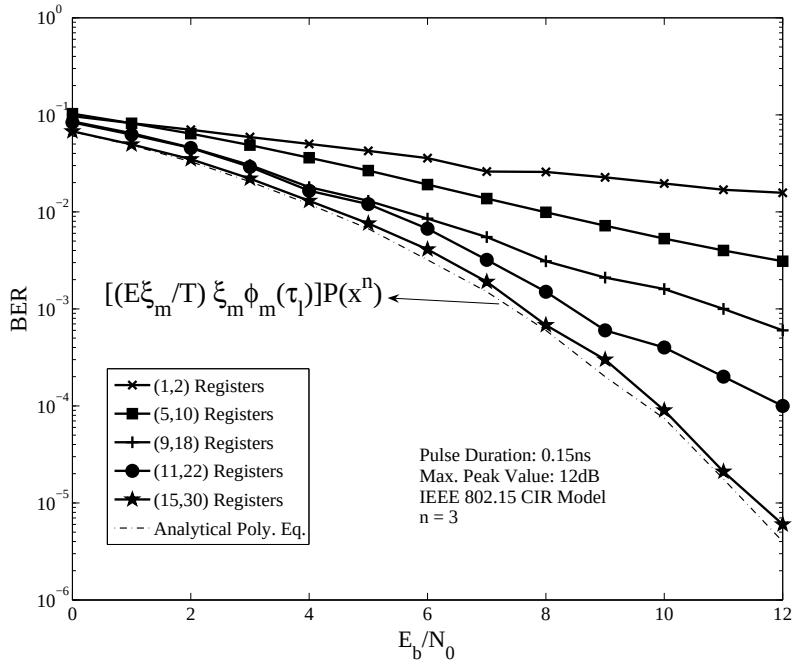

Figure 2.11: BER performance of the UWB equalizer designs of Figures 2.9 and 2.10, both of which are capable of approaching the analytical solution with a degree $n = 3$ in Equation 19 of [77] and corresponding to (i, j) memory registers, where i is used in memory-efficient design and j is in the conventional design.

context of UWB PSWF having a duration of 0.15 ns, which were transmitted every 120 ns as in [1], [77]. We obtain exactly the same BER performance as in [1], [77], as evidenced in Figure. 2.11 for both designs, despite halving the memory requirements.

2.5 Stability Analysis of the LTI UWB Channel

As outlined in Figure 1.7 of Section 1.5 showing the interconnection of each chapters and sections, we have first detailed in Section 2.2 the statistical specifications of UWB channels. These specifications have been used in Section 2.3 to develop a novel z-domain transfer function for blind channel equalization without the need of channel sounding [1]. This mathematical model was then invoked in the memory-efficient IIR UWB equalizer of Section 2.4. This background will now be used in this section to provide a tangible quantitative characterization of the UWB channel's stability.

The stability analysis found in the literature [88–91] is normally carried out *either* to mark the region of convergence for linear and non-linear systems in diverse scenarios *or* to characterize the system's stability for a statistical model of a real system. Different approaches have been followed in the stability analysis of diverse engineering fields, including automatic control [91, 92], neural networks [90] and microwave engineering [89], for example. The main objective in all the scenarios is to define the stability bounds for specific initial and variable conditions of the system.

In this section, the stability of a general LTI UWB CIR model is investigated based on Sections 2.2 and 2.3. Since the s-domain and z-domain transfer function corresponding to the UWB CIR has an extremely high number of singularities, it is not automatically guaranteed that none of the poles falls on the right-half of the s-plane or outside the unit-circle of the z-plane. Hence the stability analysis necessitates the exhaustive testing of this well-established stability criterion for a potentially excessive number of poles. We circumvent this arduous task by developing the closed-form time-domain response of the so-called homogenous, non-homogenous and vectorial LTI system, which directly demonstrates the potential instabilities. Furthermore, the normalized settling time of the step response is evaluated for diverse damping coefficients. Finally, a stability case-study is provided with the aid of Nichols charts.

A general LTI UWB CIR of the form [24] is

$$h(t) = \sum_{l=0}^{L} \sum_{k=0}^{K} b_{(k,l)} e^{j\phi_{(k,l)}} \delta(t - T_l - \tau_{(k,l)}) \tag{2.53}$$

considered, where $b_{(k,l)}$ is the weight of the kth CIR tap in the lth cluster, T_l is the delay of the lth cluster and $\tau_{(k,l)}$ is the delay of the kth MPC relative to the lth tap-cluster's commencement time T_l. The phases $\phi_{(k,l)}$ are uniformly distributed, i.e. for a bandpass

system the phase is assumed to be a random variable uniformly distributed in the range of $[0, 2\pi]$. The classic SV model [68] does not specify the number of clusters occurring. Rather, it assumes that their number is theoretically infinite and that their amplitude decreases exponentially with time; for practical purposes, an arbitrary threshold has to be introduced, so that the clusters having an amplitude below that are no longer considered in the simulations.

2.5.1 Problem Statement

Again, given the nature of the UWB CIR of Equation 2.53, the corresponding s-domain or z-domain transfer function has an extremely high number of singularities and it is not automatically guaranteed that none of the poles falls on the right-half of the s-plane or outside the unit-circle of the z-plane. In this section, we demonstrate for three specific scenarios that the LTI system described by Equation 2.53 retains stability.

We deviated from the conventional approach, where the linear system is said to be asymptotically stable if and only if all the roots of the transcendental equation describing the CIR are on the left half of the complex s-plane. Since there is a high number of roots to be examined, the corresponding stability analysis is a complex task. We circumvent this arduous task by developing the closed-form time-domain response of the LTI system, which allow us to identify any potential instability by simple inspection. These expressions are developed using the s-transform of the system model and the general form of the Leibniz integral rule [93]. To elaborate a little further, the normalized settling time and %overshoot of the step response provide a tangible quantitative characterization of the LTI system's stability. The corresponding derivation requires somewhat tedious algebraic manipulations, but again, it circumvents the arduous task of checking the position of a potentially excessive number of roots of the transcendental equation in the complex s-plane.

2.5.2 Methodology

The complex tap-values of a general LTI UWB CIR given in Equation 2.53 obey the standard Poisson-distribution, while mixed Poissonian processes describe the number of clusters, the clusters arrival times and the ray arrival times within a specific cluster [24, 94],

$$\begin{aligned} pdf_L(L) &= \frac{(\bar{L})e^{-\bar{L}}}{L!} \\ p\Big(T_l|T_{l-1}\Big) &= \Lambda_l e^{[-\Lambda_l(T_l-T_{l-1})]}, l>0 \\ p\Big(\tau_{(k,l)}|\tau_{(k-1,l)}\Big) &= \beta\lambda_1 e^{[-\lambda_1(\tau_{(k,l)}-\tau_{(k-1,l))}]} + (1-\beta)\lambda_2 e^{[-\lambda_2(\tau_{(k,l)}-\tau_{(k-1,l))}]}, k>0 \end{aligned} \quad (2.54)$$

where $\bar{L}$ is the average number of clusters, Λ_l is the cluster arrival rate, β is the probability controlling the particular mixture of the constituent Poisson processes and λ_1, λ_2 are the

ray arrival rates. These statistics will be used in our simulations of Section 2.5.4. We commence from the system model of Equation 2.53 and introduce the short-hand of:

$$C_{(i,j)} = b_{(i,j)}e^{j\phi_{(i,j)}} \quad \text{for } i = 0, 1, ..., K \\ j = 0, 1, ..., L. \tag{2.55}$$

We continue by partitioning the system model into L number of constituent clusters of CIR taps. Each of the resultant partitions can be viewed as a constituent model characterized by a Poissonian process for each ray within that cluster, as formulated below:

$$\overbrace{C_{0,0}\delta(t - T_0 - \tau_{0,0}) + \cdots + C_{K,0}\delta(t - T_0 - \tau_{K,0})}^{h^{(k,0)}cluster} \\ + \\ \overbrace{C_{0,1}\delta(t - T_1 - \tau_{0,1}) + \cdots + C_{K,1}\delta(t - T_1 - \tau_{K,1})}^{h^{(k,1)}cluster} \\ \vdots \\ \overbrace{C_{0,L}\delta(t - T_L - \tau_{K,L}) + \cdots + C_{K,L}\delta(t - T_L - \tau_{K,L})}^{h^{(k,L)}cluster}.$$

Taking the s-transform of a single constituent model yields

$$H^{(k,0)}(s) = C_{0,0}e^{-s\psi_{0,0}} + \cdots + C_{K,0}e^{-s\psi_{K,0}}, \tag{2.56}$$

where $\psi_{(m,n)}$ is defined as

$$\psi_{(m,n)} = T_n + \tau_{(m,n)} \quad \text{for } m = 0, 1, ..., K \\ n = 0, 1, ..., L.$$

Using the power series description of $\psi_{(m,n)}$ and neglecting the higher-order terms we have

$$e^{-s\psi_{(v,w)}} \approx 1 - s\psi_{(v,w)} \quad \text{for } v = 0, 1, ..., K \\ w = 0, 1, ..., L. \tag{2.57}$$

Upon substituting Equation 2.57 into Equation 2.56, we obtain the transfer function of the constituent model as

$$H^{(k,0)}(s) = \sum_{k=0}^{K} C_{k,0}\left(1 - \left[\frac{\sum_{k=0}^{K} C_{k,0}\psi_{k,0}}{\sum_{k=0}^{K} C_{k,0}}\right]s\right). \tag{2.58}$$

Finally, the overall system transfer function can be obtained by summing all the constituent transfer functions, yielding:

$$H^{(k,l)}(s) = \frac{Y(s)}{U(s)} = L\left[\sum_{k=0}^{K} C_{k,0}\left(1 - \left[\frac{\sum_{k=0}^{K} C_{k,0}\psi_{k,0}}{\sum_{k=0}^{K} C_{k,0}}\right]s\right)\right]. \tag{2.59}$$

Next, we explain the time domain system responses.

2.5.3 Time-Domain System Responses

The time-domain system model of an LTI UWB system having the impulse response of Equation 2.53 with s-domain specifications detailed in Section 2.5.2 is represented by

$$\Bigg[\sum_{l=0}^{L}\sum_{k=0}^{K} b_{(k,l)}e^{j\phi_{(k,l)}}(T_l-\tau_{k,l})\Bigg]\frac{dy(t)}{dt}+\Bigg[\sum_{l=0}^{L}\sum_{k=0}^{K} b_{(k,l)}e^{j\phi_{(k,l)}}\Bigg]y(t)$$
$$=\Bigg[\sum_{l=0}^{L}\sum_{k=0}^{K} b_{(k,l)}e^{j\phi_{(k,l)}}(T_l-\tau_{k,l})\Bigg]Lu(t), \tag{2.60}$$

where

$$u'(t)=Lu(t) \tag{2.61}$$

$$a^{(k,l)}(b,\phi,T,\tau)=\sum_{l=0}^{L}\sum_{k=0}^{K}\left(\frac{b_{(k,l)}e^{j\phi_{(k,l)}}}{b_{(k,l)}e^{j\phi_{(k,l)}}(T_l-\tau_{k,l})}\right) \tag{2.62}$$

represents the damping coefficients, predetermining the normalized settling time of the system response. More explicitly, $a^{(k,l)}(b,\phi,T,\tau)$ is a function of $b_{(k,l)}$ the phase, cluster arrival time T and ray arrival time τ. The different model parameters were specified in [24]. More specifically, for this study we have used the so-called residential NLOS system parameters of [24].

2.5.3.1 Homogenous System Response

This response is obtained by substituting $u'(t)$=0 in Equation 2.60 and solving it for $y(t)$, which gives

$$y(t)=y(t_0)e^{-a^{(k,l)}(b,\phi,T,\tau)(t-t_0)} \quad \forall\ t\geq t_0. \tag{2.63}$$

It is readily seen in Equation 2.63 that the response exhibits a decaying exponent, which is directly proportional to both the initial conditions at t=t_0 and to the damping factor $a^{(k,l)}$.

2.5.3.2 Non-Homogenous System Response

In order to obtain the corresponding response, we will use the general input $u'(t)$ in conjunction with an Integrating Factor (IF) of $e^{\int_{t_0}^{t}(a^{(k,l)}(b,\phi,T,\tau))dt}$ in order to solve Equation 2.60, yielding the following response

$$y(t)=y(t_0)e^{-\int_{t_0}^{t}(a^{(k,l)}(b,\phi,T,\tau))dt}+\int_{t_0}^{t}e^{-\int_{\gamma}^{t}(a^{(k,l)}(b,\phi,T,\tau))d\xi}u'(\gamma)d\gamma \tag{2.64}$$

Upon using the short hand of

$$\theta(t,t_0)=e^{-\int_{t_0}^{t}\sum_{l=0}^{L}\sum_{k=0}^{K}\left(\frac{b_{(k,l)}e^{j\phi_{(k,l)}}}{b_{(k,l)}e^{j\phi_{(k,l)}}(T_l-\tau_{k,l})}\right)dt}$$
$$\theta(t,\gamma)=e^{-\int_{\gamma}^{t}\sum_{l=0}^{L}\sum_{k=0}^{K}\left(\frac{b_{(k,l)}e^{j\phi_{(k,l)}}}{b_{(k,l)}e^{j\phi_{(k,l)}}(T_l-\tau_{k,l})}\right)d\xi} \tag{2.65}$$

in Equation 2.64, we can partition the overall response into the Natural Response (N_r) and Forced Response (F_r):

$$y(t) = \underbrace{y(t_0)\theta(t,t_0)}_{N_r} + \underbrace{\int_{t_0}^{t} \theta(t,\gamma)u'(\gamma)d\gamma}_{F_r}. \tag{2.66}$$

Observe in Equation 2.66 that N_r is dependent on the initial conditions $y(t_0)$, while F_r is directly proportional to both $u'(t)$ and to the damping parameters of Equation 2.65. This partitioning of the response characterizes the effect of the initial state and that of the input, before reaching the steady state value. Furthermore, the partitioning in Equation 2.66 is also helpful in designing the rise time of the LTI system describing the UWB channel as well as its %overshoot in the transient phase.

2.5.3.3 Vector Form

Upon rearranging Equation 2.60 to give a single state-model we arrive at:

$$\frac{dy(t)}{dt} = \frac{\left[\sum_{l=0}^{L}\sum_{k=0}^{K} b_{(k,l)}e^{j\phi_{(k,l)}}\right]}{\left[\sum_{l=0}^{L}\sum_{k=0}^{K} b_{(k,l)}e^{j\phi_{(k,l)}}(T_l - \tau_{k,l})\right]}y(t) + Lu(t). \tag{2.67}$$

The n-state-model can be expressed from Equation 2.67 in a vectorial form as

$$[\dot{y}(t)]_{n\times 1} = [\Delta]_{n\times n}y(t)_{n\times 1} + [\chi]_{n\times 1}u(t)_{1\times 1}, \tag{2.68}$$

where Δ is the system matrix of order n. By comparing Equation 2.60 with Equation 2.68 we hypothesize that the vector response of the state-model of Equation 2.68 is

$$y(t) = e^{\Delta(t-t_0)}y(t_0) + \int_{t_0}^{t}\left(e^{\Delta(t-\alpha)}\chi u(\alpha)\right)d\alpha. \tag{2.69}$$

To prove this hypothesis, we need the Leibniz Integral rule (see Appendix B) and the following power series expansion

$$e^{\Delta(t-t_0)} = I + \Delta(t-t_0) + \frac{\Delta^2(t-t_0)^2}{2!} + \cdots, \tag{2.70}$$

as well as its derivative given by:

$$\begin{aligned}\frac{d}{dt}e^{\Delta(t-t_0)} &= \Delta + \frac{2\Delta^2(t-t_0)}{2} + \frac{3\Delta^3(t-t_0)^2}{6} + \cdots \\ &= \Delta e^{\Delta(t-t_0)}.\end{aligned} \tag{2.71}$$

Check I: Substituting $t{=}t_0$ in the hypothesized vector response seen in Equation 2.69 we obtain

$$\begin{aligned}y(t)\big|_{t=t_0} &= e^{\{0\}}y(t_0) + \overbrace{\int_{t_0}^{t_0}\left(e^{\Delta(t-\alpha)}\chi u(\alpha)\right)d\alpha}^{=0}, \\ &= y(t_0).\end{aligned} \tag{2.72}$$

Residential	NLOS
valid range of distance	7-20m
Path Gain at the reference distance G_0[dB]	-48.7
Path Gain Exponent n	4.58
Shadowing Gain S[dB]	3.51
Frequency Dependency decaying factor k	1.53
$\bar{L}$	3.5
$\Lambda\ \left[\frac{1}{ns}\right]$	0.12
$\lambda_1, \lambda_2\left[\frac{1}{ns}\right], \beta$	1.77, 0.15,0.045
Gamma Function Γ[ns]	26.27
Nakagami Factor m_0	0.69
Decay Time constant γ_0	17.5
Standard Deviation $\sigma_{cluster}$[dB]	2.93

Table 2.4: Simulation parameters

Check II: Taking the derivative of Equation 2.69 we arrive at

$$\dot{y}(t) = \Delta e^{\Delta(t-t_0)} y(t_0) + \frac{\partial}{\partial t}\left[\int_{t_0}^{t} \left(e^{\Delta(t-\alpha)}\chi u(\alpha)\right) d\alpha\right]. \tag{2.73}$$

Applying the Leibniz integral rule (see Appendix B) we obtain

$$\dot{y}(t) \;=\; \Delta e^{\Delta(t-t_0)} y(t_0) + \Delta \int_{t_0}^{t} \left(e^{\Delta(t-\alpha)}\chi u(\alpha)\right) d\alpha + e^{\{0\}}\chi u(t) + \{0\}. \tag{2.74}$$

Finally, Equation 2.74 can be reduced to

$$\dot{y}(t) \;=\; \Delta \overbrace{\left(e^{\Delta(t-t_0)} y(t_0) + \int_{t_0}^{t} \left(e^{\Delta(t-\alpha)}\chi u(\alpha)\right) d\alpha\right)}^{y(t)} + \chi u(t). \tag{2.75}$$

It can be seen from Equations 2.72 and 2.75 that Equation 2.69 is indeed the vector response of the state-model of Equation 2.68.

2.5.4 Stability Analysis Results

This section details the step response characteristics of the LTI UWB channel derived in Section 2.5.2. Again, we have used the residential, NLOS channel parameters of [24] stated in Table 2.4. Explicitly, the normalized settling time of the system is considered. Furthermore, the conditions of stability are determined for a unity feed-forward gain with the aid of Nichols charts [95].

Let us now examine Figure 2.12, which portrays the LTI UWB channel's step-response on an exaggerated scale in order to facilitate this discussion. As indicated by the crosses in Figure 2.12, if the damping coefficient is $a(b, \phi, T, \tau) = 1.0$, the lower limit of 0.95 is crossed, when the normalized time is 4, while the upper limit of 1.05 is never crossed. A damping coefficient of $a(b, \phi, T, \tau) = 0.7$ has the lowest normalized settling time in Figure 2.12, where

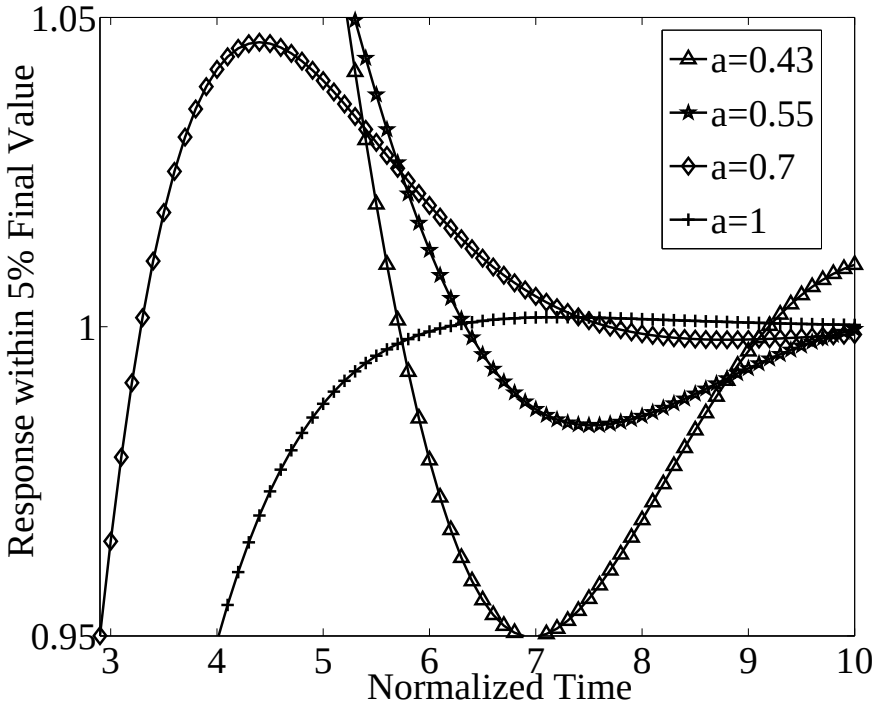

Figure 2.12: Normalized step response of the LTI UWB complex channel of Equation 2.53 for different damping coefficient values a plotted on an expanded scale.

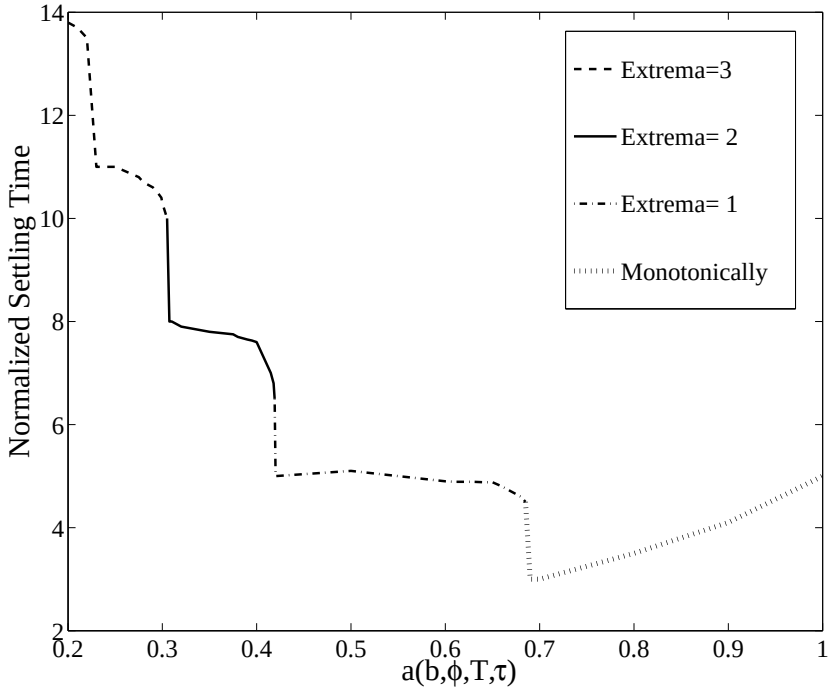

Figure 2.13: Normalized settling time of the LTI UWB channel versus the damping coefficient a of Equation 2.62.

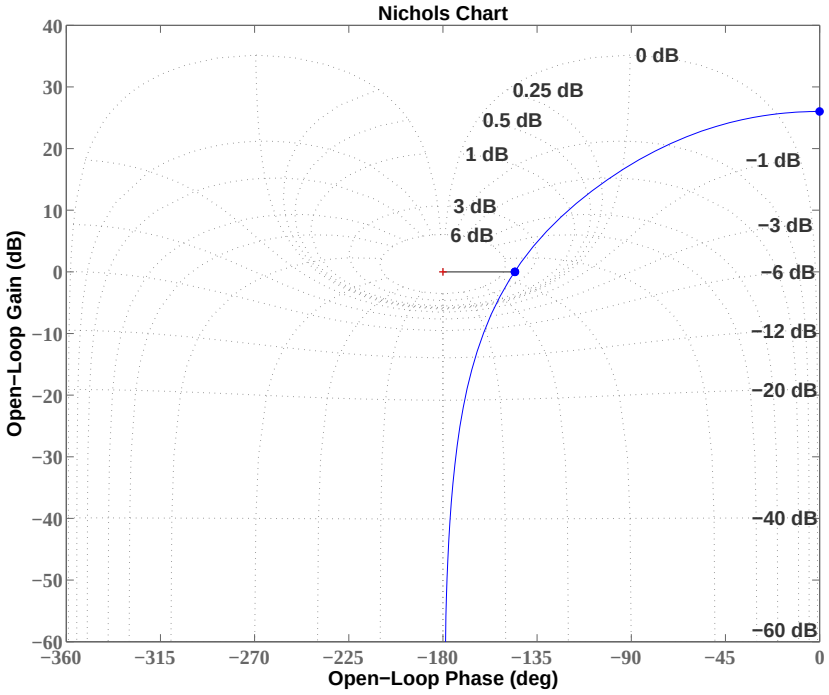

Figure 2.14: Nichols chart showing stability margins for unity feed forward gain control with parameters listed in Table 2.4

the response crosses the -5% line at an abscissa value of 3. Also observe in Figure 2.12 that when the damping coefficient is about 0.7, the time response overshoots by almost 5%, reaching its peak after about 4.4 units of normalized time.

As the damping coefficient drops further from 0.7 to about 0.43, the upper limit of the 5% band is entered into after the derivative has reached zero once (one extremum). However, the lower limit is never violated for $a = 0.43$. Since the settling-time threshold was chosen to be $\pm 5\%$, the settling time is the lowest for a damping coefficient of about 0.7. The normalized settling time versus the damping coefficient relationship plotted from a range of curves such as those exemplified in Figure 2.12 is seen in Figure 2.13, where the different line-types indicate, which of the consecutive step-response extrema fell within the $\pm 5\%$ settling-time thresholds for the first time.

The Nichols chart of Figure 2.14 shows the stability margins for a unity feed-forward gain using the parameters listed in Table 2.4. We would like to find the specific feed-forward gain, which provides a closed-loop resonance peak of 1dB. Finding the specific value of the gain, which meets this specification is not as straightforward as satisfying a direct gain-margin or phase-margin specification. This is because it is not easy to locate the specific point on the original curve exemplified in Figure 2.14 by inspection, which would become tangential to the required M-contour[1] of Figure 2.14. We proceed by trial-

[1]Curves connecting equal values of magnitude for the closed-loop response in Nichols chart [95].

and-error. For the design problem under consideration, the trial-and-error procedure gives a gain adjustment factor of $\frac{8.25}{20}$. As illustrated by Figure 2.14, a peak gain of 26 dB associated with the frequency of $4e^{-11}(\frac{rad}{sec})$, phase margin of 34.2°, delay margin of 3.19 sec with the frequency of $0.187(\frac{rad}{sec})$ confirms closed loop stability.

2.6 Mean Convergence Bound for UWB TH IR Adaptive Equalization

In Section 2.4, we have outlined the architecture of a memory efficient infinite impulse response UWB equalizer based on the transfer function of Section 2.3. In this section, we provide a rigorous analysis and derive the expression of the Mean Convergence Bound (MCB) designed for UWB TH IR adaptive equalization. When the adaptive equalizer's step size parameter μ satisfies the *necessary and sufficient* convergence bound condition, no instabilities are observed. However, if μ exceeds the upper bound, frequent instabilities may be observed.

Table 2.5 details the UWB adaptive equalization advances of the past decade. In most communication systems that employ equalizers, the channel characteristics are unknown a priori and, in many cases, the channel response is time-variant. In such a scenario, the equalizers are designed to be adjustable according to the CIR [39]. The convergence properties of the adaptive algorithms are governed by the step-size parameter. It is mandatory to find a range of step-size parameters in order to ensure the adaptive algorithm's convergence. The convergence and stability analysis of adaptive filters in diverse communication scenarios was an active area of research during the early 1990s [104, 105]. However, a rigorous derivation of the *necessary and sufficient* convergence condition to be satisfied by the filter-coefficient step size parameter μ in the context of adaptive equalization designed for UWB remains an open problem, which will be tackled in this section.

2.6.1 UWB Transmission

Consider a single user of a multiuser UWB communication system employing PPM. For simplicity, we consider binary modulation, but the proposed method can also be applied to M-ary modulation associated with $M > 2$. Let $\mathfrak{F}(t)$ denote a monocycle signalling pulse, which is usually a twice-differentiated Gaussian pulse having a width less than a nanosecond. The spectral shaping of the signalling pulse designed for binary PPM in a TH IR UWB system [12] can be formulated as

$$\psi(t) = \sum_{j=0}^{N_f-1} \mathfrak{F}(t - jT_f - c_j T_f), \tag{2.76}$$

2000	*Authors:* A. G. Showman and J. H. McClellan [96] *Contribution:* A Blind UWB Polarimetric Equalization (BPE) technique was developed that uses second-order statistics to estimate a Synthetic Aperture Radar (SAR) system's response.
2001	*Authors:* G. A. Showman and J. H. McClellan [97] *Contribution:* An UWB adaptive equalization technique was advocated to compensate for the leakage, or crosstalk between UWB channels.
2002	*Authors:* V. S. Somayazulu, J. R. Foerster and S. Roy [98] *Contribution:* A pulse based UWB system and a novel pulsed multicarrier UWB system were compared, detailing timing acquisition and characterizing the achievable performance in multipath channels.
2004	*Author:* A. G. Klein and C. R. Johnson [99] *Contribution:* A Minimum Mean Squared Error (MMSE) decision feedback equalizer (DFE) was proposed for pulse position modulated signals in the presence of intersymbol interference (ISI).
2005	*Authors:* L. Zhiwei, A. B. Premkumar and A. S. Madhukumar [100] *Contribution:* A Matching Pursuit (MP) based tap selection technique was proposed and applied to UWB indoor channel equalization in the presence of ISI and MAI.
2006	*Authors:* Y. Wang and X. Dong [101] *Contribution:* A Mean-Square Error (MSE) lower bound was derived for the frequency-domain Linear Minimum Mean-Squared Error (LMMSE) channel estimator and the optimal pilot sequence that achieves this lower bound was obtained.
2007	*Authors:* A. Parihar, L. Lampe, R. Schober and C. Leung [102] *Contribution:* A new equivalent multiple-input multiple-output (MIMO) description of 4BOK DS-UWB was developed, which facilitates the design of efficient equalizers using MIMO filter optimization techniques .
2009	*Authors:* D. Wang, L. Jiang and H. Chen [103] *Contribution:* A robust noise variance estimator based on second-order statistic was presented in order to avoid the impact of Narrowband Interference (NBI).

Table 2.5: UWB adaptive equalization advances.

where T_f is the frame duration, N_f is the number of frames per symbol and c_j is a sequence of real numbers between 0 and 1 that specifies the user-specific time-hopping code. Having specified the spectral shaping pulse $\psi(t)$ in Equation 2.76, the transmitted signal of the user of interest employing binary PPM can be written as

$$\mathfrak{O}(t) = \sum_{i=-\infty}^{\infty} \psi(t - iT_s - \beta_i \mathfrak{M}), \tag{2.77}$$

where T_s is the symbol duration, β_i represents the binary zero-or-one information symbols occurring with an equal probability of $\frac{1}{2}$ and $\mathfrak{M}$ is a fixed constant, which is a PPM parameter. Let $h(t)$ denote the impulse response of the channel that the user of interest experiences. Assume furthermore that apart from the effects of the multipath channel $h(t)$, there is an additional delay τ between the transmitted signal of the user of interest and the received signal; τ is assumed to be a real number between 0 and T_s without any loss of generality. The resultant received signal can be written as

$$x(t) = \sum_{i=-\infty}^{\infty} \mathfrak{O}_{rec}(t - iT_s - \beta_i \mathfrak{M} - \tau) + \mathfrak{N}(t), \tag{2.78}$$

where $\mathfrak{N}(t)$ is the additive noise plus the multiple-user interference, which is assumed to be a zero-mean AWGN process. We start with the problem formulation.

2.6.2 Problem Formulation

The MCB analysis is carried out by considering the LMS algorithm having equalizer weights of $\underline{\mathrm{w}} = [w_0\ w_1 \ldots w_N]$, a desired sequence $d(n)$, step size μ and adaptive equalization error $e(n)$ with the following formulation as depicted in Figure 2.15:

- The channel is causal and has a Finite Impulse Response (FIR) duration of less than T_s; i.e we have $h(t) = 0$ if $t < 0$ or $t \geq T_s$;
- The symbol synchronization at the receiver is assumed to be perfect; in other words, τ is known at the receiver;
- The input sequence is $x(n)$ and all other random stochastic processes are assumed to be second-order stationary or Wide Sense Stationary (WSS) with a mean of zero;
- Filter output: $y(n) = \underline{\mathrm{w}}^H \underline{\mathrm{x}}(n)$;
- Estimation error: $e(n) = d(n) - y(n)$;
- Variance of the desired signal $d(n)$: σ_d;

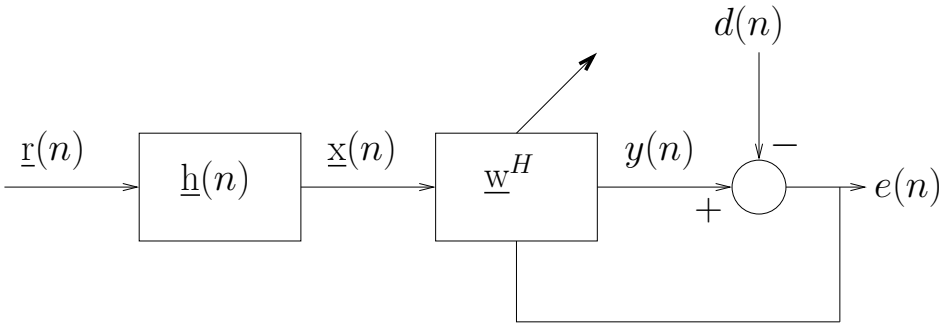

Figure 2.15: General block diagram of the adaptive equalizer

- Tap weight adaptation: $\underline{\mathrm{w}}(n+1) = \underline{\mathrm{w}} + \mu x(n) e^*(n)$;
- Correlation matrix: $\underline{\mathrm{R}} = \mathbb{E}[\underline{\mathrm{x}}(n)\underline{\mathrm{x}}^H(n)]$;
- Cross-correlation vector: $\underline{\mathrm{P}} = \mathbb{E}[\underline{\mathrm{x}}(n)d^*(n)]$;

The proposed MCB is valid for any adaptive equalization algorithm, including the Least Mean Square (LMS), the Normalized Least Mean Square (NLMS), Block Least Mean Square (BLMS), albeit there is a difference in their initialization and boundary conditions. The general equalization algorithm considered in our MCB analysis is formulated as follows:

input : $\delta(t)$,$\mathfrak{N}(t)$,$d(n)$;
output: y(n);

$\psi(t)$*: UWB pulse generation*;
$\mathfrak{O}(t)$*: Transmit signal generation*;
$x(t) = \mathfrak{O}(t) * h(t)$*: UWB pulse generation*;
$\mathfrak{N}(t)$*: AWGN Noise and Multiuser Interference addition*;
$x(n)$*: Analog-to-Digital conversion*;
Initialization of filter weights;
for $i = 1 \rightarrow$ *final iteration* **do**
    filter output calculation;
    error calculation;
    weight update;
    if *error* $\leq$*desired error* **then**
        break;
        else continue
    end
end

2.6.3 Mean Convergence Bound Derivation

In this section, we will derive the range of MCB, commencing from optimal taps of the UWB adaptive equalizer.

2.6.3.1 Optimal Taps

The optimal filter coefficients of classic equalizers have been derived in a range of studies [39, 49, 106]. In order to find the optimal filter coefficients, we have to use the technique known as *spectral factorization* [39, 106]. The optimum linear filter coefficients were formulated originally by Wiener and Hopf (1931) for the case of a continuous-time filter [106]. In case of the UWB scenario considered, a similar approach to that of Wiener and Hoff [49, 106] can be used in the discrete time-domain. We define the cost function of the adaptive transversal equalizer designed for equalizing the discertized received sequence $x(n)$ of the UWB-TH-IR system using the notations of Section 2.6.2 as the MSE of the equalizer's output formulated as:

$$\varepsilon = \mathbb{E}[e(n)e^H(n)] = \sigma_d^2 - \underline{\mathrm{w}}^H\underline{\mathrm{P}} - \underline{\mathrm{P}}^{\mathrm{H}}\underline{\mathrm{w}} + \underline{\mathrm{w}}^H\underline{\mathrm{Rw}}. \tag{2.79}$$

Equation 2.79 represents the $(N+1)$-dimensional equalizer-output error surface with N degrees of freedom for N equalizer taps. This surface is characterized by a unique minimum. At the minimum point of the error surface the cost function ε attains its minimum value. At this point, the tap-weight gradient vector $\nabla_{\underline{w}}(\varepsilon)$ is identically zero, which is the optimal point. In other words, we have:

$$\nabla_{\underline{w}}(\varepsilon) = \frac{\partial}{\partial\{w_k\}_{k=0}^N}[\Re(\varepsilon) + \Im(\varepsilon)] = \underline{0}. \tag{2.80}$$

Applying the $\nabla_{\underline{w}}$ operator to each additive term of the Equation 2.79 we obtain

$$\begin{aligned}
\nabla_{\underline{w}}(\sigma_d^2) &= 0 \\
\nabla_{\underline{w}}(\underline{\mathrm{w}}^H\underline{\mathrm{P}}) &= \frac{\partial(\underline{\mathrm{w}}^H\underline{\mathrm{P}})}{\partial\{w_k\}_{k=0}^N} = 2\underline{\mathrm{P}}, \\
\nabla_{\underline{w}}(\underline{\mathrm{P}}^H\underline{\mathrm{w}}) &= \underline{0}, \\
\nabla_{\underline{w}}(\underline{\mathrm{w}}^H\underline{\mathrm{Rw}}) &= \frac{\partial(\underline{\mathrm{w}}^H\underline{\mathrm{Rw}})}{\partial\{w_k\}_{k=0}^N}, \\
&= \frac{\partial}{\partial w_k}\Bigg(\sum_{\substack{i=0\\ i\neq k}} w_i^* \sum_{j=0}^{N} \mathrm{R}_{ij}w_j + w_k^* \sum_{j=0}^{N} \mathrm{R}_{kj}w_j\Bigg), \\
&= 2\sum_{j=0}^{N} \mathrm{R}_{kj}w_j = 2\underline{\mathrm{Rw}}.
\end{aligned} \tag{2.81}$$

Setting the expression in Equation 2.81 to zero gives

$$\underline{\mathrm{w}}_{(th)} = \underline{\mathrm{R}}^{-1}\underline{\mathrm{P}}. \tag{2.82}$$

Equation 2.82 represents the optimal weights of the adaptive UWB TH IR equalizer [106].

2.6.3.2 Mean Convergence analysis

The equalizer's weight error vector is defined as

$$\underline{\triangle} = \underline{\mathrm{w}}(n) - \underline{\mathrm{w}}_{th}. \tag{2.83}$$

Upon subtracting $\underline{\mathrm{w}}_{th}$ from both sides of the tap weight adaptation equation of Section 2.6.2, we obtain a recursive equalizer weight error vector as follows

$$\underline{\triangle}(n+1) = \underline{\triangle}(n) + \mu\underline{\mathrm{x}}(n)e^*(n) \tag{2.84}$$

and substituting the error expression of $e(n) = d(n) - y(n)$ in Equation 2.84 we arrive at

$$\underline{\triangle}(n+1) = \underline{\triangle}(n) + \mu\underline{\mathrm{x}}(n)[d^*(n) - \underline{\mathrm{x}}^H(n)(\underline{\mathrm{w}}_{th} + \underline{\triangle}(n))]. \tag{2.85}$$

Taking the expectation $\mathbb{E}[.]$ of Equation 2.85 and simplifying it further we obtain

$$\mathbb{E}[\underline{\triangle}(n+1)] = \mathbb{E}[\underline{\triangle}(n)] + \mu\Bigg(\mathbb{E}[\underline{\mathrm{x}}(n)[d^*(n)] \\ -\underline{\mathrm{w}}_{th}\mathbb{E}[\underline{\mathrm{x}}(n)\underline{\mathrm{x}}^H(n)] - \mathbb{E}[\underline{\mathrm{x}}(n)\underline{\mathrm{x}}^H(n)\underline{\triangle}(n)]\Bigg). \tag{2.86}$$

Upon using the notation of $\underline{\upsilon}(n)$=$\mathbb{E}[\underline{\triangle}(n)]$ for the mean of the weight error vector and substituting the values of the correlation matrix $\underline{\mathrm{R}}$ and cross-correlation vector $\underline{\mathrm{P}}$ in Equation 2.86, we get

$$\underline{\upsilon}(n+1) = \underline{\upsilon}(n) + \mu[\underline{\mathrm{P}} - \underline{\mathrm{R}}\underline{\mathrm{w}}_{th}] - \mu\mathbb{E}[\underline{\mathrm{x}}(n)\underline{\mathrm{x}}^H(n)\underline{\triangle}(n)]. \tag{2.87}$$

Upon inserting Equation 2.82 in Equation 2.87 and simplifying the result we obtain

$$\underline{\upsilon}(n+1) = (\underline{\mathrm{I}} - \mu\underline{\mathrm{R}})\underline{\upsilon}(n). \tag{2.88}$$

When applying a unitary Similarity Transformation (ST) (see Appendix C) to the correlation matrix $\underline{\mathrm{R}}$ in Equation 2.88, we arrive at

$$\underline{\mathrm{R}} = \underline{\mathfrak{B}\mathfrak{D}\mathfrak{B}}^H, \tag{2.89}$$

where $\underline{\mathfrak{D}}$ is the diagonal matrix with eigenvalues of $\underline{\mathrm{R}}$ on its diagonal and where $\underline{\mathfrak{B}}$ is a unitary matrix satisfying

$$\underline{\mathfrak{B}\mathfrak{B}}^H = \underline{\mathfrak{B}}^H\underline{\mathfrak{B}} = \underline{\mathrm{I}}. \tag{2.90}$$

When Equation 2.89 is substituted in Equation 2.88, we get

$$\underline{\upsilon}(n+1) = \Big(\underline{\mathfrak{B}\mathrm{I}\mathfrak{B}}^H - \mu(\underline{\mathfrak{B}\mathfrak{D}\mathfrak{B}}^H)\Big)\underline{\upsilon}(n). \tag{2.91}$$

When applying the Karhunen-Loeve Transform (KLT) (see Appendix A) to Equation 2.91, we arrive at

$$\underline{\mathfrak{B}}^H\underline{\upsilon}(n+1) = (\underline{\mathrm{I}} - \mu\underline{\mathfrak{D}})\underline{\mathfrak{B}}^H\underline{\upsilon}(n). \tag{2.92}$$

Upon substituting $\underline{\mathfrak{u}}(n)=\underline{\mathfrak{B}}^H\underline{\upsilon}(n)$ into Equation 2.92, we obtain

$$\underline{\mathfrak{u}}(n+1) = (\underline{\mathrm{I}} - \mu\underline{\mathfrak{D}})\underline{\mathfrak{u}}(n). \tag{2.93}$$

The norm square $\| \underline{\mathfrak{u}}(n) \|^2$ is equal to the norm square $\| \underline{\upsilon}(n) \|^2$, which can be verified as

$$\| \underline{\mathfrak{u}}(n) \|^2= \underline{\mathfrak{u}}^H(n)\underline{\mathfrak{u}}(n) = \underline{\upsilon}^H(n)\underline{\mathfrak{B}\mathfrak{B}}^H\underline{\upsilon}(n) =\| \underline{\upsilon}(n) \|^2 . \tag{2.94}$$

it may be readily shown from Equations 2.86, 2.88, 2.93 and 2.94 that if n tends to ∞, we have $\| \underline{\mathfrak{u}}(n) \|^2= 0$, which implies that we have $\mathbb{E}[\underline{\triangle}(n)] \rightarrow 0$, confirming that $\mathbb{E}[\underline{\mathrm{w}}(n)] \approx \mathbb{E}[\underline{\mathrm{w}}_{th}]$ i.e.

$$\lim_{n\rightarrow\infty} \| \underline{\mathfrak{u}}(n) \|^2= 0 \Rightarrow \mathbb{E}[\underline{\triangle}(n)] \rightarrow 0 \Rightarrow \mathbb{E}[\underline{\mathrm{w}}(n)] \approx \mathbb{E}[\underline{\mathrm{w}}_{th}]. \tag{2.95}$$

Taking the norm of Equation 2.93 in conjunction with the real eigenvalues λ_i, we get

$$\| \underline{\mathfrak{u}}(n+1) \|^2= \sum_{i=0}^{N}(1-\mu\lambda_i)^2 \| \underline{\mathfrak{u}}(n) \|^2 . \tag{2.96}$$

By considering Equation 2.96 it may be inferred that the *necessary and sufficient* condition, which makes Equation 2.95 valid is

$$\lim_{n\rightarrow\infty} \| \underline{\mathfrak{u}}(n) \|^2 \longrightarrow 0 \quad \Leftrightarrow \quad (1-\mu\lambda_i)^2 < 1. \tag{2.97}$$

Finally, the MCB of the step size μ of the adaptive UWB TH IR equalizer inferred from Equation 2.97 has to obey

$$0 < \mu < \frac{2}{\lambda_{max}}. \tag{2.98}$$

Sometimes it is difficult to find the eigenvalues of $\underline{\mathrm{R}}$ because of its excessive size in an UWB scenario. A more relaxed step size bound is determined by the trace $tr(.)$ as follows [106]:

$$tr(\underline{\mathrm{R}}) = tr(\underline{\mathfrak{B}\mathfrak{D}\mathfrak{B}}^H) = tr(\underline{\mathfrak{D}}) = \sum_{i=0}^{N}(\lambda_i) \geq \lambda_{max}. \tag{2.99}$$

From Equation 2.99 we get

$$0 < \mu \leq \frac{2}{tr(\underline{\mathrm{R}})}. \tag{2.100}$$

For the case of second-order stationary stochastic processes the $tr(\underline{\mathrm{R}})$ consists of the variances, hence we do not have to find the eigen-values of the correlation matrix. In the next section we characterize the rate of convergence for MCB derived in a realistic simulation environment.

2.6.3.3 Simulation Results

The system parameters are T_f=11 ns, N_f=12, T_s=132 ns. The parameter $\mathfrak{M}$ is set to 1 ns. A discrete-time equivalent model of the UWB system is used. The received signal is filtered by a pulse-shape-matched filter. The discrete-time equivalent channel we simulated

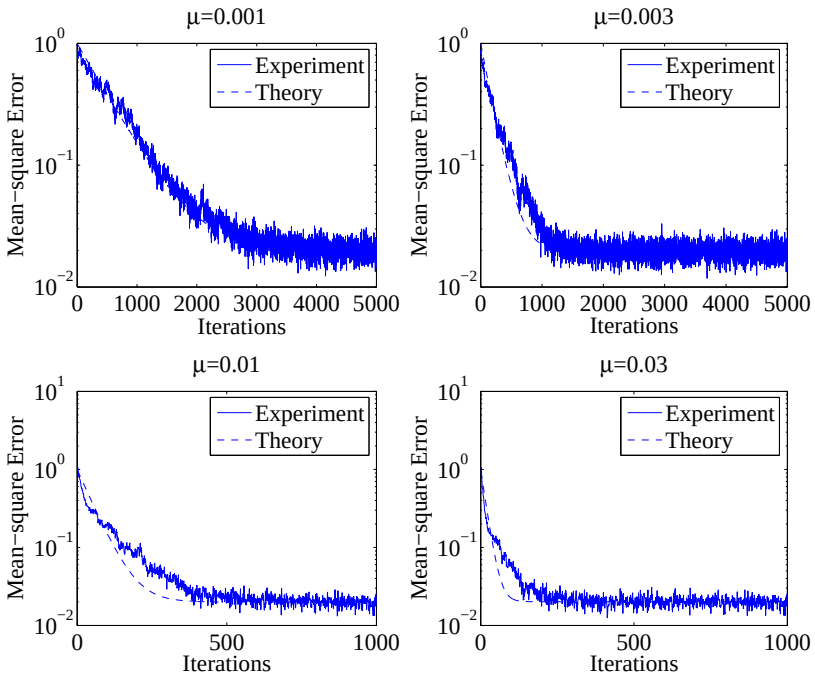

Figure 2.16: Experimental learning curves of UWB TH IR adaptive transversal equalizer for varying step size parameter μ

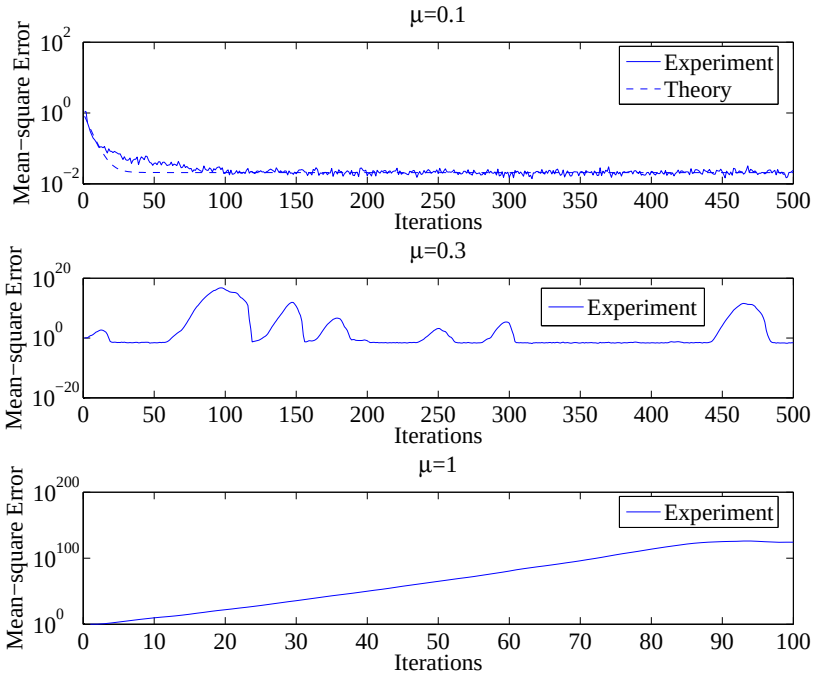

Figure 2.17: Experimental learning curves of UWB TH IR adaptive transversal equalizer for varying step size parameter μ

had 64 equally spaced taps with a tap-spacing of 1 ns. The channel taps were assumed to be independent, zero mean and Gaussian distributed with an exponentially decreasing variance. The variance of the last tap was $\frac{1}{5}$ of that of the first tap. The average channel output energy is normalized to unity for each channel realization. (Therefore, strictly speaking, the taps were not independent.) In all our simulations, we have averaged the performance over 50 randomly generated channel realizations. For these specifications the step size MCB for the adaptive UWB TH IR transversal equalizer becomes $0 < \mu < 0.271$.

Figure 2.16 shows experimental plots of the learning curves of the adaptive UWB TH IR transversal equalizer, namely the Mean-squared error versus the number of tap-updates, n. Specifically, the values for μ are 0.001, 0.003, 0.01 and 0.03. It can be readily seen from Figure 2.16 that as the step size μ is reduced, the rate of convergence is correspondingly decreased. However, no instabilities are observed, since all the step size values are within the MCB. Furthermore, a reduction in the step size parameter μ also reduces the deviation of the experimentally computed learning curves.

Figure 2.17 characterizes the fact as the step size parameter μ approaches the upper bound of 0.1, there are still no instabilities. Observe in Figure 2.17 that for $\mu = 0.1$ the rate of convergence has increased rapidly, approaching its steady state within about 100 iterations. However, as μ reaches the upper bound of 0.3, the adaptive equalizer becomes unstable and hence exhibits large output variations. The step size parameter of $\mu = 1$ makes the algorithm unstable.

2.7 Chapter Conclusions

This chapter has the following findings

- The inverse system described in Section 2.3 does not require any extra channel sounding sequence for the recovery of the received channel-contaminated UWB pulses, hence avoids any channel-sounding-related throughput reduction and therefore may be viewed as a blind technique.
- The equalizer proposed in Section 2.4 attains exactly the same BER performance as the conventional equalizer, despite requiring only half the memory, as demonstrated against the benchmarker designs provided in [1], [77].
- An efficient technique of characterizing the LTI UWB channel's stability was discussed in Section 2.5, which simply inspects the step-response of the system. This technique was then compared to the classic method of finding all the roots of the transcendental equation in the complex s-plane.

- A convenient way of selecting the channel parameters satisfying a certain settling time, %overshoot, peak response and rise-time specifications was suggested in Section 2.5, which relies on the analytical time-domain responses.

- Explicitly, it has been shown in Section 2.6 that as the step size parameter μ is reduced, the rate of convergence of the UWB TH IR adaptive transversal equalizer is correspondingly decreased. A reduction in μ also has the effect of reducing the variation in the experimentally computed learning curves, as demonstrated in Figure 2.16.

2.8 Chapter Summary

In Section 2.3, generic z-domain DTTF estimation was proposed for UWB channels, which requires no channel sounding sequence transmission and hence constitutes a blind technique. This was achieved by estimating the CIR with the aid of the information signalling pulses and then equalizing the effects of the channel by the corresponding inverse system. Furthermore, in Section 2.4 a generic IIR equalizer architecture was proposed for UWB systems, which halves the memory requirement of the conventional IIR equalizers. This was achieved by exploiting the aperiodically repeated clusters of negative-exponentially decaying segments of the CIR and hence by providing a single common delay-line between the input and output of the equalizer.

The stability of a general LTI UWB CIR model was investigated in Section 2.5. Since the s-domain and z-domain transfer function corresponding to the UWB CIR has an extremely high number of singularities, it is not automatically guaranteed that none of the poles falls on the right-half of the s-plane or outside the unit-circle of the z-plane. Hence the stability analysis necessitates the exhaustive testing of this stability criterion for a potentially excessive number of poles. We circumvented this arduous task by developing the closed-form time-domain step-response of the so-called homogenous, non-homogenous and vectorial LTI system in Section 2.5.3. Furthermore, the normalized settling time of the step response was evaluated for diverse damping coefficients. A stability case-study was provided with the aid of Nichols charts in Section 2.5.4.

Finally, in Section 2.6 we provided a rigorous analysis of the MCB for UWB TH IR adaptive equalization. Our technique is generic and thus valid for any adaptive algorithm used in a UWB scenario. Furthermore, we detailed the rate of convergence by means of varying the step size parameter μ within the bound. Our simulation results provided in Figures 2.16 and 2.17 confirm that no instabilities are observed, if μ satisfies the convergence bound conditions derived.

Chapter 3

EXIT Chart Aided UWB System Design

3.1 Introduction

In Section 2.3 the UltraWideBand (UWB) channel's z-domain transfer function was derived based on Section 2.2. Furthermore, Sections 2.5 and 2.6 provided the stability analysis and mean convergence bound for UWB Channels. The UWB channels characteristics outlined in Chapter 2 will be exploited both in this and the following chaptersones to construct UWB systems that are capable of counteracting the deliterious effects of channel. Chapter 3 commences by outlining the implications of appropriate diversity order selection in an uncoded UWB system. Then a coded UWB system based on a 2-stage concatenation of an inner and outer encoders is constructed in Section 3.3. The corresponding decoders at the receiver exchange extrinsic information for the sake of enhancing the attainable system performance. Both a Direct Sequence (DS) and a Time Hopping (TH) Pulse Position Modulated (PPM) UWB systems are studied using Extrinsic Information Transfer (EXIT) charts. We will demonstrate on the basis of the area properties of EXIT curves [107, 108] in Section 3.4 that TH-UWB has a better performance than its otherwise equivalent DS-UWB counterpart. Furthermore, it is demonstrated that classic regular Forward Error Correction (FEC) encoders are unable to arbitrarily approach the system's capacity.

A specific benefit of UWB systems is that owing to their wide transmission BandWidth (BW), it is possible to resolve a high number of independently fading MultiPath Components (MPC) of the channel, which may be coherently combined for example by a Maximal Ratio Combining (MRC) receiver in order to achieve a high multipath diversity gain. By contrast, systems using narrowband transmissions typically suffer from the lack of multi-

path diversity, since typically a lower number of multipath components can be resolved, which may even result in a single faded signal component. Hence, with the aid of appropriate UWB synchronization capable of locking onto the strongest path of the received signal, a large number of multipath components can be resolved for the sake of achieving a high multipath diversity order [12, 15].

Both the TH PPM techniques [22, 109–112] and Direct Sequence Spread Spectrum (DSSS) techniques [113–115] have been used for the implementation of UWB systems. In the former, appropriately time-shifted pulses are used to transmit baseband UWB signals, using the stylized signalling format seen in Figure 1.6. In the latter, multiple chips having a chip duration equal to the basic time-domain signalling pulse duration are used to transmit data bits, as observed in Figure 1.4. Multiple users may be supported by employing the classic Code-Division Multiple-Access (CDMA) technology.

EXIT charts have been proposed by ten Brink [107, 116] for the convergence performance analysis of iterative decoding. EXIT charts are capable of accurately predicting the so-called 'turbo cliff' position of iterative detectors, where an infinitesimally low BER may be attained upon using a sufficiently high number of iterations [117–121]. In this chapter, we analyze the detection convergence and design of iteratively decoded UWB systems with the aid of EXIT charts, which visualize the evolution of the input/output mutual information exchange between the inner and outer decoders in consecutive iterations. The application of EXIT charts is based on two main assumptions, which are realistic, when using sufficiently long interleavers. These assumptions are that the *a priori* Logarithmic Likelihood Ratio (LLR) values of adjacent soft-values are fairly uncorrelated and that the Probability Density Function (PDF) of the *a priori* LLR values is Gaussian [122]. Recently, studying the convergence behaviour of iterative decoding has attracted considerable research attention [107, 116, 123–131].

The novelty and rationale [4, 5] of this chapter can be summarised as follows:

1. ***Uncoded UWB System**: We quantify the performance of uncoded TH Impulse Radio (IR) operating in UWB propagation channels as a function of the diversity order. We select the L strongest MPCs from the N_r resolvable MPCs for MRC in order to achieve the best attainable performance gain in both single-user and full-load scenarios. Three classic detectors are used, namely the correlation , the Zero Forcing (ZF) and the Minimum Mean Square Eorror (MMSE). Our results suggest that a diversity order of L=20 approaches the maximum attainable gain of $18dB$ and $12dB$ in single-user and full-load scenarios for N_u=63 users, when employing a spreading factor of N_s=63 in comparison to the "no-diversity" configuration.*

2. ***Coded UWB System:** Substantial performance improvements can be attained by serially concatenated channel encoding combined with a Unity Rate Code (URC) for*

transmission over the IEEE 802.15.3a UWB channel. We compare the performance of the iterative decoding aided correlation and MMSE detectors, when exchanging extrinsic information between the URC's decoder as well as the outer Recursive Systematic Convolutional (RSC) code's decoder. The iterative decoding convergence analysis of the proposed system is carried out with the aid of EXIT charts. As expected, the iteratively decoded fully-loaded system employing MMSE detection outperforms its lower-complexity counterpart employing the equivalent correlation detector. Explicitly, UWB DS-CDMA using the MMSE detector attains a BER of 10^{-5} *at* $\frac{E_b}{N_o} = 2dB$*, when supporting* $N_u = 32$ *users employing* $i = 12$ *decoding iterations, while the same system using the correlation detector has an excessive BER [4].*

3. *Finally, we analyse the decoding convergence of TH and DS-CDMA UWB systems operating in a multipath channel environment using EXIT charts. The UWB systems under study are constituted either by a serially concatenated Pulse Position Modulated TH or a code-synchronous DS-CDMA system communicating over uncorrelated multipath Nakagami fading channels. It is demonstrated that the beneficial effects of multipath diversity allow us to reduce the minimum required SNR. More explicitly, it is shown based on area properties of EXIT charts that TH outperforms DS-CDMA in UWB scenario considered [5].*

The rest of the chapter is organised as follows. The choice of the appropriate diversity order is discussed in Section 3.2 in the context of an uncoded TH IR UWB system using MRC. A novel EXIT chart aided DS-CDMA UWB system design is proposed in Section 3.3. Furthermore, we provide a comprehensive comparative analysis of TH-UWB and DS-UWB using EXIT Charts in Section 3.4. Our conclusions are presented in Section 3.5, followed by the chapter's summary in Section 3.6.

3.2 Implications of Diversity Order Selection

Table 3.1 gives an overview of the last decade's technical advances on the topic of diversity order selection. The optimal diversity combiner designed for transmission over fading channels is constituted by the MRC scheme, where multiple copies of the same signal are combined coherently so as to maximise the instantaneous SNR at its output. The performance versus affordable complexity issues have dominated the study of multipath combining receivers that process only a subset of the resolvable multipath components. Naturally, the number of MPCs that can be combined is limited by the affordable implementational complexity and the associated channel estimation accuracy requirements [15].

A comprehensive statistical model of UWB propagation channels was provided in [24] for the frequency range spanning from 3 to 10 GHz, which was adopted by the IEEE 802.15.4a

2000	*Authors:* S. W. Kim [132] *Contribution:* The relative benefits of rate and power control techniques were presented in terms of the achievable channel estimation error, diversity order and outage probability.
2002	*Authors:* S. X. Ng and L. Hanzo [133] *Contribution:* Space-time block coded in-phase/quadrature-phase (IQ)-interleaved trellis coded modulation (TCM) and turbo TCM (TTCM) schemes were proposed, which are capable of quadrupling the diversity order of conventional symbol-interleaved TCM and TTCM schemes.
2003	*Authors:* Z. Chen, J. Yuan, B. Vucetic and Z. Zhou [134] *Contribution:* A systematic method of constructing full-rate space-time block codes with a full diversity order was proposed.
2004	*Author:* N. Prasad and M. K. Varanasi [135] *Contribution:* For an uncoded K-transmit and N-receive antenna aided coherent narrow-band communication system, It was shown that the error probability is limited by error propagation and that the attainable diversity order is limited to N-K+1.
2006	*Authors:* E. Sengul, E. Akay and E. Ayanoglu [136] *Contribution:* Assuming that K and N are the number of antennas at the transmitter and the receiver, respectively, it was shown that beamforming based on the transmission of a single symbol from all transmit antennas at the same time is capable of achieving the maximum spatial diversity order of K·N.
2008	*Authors:* Y. S. Chan, P. C. Cosman and L. B. Milstein [137] *Contribution:* The time-variant diversity order of the channel, defined as the ratio of the overall bandwidth of the system to the coherence bandwidth of the channel was involved in order to control the video-quality of a video-codec.
2009	*Authors:* Y. Jing and H. Jafarkhani [24] *Contribution:* The idea of relay selection by allowing more than one relay to cooperate was generalized.

Table 3.1: Advances in diversity order selection.

Task Group as the standard model for the evaluation of UWB system proposals. The model captures the frequency-dependence of the path gain as well as several generalizations of the SalehValenzuela model [68], such as the mixed Poissonian distributed time of arrival statistics and the delay-dependent cluster decay constants.

Against this background, in the rest of this section we characterize a UWB-TH-IR system. More specifically, we select the L strongest MPCs from the N_r resolvable MPCs for MRC in order to achieve the best attainable performance in both single-user and full-load multi-user scenarios. In Section 3.2.2.3 we will characterize the Correlation, the ZF and the MMSE detectors, respectively. The gains achieved by the the different detectors as a function of the diversity order are detailed.

3.2.1 Uncoded UWB System Model

Figure 3.1 potrays the schematic of the system considered in this section, where 16-ary symbols are transmitted within a TH interval T_H at a rate of R_H. We have considered slow TH, therefore the ratio of signalling interval duration T_s to TH interval T_H is less than 1. As shown in Figure 3.1, during a signalling interval duration of T_s seconds, b message bits of the kth user are loaded into the symbol buffer. The corresponding signalling waveforms were potrayed in Figure 1.6. We denote the transmitted symbol as $\zeta^{(k)}$, where we have $\zeta^{(k)} \in \{0, 1, \cdots, 16\}$ for 16-ary signalling. The 16-ary symbol $\zeta^{(k)}$ is temporarily stored in the buffer, where it awaits its time-slot, in which it is to be transmitted. Since a slow TH scheme's frame duration T_f is equal to the symbol duration T_s, therefore each transmitted time-domain pulse $\Psi(t)$ conveys a 16-ary symbol. In this section, we have used Orthogonal Prolate Spheroidal Wave Function (OPSWF) based signalling pulses $\Psi(t)$ generated by the pulse generator, as seen in Figures 2.6 and 2.7.

As shown in Figure 3.1, the transmitter generates a time-domain pulse $\Psi(t - jT_f)$, where j represents the frame index, $\Psi(t)$ is defined within the interval of $[0, T_h)$, which is normalized to ensure that we have $\int_0^{T_h} \Psi^2(t) = T_h$ in the context of each 16-ary symbol. In Figure 3.1, $\upsilon^{(k)}$ represents the Pesudo-Noise (PN) code based TH pattern assigned to user k, where $\upsilon^{(k)}$ are integers assuming values in the range of $0 < \upsilon^{(k)} \leq (N_s - 1)$, with N_s being the spreading factor. The TH pattern imposes a PN-code-dependent time shift on the pulse during every frame. Each PN-code-dependent time shift is a discrete-time value given by $\upsilon^{(k)} T_c$ and obeying $0 < \upsilon^{(k)} T_c \leq (N_s - 1) T_c$. In the context of baseband 16-ary pulse position modulation, one of the 16 possible time slots within the TH chip determined by the TH pattern is activated for transmission, signalling the presence of a pulse. The 16-ary symbol $\zeta^{(k)}$ assuming a value from the range of $0 < \zeta^{(k)} \leq 16$ imposes a further $\zeta^{(k)} T_h$ seconds of information symbol-dependent time shift on the time domain pulse position $\Psi(t)$, as shown in Figure 3.1 and in Figure 1.6. Then the combined signal

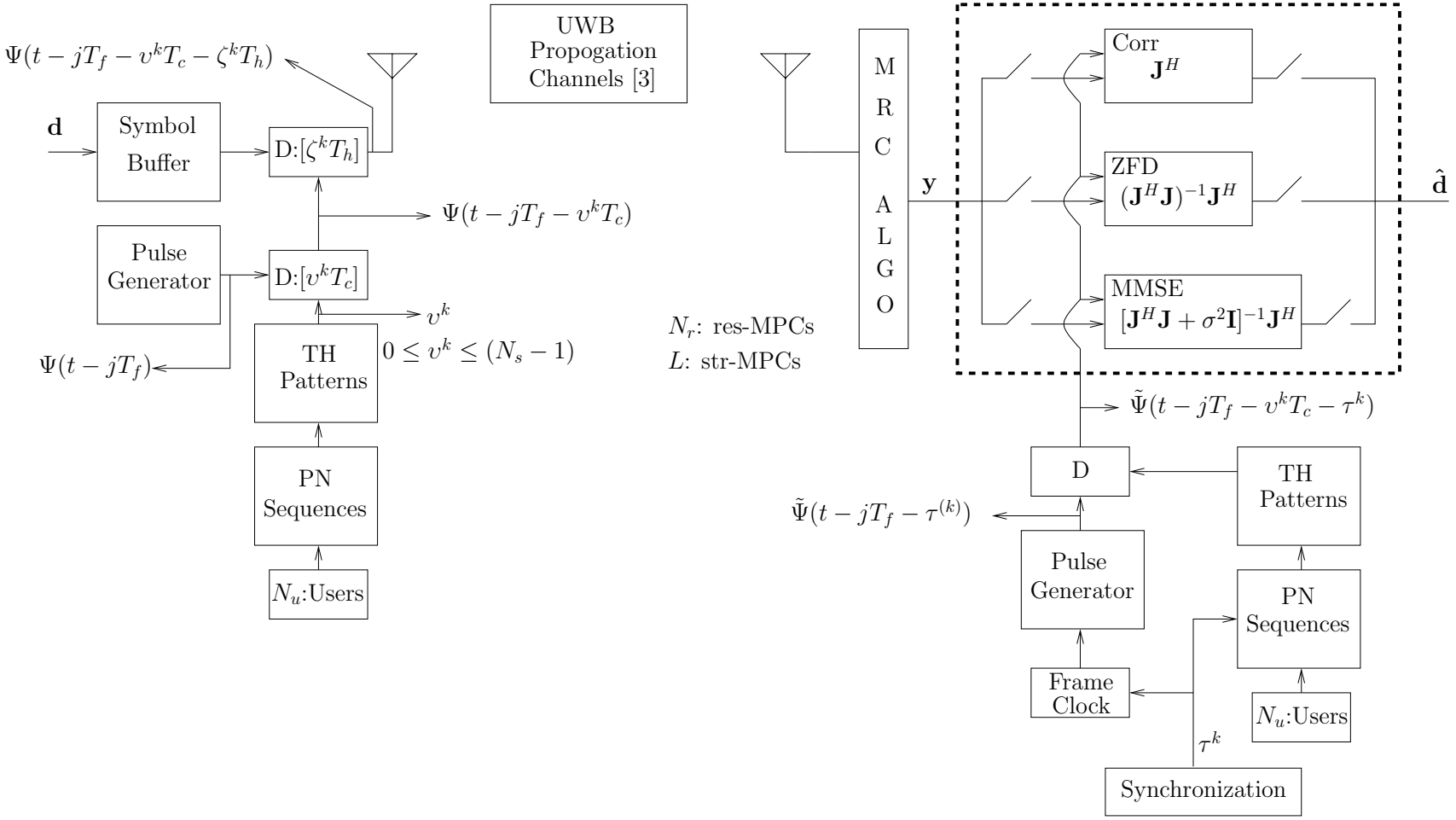

Figure 3.1: Schematic of the uncoded UWB-TH-IR system having N_r resolvable MPCs and involving the L strongest MPCs in conjunction with three different detectors.

of N_u users is transmitted.

After transmission over the UWB propagation channel [24] based on indoor channel measurements between 3.1 GHZ to 10.6 GHz over a range of less than 10 meters and contaminated by Additive White Gaussian Noise (AWGN) having a variance of $\frac{N_o}{2}$ per dimension, the signal is fed into a MRC block, as shown in Figure. 3.1. The MRC combines the MPCs so as to maximise the instantaneous SNR at its output. In this section, we select the L strongest MPCs from the N_r resolvable MPCs. After the MRC block, the received signal $\mathbf{y}$ is fed into the detector block of Figure 3.1 supported by the information required to estimate the received data $\hat{\mathbf{d}}$.

The Corr, ZFD and MMSE detectors are used to estimate the data $\hat{\mathbf{d}}$. Based on the knowledge of the path delays $\tau^{(k)}$, the pulse generator generates a time domain pulse $\Psi(t-jT_f-\tau^{(k)})$ for the jth frame and the TH pattern generator outputs the corresponding TH pattern value or synonymously, the address code $\upsilon^{(k)}$, as shown in Figure 3.1 and in Figure 1.6. The TH pattern $\upsilon^{(k)}$ provides a time shift of $\upsilon^{(k)}T_c$ seconds for the time-domain pulse $\Psi(t-jT_f-\tau^{(k)})$, which yields $\Psi(t-jT_f-\upsilon^{(k)}T_c-\tau^{(k)})$. This information is provided for each detector in order to estimate the data $\hat{\mathbf{d}}$. In the next section we briefly highlight the UWB transmitter and detector schemes.

3.2.2 UWB Transmission and Detection

3.2.2.1 Transmitted Signal

The UWB-TH-IR signal is formulated as [12]

$$s^{(k)}(t) = \sum_{j=-\infty}^{\infty} \Psi(t - jT_f - \upsilon^{(k)}T_c - \zeta^{(k)}T_h), \tag{3.1}$$

where $\Psi(t)$ is, again, the OPSWF signalling pulse shape, T_f is the frame time, $\upsilon^{(k)}$ represents the PN code based TH pattern assigned to user k, T_c is the time shift based on the TH code, where the code repeats after a certain interval, $\zeta^{(k)}$ corresponds to the data symbols of user k, while T_h is small shift in the pulse position, either forward or backward to represent the modulating data symbol. The Pulse Repetition Frequency (PRF) is the reciprocal of T_F. The frame time T_F will be of the order of 1000 times the actual pulse width.

In Figure 3.2, we show the output of a simple TH aided binary PPM UWB transmitter, where T_F is the frame duration, T_{PP_n} is the PPM-related shift in the pulse position, either forward or backward with respect to the nominal signalling instant to represent the binary stream, T_{CH_n} is the time shift based on the unique time hopping code of a specific user, where the code repeats after a certain interval.The schematic characterises a single-user

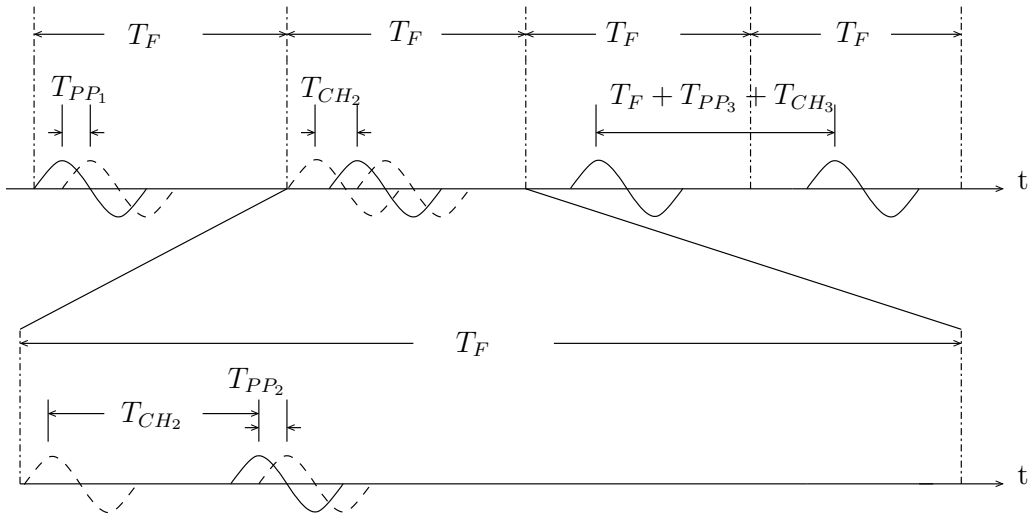

Figure 3.2: A binary TH-PPM system output.

scenario, which can be readily extended to the multi-user scenario by using different time-hopping PN codes for the different users, as seen in Figure 3.1.

3.2.2.2 Channel Model

In this section the UWB-TH-IR system considered is evaluated using the UWB multipath channel model based on indoor channel measurements between 3.1 GHZ to 10.6 GHz over a range of 7 to 10 meters and detailed in Section 2.2 based on [24]. Here we briefly outline the channel model used in our analysis. The complex baseband channel impulse response of the Saleh-Valenzuela (SV) model is given in general as [68]

$$h(t) = \sum_{l=0}^{N} \sum_{k=0}^{K} \alpha_{(k,l)} e^{(\psi_{(k,l)})} \delta(t - T_l - \tau_{k,l}), \tag{3.2}$$

where $\alpha_{(k,l)}$ is the tap weight of the kth component in the lth cluster, T_l is the delay of the lth cluster and $\tau_{k,l}$ is the delay of the kth MPC relative to the lth cluster's arrival time T_l. The phases $\psi_{(k,l)}$ are uniformly distributed, i.e. for a bandpass system the phase is assumed to be a uniformly distributed random variable from the range $[0, 2\pi]$. Further details were provided in Section 2.2.

3.2.2.3 Detection Schemes

The discretized received composite signal can be represented in matrix form as [49]:

$$\mathbf{y} = \mathbf{J}\mathbf{d} + \mathbf{n}, \tag{3.3}$$

where $\mathbf{n}$ is the noise sequence consisting of noise samples that are zero mean Gaussian variables having a variance of σ^2 and has a covariance matrix of $\mathbf{R}_n = E[\mathbf{n}\mathbf{n}^H]$, $\mathbf{J}$ is the overall system matrix and $\mathbf{d}$ is the user's data vector.

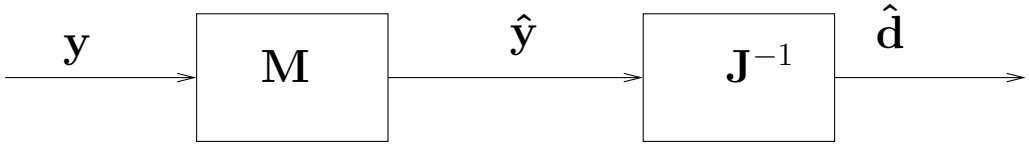

Figure 3.3: Two stage filters.

3.2.2.3.1 Correlation Detector

The correlation detector is constituted by two filtering stages. The pre-whitening filter [49] is followed by the matched filter, as depicted in Figure 3.3. The Cholesky decomposition of the noise covariance matrix $\mathbf{R}_n$ is given by

$$\mathbf{R}_n = \mathbf{L}\mathbf{L}^{\mathbf{H}}, \tag{3.4}$$

where $\mathbf{L}$ is a lower triangular matrix having real-valued elements on its main diagonal. The z-domain transfer function of the pre-whitening filter is $\mathbf{L}^{-1}$ [138]. The output of the pre-whitening filter can be expressed as

$$\mathbf{y}' = \mathbf{L}^{-1}\mathbf{y} = \mathbf{L}^{-1}\mathbf{J}\mathbf{m} + \mathbf{L}^{-1}\mathbf{n}. \tag{3.5}$$

The discrete transfer function $\mathbf{T_{Mf}}$ of the matched filter may be formulated as [139]:

$$\mathbf{T_{Mf}} = (\mathbf{L}^{-1}\mathbf{J})^{\mathbf{H}} = \mathbf{J}^{\mathbf{H}}(\mathbf{L}^{-1})^{\mathbf{H}}. \tag{3.6}$$

Finally, combining Equations 3.5 and 3.6 provides joint estimates of the data symbols for the correlation detector expressed as:

$$\hat{\mathbf{d}}_{\mathbf{Corr}} = \mathbf{y}'' = \mathbf{T}_{\mathbf{MF}}\mathbf{y}' = \mathbf{J}^{\mathbf{H}}\mathbf{R}_{\mathbf{n}}^{-\mathbf{1}}\mathbf{y}. \tag{3.7}$$

Equation 3.7 can be expanded into the Multiple Access Interference (MAI) and InterSymbol Interference (ISI) terms as follows:

$$\hat{\mathbf{d}}_{\mathbf{Corr}} = \underbrace{diag(\mathbf{J}^{\mathbf{H}}\mathbf{R}_{\mathbf{n}}^{-\mathbf{1}}\mathbf{J})\mathbf{d}}_{symbols} + \underbrace{\overline{diag}(\mathbf{J}^{\mathbf{H}}\mathbf{R}_{\mathbf{n}}^{-\mathbf{1}}\mathbf{J})\mathbf{m}}_{ISI,MAI} + \underbrace{\mathbf{J}^{\mathbf{H}}\mathbf{R}_{\mathbf{n}}^{-\mathbf{1}}\mathbf{n}}_{noise}. \tag{3.8}$$

It becomes clear from Equations 3.7 and 3.8 that the correlation detector is inefficient in terms of mitigating the MAI and ISI imposed in a multiuser and multipath scenario.

3.2.2.3.2 Zero Forcing Detector

The Zero Forcing Detector (ZFD) is similar to the zero-forcing linear equalizer [49]. The data estimates at the output of the ZFD are

$$\hat{\mathbf{d}}_{\mathbf{ZFD}} = \underbrace{\mathbf{d}}_{Data} + \underbrace{(\mathbf{J}^{\mathbf{H}}\mathbf{R}_{\mathbf{n}}^{-\mathbf{1}}\mathbf{J})^{-1}\mathbf{J}^{\mathbf{H}}\mathbf{R}_{\mathbf{n}}^{-\mathbf{1}}\mathbf{n}}_{Noise}, \tag{3.9}$$

which can be reduced to

$$\hat{\mathbf{d}}_{\mathbf{ZFD}}\Big|_{\mathbf{R}_n=\sigma^2 I} = (\mathbf{J^H J})^{-1}\mathbf{J^H y}, \tag{3.10}$$

where again I is an identity matrix. It is evident from Equations 3.9 and 3.10 that the ZFD decorrelates the MAI and ISI and forces them to zero. However, the removal of the ISI and MAI is performed at the expense of noise enhancement.

3.2.2.3.3 MMSE Detector

The MMSE detector minimises the simple quadratic form [139]

$$Q(\hat{\mathbf{d}}) = E\left[(\mathbf{d}-\hat{\mathbf{d}})^H(\mathbf{d}-\hat{\mathbf{d}})\right], \tag{3.11}$$

where $\hat{\mathbf{d}}$ is the estimate of the data $\mathbf{d}$. Upon invoking the well-known Orthogonality Principle of [140]

$$E\left[(\mathbf{d}-\hat{\mathbf{d}})\mathbf{y}^H\right] = 0, \tag{3.12}$$

and substituting $\hat{\mathbf{d}} = \mathbf{Py}$ in Equation 3.12 and then solving for $\mathbf{P}$, we arrive at

$$\mathbf{P} = \mathbf{R}_{dy}\mathbf{R}_y^{-1}, \tag{3.13}$$

where

$$\mathbf{R}_{dy} = E\left[\mathbf{dy}^H\right], \tag{3.14}$$

$$\mathbf{R}_y = E\left[\mathbf{yy}^H\right], \tag{3.15}$$

represent the corresponding covariance matrices. Substituting Equation 3.3 into

$$\mathbf{R}_{dy} = E\left[\mathbf{dy}^H\right], \tag{3.16}$$

$$\mathbf{R}_y = E\left[\mathbf{yy}^H\right], \tag{3.17}$$

we arrive at

$$\mathbf{R}_{dy} = \mathbf{R}_d\mathbf{J}^H, \tag{3.18}$$

$$\mathbf{R}_y = \mathbf{J}\mathbf{R}_d\mathbf{J}^H + \mathbf{R}_n, \tag{3.19}$$

where $\mathbf{R}_d = E\left[\mathbf{dd}^H\right]$ is the covariance matrix of the data. Substituting Equations 3.18 and 3.19 in Equation 3.13 we obtain

$$\begin{aligned}\mathbf{P} &= \mathbf{R}_d\mathbf{J}^H(\mathbf{J}\mathbf{R}_d\mathbf{J}^H + \mathbf{R}_n)^{-1} \\ &= (\mathbf{J}^H\mathbf{R}_n^{-1}\mathbf{J} + \mathbf{R}_d^{-1})^{-1}\mathbf{J}^H\mathbf{R}_n^{-1}.\end{aligned} \tag{3.20}$$

Hence, the MMSE detector's estimated bits $\hat{\mathbf{d}}_{MMSE}$ can be expressed as

$$\hat{\mathbf{d}}_{MMSE} = (\mathbf{J}^H\mathbf{R}_n^{-1}\mathbf{J} + \mathbf{R}_d^{-1})^{-1}\mathbf{J}^H\mathbf{R}_n^{-1}\mathbf{y}. \tag{3.21}$$

Residential	LOS	NLOS
valid Range of d	7-20m	7-20m
$G_0[dB]$	-43.9	-48.7
$\overline{L}$	3	3.5
$\Lambda[1/ns]$	0.047	0.12
$\lambda_1, \lambda_2[1/ns], \beta$	1.54,0.15,0.095	1.77,0.15,0.045
$\Gamma[ns]$	22.61	26.27
k_γ	0	0
$\gamma_0[ns]$	12.53	17.50
$\sigma_{cluster}$	2.75	2.93

Table 3.2: Parameters for channel models CM 1 and CM 2 (Residential)

Substituting Equation 3.3 into Equation 3.21 and partitioning it for the desired symbols, the MAI, ISI and noise are formulated as

$$\begin{aligned}
\hat{\mathbf{d}}_{MMSE} &= \left[(\mathbf{J}^H\mathbf{R}_n^{-1}\mathbf{J}+\mathbf{R}_d^{-1})^{-1}\mathbf{J}^H\mathbf{R}_n^{-1}\right]\mathbf{J}\mathbf{d}+ \\
&\quad (\mathbf{J}^H\mathbf{R}_n^{-1}\mathbf{J}+\mathbf{R}_d^{-1})^{-1}\mathbf{J}^H\mathbf{R}_n^{-1}\mathbf{n} \\
&= \underbrace{diag\Big(\left[\mathbf{I}_{KN}+(\mathbf{R}_d\mathbf{J}^H\mathbf{R}_n^{-1}\mathbf{J})^{-1}\right]^{-1}\Big)\mathbf{d}}_{symbols} \\
&+ \underbrace{\overline{diag}\Big(\left[\mathbf{I}_{KN}+(\mathbf{R}_d\mathbf{J}^H\mathbf{R}_n^{-1}\mathbf{J})^{-1}\right]^{-1}\Big)\mathbf{d}}_{ISI,MAI} \\
&+ \underbrace{(\mathbf{J}^H\mathbf{R}_n^{-1}\mathbf{J}+\mathbf{R}_d^{-1})^{-1}\mathbf{J}^H\mathbf{R}_n^{-1}\mathbf{n}}_{noise}. \qquad (3.22)
\end{aligned}$$

From Equations 3.21 and 3.22, it can be seen that unlike the correlation detector, the MMSE detector attempts to achieve a balance between eliminating the different types of data impairments including the noise, MAI and ISI in order to minimize the mean squared estimation error in the simple quadratic form [139] $Q(\hat{\mathbf{d}}) = E\left[(\mathbf{d}-\hat{\mathbf{d}})^H(\mathbf{d}-\hat{\mathbf{d}})\right]$, while the correlation detector simply estimates Equation 3.7 and hence fails to balance MAI and ISI produced by the multiuser and multipath environment. Explicitly, MMSE detection has a superior ability to mitigate the effects of MAI and ISI imposed in a multipath and multiuser scenario.

3.2.3 Results and Discussion

In order to simulate a realistic scenario, we have used the UWB propagation channel model of Section 2.2, which is based on indoor channel measurements between 3.1 GHZ to 10.6 GHz over a range of 7 to 10 meters [24]. We have considered the extreme cases of a single-user $N_u = 1$ and the full-load of $N_u = 63$ multiuser scenarios. The spreading factor of

$N_s = 63$ was employed. The L strongest MPCs have the 85% of the total energy received from N_r resolvable paths, which were combined by the MRC algorithm. Table 3.2 illustrates the channel parameters extracted from Table 2.2 of Section 2.2 and used in our simulations.

Spreading Factor	$0 < N_s \leq 63$
No. of Users	$N_u = 1, 3, 13, 23, 33, 43, 53, 63$
Data Burst Length Per User	$B = 1000$
Number of Resolvable Paths	$N_r = 30$
Number of Strongest Paths	$L = 1, 5, 10, 20$
Detector I	Corr
Detector II	ZF
Detector III	MMSE

Table 3.3: Simulation system parameters for uncoded UWB-TH-PPM

The transmission burst length B of a user is a parameter, which affects the amount of ISI imposed by overlapping symbols. When using $B = 1000$ and $N_u = 63$, a high level of ISI and MAI is imposed. The diversity order of combining $L = 20$ independently fading components from the total of $N_r = 30$ resolvable MPCs has the same beneficial fading-mitigation effect as transmitting via the same number of independently fading multiple antennas using Space Time Coding (STC) for example. However, the number of MPCs that can be combined is limited by the power consumption, implementational complexity and the channel estimation accuracy complexity. Table 3.3 summarises the system parameters used in our simulations.

Assumptions: We have assumed that the receiver has achieved perfect synchronization for detecting the received signal and it also has the perfect knowledge of the transmission delay τ^k. Furthermore, we assume that the receiver employs a TH pattern replica, which is generated by a local PN generator, as shown in Figure 3.1.

Figure 3.4 shows the achievable performance gain of the UWB-TH-IR system in case of a single-user i.e. for $N_u = 1$ with a diversity order of $L = 20$, where the strongest $L = 20$ paths were selected from $N_r = 30$ resolvable paths. As seen in Figure 3.4, the ZF and MMSE detectors achieve a performance close to that recorded for the AWGN channel. Diversity gains of 18dB and 16dB were recorded for the ZFD and MMSE detectors at a BER of 10^{-4}. By contrast, there is no BER improvement for the correlation detector owing to its inability to mitigate the ISI.

Figure 3.5 shows the performance gain of the UWB-TH-IR system in case of a full-load of $N_u = 63$ users and a diversity order of $L = 20$, when selecting the strongest $L = 20$ paths from $N_r = 30$ resolvable paths. A spreading factor of $N_s = 63$ was used. As Figure 3.5 suggests, the ZF and MMSE detectors achieve a performance gain of 5dB and 12dB at a

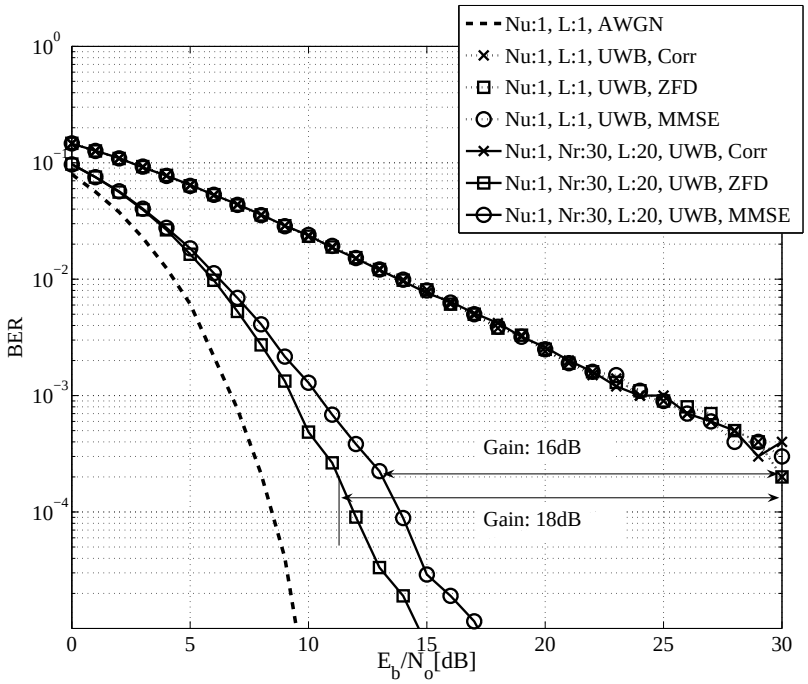

Figure 3.4: BER versus $\frac{E_b}{N_o}$[dB] for the uncoded UWB-TH-IR system supporting $N_u = 1$ user for a diversity order of $L = 20$ selecting the strongest ones from $N_r = 30$ resolvable MPCs and using a spreading factor of $N_s = 63$. No FEC was employed. The channel parameters and system parameters are summarized in Tables 3.2 and 3.3

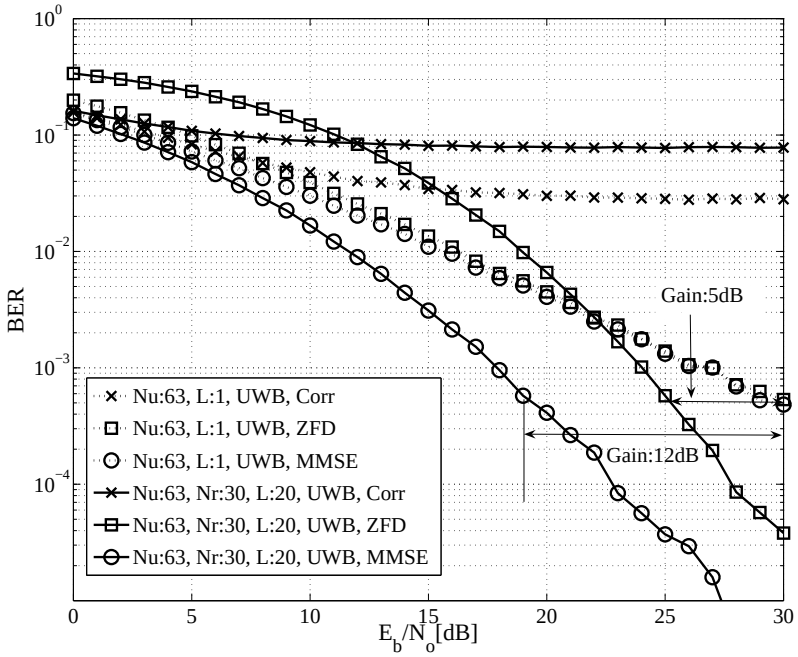

Figure 3.5: BER vs $\frac{E_b}{N_o}$[dB] for uncoded UWB-TH-IR system with users $N_u = 63$, diversity order $L = 20$, resolvable MPCs $N_r = 30$ and spreading factor $N_s = 63$. No FEC was used. The channel parameters and system parameters are summarized in Tables 3.2 and 3.3

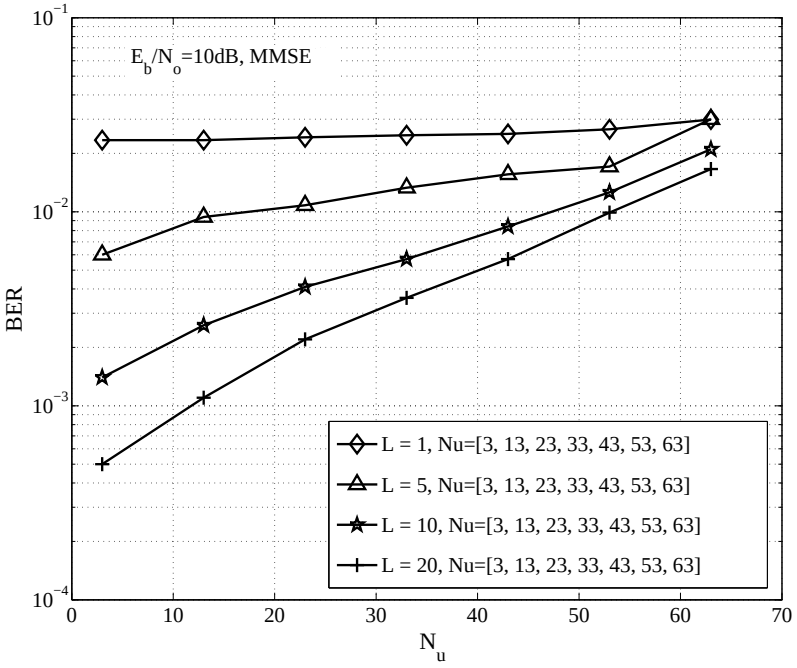

Figure 3.6: BER versus the number of users at $\frac{E_b}{N_o} = 10$[dB] for the uncoded UWB-TH-IR system for a diversity order of $L = 20$ selecting the strongest ones from $N_r = 30$ resolvable MPCs, when using a spreading factor of $N_s = 63$ and $N_u = 63$ users. The channel parameters and system parameters are summarized in Tables 3.2 and 3.3

BER of 10^{-4}. The ZF performs poorly at low $\frac{E_b}{N_o}$ values, since it enhances the effects of noise, as shown in Equations 3.9 and 3.10. Finally, Figure 3.6 depicts the performance trends for the MMSE detector upon varying the diversity order L and the number of users N_u at $\frac{E_b}{N_o}$=10dB.

3.3 EXIT Chart Aided DS-CDMA UWB Design

Tables 3.4 and 3.5 provide a historical overview of different coding schemes used in UWB communications. Section 3.2 characterized the performance of an uncoded UWB system using diversty seclection in order to enhance the achievable performance. However, the number of resolvable MPCs that can be utilized for diversity combining are limited by affordable power consumption issues and system complexity [15, 39]. Therefore we are unable to improve the attainable BER performance by simply increasing the number of resolvable paths beyond a certain limit, as argued in Section 3.2.1. In this section, we will provide a channel coded UWB design which will expliot the available resolvable paths with the aid of iterative detection in order to achieve a better performance than the system detailed in Section 3.2.1. This will be our first coded UWB design, which will be further improved in subsequent chapters in order to enhance system performance, as detailed in

2001	*Authors:* G. M. Maggio, N. Rulkov and L. Reggiani [141] *Contribution:* A pseudo-chaos based modulation scheme was proposed for UWB impulse-radio communication systems.
2004	*Authors:* E. Baccarelli and M. Biagi [142] *Contribution:* A low-complexity adaptive channel decoding scheme was introduced for UWB impulse radio systems impaired by multiuser interference (MUI). Depending on the MUI level, the proposed scheme may switch from a hard-detection mode to a soft-detection mode.
2005	*Author:* X. Cheng and W. Zhu [143] *Contribution:* A subspace based detection method was proposed for Space-Time Block Coded (STBC) UWB transmissions. At this stage we would like to note that the employment of transmit-diversity-oriented STBC may be expected to have limited diversity benefits, since the receiver has access to a high number of MPCs and hence may be able to approach a near-gaussian performance. Nonetheless, STBCs may be used to achieve transmit diversity in order to limit the receive diversity order in the interest of minimizing the receiver's complexity.
2006	*Authors:* B. U. Riaz, M. Pun and C. C. Kuo [144] *Contribution:* Low-complexity, low-rate super-orthogonal turbo codes (SOTC) were proposed in this work to replace the implicit repetition code (RC) in ultra-wide band impulse radio (UWB-IR) systems to improve the achievable transmission range and system throughput.
2007	*Authors:* J. I. Jamp and L. E. Larson [145] *Contribution:* Spectral-shaping coding techniques were proposed for interference mitigation, which based on look-ahead block inversion applied to UWB time-hopped signals, by changing both the time offsets and the polarity of each pulse.
2008	*Authors:* R. A. Riaz, M. El-Hajjar, Q. Z. Ahmed, S. X. Ng, S. Chen and L. Hanzo [4] *Contribution:* EXIT charts have been used for the first time to characterize the performance of coded DS CDMA UWB systems.

Table 3.4: Advances in channel coding schemes used in UWB communications part(1).

2009	*Authors:* D. Kim [146] *Contribution:* A tractable and compact closed-form expression was derived for characterizing the error-probability as a function of the signal-to-interference-plus-noise ratio (SINR) for channel coded M-ary orthogonal systems taking into consideration both inter-pulse interference (IPI) and multiple-access interference (MAI) in dense multipath UWB channels.

Table 3.5: Advances in channel coding schemes used in UWB communications part(2).

Section 1.5.

We investigate an iterative detection aided DS-CDMA UWB system capable of resolving a high number of received signal components for the sake of increasing the achievable diversity gain. Iterative detection exchanging extrinsic information between the inner URC's decoder and the outer convolutional code's decoder is employed and analysed using EXIT charts. The URC is capable of completely eliminating the system's error-floor as well as facilitating operation at the lowest possible turbo-cliff SNR without significantly increasing the associated complexity or interleaver delay, as detailed in [122].

Several authors [147] have considered the iterative decoding of diverse spectrally efficient modulation schemes. In [107], the turbo principle was used for iterative soft demapping in the context of multilevel modulation schemes combined with channel decoding. In [148], URCs were used for designing low complexity turbo codes suitable for both bandwidth and power-limited systems having stringent requirements. In this section, we analyse the performance of an iteratively decoded UWB DS-CDMA system employing two different detectors, namely an iterative correlation receiver and an iterative MMSE receiver using EXIT charts. We continue with a brief conceptual tutorial on EXIT charts.

3.3.1 EXIT Charts: A Brief Tutorial

A detailed tutorial on EXIT chart was provided by Tuchler in [149] and in Section 3.1 of [122]. This technique computes the mutual information of the output extrinsic and input a-priori components corresponding to a specific bit for each of the iterative SISO blocks. More specifically, the mutual information of the LLRs and the legitimate bipolar BPSK bits is given by [150]

$$\mathbf{I} = \frac{1}{2} \sum_{c \in \{+1,-1\}} \int_{-\infty}^{\infty} p_L(x|c) \cdot log_2 \left[\frac{2p_L(x|c)}{p_L(x|+1) + p_L(x|-1)} \right] dx \tag{3.23}$$

where $p_L(x|c)$ is the conditional probability distribution of the LLRs. We can now substitute the conditional probability distribution of the extrinsic information L_e and that

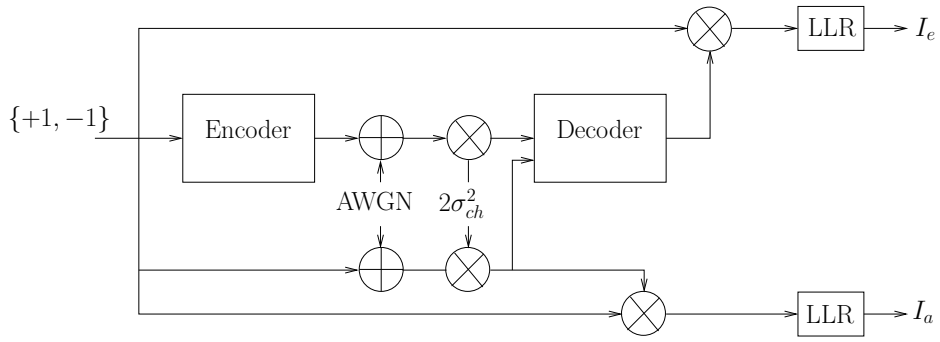

Figure 3.7: EXIT chart block diagram

of the a-priori information L_a into Equation 3.23 in order to derive the mutual information between either I_e or I_a and the legitimate bipolar bits, respectively. The distribution of the LLRs required in Equation 3.23 can be approximated by the experimentally generated LLR histogram or by using the potentially less computationally demanding but typically less accurate Gaussian distribution. EXIT charts constitute an excellent tool designed for analysing the convergence behaviour of an iterative decoding/detection scheme without performing time-consuming bit-by-bit Monte-Carlo simulations. An EXIT chart based analysis of the iterative decoder provides an insight into its decoding convergence behaviour. The main objective of employing EXIT charts [107, 116], is to predict the convergence behaviour of the iterative decoder by examining the evolution of the input/output mutual information exchange between the inner and outer decoders in consecutive iterations. The application of EXIT charts is based on the two assumptions that upon assuming large interleaver lengths,

1. The *a priori* LLR values are fairly uncorrelated;
2. The *a priori* LLR values exhibit a Gaussian PDF.

Next we briefly highlight the concept of 2D EXIT charts.

3.3.1.1 Two-Dimensional EXIT Charts

Two-Dimensional EXIT charts visualize the mutual information of one of the constituent decoders versus the mutual information of the other constituent decoder. The provision of extrinsic information may also be modelled by a so-called a priori channel. In other words, the output of the lower branch in Figure 3.7 determines the value of the horizontal axis of the EXIT chart and the output of the upper branch determines the value on the vertical axis. Both values range between 0 and 1. For the next half iteration constituted by the provision of extrinsic information emanating from the second constituent decoder the coordinate asix are swapped and interchange their roles. More explicitly, the output of

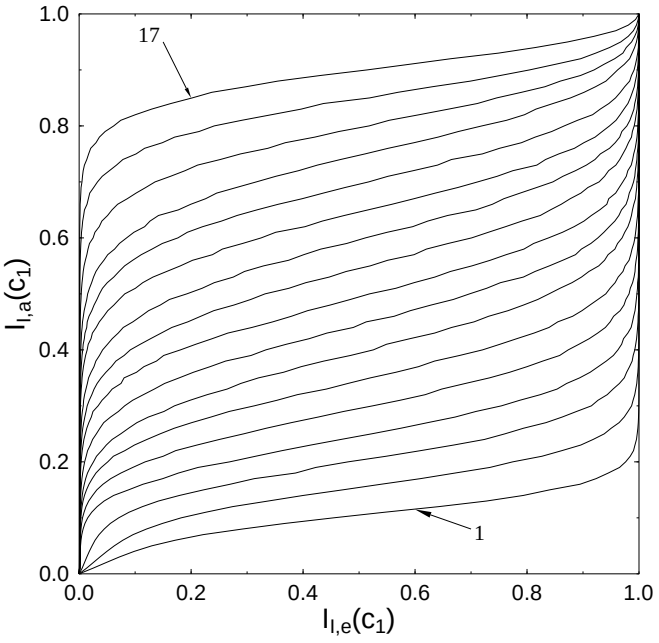

Figure 3.8: EXIT curves of the outer decoder of Figure 3.7 using 17 different RSC codes of half-rate memory-1. The lowest-rate code is denoted by the arrow 1 and the highest-rate code by 17.

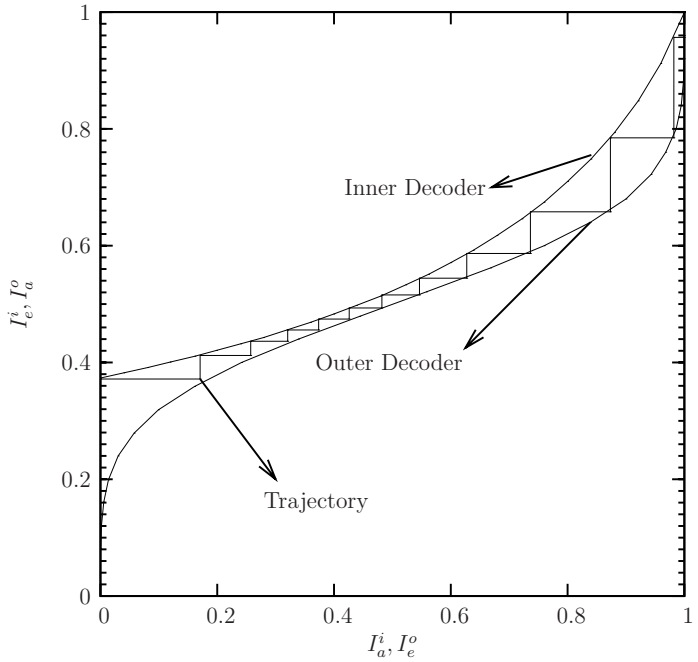

Figure 3.9: EXIT chart with decoding trajectory, where the inner code is constituted by a URC detector and the outer code is half-rate memory-1 RSC. The 12 vertical steps of the stair-case-shaped decoding trajectories indicate 12 iterations.

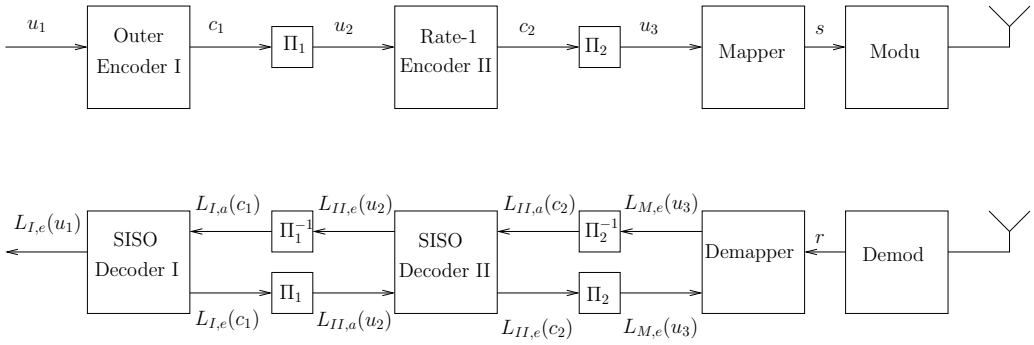

Figure 3.10: General three-stage concatenated system model.

decoder one becomes the a priori input of the other decoder. Examples of 2D EXIT charts are shown in Figures 3.8 and 3.9. Further details can be found in [107, 116, 122]

3.3.1.2 Three-Dimensional EXIT Charts

In this section, the approach presented in [108] is adopted in order to provide the EXIT chart analysis of the general three-stage concatenated system model of Figure. 3.10. Since both decoder II and the demapper have two inputs and a single output, these are two abscissa axes and a vertical axis, leading to a 3D EXIT chart.

Let $I_{\cdot,a}(x)$, $0 \leq I_{\cdot,a}(x) \leq 1$, denote the mutual information (MI) between the *a priori* LLRs $L_{\cdot,a}(x)$ as well as the corresponding bits x and let $I_{\cdot,e}(x)$, $0 \leq I_{\cdot,e}(x) \leq 1$, denote the MI between the *extrinsic* LLRs $L_{\cdot,e}(x)$ and the corresponding bits x, where the subscript $(\cdot)$ is used to distinguish the different constituent decoders, i.e. Decoder I, Decoder II and the demapper. We will now briefly illustrate the concept of 3D EXIT charts. As seen from Figure 3.10, the input of Decoder II is constituted by the *a priori* input $L_{II,a}(c_2)$ and the *a priori* input $L_{II,a}(u_2)$ provided after bit-deinterleaving by the demapper and Decoder I, respectively. Therefore, the EXIT characteristic of Decoder II can be described by the following two EXIT functions [107, 108]:

$$\begin{aligned} I_{II,e}(c_2) &= T_{II,c_2}[I_{II,a}(u_2), I_{II,a}(c_2)], \\ I_{II,e}(u_2) &= T_{II,u_2}[I_{II,a}(u_2), I_{II,a}(c_2)]. \end{aligned} \tag{3.24}$$

On the other hand, the EXIT characteristic of the demapper as well as that of Decoder I are each dependent on a single *a priori* input, namely on $L_{M,a}(u_3)$ and $L_{I,a}(c_1)$, respectively, both of which are provided by the rate-1 Decoder II after appropriately ordering the bits, as seen in Figure. 3.10. The EXIT characteristic of the demapper is also dependent on the associated E_b/N_0 value. Consequently, the corresponding EXIT functions of the

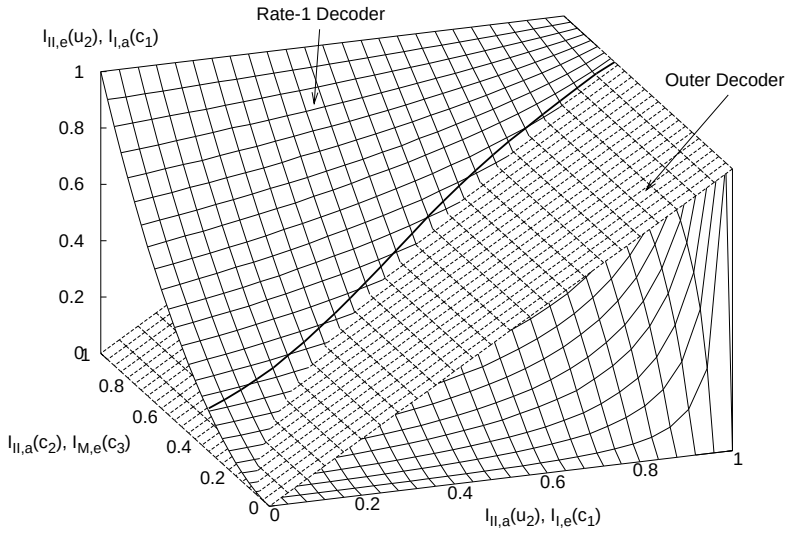

Figure 3.11: 3D EXIT chart of decoder II and decoder I

demapper and Decoder I of Figure 3.10, respectively, may be written as

$$\begin{aligned} I_{M,e}(u_3) &= T_{M,u_3}[I_{M,a}(u_3), E_b/N_0], \\ I_{I,e}(c_1) &= T_{I,c_1}[I_{I,a}(c_1)]. \end{aligned} \tag{3.25}$$

As an example of the 3D EXIT chart of Decoder II and Decoder I is shown in Figure 3.11. For this specific example, Encoder I is a half-rate memory-1 RSC code having octally represented generator polynomials of $(G_r, G) = (3, 2)_8$, where G_r is the feedback polynomial, while Encoder II is a simple rate-1 accumulator, described by the pair of octal generator polynomials $(G/G_r) = (2/3)_8$. Similarly, a 3D EXIT chart for demapper of Figure 3.11 can be drawn which is not included here. The detailed description of 2D and 3D EXIT charts can be found in [107, 116, 122]. Next we elaborate on the channel coded DS-CDMA UWB model.

3.3.2 Channel Coded UWB System Model

Figure 3.12 shows the discrete-time baseband model of the iteratively detected DS-CDMA UWB system. Each user transmits a data symbol sequence $\mathbf{m}^{(u)}$ consisting of N elements at symbol intervals T_s. Each data symbol $\mathbf{m}_n^{(u)}$ of user u is repeated S times and the resultant S-dimensional vector is multiplied by the S chips of the specific signature sequence $\mathbf{s}^{(u)}$, having a period of S. Each of the U channels is described by the UWB Channel Impulse Response (CIR) $\mathbf{h}^{(u)}$ consisting of W samples during the chip interval $T_c = \frac{T_s}{S}$.

As shown in Figure 3.12, the received complex-valued symbols are first detected by

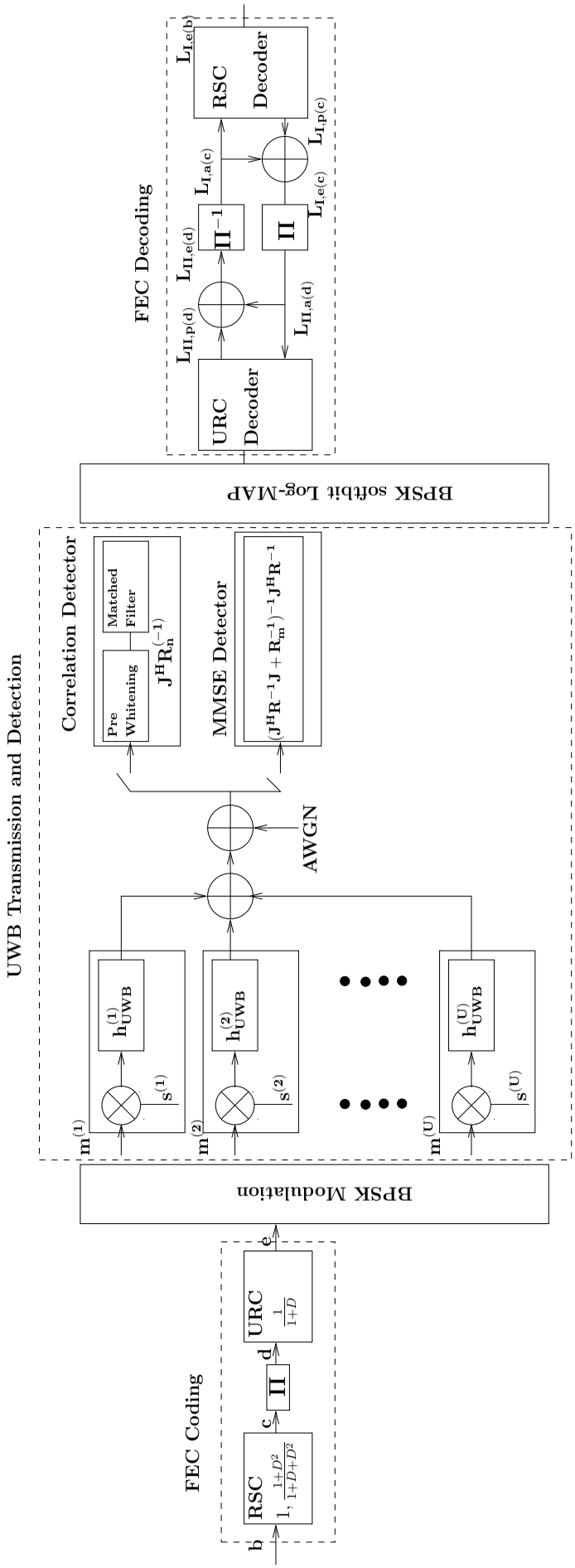

Figure 3.12: The proposed iteratively decoded DS-CDMA UWB system model.

the correlation or MMSE detector in order to produce the corresponding estimated data bits $\hat{\mathbf{m}}$, which are fed into the BPSK softbit demodulator for calculating the LLRs based on the Log Maximum Aposteriori Probability (Log-MAP) algorithm [147]. As seen in Figure 3.12, the URC decoder processes the information forwarded to it by the BPSK softbit demodulator in conjunction with the *a priori* information in order to generate the *a posteriori* probability. The *a priori* LLR values output by the URC decoder are subtracted from the *a posteriori* LLR values provided by the log-MAP algorithm for the sake of generating the extrinsic LLR values $L_{II,e(d)}$, as seen in Figure 3.12. Next, the soft bits $L_{I,a(c)}$ are passed to the convolutional decoder of Figure 3.12 in order to compute the *a posteriori* LLR values $L_{I,p(c)}$ provided by the Log-MAP algorithm for all the channel-coded bits. During the last iteration only the LLR values $L_{I,e(b)}$ of the original uncoded systematic information bits are required, which are passed to the hard decision based RSC decoder in order to determine the estimated transmitted source bits. As seen in Figure 3.12, the extrinsic information $L_{I,e(c)}$ is generated by subtracting the *a priori* information from the *a posteriori* information according to $\left[(L_{I,p(c)} - L_{I,a(c)})\right]$, which is then fed back to the URC decoder as the *a priori* information $L_{II,a(d)}$ after appropriately reordering them using the interleaver of Figure 3.12.

3.3.3 UWB Transceiver

3.3.3.1 DS-UWB Baseband Signal

In direct sequence UWB systems, which are analogous to conventional DSSS systems [43], the signalling pulse transmissions are controlled by a pseudo random noise code, obeying an appropriate finite-bandwidth chip waveform generating an UWB signal. The v^{th} data bit of user u can be transmitted using binary pulse amplitude modulation (BPAM) and the transmitted signal $g^{(u)}(t)$ is formulated as:

$$g^{(u)}(t) = \sum_{v=0}^{\infty} \sum_{q=0}^{S-1} \psi(t - vT_s - qT_c) s_q^{(u)} m_v^{(u)}, \tag{3.26}$$

where $\psi(t)$ is the chip waveform representing the UWB pulse, which controls the bandwidth of the UWB signal, $m_v^{(u)}$ corresponds to the data information of user u, T_c is the chip duration and $s_q^{(u)}$ is the q^{th} chip of the spreading code of user u. We assume that a block of data consisting of M bits is transmitted within the block duration of $0 < t \leq MT_b = T_s$, where T_b is the bit duration. The DS-SS waveform $s^{(u)}(t)$ of user u consists of a periodic PN sequence having a length of S chips, which can be expressed as

$$s^{(u)}(t) = \sum_{q=0}^{S-1} s_q^{(u)} \psi(t - qT_c), \tag{3.27}$$

where $s_q^{(u)}$ assumes a value of +1 or -1.

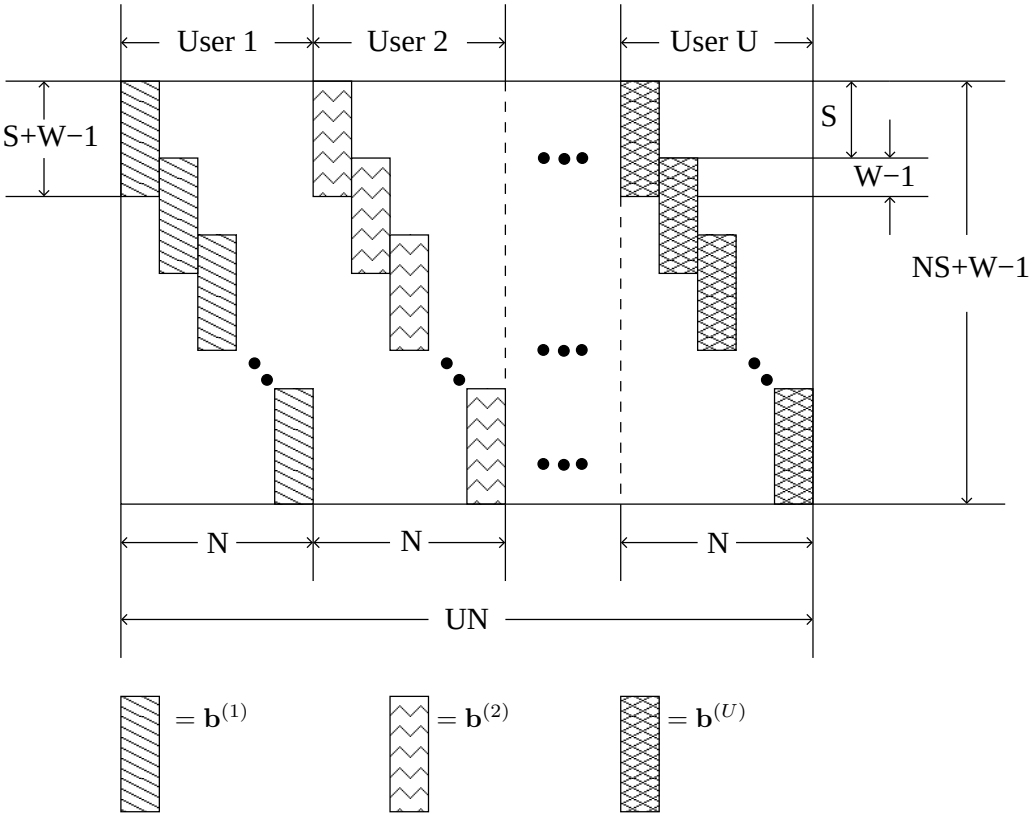

Figure 3.13: Stylized structure of the system matrix $\mathbf{J}$, where $\mathbf{b}^{(1)}$,$\mathbf{b}^{(2)}$ and $\mathbf{b}^{(U)}$ are column vectors representing the combined impulse responses of users 1, 2, and U, respectively as seen in Equation 3.30 © Hanzo *et. al.* [49].

3.3.3.2 Channel Model

The complex valued low-pass multipath CIR can be expressed as [68, 151]

$$h(t) = \sum_{x=0}^{\infty} \sum_{z=0}^{\infty} \alpha_{zx} e^{j\phi_{zx}} \delta(t - T_x - \tau_{zx}), \tag{3.28}$$

where the gain of the z^{th} ray of the x^{th} cluster is α_{zx} and its phase is ϕ_{zx}, while T_x is the x^{th} cluster's arrival time and τ_{zx} is the z^{th} ray of the x^{th} cluster's arrival time. The remaining details concerning the channel model can be found in Section 2.2.

3.3.3.3 Receiver Model

The composite transmitted data sequence of the U users can be written as

$$\mathbf{m} = \left[\mathbf{m}^{(1)T}, \mathbf{m}^{(2)T}, ..., \mathbf{m}^{(U)T}\right]^T, \tag{3.29}$$

where $m_j = m_n^{(u)}$ for $j = n + N(u-1)$, $u = 1, 2, ..., U$ and $n = 1, 2...., N$. The overall

system matrix **J** can be interpreted as

$$[\mathbf{J}]_{ij} = \begin{cases} b_n^{(u)}(l) & \text{for } u = 1, 2, ..., U;\ n = 1, 2, ..., N \\ & l = 1, 2, ..., S + W - 1 \\ 0 & \text{otherwise,} \end{cases} \tag{3.30}$$

where $i = 1, ..., NS + W - 1$, $j = 1, ..., UN$. The structure of the system matrix considered is highlighted in Figure 3.13. In Equation 3.30 the combined impulse response, $\mathbf{b}_n^{(u)}$ is given by:

$$\begin{aligned} \mathbf{b}_n^{(u)} &= \left[b_n^{(u)}(1), b_n^{(u)}(2), ..., b_n^{(u)}(l), ..., b_n^{(u)}(S + W - 1)\right]^T \\ &= \mathbf{s}^{(u)} * \mathbf{h}_n^{(u)}, \end{aligned} \tag{3.31}$$

where $u = 1, 2, ..., U$, $n = 1, 2...., N$, $l = 1, 2, ..., S + W - 1$. Furthermore, $\mathbf{s}^{(u)}$ and $\mathbf{h}_n^{(u)}$ are the corresponding S-chip spreading sequence vector and the W-chip CIR vector encountered at the chip rate of $\frac{1}{T_c}$, which are defined as

$$\mathbf{s}^{(u)} = \left[s_1^{(u)}, s_2^{(u)}, .., s_q^{(u)}, ..., s_S^{(u)}\right]^T, \tag{3.32}$$

and

$$\mathbf{h}_n^{(u)} = \left[h_n^{(u)}(1), h_n^{(u)}(2), .., h_n^{(u)}(w), ..., h_n^{(u)}(W)\right]^T, \tag{3.33}$$

where we have $u = 1, ..., U$, $q = 1, ..., S$, $w = 1, ..., W$ and $n = 1, ..., N$. The discretised composite received signal can be expressed as

$$\mathbf{y} = \mathbf{Jm} + \mathbf{n}, \tag{3.34}$$

where we have

$$\mathbf{y} = [y_1, y_2, ..., y_{NS+W-1}]^T, \tag{3.35}$$

and

$$\mathbf{n} = [n_1, n_2, ..., n_{NS+W-1}]^T, \tag{3.36}$$

with **n** representing the noise sequence, which has a covariance matrix of $\mathbf{R}_n = E[nn^H]$. In what follows we will discuss the operation of the iterative correlation and MMSE receivers.

3.3.3.3.1 Detector I

The correlation detector is constituted by two filtering stages. The pre-whitening filter [49] is followed by the matched filter, as depicted in Figure. 3.12. The estimates of the data symbols provided by the correlation detector may be expressed as:

$$\hat{\mathbf{m}}_{\mathbf{Corr}} = \mathbf{y}'' = \mathbf{T}_{\mathbf{MF}}\mathbf{y}' = \mathbf{J}^{\mathbf{H}}\mathbf{R}_{\mathbf{n}}^{-\mathbf{1}}\mathbf{y}. \tag{3.37}$$

The remaining details of the detector can be found in Section 3.2.2.3.

Spreading Factor	$N_s = 32$
No. of Users	$U = 20, 32$
Data Burst Length Per User	$N = 10$
$\Lambda\left[\frac{1}{nsec}\right]$(Cluster Arrival Rate)	0.0233
$\lambda\left[\frac{1}{nsec}\right]$(Ray Arrival Rate)	2.5
Γ(Cluster Decay Factor)	7.1
γ(Ray Decay Factor)	4.2
Outer Channel Code	RSC(2,1,5)
Inner Code	Rate 1 Code (URC)
Detector I	Correlation
Detector II	MMSE

Table 3.6: System parameters

3.3.3.3.2 Detector II

The MMSE detector's estimated bits $\hat{\mathbf{m}}_{MMSE}$ can be expressed as

$$\hat{\mathbf{m}}_{MMSE} = (\mathbf{J}^H \mathbf{R}_n^{-1} \mathbf{J} + \mathbf{R}_m^{-1})^{-1} \mathbf{J}^H \mathbf{R}_n^{-1} \mathbf{y}, \tag{3.38}$$

while the remaining details of the detector can be found in Section 3.2.2.3.

3.3.4 Simulation Results

In this section we present our system performance results. The system considered in this section obeys the schematic of Figure 3.12 and employs the parameters outlined in Table 3.6 for transmission over the IEEE 802.15.3a channel model [64]. The proposed system model employs a RSC code as the outer encoder and a URC as the inner encoder. We use a memory-two half-rate RSC code having a generator polynomial of $\left[1, \frac{1+D^2}{1+D+D^2}\right]$ and a memory-one recursive URC having a generator polynomial of $\left[\frac{1}{1+D}\right]$, as illustrated Figure 3.12.

Figures 3.14 and 3.15 present the EXIT chart of the systems employing the correlation and MMSE detectors, respectively. These results were recorded for the fully-loaded system supporting $U = 32$ users with the aid of a spreading factor of $N_s = 32$ for transmission over the channel specified in Table 3.6. Observe from Figure 3.15 that an open convergence tunnel is formed around $\frac{E_b}{N_o} = 2.0dB$. This implies that according to the predictions of the EXIT chart seen in Figure 3.15, the iterative decoding process is expected to converge at an $\frac{E_b}{N_o}$ value between 1dB and 2dB. The EXIT chart based iterative detection convergence predictions can be verified by the simulation-based iterative decoding trajectory of Figure 3.15, where the trajectory was recorded at $\frac{E_b}{N_o} = 2.0dB$, while using an interleaver

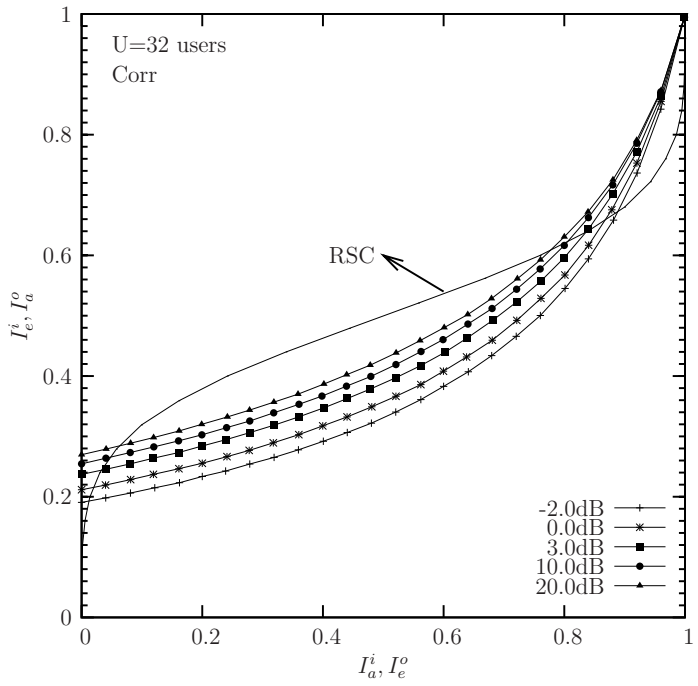

Figure 3.14: EXIT charts and iterative decoding trajectory of the UWB DS-CDMA system using correlation detector and the parameters of Table 1.

length of $I = 100,000$ bits. By contrast, the EXIT curve of Figure 3.14 recorded for the correlation detector shows no open convergence tunnel, not even when we have a high SNR of $\frac{E_b}{N_o} = 20.0dB$. The reason for this is that the correlation detector is incapable of mitigating the MAI and ISI.

Figure 3.16 shows the BER curves recorded for the correlation and MMSE detectors, when supporting $U = 20$ users with the aid of a spreading factor of $N_s = 32$. It is clear from Figure 3.16 that the MMSE detector has a superior performance from the very first iteration onwards.

Finally, Figure 3.17 portrays the BER curves recorded for the system employing the correlation and MMSE detectors, respectively for the fully-loaded system supporting $U = 32$ users with the aid of a spreading factor of $N_s = 32$, while employing the system parameters outlined in Table I. As predicted by the EXIT charts of Figures 3.14 and 3.15, the MMSE detector outperforms the correlation detector also in terms of the BER curves of Figure 3.17.

3.4 EXIT Chart Based Comparative Analysis of DS/TH UWB

Our detailed discussion of diversity order selection was provided in Section 3.2 for an uncoded UWB system while the achievable performance enhancements of a channel coded UWB system was quantified in Section 3.3. These results enable us to provide a comprehensive comparative study of DS-CDMA and TH-PPM UWB systems. In this section, a

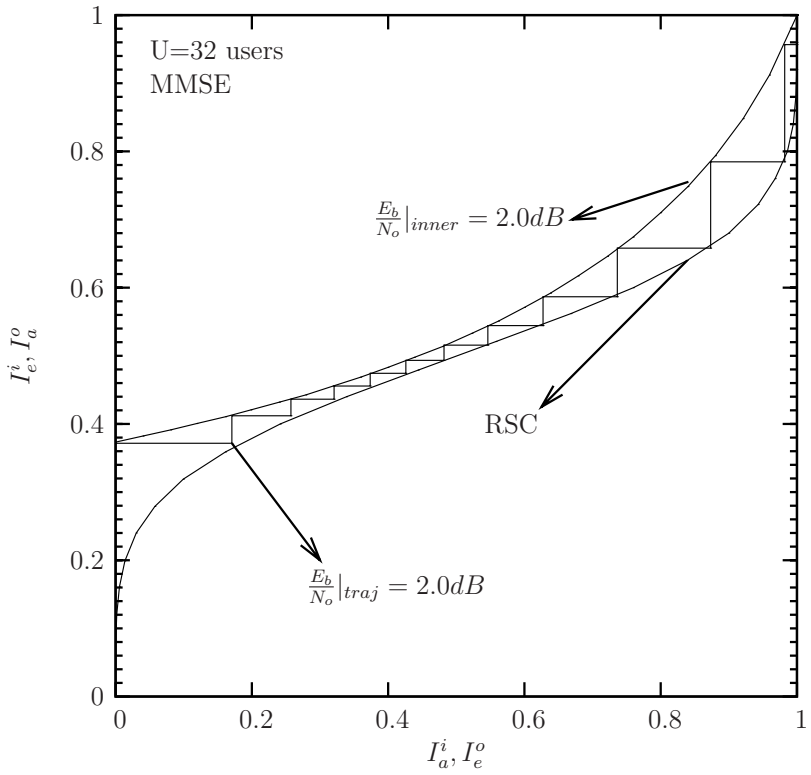

Figure 3.15: EXIT charts and iterative decoding trajectory of the UWB DS-CDMA system using the MMSE detector and the parameters of Table 1.

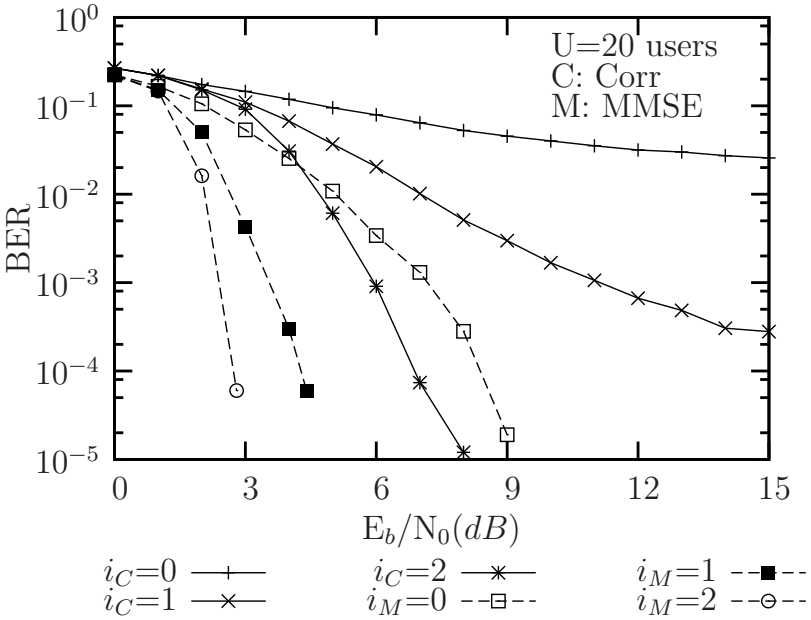

Figure 3.16: BER performance comparison of correlation and MMSE detectors using an interleaver length $I = 100,000$ bits for a variable number of iterations and using the system parameters of Table 1.

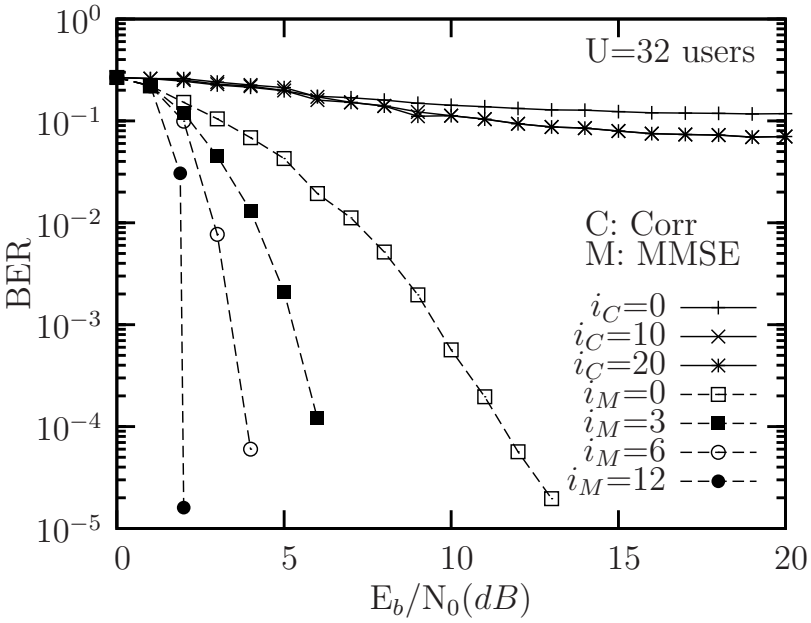

Figure 3.17: BER performance of correlation detector while using an interleaver length $I = 100,000$ bits for a variable number of iterations, 32 users and using the system parameters outlined in Table 1.

DS-CDMA and a corresponding TH-PPM UWB system will be analyzed using the same iterative detection scheme as detailed in Section 3.3.2 with the aid of EXIT charts. Under the same load, channel and diversity order conditions, the performance of both systems will be analyzed using the area properties of EXIT charts [107, 116, 129]. This analysis is important since the best performing multiple access technique will be used in subsequent chapters for near-capacity UWB system.

Digital imaging and multimedia applications typically require high data wireless links [152–154] and UWB systems have the capacity to fulfil the requirements of low-cost, high-speed digital indoor networks. For example, a bit rate of 110 Mbps may be achieved at a distance of 10m and 480 Mbps at a distance of 2m. Both TH-PPM [22, 109] and DS Spread Spectrum (SS) techniques have been used for the implementation of UWB systems. In this section their performance will be compared. As detailed in Section 3.3.1, the main objective of employing EXIT charts [107, 116] is to predict the convergence behaviour of the iterative decoding process seen in the schematic of Figure 3.18 by examining the evolution of the input/output Mutual Information (MI) exchange between the constituent decoders in consecutive iterations [122].

3.4.1 System Architecture

Figure 3.18 portrays the block diagram of the DS/TH UWB system employing a RSC code as the outer encoder and a URC as the inner encoder. We employed a memory-two half-rate RSC code having a generator polynomial of $[1, (1 + D^2)/(1 + D + D^2)]$ and a memory-one

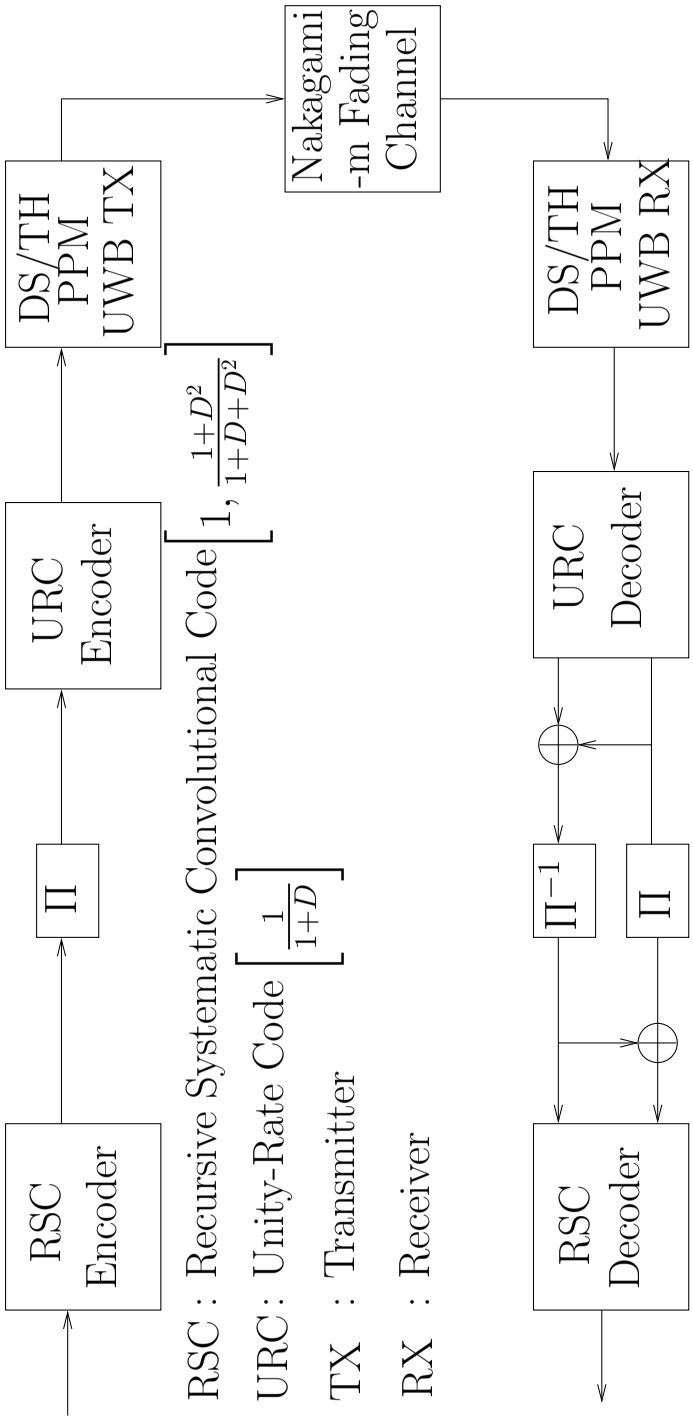

Figure 3.18: System block diagram of the DS/TH UWB system employing RSC as the outer encoder and URC as the inner encoder

recursive URC having a generator polynomial of $[1/(1+D)]$. As a benefit of its infinite impulse response, the URC was shown to efficiently spread the extrinsic information [122] and hence to facilitate iterative decoding convergence to an infinitesimally low BER.

3.4.1.1 Multiple Access and UWB Transceiver Architecture

First, we detail the multiple access techniques employed and then provide a brief overview of the transceiver.

3.4.1.1.1 TH-UWB

The transmitted TH-UWB signal conveying the M-ary symbol is generated by invoking several frames as potrayed in Figure 3.2, which were generated using the system architecture of Figure 3.1. In this section, we arrange for each symbol to invoke L number of frames. Then the transmitted singal of the kth user can be expressed as:

$$u^{(k)}(t) = \sum_{m=0}^{\infty} \sum_{l=0}^{L} \varphi(t - mT_s - lT_f - s_m^{(k)}(l)T_h), \tag{3.39}$$

where $\varphi(t)$ is the time domain UWB signalling pulse, $T_s = NT_f$ is the symbol duration, T_f is the frame duration, T_h denotes the time slot duration and $s_m^{(k)}(l)$ is the kth user's mth symbol generated by the TH code:

$$\begin{aligned} \mathbf{S}_m^{(k)} &= \left[s_m^{(k)}(1), s_m^{(k)}(2), \cdots, s_m^{(k)}(L) \right] \\ &= \mathbf{X}^{(k)} \cdot \mathbf{1} \oplus \mathbf{t}_m^{(k)}, \end{aligned} \tag{3.40}$$

where $\mathbf{1}$ is the unit vector of length L and $\oplus$ denotes modulo addition in the finite Galois Field having Q elements, $\mathbf{X}^{(k)}$ is the M-ary transmitted signal and $\mathbf{t_m^{(k)}}$ is the TH address code of user k given by:

$$\mathbf{t_m^{(k)}} = \left[t_m^{(k)}(1), t_m^{(k)}(2), ..., t_m^{(k)}(L) \right]. \tag{3.41}$$

Furthermore, user k has a specific TH address code defined as above.

3.4.1.1.2 DS-CDMA UWB

In this section, the DSSS transmitted UWB signal generated by the architecture of Figure 3.12 can be expressed as

$$u^{(k)}(t) = \sum_{m=0}^{\infty} \sum_{n=0}^{N-1} \varphi(t - mT_s - nT_c) c_n^{(k)} d_n^{(k)}, \tag{3.42}$$

where we assume that a block of data consisting of M bits is transmitted within the transmitted frame duration of $0 < t \leq MT_b = T_s$, T_b is the bit duration, $d_n^{(k)}$ corresponds

to the data information, T_c is the chip duration and $c_n^{(k)}$ is the n^{th} chip of the spreading code for user k. The DS-SS waveform $c^{(k)}(t)$ of user k consists of a periodic PN sequence having a period of N. The remaining details can be found in Section 3.3.3.1.

3.4.1.1.3 MMSE Detector

For the convenience, we will provide the characterising equations of the MMSE detector. Further details of the MMSE detector can be found in Section 3.2.2.3.

Nakagami-m Fading: In this section, both the TH-UWB and DS-UWB both are evaluated using UWB multipath channel model based on indoor channel measurements between 3.1 GHZ to 10.6 GHz over a range of less than 10 meters. The model accepted by the IEEE 802.15.3 standard and considered here may be expressed as [155]

$$h(t) = \sum_{s=1}^{S} h_s e^{j\phi_s} \delta(t - sT_\psi), \tag{3.43}$$

where S represents the number of resolvable multipaths, h_s and ϕ_s are the gain and phase of the sth resolvable multipath component, while sT_ψ represents the corresponding delay of the sth multipath component.

According to [78], measurements suggest that the UWB channels obeys the Nakagami distribution, which has been validated by using the Kolmogorov-Smirnov testing with a significance level of 1 percent. Hence explicitly, the fading amplitude h_s is assumed to obey an independent Nakagami-m distribution having a PDF [81]

$$P_{h_s}(r) = \frac{2m_s^{m_s} r^{2m_s-1}}{\Gamma(m_s)\Omega_s^{m_s}} e^{\frac{-m_s r^2}{\Omega_s}}, \qquad r > 0 \tag{3.44}$$

where m_s is the Nakagami fading parameter defined as:

$$m_s = \frac{E^2\left[r^2\right]}{var(r^2)}, \tag{3.45}$$

whre the parameter Ω_s is given by

$$\Omega_s = E\left[r^2\right]. \tag{3.46}$$

The vth moment of the random variable r is given by:

$$E\left[r^v\right] = \frac{\Gamma\left(m_s + \frac{v}{2}\right)}{\Gamma(m_s)} \left(\frac{\Omega}{m_s}\right)^{\frac{v}{2}}, \tag{3.47}$$

while $\Gamma(\cdot)$ is the gamma function defined as

$$\Gamma(m_s) = \int_0^\infty x^{m_s-1} e^{(-x)} dx. \tag{3.48}$$

We assume in our analysis that the phase rotation due to fading channel is uniformly distributed in $[0, 2\pi]$.

MMSE Detection: The received signal vector can be expressed for both the TH-UWB and DS-UWB systems as [139]

$$\mathbf{y} = \mathbf{J}\mathbf{b} + \mathbf{n}, \tag{3.49}$$

where $\mathbf{J}$ is the overall system matrix, $\mathbf{b}$ is the information symbol vector, while $\mathbf{n}$ denotes the AWGN vector having $E[\boldsymbol{nn}^H] = 2\sigma_n^2\boldsymbol{I}$ with $\boldsymbol{I}$ being the identity matrix of appropriate dimension. The MMSE multiuser detector's weight vector $\mathbf{P}$ [139] can be expressed as:

$$\begin{aligned} \mathbf{P} &= \mathbf{R}_b\mathbf{J}^H(\mathbf{J}\mathbf{R}_b\mathbf{J}^H + \mathbf{R}_n)^{-1} \\ &= (\mathbf{J}^H\mathbf{R}_n^{-1}\mathbf{J} + \mathbf{R}_b^{-1})^{-1}\mathbf{J}^H\mathbf{R}_n^{-1}, \end{aligned} \tag{3.50}$$

where $\mathbf{R}_b$ is the covariance matrix of information symbols and $\mathbf{R}_n$ is the covariance matrix of the noise.

3.4.2 Comparative Study

3.4.2.1 Simulation Configuration

The simulation configuration outlined in Figure 3.18 is summarised as follows:

- The bit-duration to chip-duration ratio or the spreading factor is fixed to 10 for both the TH and DS-CDMA schemes in all the simulations.

- The URC depicted in Figure 3.18 is used.

- The half-rate RSC encoding and decoding schemes obey the RSC-2-(7,5) specifications, namely they have a memory of two and octally represented generator polynomials of (7,5).

- To generate statistically independent LLRs an interleaver length of 1000 000 bits was used.

- The Nakagami-m distribution corresponds to the Rayleigh distribution, since we fixed the fading parameter to $m = 1$.

- A single as well as seven and fifteen resolvable paths have been considered for the single-user scenario.

- Again, we used BPSK modulation combined with a half-rate $R = 0.5$ RSC code. The relationship between the Signal to Noise Ratio (SNR) and the SNR per bit is given by

$$E_c/N_o = SNR/bps, \tag{3.51}$$

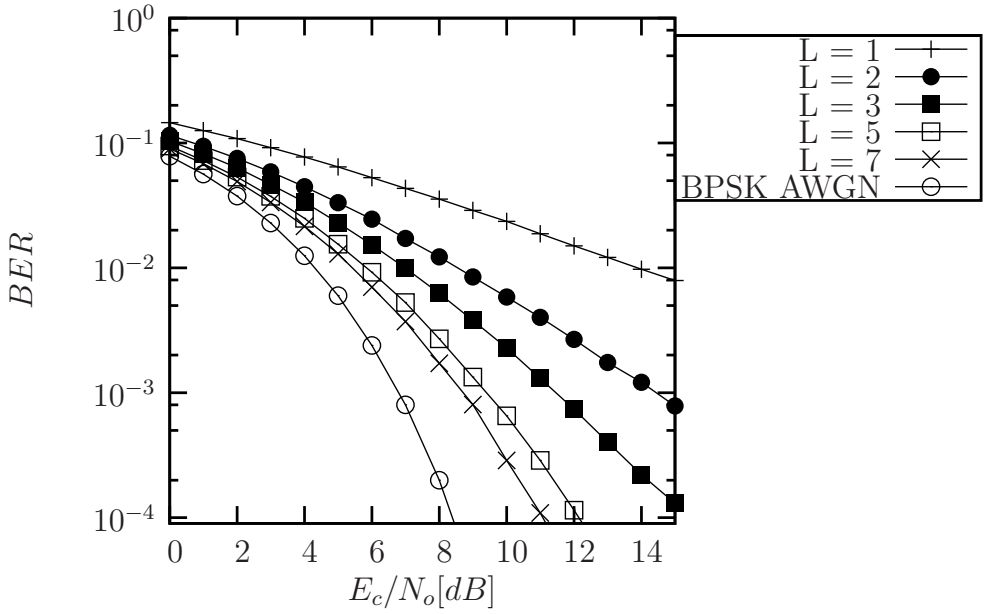

Figure 3.19: BER versus $E_c/N_o[dB]$ performance for the DS/TH UWB systems over multipath Rayleigh ($m = 1$) fading channels upon varying the diversity order L, in the single user senario with a bit-duration to chip-duration ratio $N = 10$.

where *bps* is the number of bits per BPSK modulated symbol in our system, which is one in the absence of channel coding.

3.4.2.2 Simulation Results

Figure 3.19, portrays the benefits of diversity. It depicts the BER as a function of the average received SNR per bit for the DS-CDMA/TH UWB systems in a multipath Rayleigh fading environment associated with $m = 1$. The curves seen in Figure 3.19 are parameterised by the diversity order of $L = 1, 3, 5, 7, 15$. Only a single set of curves was plotted, since the DS/TH BER curves were found to be indistinguishable and as expected, the BER improves, as the diversity order increases.

Figures 3.20, 3.21 and 3.22 depict the EXIT charts and the corresponding iterative decoding trajectories for the serial concatenated TH system using a URC concatenated with the RSC-2-(7,5) code under various SNR conditions for BPSK modulated transmissions over Rayleigh fading channels associated with $L = 1$, $L = 7$ and $L = 10$, respectively. The iterative decoding trajectories of Figures 3.20, 3.21 and 3.22 correspond to an I=1 000 000 bit interleaver. A critical point to observe in these graphs is represented by the areas under the detector's EXIT curves corresponding to the SNR value of zero dB. It can be seen from Figures 3.20 to 3.22 that this area increases, as the multipath channel's diversity order L increases. Thus, the system's capacity increases with the increase of diversity gain [129, 156]. A critical performance indicator of the iterative detection aided

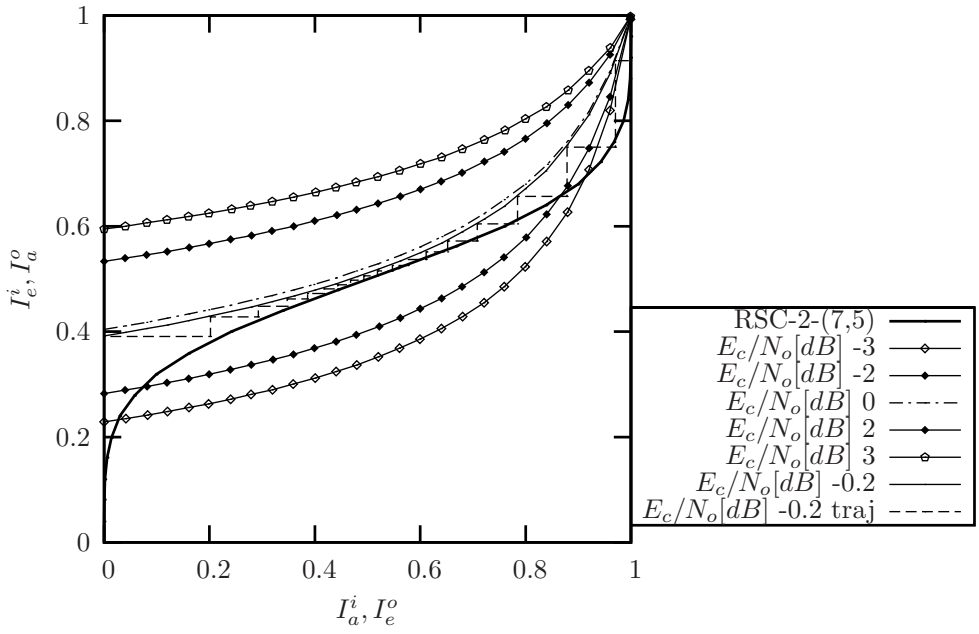

Figure 3.20: EXIT charts and iterative decoding trajectory for the TH serial concatenated system of a URC inconjunction with the RSC-2-(7,5) scheme under the various E_c/N_o[dB] conditions for the single-user BPSK modulated transmission over the dispersive Rayleigh fading channel having $L = 1$ path.

system is constituted by the SNR threshold value that allows the formation of a narrow but open "tunnel" between the detector's EXIT chart curve and the channel decoder's EXIT curve. It can be seen from Figures 3.20 to 3.22 that these E_c/N_o threshold values are approximately -0.2, -0.6 and -1.1 dB for the diversity orders of $L = 1$, $L = 7$ and $L = 10$, respectively. This indicates that decoding convergence to an infinitesimally low BER may be achieved at a reduced SNR value, as the diversity order increases.

To consider the same scenarios for the DS-UWB system, Figures 3.23, 3.24 and 3.25 illustrate the EXIT charts and the corresponding Monte-Carlo simulation-based iterative decoding trajectories for the serial concatenated DS system combined with a URC and the RSC-2-(7,5) schemes under various SNR conditions for BPSK modulated transmissions over Rayleigh fading channels, when using MPCs of $L = 1$, $L = 7$ and $L = 10$ paths, respectively. The iterative decoding trajectories, again, correspond to an I=1 000 000 bit interleaver. Similar performance trends to those of the TH based scheme can be observed from the EXIT charts of the DS system. Specifically, the system's capacity increases upon increasing the diversity gain, and a lower E_c/N_o threshold value is required in order to create an open convergence tunnel, as the diversity order increases. However, by carefully comparing Figures 3.23 to 3.25 *to* Figures 3.20 to 3.22, it can be concluded that the performance of the iterative TH-UWB system is slightly better than that of the iterative DS-UWB system, in the single-user senario. The area under the EXIT curve of the amalgamated detector and URC decoder is related to the achievable rate of the system [107, 116, 129]. The larger

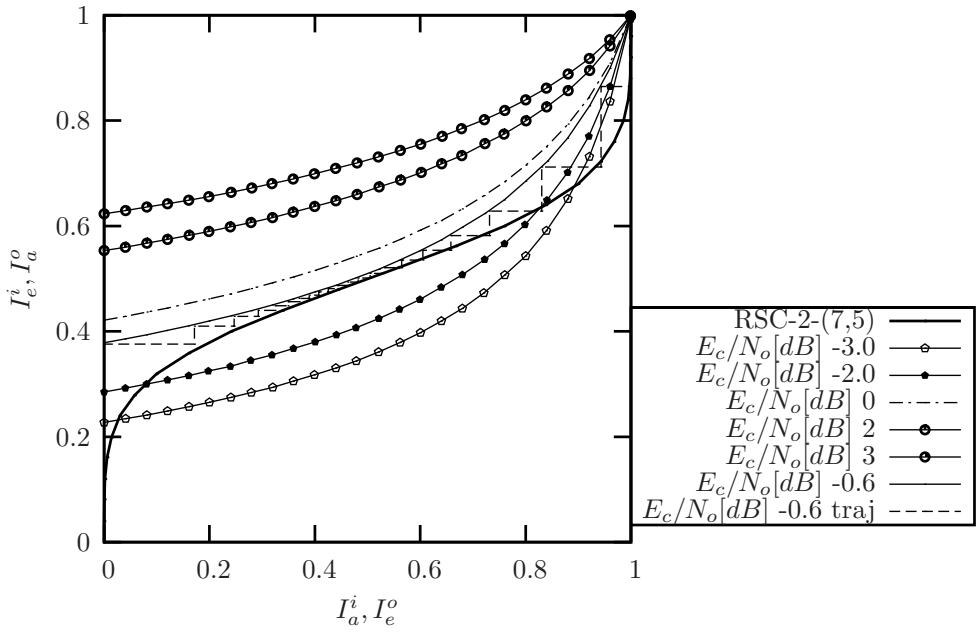

Figure 3.21: EXIT charts and iterative decoding trajectory for the TH serial concatenated system of a URC inconjunction with the RSC-2-(7,5) scheme under the various E_c/N_o[dB] conditions for the single-user BPSK modulated transmission over the dispersive Rayleigh fading channel having $L = 7$ paths.

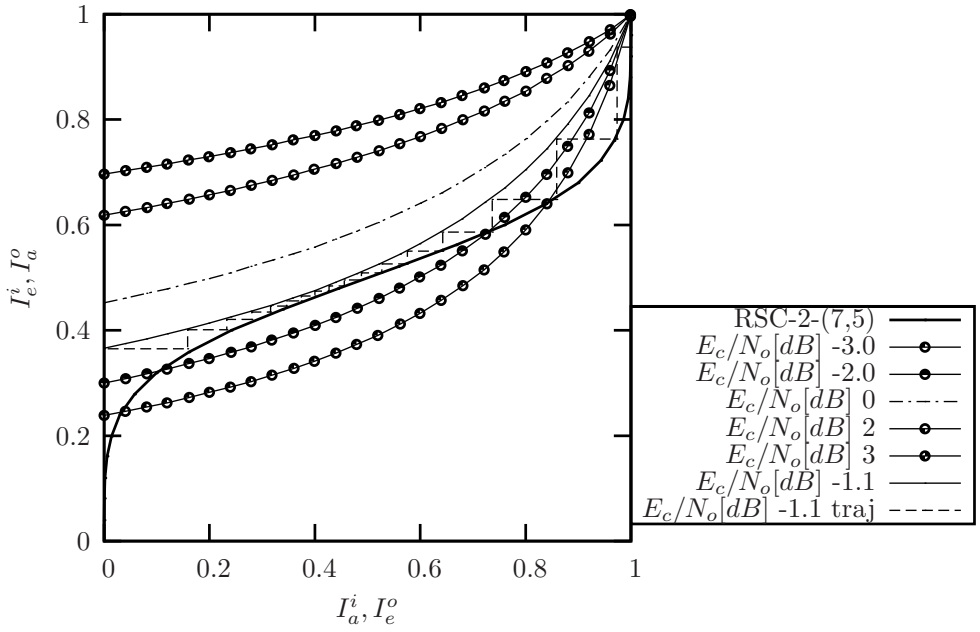

Figure 3.22: EXIT charts and iterative decoding trajectory for the TH serial concatenated system of a URC inconjunction with the RSC-2-(7,5) scheme under the various E_c/N_o[dB] conditions for the single-user BPSK modulated transmission over the dispersive Rayleigh fading channel having $L = 10$ paths.

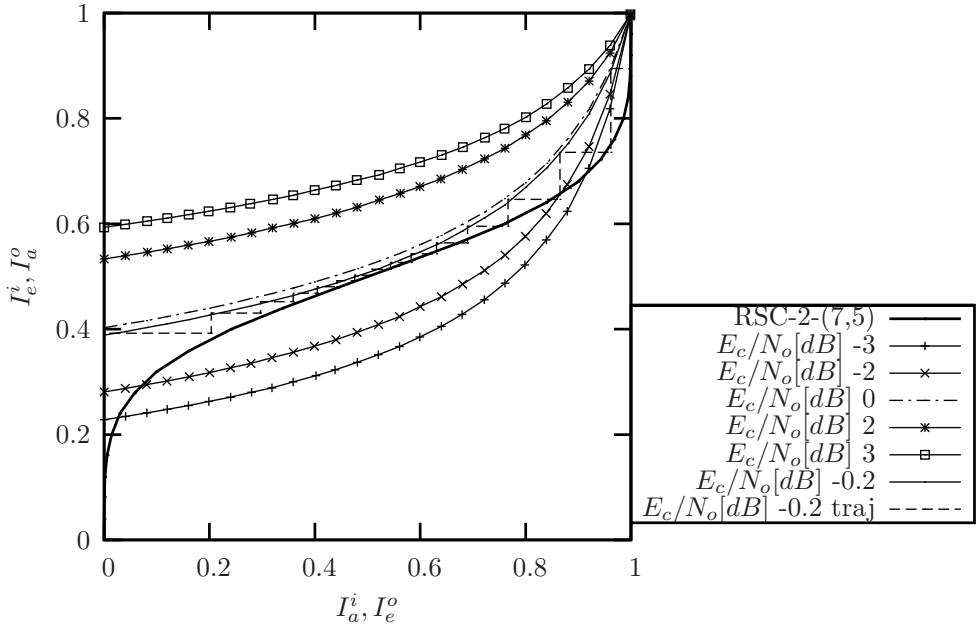

Figure 3.23: EXIT charts and iterative decoding trajectory for the DS serial concatenated system of a URC inconjunction with the RSC-2-(7,5) scheme under the various E_c/N_o[dB] conditions for the single-user BPSK modulated transmission over the dispersive Rayleigh fading channel having $L = 1$ path.

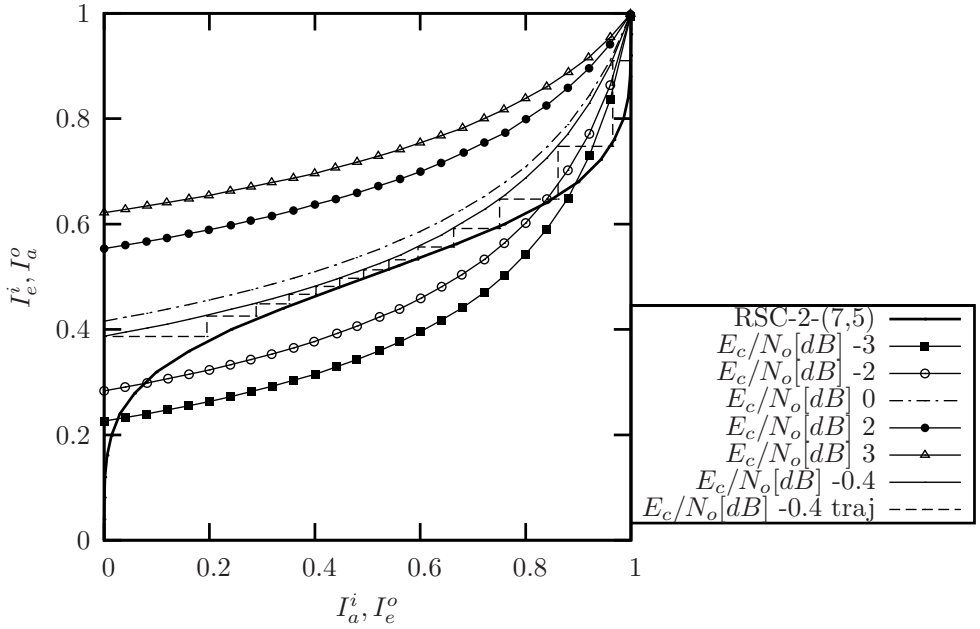

Figure 3.24: EXIT charts and iterative decoding trajectory for the DS serial concatenated system of a URC inconjunction with the RSC-2-(7,5) scheme under the various E_c/N_o[dB] conditions for the single-user BPSK modulated transmission over the dispersive Rayleigh fading channel having $L = 7$ paths.

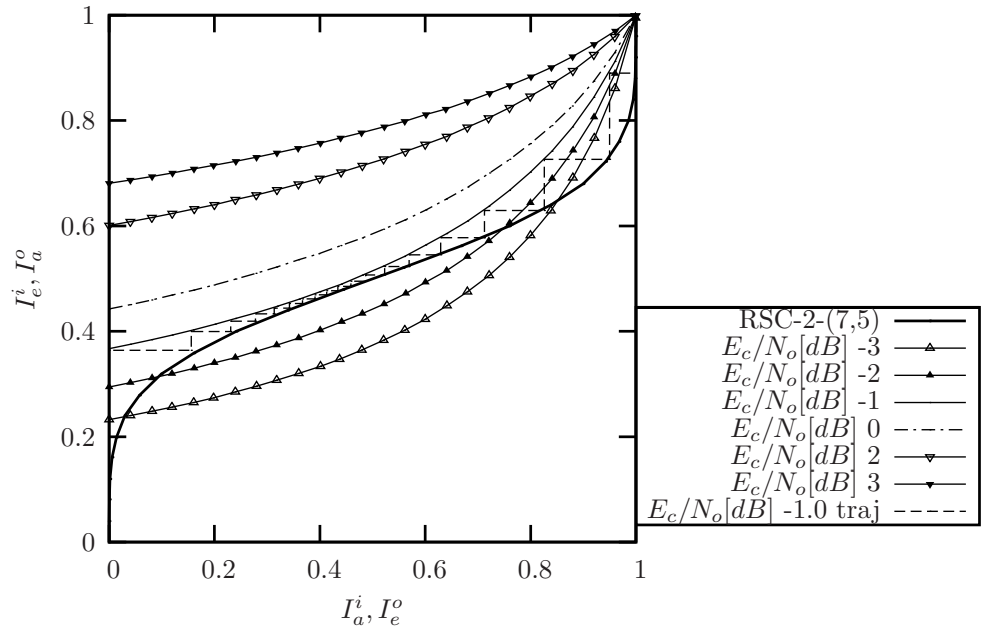

Figure 3.25: EXIT charts and iterative decoding trajectory for the DS serial concatenated system of a URC inconjunction with the RSC-2-(7,5) scheme under the various E_c/N_o[dB] conditions for the single-user BPSK modulated transmission over the dispersive Rayleigh fading channel having $L = 10$ paths.

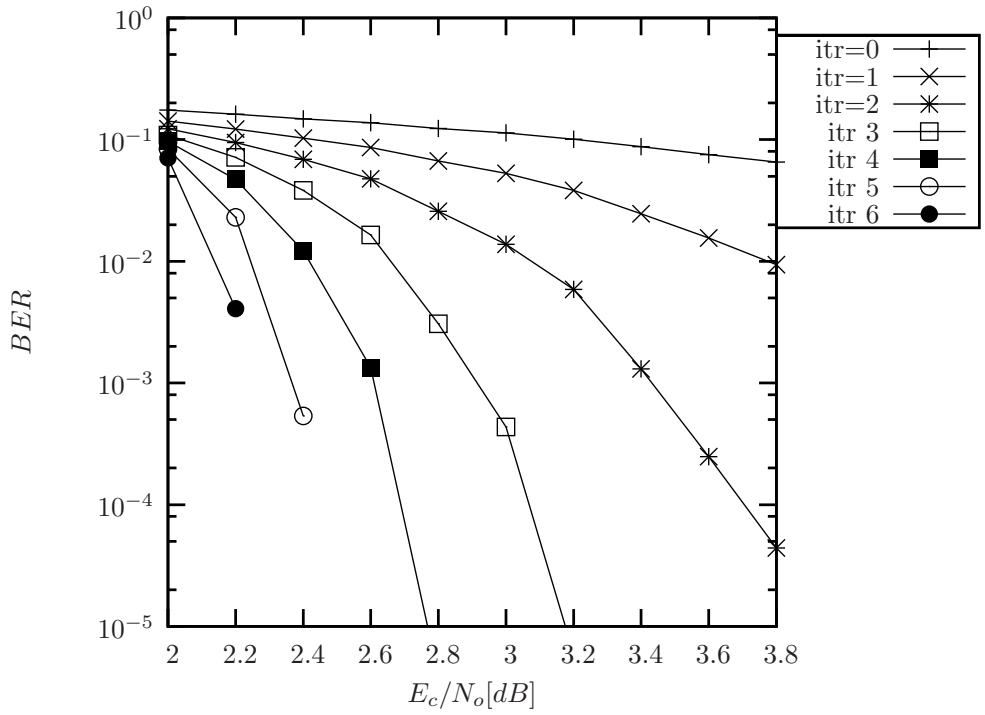

Figure 3.26: Bit error rate iterative decoding convergence performance for the TH serial concatenated system of a URC with the RSC-2-(7,5) under the various E_c/N_o[dB] conditions for the single-user BPSK modulated transmission over the Rayleigh fading channel of $L = 10$ paths.

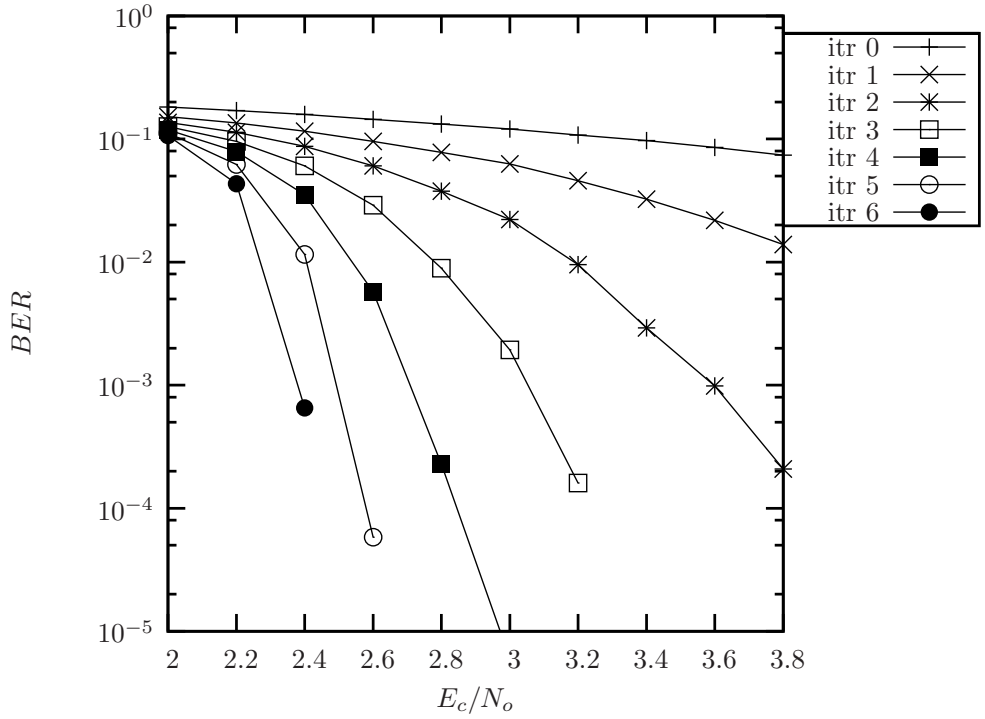

Figure 3.27: Bit error rate iterative decoding convergence performance for the DS serial concatenated system of a URC with the RSC-2-(7,5) under the various E_c/N_o[dB] conditions for the single-user BPSK modulated transmission over the Rayleigh fading channel of $L = 10$ paths.

this area the higher the attainable rate. Observe for example in Figures 3.22 and 3.25 that for the diversity order of $L = 10$, the areas under the EXIT curves of the TH-based detector and the DS-based detector are $A_E^{\text{TH}} = 0.57$ and $A_E^{\text{DS}} = 0.56$, respectively at the E_c/N_o value of -1.0 dB. Since we have $A_E^{\text{TH}} > A_E^{\text{DS}}$, the iterative TH-based system can attain an open convergence tunnel at a slightly lower SNR value.

Figures 3.26 and 3.27 show the iterative decoder's convergence performance for the TH-UWB and DS-UWB schemes for a single-user senario in conjunction with BPSK modulated transmissions, respectively, when communicating over a Rayleigh fading channel having a diversity order of $L = 10$. An interleaver length of I=1 000 000 was used again.

3.4.3 DS versus TH Comparison

TH-PPM and DS-CDMA have their own merits and disadvantages. In the former, the trains of time shifted pulses of PPM are used to transmit baseband UWB signals. The achievable transmission performance is enhanced by the employment of multiple pulses to transmit a single symbol [22]. In the latter, multiple chips having a chip duration equal to that of the basic time-domain signal are used to transmit data bits. Multiple access capability may be provided by employing the classic CDMA tecniques [44].

It was shown in Section 3.4.2.2 that TH-PPM UWB outperforms DS-CDMA UWB on

the basis of the area properties of the EXIT charts [107, 116, 129] using the simulation parameters detailed in Section 3.4.2.1. More explicitly, it was shown by observing Figures 3.22 and 3.25 that for the diversity order of $L = 10$, the areas under the EXIT curves of the TH-based detector and the DS-based detector are $A_E^{\mathrm{TH}} = 0.57$ and $A_E^{\mathrm{DS}} = 0.56$, respectively at the E_c/N_o value of -1.0 dB. Since we have $A_E^{\mathrm{TH}} > A_E^{\mathrm{DS}}$, the iterative TH-based system can attain a convergence tunnel at a slightly lower SNR value.

3.5 Chapter Conclusions

The following conclusions can be inferred from the chapter

- It can be stated on the basis of Section 3.2 that the selection of N_r resolvable paths from the L strongest paths of the UWB channel gives a remarkable performance gain, which is similar to that achieved by the same number of antennas combined with STC provided that the antennas experience independent fading. However, the number of MPCs that can be combined by the MRC scheme is limited by the affordable power consumption and complexity. Our results suggest that a diversity order of L=20 approaches the maximum attainable gain of 18dB and 12dB over the no-diversity configuration in single-user and full-load scenarios for N_u=63, when employing a spreading factor of N_s=63 for an uncoded UWB system.

- It was shown in Section 3.3 using a coded UWB system that an iteratively decoded fully-loaded DS-CDMA UWB system employing MMSE detection outperforms its lower-complexity counterpart employing the equivalent correlation detector. Explicitly, UWB DS-CDMA using the MMSE detector attains a BER of 10^{-5} at $\frac{E_b}{N_o} = 2dB$, when supporting $N_u = 32$ users employing $i = 12$ decoding iterations, while the same system using the correlation detector operates at an excessive BER of 10^{-1}.

- Finally, it can be inferred from Section 3.4 that in a single-user senario, the scheme based on the iterative TH-UWB system achieves a higher rate than the scheme based on the iterative DS-UWB system. Explicitly, the areas under the EXIT chart curves of the TH-based detector and the DS-based detector are $A_E^{\mathrm{TH}} = 0.57$ and $A_E^{\mathrm{DS}} = 0.56$, respectively. Since we have $A_E^{\mathrm{TH}} > A_E^{\mathrm{DS}}$, the iterative TH-based system is capable of attaining a convergence tunnel at a lower SNR value.

3.6 Chapter Summary

In Section 3.2, we quantified the achievable diversity gain of an uncoded UWB system operating in UWB propagation channels as a function of the diversity order. We selected

the L strongest MPCs from the N_r resolvable MPCs for MRC in order to achieve the best attainable performance gain in both single-user and full-load multiuser scenarios. Three classic detectors were used, namely the correlation, the ZF and the MMSE detector. However, the number of resolvable MPCs that can be utilized for diversity combining is limited by the affordable power consumption, design complexity and channel estimation [15, 39].

Section 3.3 provided a solution, suggesting a channel coded UWB design, which exploited the available number of resolvable paths with the aid of iterative detection to obtain a better performance than the system detailed in Section 3.2.1. This channel coded UWB model is the basis for our subsequent chapters, since the same model will be enhanced using different coding techniques in order to achieve a near-capacity performance.

Finally, Section 3.4 provided a comprehensive comparative study of DS-CDMA and TH-PPM UWB systems on the basis of Sections 3.2 and 3.3. We employed the diversity order selection technique of Section 3.2 and the channel coded system model of Section 3.3.2 with the aid of EXIT charts in order to quantify the performance of the DS-CDMA and TH-PPM UWB systems considered. It was shown that TH-PPM slightly outperformed DS-CDMA.

Chapter 4

Near-Capacity UWB System Design Using Irregular Variable Length Codes and Self-Concatenated Codes

4.1 Introduction

Section 3.3.2 covered the basic structure of channel coded UltraWideBand (UWB) systems using classic regular Forward Error Correction (FEC) encoders, which were investigated with the aid of Extrinsic Information Transfer (EXIT) charts. Naturally, the model of Section 3.3.2 provided a better performance than the uncoded UWB model of Section 3.2.1, but also demonstrated the inability of regular FEC encoders to arbitrarily approach the UWB system's capacity, as discussed in Section 1.5. In this chapter, we will provide the solutions for this open problem. In the first half of the chapter, we will use the family of Irregular Variable Length Codes (IrVLC) [157, 158] invoking two- and three-stage concatenated iteratively detected UWB Time-Hopping (TH) Pulse Position Modulated (PPM) Impulse Radio (IR) in order to approach the UWB system's capacity. In this chapter, we will detail our comparison between the two- and three-stage concatenated UWB system model using IrVLCs with the aid of EXIT charts. In Section 4.4, we will address the issue of complexity and interleaver size for the IrVLCs, as discussed in Section 1.5. The design alternative of employing sophisticated binary Self-Concatenated Convolutional Codes (SeCCC) [59, 159] using different puncturing rates will be presented in Section 4.4.1, which will be used to construct a low complexity near-capcity UWB system having a moderate interleaver size.

We have used IrVLCs [157, 158] in our two- and three-stage concatenated UWB time-hopping spread-spectrum impulse radio systems, because in addition to approaching the achieveable system capacity as a benefit of their irregular design, they contribute towards the desirable design objective of losslessly compressing the input bit-stream. The serial concatenation [56] and iterative decoding [57] of an irregular outer code with a regular inner code was proposed by Tüchler and Hagenauer in [130]. The irregular outer codec is comprised of a number of component codes, having a variety of coding rates. These different-rate component codes are invoked in order to generate specific fractions of the encoded bit sequence, which may be specifically chosen in order to shape the EXIT function [150] of the irregular outer code so that it matches that of the regular inner code. This facilitates the creation of an open EXIT chart tunnel [160] and the achievement of iterative decoding convergence to an infinitesimally low probability of error at channel Eb/N0 values that are close to the channel's capacity bound. Both Irregular Convolutional Codes (IrCC) [130], [161–165] and IrVLCs [157] have been proposed for employment as outer irregular codes.

The concept of concatenated coding schemes was proposed by Forney in [166]. The concept of employing low-complexity constituent codes to design a powerful amalgamated code was then revived by Berrou *et al.* in the context of Turbo codes, which constitute a class of FEC codes based on Parallel Concatenated Convolutional Codes (PCCC) of two or more constituent codes [167]. They are high-performance codes capable of operating near the Shannon limit [168] Since their invention they have found diverse applications in bandwidth-limited communication systems, where the maximum achievable information rate has to be supported in the presence of transmission errors due to both the Additive White Gaussian Noise (AWGN) and channel fading. Various Turbo Trellis Coded Modulation (TTCM) schemes were proposed in [169], [170] and [171]. Serially Concatenated Convolutional Codes (SCCC) [172] have been shown to yield a performance comparable, and in some cases superior, to turbo codes. Iteratively-Decoded Self-Concatenated Convolutional Codes (SeCCC-ID) proposed by Benedetto *et al.* [58] and Loeliger [59] constitute another attractive family of iterative detection aided schemes.

In this chapter, the convergence behaviour of iteratively decoded UWB time-hopping spread-spectrum impulse radio systems has been analyzed using EXIT charts as detailed in Section 3.3.1. An infinitesimally low Bit-Error Rate (BER) may only be achieved by an iterative receiver, if an open tunnel exists between the EXIT curves of the two Soft-Input Soft-Output (SISO) components. The convergence analysis and the best activation order of the component codes has been studied in the context of multiple-stage concatenated codes [108]. Furthermore, this technique computes the mutual information of the output extrinsic and input *a-priori* components corresponding to the associated bits for each of the iterative SISO blocks.

The novelty and rationale [2, 6, 7, 9] of this chapter can be summarised as follows:

1. *IrVLCs designed for serial concatenated and iteratively decoded TH-PPM UWB Spread-Spectrum (SS) IR systems are considered. The proposed design is capable of operating at low Signal-to-Noise Ratios (SNR) in Nakagami-m fading channels achieved with the aid of joint source and channel coding schemes. A number of component VLC codebooks having different coding rates are utilized by the IrVLC scheme for encoding specific fractions of the input source symbol stream. EXIT charts are used to select these fractions in order to shape the inverted EXIT curve of IrVLC according to the EXIT curve of the inner decoder, so that their shapes match closely [2].*

2. *We extend the concept of two-stage Extrinsic Information (EI) exchange between the unity-rate code's decoder and an IrVLC decoder to a three-stage scheme constituted by a unity-rate decoder, an IrVLC decoder and the TH-PPM-UWB detector. The technique of EXIT charts is utilized to the best of our knowledge for the first time to design the serial concatenation of the TH-PPM-UWB detector, unity-rate decoder and an IrVLC outer decoder in order to attain a good performance even at near-capacity SNR values. We contrast the two-stage Iterative Decoder (ID) to the three-stage scheme and demonstrate that the three-stage scheme outperforms the two-stage arrangement. The three-stage IrVLC-aided TH-PPM-UWB scheme allows us to accurately shape the EXIT curves in order to create a marginally open EXIT tunnel, which facilitates near-capacity operation [6, 9].*

3. *Finally, We design a near-capacity iteratively decoded TH-PPM-UWB-IR-SeCCC system using EXIT charts. More explicitly, the powerful tool of EXIT charts is used to appropriately select the coding rates of the SeCCCs in order to shape the inverted EXIT curve of the TH-PPM-UWB-IR-SeCCC system and hence to match it with that of the inner decoder for the sake of achieving an infinitesimally low BER at near-capacity SNR values. Quantitatively, the proposed TH-PPM-UWB-IR-SeCCC design becomes capable of performing within about 0.9 dB of the Nakagami-m fading channel's capacity [7].*

This chapter is organised as follows. In Section 4.2, a brief background is presented with an overview of the difference between two- and three-stage iterative detection schemes, as detailed further in [122]. In Sections 4.3 and 4.3.1, our two-stage concatenated iteratively detected UWB TH IR design is presented, followed by Section 4.3.2 that highlights the three-stage concatenated UWB TH IR philosophy using iterative detection for the sake of achieving an enhanced performance. The alternative design of near-capacity iteratively decoded TH-PPM-UWB-IR-SeCCC was then used to replace the IrVLCs of Section 4.3 which have a low complexity and a moderate interleaver size as presented in Section 4.4. Finally, we conclude our findings in Section 4.5.

4.2 Background

Concatenated Codes (CC) have been proposed in [173]. However, at the time of its conception it was deemed to have an excessive complexity and hence it failed to attract immediate research interests. It was not until the discovery of turbo codes [174] that efficient iterative decoding of concatenated codes became a reality at a low complexity by employing simple constituent codes. Since then, the appealing iterative decoding of concatenated codes has inspired numerous researchers to extend the technique to other transmission schemes consisting of a concatenation of two or more constituent decoding stages [57, 58, 175–189].

In [180] iterative decoding was invoked for exchanging extrinsic information between a soft-output symbol detector and an outer channel decoder in order to combat the effect of Inter-Symbol Interference (ISI). In [181] iterative decoding was carried out by exchanging information between an outer convolutional decoder and an inner Trellis Coded Modulation (TCM) decoder. The authors of [182, 183] presented a unified theory of Bit-Interleaved Coded Modulation (BICM). On the other hand, the employment of the iterative detection principle in [184] was considered for iterative soft demapping in the context of BICM, where a soft demapper was used between the multilevel demodulator and the channel decoder. In addition, iterative multiuser detection and channel decoding was proposed in [188] for CDMA schemes. Finally, in [189] an iteratively detected scheme was proposed for the Rayleigh fading MIMO channel, where an orthogonal STBC scheme was considered as the inner code combined with an additional block code as the outer channel code.

In general a so-called recursive inner code having Infinite Impulse Response (IIR) is needed in order to maximise the achievable interleaver gain and hence to avoid the average BER floor, when employing iterative decoding [197] because an IIR spreads the extrinsic information efficiently. This principle has been adopted by several authors for designing serially concatenated schemes, where unity-rate inner codes having an IIR were employed for designing low complexity iterative detection aided schemes suitable for bandwidth- and power-limited systems having stringent BER requirements [127, 148, 193, 196, 198].

Semi-analytical tools devised for investigating the convergence behaviour of iteratively decoded systems have attracted considerable research attention [107, 108, 116, 126, 127, 129, 130, 149, 199]. In [107], ten Brink proposed the employment of the so-called EXIT characteristics for describing the flow of extrinsic information between the soft-in soft-out constituent decoders. The computation of EXIT charts was further simplified in [149] to a time averaging, when the PDF of the information communicated between the input and output of the constituent decoders was symmetric and consistent. A tutorial introduction to EXIT charts can be found in [129]. The concept of EXIT chart analysis has been extended to three-stage concatenated systems in [108, 194, 195]. The major contributions on iterative detection and its convergence analysis are summarised in Tables 4.1 and 4.2. Next

1966	*Authors:* Forney [173] *Contribution:* promoted concatenated codes.
1974	*Authors:* Bahl *et al.* [190] *Contribution:* invented the Maximum A-Posteriori (MAP) algorithm.
1993	*Authors:* Berrou *et al.* [174] *Contribution:* invented the turbo codes and showed that the iterative decoding constitutes an efficient way of improving the attainable performance without an excessive complexity.
1995	*Authors:* Robertson *et al.* [191] *Contribution:* proposed the log-MAP algorithm that results in a similar performance to that of the MAP algorithm at significantly lower complexity. *Authors:* Divsalar *et al.* [175] *Contribution:* extended the turbo principle to multiple parallel concatenated codes.
1996	*Authors:* Benedetto *et al.* [57] *Contribution:*extended the turbo principle to serially concatenated block and convolutional codes.
1997	*Authors:* Benedetto *et al.* [181] *Contribution:* proposed an iterative detection scheme, where iterations were carried out between the outer convolutional code and inner TCM decoders. *Authors:* Caire *et al.* [182, 183] *Contribution:* presented the BICM concept and its design rules. *Authors:* Li *et al.* [185–187] *Contribution:* combined the BICM principle with iterative detection.
1998	*Authors:* Benedetto *et al.* [58, 192] *Contribution:* studied the design of multiple serially concatenated codes. *Authors:* Brink *et al.* [184] *Contribution:* introduced a soft demapper between the multilevel demodulator and the channel decoder in an iteratively detected coded system.
1999	*Authors:* Wang *et al.* [188] *Contribution:* proposed iterative multiuser detection and channel decoding for channel coded CDMA systems.
2000	*Authors:* Divsalar *et al.* [127, 148] *Contribution:* employed unity-rate inner codes for designing low-complexity iterative detection schemes suitable for bandwidth and power limited systems having stringent BER requirements. *Authors:* ten Brink [107] *Contribution:* proposed the employment of EXIT charts for analysing the convergence behaviour of iteratively detected systems.

Table 4.1: Major concatenated schemes and iterative detection (Part 1) [122].

2001	*Authors:* Lee [193] *Contribution:*studied the beneficial effect of precoding on serially concatenated systems communicating over dispersive channels. *Authors:* ten Brink [116, 194] *Contribution:* extended the employment of EXIT charts to three-stage parallel concatenated codes. *Authors:* EL Gamal *et al.* [126] *Contribution:* used SNR measures for studying the convergence behaviour of iterative decoding.
2002	*Authors:* Tüchler *et al.* [149] *Contribution:* simplified the computation of EXIT charts. *Authors:* Tüchler *et al.* [130] *Contribution:* compared several algorithms predicting the decoding convergence of iterative decoding schemes. *Authors:* Tüchler *et al.* [195] *Contribution:* extended the EXIT chart analysis to three-stage serially concatenated systems.
2003	*Authors:* Sezgin *et al.* [189] *Contribution:* proposed an iterative detection scheme where a block code was used as an outer code and STBC as an inner code.
2004	*Authors:* Tüchler *et al.* [161] *Contribution:* proposed a design procedure for creating systems exhibiting beneficial decoding convergence depending on the block length.
2005	*Authors:* Lifang *et al.* [196] *Contribution:*showed that non-square QAM can be decomposed into a parity-check block encoder having a recursive nature and a memoryless modulator. Iterative decoding was implemented with an outer code for improving the achievable system performance. *Authors:* Brännström *et al.* [108] *Contribution:*considered EXIT chart analysis for multiple concatenated codes using 3-dimensional charts and proposed a way for finding the optimal activation order.
2008	*Authors:* Maunder *et al.* [158] *Contribution:* designed irregular variable length codes for near-capacity joint source and channel coding aided systems.

Table 4.2: Major concatenated schemes and iterative detection (Part 2) [122].

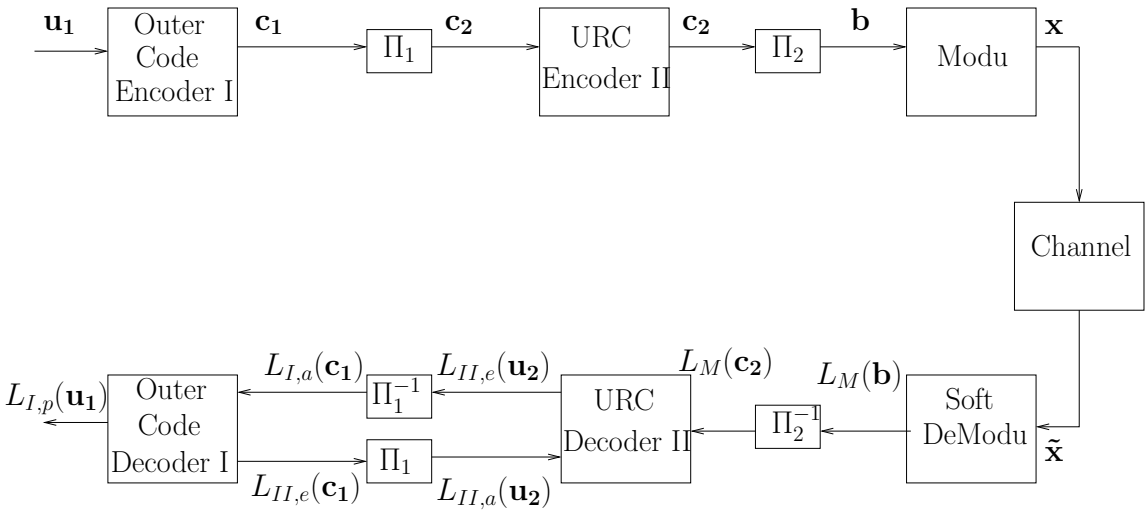

Figure 4.1: Block diagram of two-stage iterative detection scheme.

we will provide a brief tutorial about Two-stage, Three-stage iterative detection schemes and IrVLC.

4.2.1 Two-Stage Iterative Detection Scheme

Figure 4.1 potrays the principle of two-stage iterative detection schemes.The URC Decoder II processes the information forwarded by the soft demodulator in conjunction with the *a priori* information $L_{II,a}(\mathbf{u}_2)$ in order to generate the *a posteriori* probability. The *a priori* LLR values of the URC decoder are subtracted from the *a posteriori* LLR values for the sake of generating the extrinsic LLR values $L_{II,e}(\mathbf{u}_2)$, as seen in Figure 4.1. Next, the soft bits $L_{I,a}(\mathbf{c}_1)$ are passed to the outer Decoder I of Figure 4.1 in order to compute the *a posteriori* LLR values for all the channel-coded bits. As seen in Figure 4.1, the extrinsic information $L_{I,e}(\mathbf{c}_1)$ is then fed back to the URC Decoder II as the *a priori* information $L_{II,a}(\mathbf{u}_2)$ after appropriately ordering the corresponding values using the interleaver Π_1 of Figure 4.1. The soft-in soft-out Decoder II of Figure 4.1 exploits the *a priori* information for the sake of providing improved extrinsic LLR values, which are then passed to the outer Decoder I and then back to Decoder II for further iterations.

Note that the exchange of extrinsic information is carried out between the outer Decoder I and the URC Decoder II only, while no iterations are carried out between the URC Decoder II and the soft demodulator.

4.2.2 Three-Stage Iterative Detection Scheme

Figure 4.2 highlights the principle of three-stage iterative detection schemes. Iterative extrinsic information exchange is carried out between the soft demodulator, soft-in soft-out

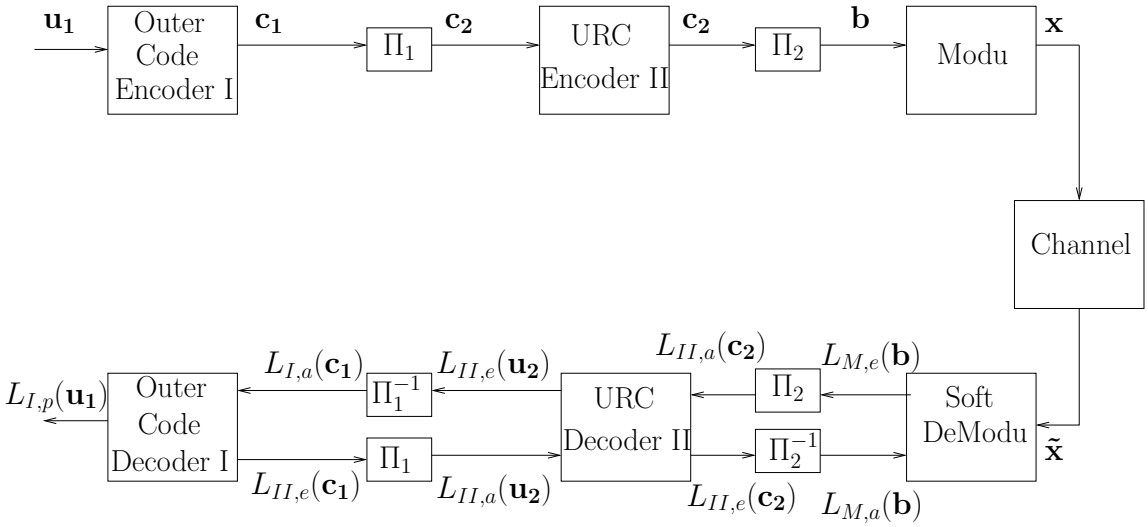

Figure 4.2: Block diagram of three-stage iterative detection scheme.

URC Decoder II and the soft-in soft-out outer Decoder I. The specific activation order of the extrinsic information exchange between the three constituent decoders plays an important role in achieving the best possible performance. The iterative process is performed for a number of consecutive iterations. During the last iteration, only the LLR values $L_{I,p}(\mathbf{u_1})$ of the original uncoded systematic information bits $\mathbf{u}_1$ are required, which are passed to a hard decision decoder in order to determine the estimated transmitted source bits $\tilde{\mathbf{u}}_1$, as shown in Figure 4.2.

4.2.3 Irregular Variable Length Codes

Irregular coding has been proposed for the reliable transmission of information at channel SNRs that are close to the channels capacity bound [39] without requiring an excessive decoding complexity and latency. The concept was originally introduced in the context of Low-density Parity Check Codes (LDPC) codes in [200, 201]. These may be represented using bipartite graphs [202], comprising a number of check nodes and a number of variable nodes. In the bipartite graph [202] of an irregular LDPC code, the check nodes are connected to various numbers of variable nodes and vice versa [124]. This is in contrast to regular LDPC codes, where all check nodes are connected to the same number of variable nodes and vice versa. Hence, a higher degree of freedom is facilitated during the design of irregular LDPC codes and this supports operation at channel SNRs that are closer to the channels capacity bound [124]. Indeed, irregular LDPC operation within 0.13 dB of the channels SNR capacity bound was demonstrated in [124]. We can construct an irregular code with the average rate 1/2 as indicated in Figure 4.3. We have the following constraints

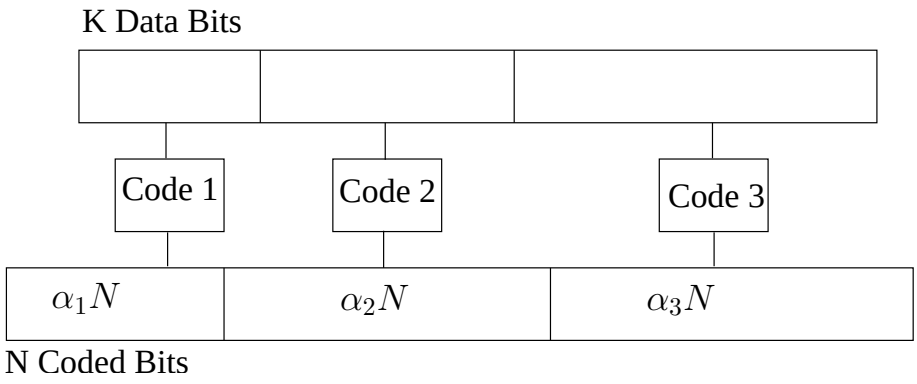

Figure 4.3: Irregular code.

on the α_k in the FEC code:

$$\sum_{k=1}^{L_R} \alpha_k = 1, \tag{4.1}$$

$$\sum_{k=1}^{L_R} \alpha_k R_k = 1/2, \tag{4.2}$$

where L is the LLR values, R is the code rate and $\alpha_k \in [0, 1]$ with $k = 1, \cdots, L_R$. IrVLC uses a number of component Variable Length Coding (VLC) codebooks with different coding rates in order to encode specific fractions of the input source symbol stream [203]. The corresponding lengths of these fractions can be selected with the aid of EXIT charts in order to shape the inverted EXIT curve of the IrVLC, so that it does not cross the EXIT curve of the inner decoder. This will enable us to have an open EXIT chart tunnel at low values of SNRs.

4.3 Two-Stage and Three-Stage Concatenated UWB Using IrVLCs

The background presented in Section 4.2 enables us to solve the open problem stated in Chapter 3 and discussed in Section 1.5 namely that the classic regular FEC encoders presented in Section 3.3.2 are unable to arbitrarily approach the UWB system's capacity. In this section, we will use the two- and three-stage concatenated UWB TH impulse radio system using IrVLCs with the aid of EXIT charts in order to achieve a near-capacity performance. We will exploit the basic properties of IrVLCs discussed in Section 4.2.3 in order to create an open EXIT chart tunnel at low values of SNRs.

4.3.1 Two-Stage Concatenation

In this section the design of IrVLCs for two-stage serial concatenated and iteratively decoded TH-PPM UWB spread-spectrum Impulse radio system is considered. The proposed design is capable of operation at low SNR in Nakagami-m fading channels, when invoking joint source and channel coding schemes. A number of component VLC codebooks having different coding rates is utilized by our IrVLC scheme for encoding specific fractions of the input source symbol stream. The EXIT charts are used to select these fractions in order to appropriately shape the inverted EXIT curve of the IrVLC scheme according to the EXIT curve of the inner decoder. The proposed scheme can achieve a near-zero BER at low SNR values.

The design considered in Figure 4.4 assumes having 16-ary source symbol values obeying a PDF resulting from the Lloyd-Max (LM) quantization of independent Laplacian distributed values. The abscissa values of the PDF are between 0.002 and 0.16 for the 4-bit LM quantization of a Gaussian source. The entropy values corresponding to the PDF are between 2.6 bits/symbol and 8.74 bits/symbol, with an overall source entropy of 3.5 bits per VLC symbol.

Again, the source symbol frame $\mathbf{\Psi}$ has $Q = 16$-ary values with 4-bit source symbols $\{\Psi_q\}_{q=1}^{Q} \in [1 \dots 16]$, which constitute the Q components of the set $\{\mathbf{\Psi^q}\}_{q=1}^{Q}$. The number of symbols in the source symbol component Ψ^q obtained from the source symbol frame Ψ is denoted by Q^q. In our proposed design $Q^1 = Q$ is considered as our benchmarker for the VLC based scheme and Q^{16} for the IrVLC-TH-PPM UWB arrangement. Furthermore, in the IrVLC-TH-PPM UWB scheme $\{Q^q\}_{q=1}^{Q}$ values are selected in order to ensure that the inverted EXIT curve of the IrVLC scheme does not cross the EXIT curve of inner encoder.

The transmission frame component $\mathbf{\Upsilon^q} = \{\mathbf{VLC}^{q,\Psi_{j^q}^q}\}_{q^q=1}^{Q^q}$ is constituted by the concatenation of Q^q number of VLC codewords that represent the Q^q number of source symbols in the source symbol frame component $\mathbf{\Psi^q}$. The codeword $\mathbf{VLC}^{q,k}$ having a length of $W^{q,k}$ is represented by the specific source symbols having the index of $k \in [1 \dots 16]$ encoded by the corresponding VLC code book $\mathbf{VLC}^q$. The set of Q VLC codebooks $\{\mathbf{VLC}^q\}_{q=1}^{Q}$ has a range of coding rates $\{R^q\}_{q=1}^{Q} \in [0, 1]$.

The concatenated frame $\mathbf{\Psi}$ constituted by the components $\{\mathbf{\Psi^q}\}_{q=1}^{Q}$ as shown in Figure 4.4 has a length of $\sum_{q=1}^{Q} W^q$ bits. The interleaved and URC-based precoded bits are forwarded to a buffer, as depicted in the schematic of Figure 4.4. These bits are transmitted by the TH-PPM modulator. The TH-PPM-UWB signal conveying the M-ary source symbols is generated with the aid of several TH frames, for example L number of TH frames. The frame duration T_F is related to the symbol interval T_S by $T_S = LT_F$. Furthermore, the desired time shift T_{CH} within a TH frame is generated by the TH code. As seen in Figure 4.4, we have used a PN generator for this purpose. The details of TH UWB

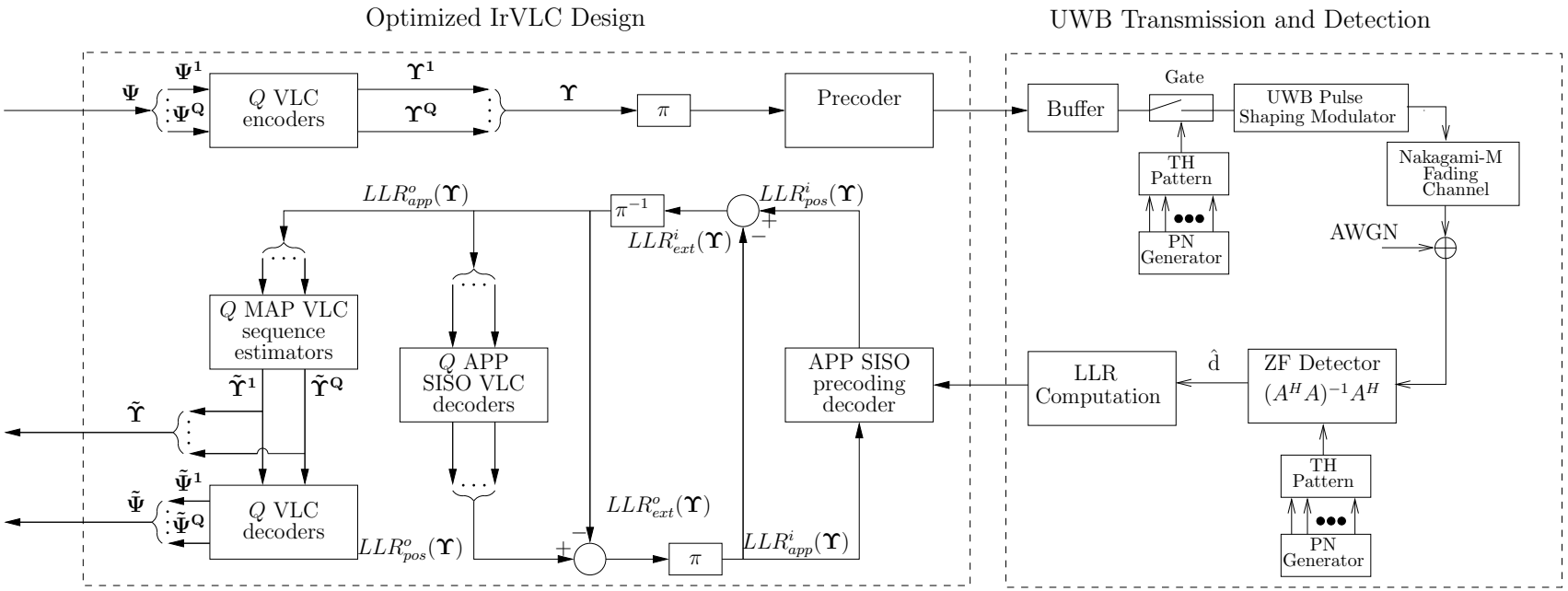

Figure 4.4: Schematic of the IrVLC and regular VLC-based TH-PPM-UWB schemes. In the IrVLC coded scheme Q^{16}, whilst Q^1 in the regular VLC-coded benchmarker scheme.

transmissions were discussed earlier in Sections 3.2.2, 2.2, 3.2.2.3, but to allow the reader to consult this chapter in isolation, a brief review is provided in Section 4.3.1.1.

Again, the TH-PPM-UWB system was evaluated using the UWB multipath channel model of Section 2.2, which was based on indoor channel measurements carried out between 3.1 GHz and 10.6 GHz over a range of less than 10 meters. Each path of the transmitted signal is Nakagami-m faded and also corrupted by the AWGN and a Jamming signal having single-sided power spectral densities of N_0 and N_J, respectively.

The receiver's schematic is also shown in Figure 4.4, where the ZFD is used to estimate the data $\hat{\mathrm{d}}$. The ZFD detector has the capability to combat the effects of both the Multiple Access Interference (MAI) and ISI at the expense of enhancing the noise at low SNRs. After the ZFD, the corresponding symbol probabilities and LLRs are computed, which are then fed to the unity-rate decoder of Figure 4.4.

4.3.1.1 UWB Transceiver Model

In this section, we will recite the basic characteristic equations of the UWB transmission and detection schemes considered. Further details of the TH-PPM-UWB system, the channel model and ZF detector can be found in Sections 3.2.2, 2.2, 3.2.2.3, respectively.

TH-PPM UWB: A general TH-PPM-UWB signal may be described as:

$$g(t) = \sum_{n=-\infty}^{\infty} \phi(t - nT_F - T_{PP_n} - T_{CH_n}), \tag{4.3}$$

where $\phi(t)$ is the reference pulse shape, T_F is the frame duration, T_{PP_n} is a small shift in the pulse position, either forward or backward in order to represent the binary stream and finally, T_{CH_n} is the time shift based on the time hopping code, where the TH pattern repeats itself after a certain number of hops. As shown in Figure 4.4, we have used PN codes to control the TH pattern. PN codes have beneficial Auto-CorreLation (ACL) and Cross-CorreLation (CCL) properties of ISI and MAI mitigation.

Channel Model The model accepted by the IEEE 802.15.3 standard and considered here can be expressed as [155]

$$h(t) = \sum_{r=1}^{R} h_r e^{j\varphi_r} \delta(t - rT_\varphi), \tag{4.4}$$

where R represents the number of resolvable paths, h_r and φ_r are the gain and phase of the rth resolvable multipath component, while rT_φ represents the corresponding delay of the rth multipath component.

The transmitted signal is also corrupted by AWGN and by a Partial Band Noise Jamming (PBNJ) signal having single-sided power spectral densities of N_0 and N_J, respectively.

We assume that the PBNJ signal jams a fraction $0 \leq \rho \leq 1$ of the total spread spectrum bandwidth W_{ss}. We also assume that the PBNJ signal is contiguous. Thus, the probability that a band or a tone is jammed is given by ρ, while the probability that the band is not jammed is $(1-\rho)$.

Zero Forcing Detector The discrete-time received composite multiuser signal can be represented in matrix form as [49]:

$$\mathbf{y} = \mathbf{A}\mathbf{d} + \mathbf{n}, \tag{4.5}$$

where $\mathbf{n}$ is the noise sequence, which has a covariance matrix of $\mathbf{R}_n = E[nn^H]$, $\mathbf{A}$ is the overall system matrix and $\mathbf{d}$ is the user data vector. The data estimates at the output of ZFD is

$$\hat{\mathbf{d}}_{\mathbf{ZFD}}\Big|_{\mathbf{R}_n=\sigma^2 I} = (\mathbf{A}^{\mathbf{H}}\mathbf{A})^{-\mathbf{1}}\mathbf{A}^{\mathbf{H}}\mathbf{y}. \tag{4.6}$$

If it is assumed in Equation 4.6 that $\mathbf{n}$ consists of noise samples that are zero mean Gaussian variables having a variance of σ^2, then its covariance matrix is given by $\mathbf{R}_n = \sigma^2 I$, where I is the identity matrix. In the next section, we detail the performance of our two-stage IrVLC TH-PPM-UWB scheme with the aid of EXIT chart analysis.

4.3.1.2 EXIT Chart Performance Analysis

In our proposed IrVLC-TH-PPM-UWB scheme, 16 different VLC codebooks $\{\mathbf{VLC}^q\}_{q=1}^{Q}$ having coding rates in the range of $[0.25, 0.95]$ are used. Furthermore, Variable Length Error Correcting (VLEC) codes are utilised. For the conventional regular VLC benchmarker scheme we employed a single VLC codebook which was analogous to the IrVLC-TH-PPM-UWB constituent scheme $\mathbf{VLC}^{10}$ associated with a coding rate of $R = 0.5$.

Figure 4.5. depicts the inverted EXIT curves for the bit-based APP SISO VLC decoding of the aforesaid 16 different-rate VLC codebooks combined with the unity rate decoder's EXIT curves at E_b/N_0 values of 6.4 and 6.5 dB for transmission over an independently-fading Nakagami channel. The EXIT curves were generated using uncorrelated Gaussian distributed *a priori* LLRs. The inverted EXIT curve of the IrVLC scheme shown in Figure 4.5 was generated by the appropriately weighted superposition of the 16 component VLC codes inverted EXIT curves. The specific number of source symbols encoded by the specific code Q^q is proportional to the weight applied to the inverted EXIT curve of the component VLC codebook $\mathbf{VLC^q}$.

Using the EXIT-chart-matching algorithm of [149], it has been found that it is sufficient to use only four of the 16 VLC components to encode a non-zero number of source symbols in order to ensure that the IrVLC coding rate matches that of the regular VLC benchmarker scheme, namely 0.5. Furthermore, these four components also ensure that the inverted IrVLC EXIT curve did not cross the unity rate decoder's EXIT curve at E_b/N_0 of 6.4 dB.

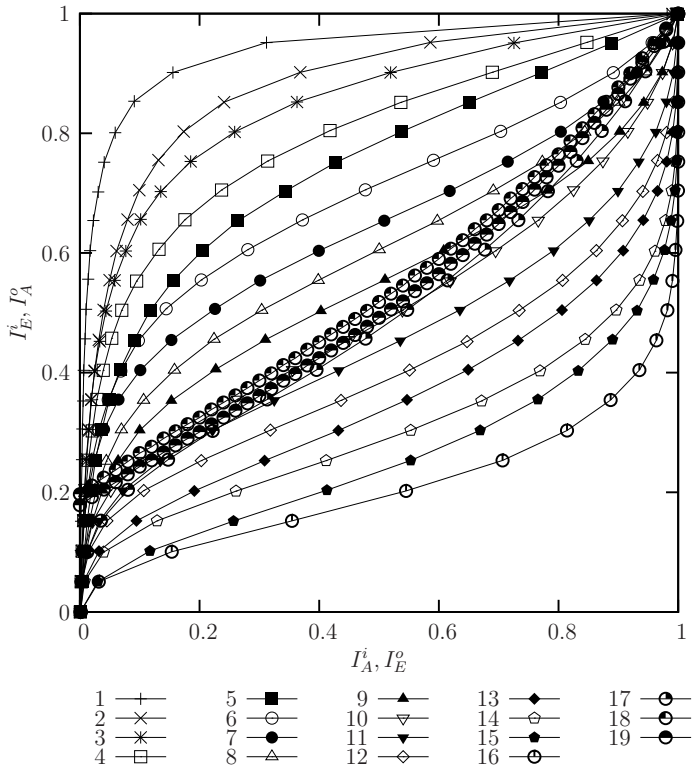

Figure 4.5: Inverted VLC EXIT curves and unity rate decoder EXIT curves, assuming an interference-free, uncorrelated Nakagami-m fading channel. Each "i" legend corresponds to respective rows of Table 4.3.

It can readily be seen from Figure 4.5 that an infinitesimally low BER can be achieved by the IrVLC-TH-PPM-UWB scheme for sufficiently high E_b/N_0 values, as predicted by the presence of an open EXIT chart tunnel in Figure 4.6. Observe in Figure 4.6, however, that the Monte-Carlo simulation based decoding trajectory does not perfectly match the EXIT curves owing to using a limited interleaver memory. Hence an infinitesimally low BER is only achieved for E_b/N_0 values in excess of 6.4 dB. This is not possible for the benchmark VLC based scheme for E_b/N_0 values below 6.5 dB. Again, the VLC code rates summerized in Table 4.3 were used.

Analogous to the IrVLC design of Figure 4.5 created for the interference-free channel, we have also designed an IrVLC code for the Nakagami-m fading channel contaminated by partial band jamming, assuming $E_b/N_J = 10$dB and an interference probability of $\rho = 0.1$. The weight values of $J^n, n = 1, \ldots, 16$ optimized for this particular jammed channel are [0 0 0 0.22 0 0 0 0.27 0 0.05 0 0.3 0 0 0 0].

Figure 4.6 corroborates the results of Figure 4.5 by recording the MI values at the output of the inner and outer decoders. The trajectory steps follow the EXIT curves of the inner and outer IrVLC decoder. Furthermore the BER versus E_b/N_0 results of Figure 4.7 verify the performance predictions of Figure 4.6. Both Figures 4.6 assumed 4.7 are $E_b/N_J = 10$dB, 16 source symbol values and a precoder memory of $L = 3$. Naturally,

1. VLC^1, R^1=0.95, Q^1=0	11. VLC^{11}, R^{11}=0.45, Q^{11}=0
2. VLC^2, R^2=0.89, Q^2=0	12. VLC^{12}, R^{12}=0.4, Q^{12}=0.5Q
3. VLC^3, R^3=0.85, Q^3=0	13. VLC^{13}, R^{13}=0.35, Q^{13}=0
4. VLC^4, R^4=0.8, Q^4=0.18Q	14. VLC^{14}, R^{14}=0.3, Q^{14}=0
5. VLC^5, R^5=0.75, Q^5=0	15. VLC^{15}, R^{15}=0.25, Q^{15}=0
6. VLC^6, R^6=0.7, Q^6=0.12Q	16. VLC^{16}, R^{16}=0.2, Q^{16}=0
7. VLC^7, R^7=0.65, Q^7=0	17. $IrVLC$=0.5
8. VLC^8, R^8=0.60, Q^8=0.2Q	18. $PrecoderSNR$=6.5dB
9. VLC^9, R^9=0.55, Q^9=0	19. $PrecodeSNR$=6.4dB
10. VLC^{10}, R^{10}=0.5, Q^{10}=0.2Q	20. EXIT Open Tunnel 6.4dB

Table 4.3: VLC parameters and code rates

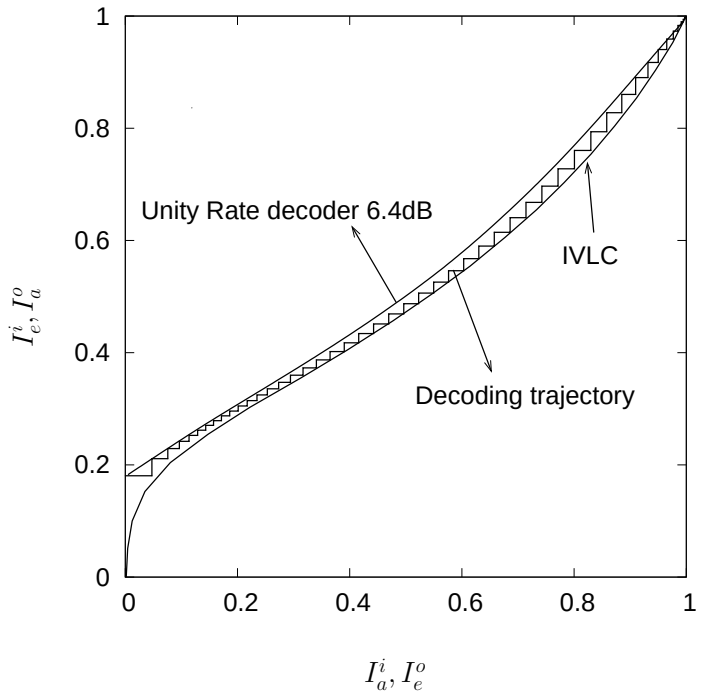

Figure 4.6: IrVLC and unity rate decoder EXIT curves as well as decoding trajectory, assuming an interference-free, uncorrelated Nakagami-m fading channel.

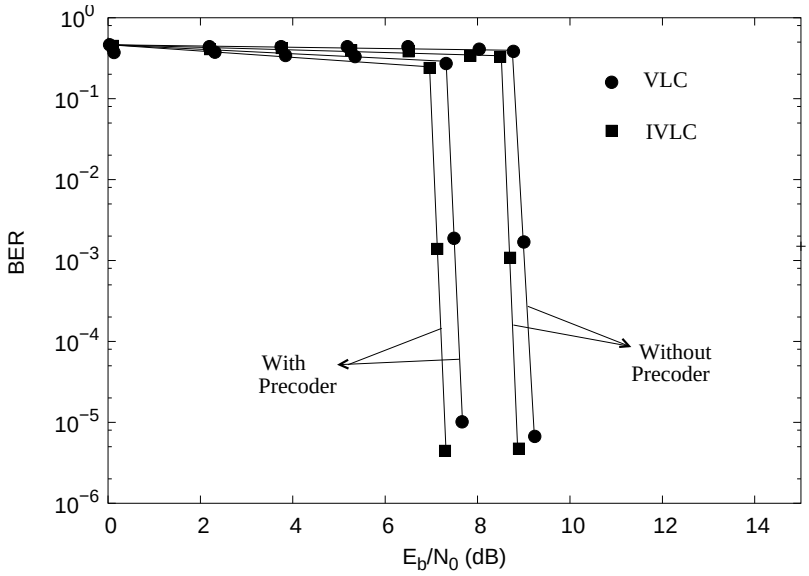

Figure 4.7: BER versus SNR performance of the VLC and IrVLC based schemes, in jammed as well as an interference-free, uncorrelated Nakagami-m fading channels with 30 iterations.

the improvement in BER observed in Figure 4.7 is achieved at the expense of an increased complexity.

4.3.2 Three-Stage Concatenation

In Section 4.3.1 we detailed the concept of two-stage concatenated EI exchange between the unity-rate code's decoder and an IrVLC decoder scheme. In this section we extend this concept to a three-stage architecture constituted by a unity-rate decoder, an IrVLC decoder and the TH-PPM-UWB detector, which will be detailed in the context of Figure 4.8. Again, the technique of EXIT charts is utilized to the best of our knowledge for the first time to design the serial concatenation of the TH-PPM-UWB detector, unity-rate decoder and an IrVLC outer decoder in order to attain a good performance even at near-capacity SNR values. We contrast the two-stage Iterative Decoder (ID) philosophy to that of the three-stage scheme and demonstrate that the three-stage scheme outperforms the two-stage arrangement. The practical rationale of the proposed system design procedure is that the three-stage IrVLC-aided TH-PPM-UWB scheme allows us to accurately shape the EXIT curves in order to create a marginally open EXIT tunnel, which facilitates near-capacity operation as detailed for example in [122, 149].

We advance the design of TH-PPM-UWB systems with the aid of sophisticated channel coding in the interest of approaching the attainable capacity. More specifically, our near-capacity TH-PPM-UWB design exploits the fact that analogous to Irregular Convolutional Coding (ICC) [149], the family of IrVLCs [158] as detailed in Section 4.2.3 employs a number of component VLC codebooks having different coding rates [203] for encoding

particular fractions of the input source symbol stream. The appropriate lengths of these fractions may be chosen with the aid of EXIT charts [116] in order to shape the inverted EXIT curve of the IrVLC codec to ensure that it does not cross the EXIT curve of the inner channel codec. In this way, an open EXIT chart tunnel may be created even at near-capacity values of the SNR.

A powerful technique of enhancing the achieveable iterative detection gain is constituted by precoders, which improve the EI exchange between the channel decoder and the detector [204]. The precoder imposes memory upon the channel, thus resulting in an IIR. Hence, SISO schemes substantially benefit from the employment of low-complexity unity-rate precoders without reducing the effective throughput of the system.

Figure 4.8 is the extension of Figure 4.4 in Section 4.3.1. We have assumed the same UWB TH-PPM impulse radio transceiver model as detailed in Section 4.3.1.1. In this section, we will only highlight the three-stage concatenated model of Figure 4.8 in order to contrast it to Figure 4.4 of Section 4.3.1. The other details of the transceiver can be found in Section 4.3.1.1. The EXIT chart based performance analysis of the three-stage versus two-stage architectures will be presented after the three-stage model's description.

Similarly to the two-stage scheme of Figure 4.4, in Figure 4.8 we assume 16-ary VLC source symbol values obeying a 16-ary discrete PDF resulting from the LM quantization of independent Laplacian distributed source samples. As in the context of Figure 4.4, the symbol probabilities are between 0.002 and 0.16, when considering 4-bit LM quantization. Again, the entropy of the 16 symbols obeying these probabilities lies between 2.6 bits/symbol and 8.74 bits/symbol, with an overall source entropy of 3.5 bits per VLC symbol. The rationale of the proposed IrVLC coding scheme is that given this non-uniform probability of occurance for the 16 VLC symbols, the VLC scheme is capable of data compression as well as of high-integrity detection at near-capacity SNRs.

As for the two-stage arrangement of Figure 4.4, the transmitter shown in Figure 4.8 transmits the source symbol frame $\mathbf{\Theta}$, which comprises J number of source symbols having the $K = 16$-ary values $\{\Theta_j\}_{j=1}^{J} \in [1 \dots K]$. These source symbols are decomposed into N number of components $\{\mathbf{\Theta^n}\}_{n=1}^{N}$, where we opted for $N = 16$ in the case of the IrVLC-TH-PPM-UWB scheme considered and $N = 1$ in the case of the regular VLC-based benchmarker scheme. The number of symbols in the source symbol frame $\mathbf{\Theta}$, which is decomposed into the source symbol frame component $\mathbf{\Theta^n}$ is specified as J^n, where we have $J^1 = J$ in the case of the VLC-based scheme. By contrast, in the case of the IrVLC-based scheme, the specific values of $\{J^n\}_{n=1}^{N}$ may be appropriately chosen in order to shape the inverted EXIT curve of the IrVLC codec, so that it does not cross the EXIT curve of the precoder as detailed in [205].

Each of the N source symbol frame components $\{\mathbf{\Theta^n}\}_{n=1}^{N}$ is VLC-encoded using the cor-

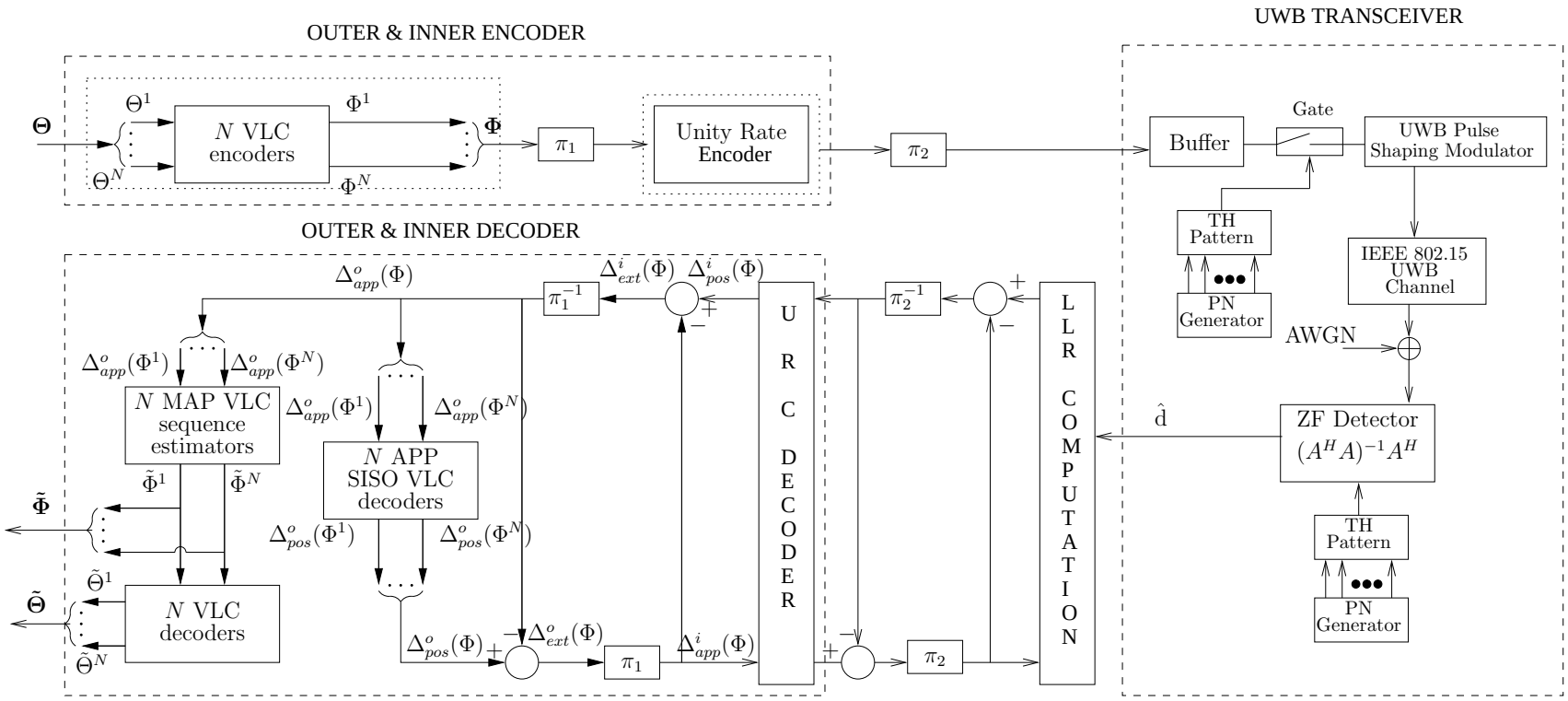

Figure 4.8: Schematic of the IrVLC and VLC-based TH-PPM-UWB schemes. In the IrVLC coded scheme we have $Q = 16$, whilst $Q = 1$ in the VLC-coded scheme.

responding codebook from the set of N VLC codebooks $\{\mathbf{VLC}^n\}_{n=1}^N$, having a range of coding rates $\{R^n\}_{n=1}^N \in [0,1]$. The specific source symbols having the value of $k \in [1 \dots K]$ and encoded by the specific VLC codebook $\mathbf{VLC}^n$ are represented by the codeword $\mathbf{VLC}^{n,k}$, which has a length of $I^{n,k}$ bits. The J^n number of VLC codewords that represent the J^n number of source symbols in the source symbol frame component $\mathbf{\Theta^n}$ are concatenated to provide the transmission frame component $\mathbf{\Phi^n} = \{\mathbf{VLC}^{n,\Theta_{j^n}^n}\}_{j^n=1}^{J^n}$.

Depending on the specific length of the VLC codewords, the number of bits comprised by each transmission frame component $\mathbf{\Phi^n}$ will typically vary slightly from frame to frame. In order to facilitate the VLC decoding of each transmission frame component $\mathbf{\Phi^n}$, it is necessary to explicitly convey its length $I^n = \sum_{j^n=1}^{J^n} I^{n,s_{j^n}^n}$ to the receiver with the aid of side information. The N transmission frame components $\{\mathbf{\Phi^n}\}_{n=1}^N$ encoded by the different IrVLC component codes are concatenated at the transmitter, as shown in Figure 4.8. The resultant transmission frame $\mathbf{\Phi}$ has a length of $\sum_{n=1}^N I^n$ bits. Following the bit interleaver π_1, the transmission frame $\mathbf{\Phi}$ is precoded and then interleaved again by the bit interleaver π_2. The interleaved bits are sent to the buffer depicted in Figure 4.8. These bits are transmitted by the TH-PPM modulator. In the next section, we present the derivation of soft information.

4.3.2.1 Derivation of Soft Information

The LLRs output by the demodulator corresponding to the ith bit b_i, given that $\hat{\mathbf{d}} = \left[d_0, d_1, \dots, d_{M-1}\right]$ is received, which represents the set of M detector outputs in Figure 4.8 may be expressed as [206]

$$\Theta_p^M(i|\hat{\mathbf{d}}) = \log\left[\frac{P_p^M(b_i=1|\hat{\mathbf{d}})}{P_p^M(b_i=0|\hat{\mathbf{d}})}\right], \tag{4.7}$$

where $P(\cdot)$ denotes the probability of an event, the superscript M indicates the M-ary demodulator and the subscript p denotes *a posteriori* probability. In order to compute the LLRs, which represents the set of M outputs of the detector in Figure 4.8, we need the probability that the mth symbol s_m, $m = 0, \dots, M-1$ was transmitted, given that the signal $\hat{\mathbf{d}}$ is received. This probability is given by

$$P_p^M(s_m|\hat{\mathbf{d}}) = \frac{p(\hat{\mathbf{d}}|s_m)P(s_m)}{p(\hat{\mathbf{d}})}, \tag{4.8}$$

where $p(\hat{\mathbf{d}}|s_m)$ is the PDF of the received signal $\hat{\mathbf{d}}$, given that s_m is transmitted. Furthermore, $P(s_m)$ is the *a priori* probability of the symbol s_m, while $p(\hat{\mathbf{d}}) = \sum_{m=0}^{M-1} p(\hat{\mathbf{d}}|s_m)P(s_m)$ is the probability of receiving the signal set $\hat{\mathbf{d}}$, which is independent of $s_m, m = 0, \dots, M-1$, for a given $\hat{\mathbf{d}}$. Moreover, for equiprobable symbols, we have $P(s_m) = 1/M$. Hence, the PDF $p(\hat{\mathbf{d}}|s_m)$ uniquely and unambiguously describes the statistics required for estimating

the probability $P(s_m|\hat{\mathbf{d}})$. For independent fading of the M tones, the PDF $p(\hat{\mathbf{d}}|s_m)$ is given by

$$p(\hat{\mathbf{d}}|s_m) = f_{\hat{d}_m}(x_m|s_m) \prod_{n=0,n\neq m}^{M-1} f_{\hat{d}_n}(x_n|s_m), \tag{4.9}$$

where $f_{\hat{d}_n}(x_n|s_m)$ represents the PDF of the nth diversity combiner output, $n = 0, 1, \ldots, M-1$, given that s_m is transmitted.

We derive the soft information from the channel's output observations, assuming a somewhat simplistic but tractable interference-free channel model. This is because we aim to derive an expression for the soft information, which may be computed using the parameters that may be either known or readily estimated at the receiver. By contrast, if the soft information is derived by considering the presence of PBNJ, the desired expression will be a function of parameters such as the Signal-to-Jammer Ratio (SJR) and the PBNJ duty factor ρ, which are not known at the receiver. Hence, our analysis may result in sub-optimal soft information, but we will nevertheless demonstrate in Section 4.3.3 that valuable performance improvements can be achieved using this approach.

Assuming that s_m is transmitted in the lth hop, it can be readily shown that for independent Rayleigh fading, the PDF of the noise-normalized detector U_{ml} may be expressed as [39]

$$f_{U_{ml}}(y_m|s_m) = \frac{1}{1+\gamma_h} e^{\frac{-y_m}{1+\gamma_h}}, \qquad y_m \geq 0, \tag{4.10}$$

where $\gamma_h = bRE_b/(N_0 L)$ is the SNR per hop, E_b is the transmitted energy per bit and $b = \log_2 M$ is the number of bits per symbol.

Similarly, for all the interfering values associated with $n = 0, 1, \ldots, M-1, n \neq m$, the corresponding PDF is given by

$$f_{U_{nl}}(y_n|s_m) = e^{-y_n}, \qquad y_n \geq 0. \tag{4.11}$$

From Equation 4.10, using the Characteristic Function (CF) approach [39] [1], we can derive the PDF of the linear combiner's output $\hat{d}_m$ seen in Figure 4.8, which can be expressed as

$$f_{\hat{d}_m}(x_m|s_m) = \frac{x_m^{L-1}}{(1+\gamma_h)^L \Gamma(L)} e^{-x_m/(1+\gamma_h)}. \tag{4.12}$$

Similarly, for all the non-signal tones, $n = 0, 1, ..., M-1, n \neq m$ we have

$$f_{\hat{d}_n}(x_n|s_m) = \frac{x_n^{L-1}}{\Gamma(L)} e^{-x_n}. \tag{4.13}$$

Inserting Equations 4.12 and 4.13 in Equation 4.9 and after further simplifications, we have

$$p(\hat{\mathbf{d}}|s_m) = \left[\frac{1}{(1+\gamma_h)^L} \frac{1}{\Gamma^M(L)} \prod_{n=0}^{M-1} x_n^{L-1} e^{-x_n} \right] \exp\left(\frac{x_m \gamma_h}{1+\gamma_h} \right). \tag{4.14}$$

[1] The CF is the Fourier transform of the PDF and we exploited the fact that CF of a sum of random variables is the product of their individual CFs [39].

We can see in Equation 4.14 that all the terms except the last exponential-term are common, for any of the mth symbol, $m = 0, 1, ..., M-1$. Since the computation of the LLRs requires the logarithm of the bit probabilities, we consider the common terms as a normalization factor and express the normalized probability $p(\hat{\mathbf{d}}|s_m)$ as

$$p(\hat{\mathbf{d}}|s_m) = \exp\left(\frac{x_m \gamma_h}{1+\gamma_h}\right). \tag{4.15}$$

Upon inserting Equation 4.14 into Equation 4.8, we can derive the corresponding symbol probabilities. The resultant bit probabilities can be derived from the symbol probabilities, assuming the bits-to-symbol mapping of [207]:

$$P_p^M(b_i = 0|\hat{\mathbf{d}}) = \sum_{t=0}^{M/2-1} P_p^M(s_m|\hat{\mathbf{d}}), \qquad m = t + \lfloor \frac{t}{2^i} \rfloor 2^i, \tag{4.16}$$

where $\lfloor x \rfloor$ represents the largest integer less than or equal to x. Finally, the LLRs Ψ_p^M are computed from the bit probabilities using Equation 4.7 and after subtracting the *a priori* LLRs, the extrinsic LLRs may be fed to the decoder.

In the foregoing analysis, we noted that the knowledge of the receiver's SNR is required in order to compute the symbol probabilities from Equation 4.15. In non-coherent detection aided systems, especially in UWB-TH-IR-PPM, accurate estimation of the channel during a time hopping interval, which is typically a fraction of the symbol interval may not be practicable. However, the SNR may be estimated to a reasonable degree of accuracy by computing a running average of the received AWGN power over a sufficiently large number of say 20, received samples. We assume here that the received SNR is accurately known at the receiver. In the next section, we present the EXIT chart based comparative analysis of the two- and three-stage concatenated schemes.

4.3.3 EXIT Chart Analysis of Two-Stage versus Three-Stage Architectures

In this section, we present the EXIT chart based comparative performance analysis of two- and three-stage concatenated iteratively detected TH-PPM UWB systems using IrVLCs. We have used $N = 16$-component VLC codebooks $\{\mathbf{VLC}^n\}_{n=1}^N$ in the TH-PPM-UWB scheme having approximately equally spaced coding rates in the range of $[0.2, 0.95]$. Moreover, unless otherwise stated, we employ the following parameter values: source symbol frame length of $J = 80,000$, outer code rate of $R = 0.5$, TH-PPM-UWB spreading factor of $M = 16$ and a diversity order of $L = 3$. In each case, we employ a Variable Length Error Correcting (VLEC) codebook [203] that is tailored to the source symbol values' probabilities of occurrence. Again, these codes compress the unequal probability input data symbols for the sake of achieving a near-entropy source-rate and an infinitesimally low BER at near-capacity SNRs. By contrast, in the VLC benchmarker scheme, we employ just $N = 1$ VLC

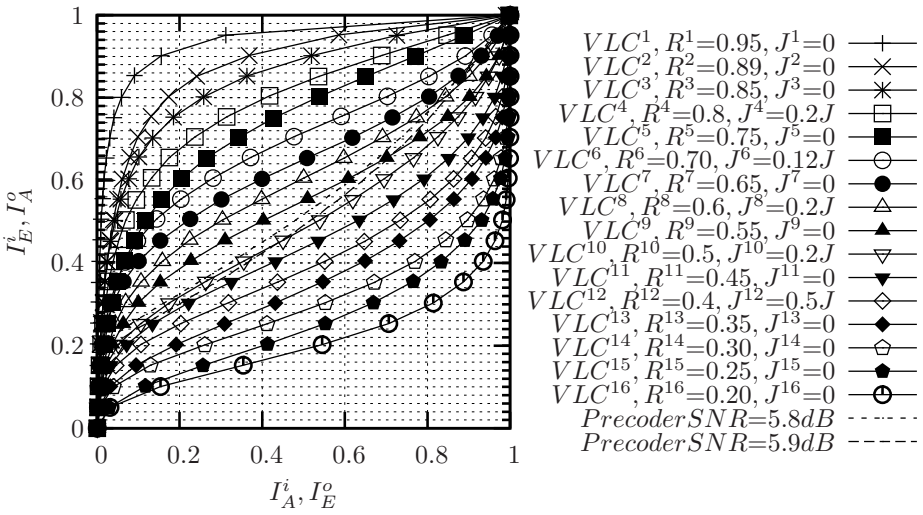

Figure 4.9: Inverted VLC EXIT curves and EXIT curves of the unity rate precoder's decoder assuming an uncorrelated Nakagami-m fading channel.

codebook, which is identical to the VLC codebook $\mathbf{VLC}^{10}$ of the IrVLC scheme, having a coding rate of $R = 0.5$. Note that this coding rate results in an average interleaver length of $J \cdot \frac{E}{R}$ bits.

The inverted EXIT curve of the IrVLC scheme is also shown in Figure 4.9, assuming an uncorrelated Nakagami-m fading channel contaminated by PBNJ characterised by $\frac{E_b}{N_J} =$ 10dB and a jamming factor of $\rho = 0.1$. This was obtained as the appropriately weighted superposition of the $N = 16$ component VLC codebooks' inverted EXIT curves, where the weight applied to the inverted EXIT curve of the component VLC codebook $\mathbf{VLC^n}$ is proportional to the specific number of source symbols employed for encoding J^n [149]. Using the approach of [149], the values of $\{J^n\}_{n=1}^N$ given in Figure 4.9 were designed so that the IrVLC, composite coding rate matches that of our regular VLC benchmarker scheme, namely 0.5. Furthermore, we ensured that the inverted IrVLC EXIT curve did not cross the unity-rate decoder's EXIT curve at $\frac{E_b}{N_0}$ of 5.9dB. We note that only four of the 16 VLC components were indeed activated by the algorithm of [149] in order to encode a non-zero number of source symbols. As shown in Figure 4.9, the presence of an open EXIT chart tunnel implies that an infinitesimally low BER may be achieved by the TH-PPM-UWB scheme for $\frac{E_b}{N_0}$ values above 5.9dB. By contrast, an open EXIT chart tunnel is not afforded for $\frac{E_b}{N_0}$ values below 5.8dB in the case of the VLC-based benchmarker scheme.

Analogous to the IrVLC design of Figure 4.9, we have also designed IrVLC codes for various jamming scenarios in Nakagami-m fading channels in the context of both the two-stage and three-stage ID aided schemes. The design parameter values are listed in Table 4.4, where the relevant minimum values of $\frac{E_b}{N_0}(dB)$ or $\frac{E_b}{N_J}(dB)$ at which an open convergence tunnel is formed are shown alongside the specific fractions of the source symbol frame encoded by each component code of the IrVLC scheme given by $\alpha_n = \frac{J^n}{J}$. Owing to

Channel	S	Convergence Min. Value				$\alpha_n=\frac{J^n}{J}$ values
		IrVLC		VLC		
		The.	Act.	The.	Act.	
Interf. free	2	5.7	5.7	5.9	5.9	[0,0,0,0.18,0,0.12,0, 0.18,0,0,0,0.52,0,0,0,0]
	3	4.7	4.8	5.0	5.1	[0,0,0,0.26,0,0.24,0,0, 0,0,0,0.34,0.13,0.03,0,0]
$\frac{E_b}{N_J}$=10 ρ=0.1	2	6.6	6.7	6.9	7	[0,0,0,0.24,0,0,0,0.22, 0,0.03,0,0.5,0,0,0,0]
	3	5.8	5.9	6.1	6.2	[0,0,0,0,0.18,0,0.27,0,0, 0,0,0,0.55,0,0,0,0]
$\frac{E_b}{N_J}$=10 $\rho = 0.5$	2	9.4	10.4	9.8	10.7	[0,0,0,0.08,0,0.16,0.11, 0,0,0.5,0,0,0,0,0,0]
	3	6.8	7.5	7.9	8.7	[0,0,0,0.13,0,0.32,0,0, 0,0,0,0.55,0,0,0,0]

Table 4.4: Parameter values for the IrVLC based concatenated schemes Figure 4.8.

using a finite-length VLC symbol-interleaver, the Monte-Carlo simulation-based decoding trajectory may not accurately match the EXIT curves. Hence both the EXIT-chart based as well as the Monte-Carlo simulation-based convergence-SNR values are shown in Table 4.4 for both the IrVLC and the VLC schemes. Here the theoretical values imply those predicted by the EXIT chart analysis, while the actual values are those achieved in the symbol-by-symbol Monte Carlo simulations. The code rates of the IrVLC's component codes used in our simulations are $[0.95, 0.89, 0.85, 0.8, 0.75, 0.7, 0.65, 0.6, 0.55, 0.5, 0.45, 0.4,$ $0.35, 0.3, 0.25, 0.2]$.

Figure 4.10 provides the BER performance of both the two-stage and the three-stage schemes versus $\frac{E_b}{N_J}$, assuming $\frac{E_b}{N_0}$=10 dB and ρ=0.5. It becomes explicit from Figure 4.10 that the three-stage scheme yields an improvement of nearly 3 dB over the two-stage IrVLC. The performance gain achieved by the three-stage scheme is at the expense of a slightly higher complexity, imposed by the extra interleaver and decoder. Figure 4.10 demonstrates that the three-stage scheme outperforms the corresponding VLC-based arrangement by 1.1 dB. The effect of reducing the number of iterations in both the two-stage and three-stage schemes is characterized in Figure 4.11. Finally, Figure 4.12 portrays the EXIT curves of the IrVLC and unity-rate decoders as well as the corresponding decoding trajectory, assuming an interference free, uncorrelated Nakagami-m fading channel for an SNR of 5.9dB.

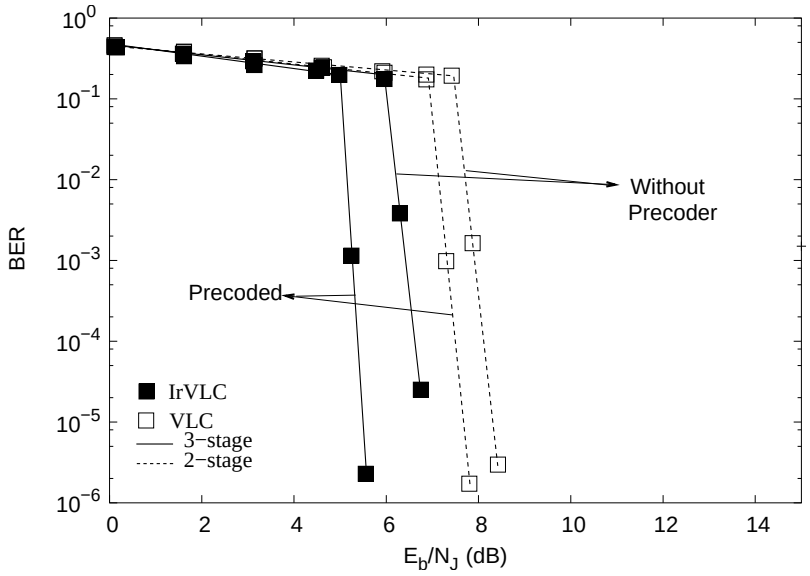

Figure 4.10: BER versus $\frac{E_b}{N_J}$ performance of the two-stage and three-stage VLC and IrVLC based schemes in jammed, uncorrelated Nakagami-m fading channels assuming $\frac{E_b}{N_o}$=10 dB and ρ=0.5.

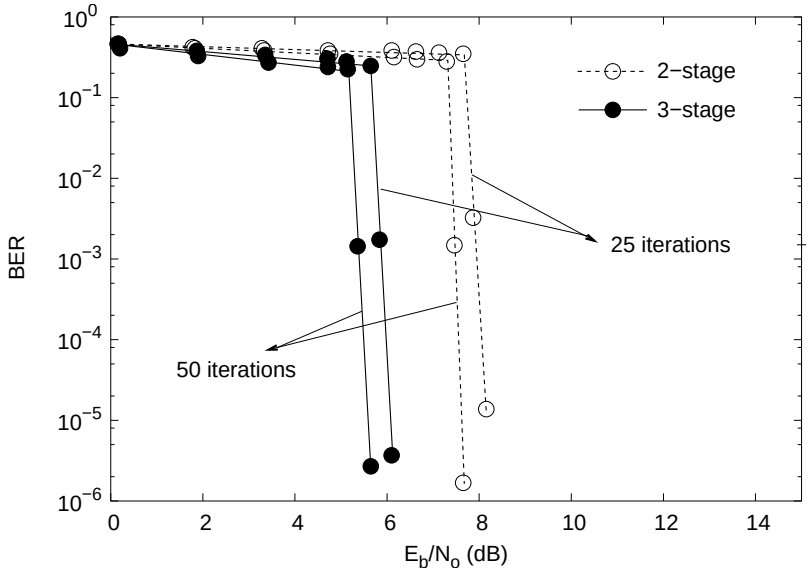

Figure 4.11: BER versus $\frac{E_b}{N_o}$ performance of the two-stage and three-stage VLC and IrVLC based schemes in jammed, uncorrelated Nakagami-m fading channels assuming $\frac{E_b}{N_J}$=10 dB and ρ=0.1.

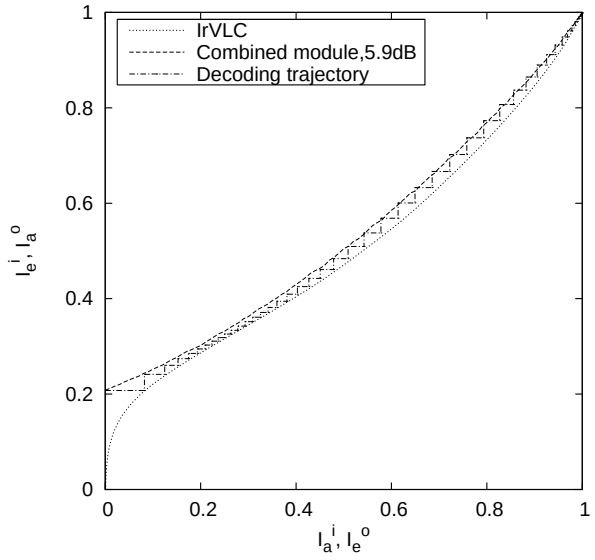

Figure 4.12: IrVLC and Unity-rate decoders EXIT curves as well as decoding trajectory, assuming jammed, uncorrelated Nakagami-m fading channels with ρ=0.1.

4.4 Near-Capacity UWB Design using SeCCCs

The two- and three-stage concatenated UWB systems presented in Sections 4.3.1 and 4.3.2 are capable of providing a near-capacity performance, as discussed in Sections 4.3.1.2 and 4.3.3. However, this is achieved at the cost of an increased complexity and delay, owing to their large interleaver sizes, as presented in Sections 1.5 and 4.1. In this section, we will firstly introduce the concept of binary SeCCC in Section 4.4.1, which will then be used in Section 4.4.3 in order to construct a moderate-complexity near-capacity TH UWB system.

4.4.1 Binary Self-Concatenated Code Design

In this section we will first elaborate on our binary self-concatenated code design, which will be used in the following section to construct a near-capacity TH-PPM-IR-UWB-SeCCC architecture. As part of the prior art, an SeCCC-ID scheme was designed using Trellis Coded Modulation (TCM) as constituent codes with the aid of EXIT charts in [208]. The design proposed in [208] was symbol-based, since the TCM scheme employs a symbol-based MAP algorithm. However, this symbol based MAP algorithm assumes that the bits of a symbol are independent, although in reality this is not the case, because they were FEC-coded before being mapped to the TCM symbols. Given the limited accuracy of this assumption, the system of [208] had the inherent problem of exhibiting a mismatch between the EXIT curve and the bit-by-bit Monte-Carlo simulation based decoding trajectory. To elaborate a little further, the main reason for the mismatch was that the EXIT charts were generated based on the assumption that the *extrinsic* information and the systematic

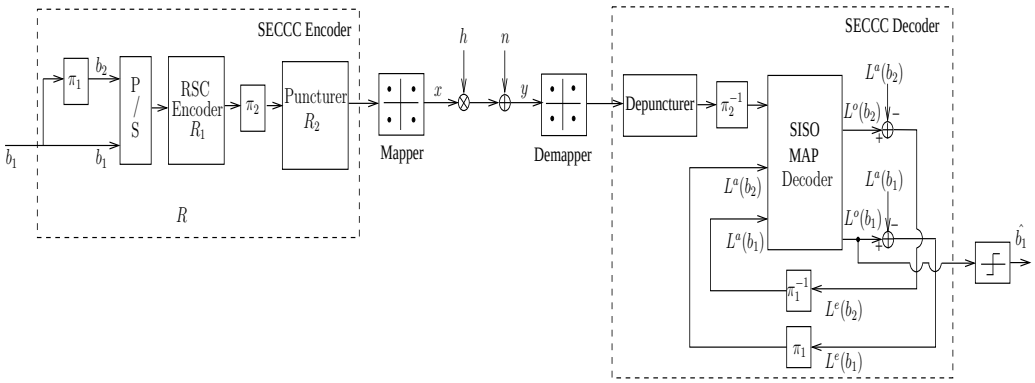

Figure 4.13: SeCCC-ID system

information part of each TCM encoded symbol are independent of each other, which had a limited validity, since both the systematic and the parity bits were being transmitted together as a single 2^{n+1}-ary symbol. Hence, the coded bits in each TCM symbol are correlated [199, 209, 210]. Nonetheless, it was found that the EXIT charts of the symbol-based SeCCC scheme can be beneficially used as upper bounds, since the actual EXIT chart tunnel is always wider than the predicted EXIT chart tunnel. Hence, the analysis was still valid, since it assisted the authors of [208] in finding the minimum E_b/N_o, beyond which decoding convergence was achieved. In the next section, we will demonstrate that the SeCCC is a low-complexity scheme invoking only a single encoder and a single decoder. The EXIT chart based analysis of the iterative decoder provides us with an insight into its decoding convergence behaviour and hence it is helpful for finding the best coding schemes for SeCCCs.

We eliminate the mismatch inherited by the symbol-based design by proposing a bit-based SeCCC-ID design in order to create flexible regular SeCCC schemes capable of efficiently operating over both AWGN and uncorrelated Rayleigh fading channels. EXIT charts are used to characterize the convergence behaviour of these schemes. We will demonstrate that some of the proposed SeCCC schemes perform within about 1 dB from the AWGN and Rayleigh fading channel's capacity [3].

We consider a rate $R = 1/2$ SeCCC scheme as an example to highlight the various system concepts considered in this section. In all the examples we use Gray-coded Quadrature Phase-Shift Keying (QPSK) modulation. Both the AWGN as well as the uncorrelated Rayleigh fading channels are considered. As shown in Figure 4.13, the input bit sequence $\{b_1\}$ of the self-concatenated encoder is interleaved for yielding the bit sequence $\{b_2\}$. The resultant bit sequences are parallel-to-serial converted and then fed to the RSC encoder using the generator polynomials of $G_0 = 13, G_1 = 15, G_2 = 17$, expressed in octal format, while having a rate $R_1 = \frac{1}{3}$ and memory of $\nu = 3$. Hence for every bit input to the SeCCC encoder there are six output bits of the RSC encoder. At the output of the encoder there

is an interleaver and then a rate $R_2 = \frac{1}{3}$ puncturer, which consistently punctures (i.e. does not transmit) two bits out of three encoded bits. Hence, the overall code rate, R can be derived based on [211] as:

$$R = \frac{R_1}{2 \times R_2} = \frac{1}{2}\left(\frac{1}{3\left(\frac{1}{3}\right)}\right) = \frac{1}{2}. \tag{4.17}$$

Therefore, the number of encoded bits at the output of the puncturer is reduced from six to two bits, yielding (c_0c_1). Puncturing of some of the redundant bits is used in order to increase the achievable bandwidth efficiency η. It can be observed that different codes can be designed by changing R_1 and R_2. These bits are then mapped to a QPSK symbol as $x = \mu(c_0c_1)$, where $\mu(.)$ is the Gray-coded bit-to-symbol mapping function. Hence the bandwidth efficiency is given by $\eta = 1$ bit/s/Hz for a Nyquist roll-off-factor of α=0. The QPSK symbol x is then transmitted over the communication channel. At the receiver side of Figure 4.13 the received symbol is given by: $y = hx + n$, where h is the channel's non-dispersive fading coefficient and n is the AWGN having a variance of $\frac{N_0}{2}$ per dimension. This signal is then input to a soft demapper for calculating the conditional PDF of receiving y, when $x^{(m)}$ was transmitted:

$$pdf(y|x^{(m)}) = \frac{1}{\pi N_0} \exp\left(-\frac{\left|y - hx^{(m)}\right|^2}{N_0}\right), \tag{4.18}$$

where $x^{(m)} = \mu(c_0c_1)$ is the hypothetically transmitted QPSK symbol for $m \in \{0, 1, 2, 3\}$. Then the soft-values obeying these PDFs are passed to a soft depuncturer, which converts them to bit-based LLRs and inserts zero LLRs at the punctured bit positions. These LLRs are then deinterleaved and fed to the SISO MAP decoder of Figure 4.13 [212]. A self-concatenated decoder is employed, which first calculates the extrinsic LLRs of the information bits, namely $L_e(b_1)$ and $L_e(b_2)$. Then they are appropriately interleaved to yield the *a priori* LLRs of the information bits, namely $L_a(b_1)$ and $L_a(b_2)$, as shown in Figure 4.13. Self-concatenated decoding proceeds, until a fixed number of iterations is reached. In the next section, we explain the procedure for SeCCC code design of Figure 4.13 using EXIT charts.

4.4.2 Code Design Procedure Using EXIT Charts

Again, EXIT charts constitute a powerful tool designed for analysing the convergence behaviour of concatenated codes without time-consuming bit-by-bit Monte-Carlo simulation of the actual system, as discussed in Section 3.3.1. They analyse the input/output mutual information characteristics of a SISO decoder by modelling the *a priori* LLRs and computing the corresponding mutual information between the extrinsic LLRs and the bit-decisions. However, the employment of EXIT charts assumes having a sufficiently high

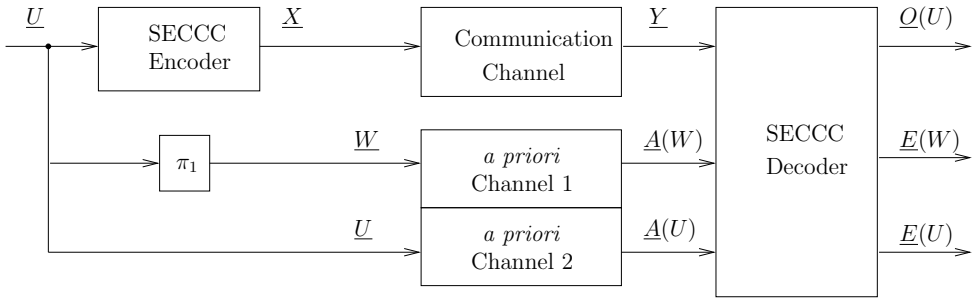

Figure 4.14: Decoding model for an SeCCC-ID scheme [208].

interleaver length, so that the extrinsic LLRs can be rendered independent Gaussian distributed. The SNR value, where the turbo-cliff [167] associated with a sudden drop of the BER curve of a concatenated code appears can be successfully predicted with the aid of EXIT charts.

The decoding model of the SeCCC-ID scheme can be represented by Figure 4.14. The information bit sequence is $\underline{U}$, which is encoded, yielding the coded symbol sequence $\underline{X}$, that is then transmitted over the communication channel. The received symbol sequence is given by $\underline{Y}$, which is then fed to the SISO SeCCC decoder of Figure 4.14. The so-called *a priori* channel models the *a priori* probabilities of the information bit sequence $\underline{U}$ by $\underline{A}(U)$ and its interleaved version $\underline{W}$ by $\underline{A}(W)$. The SeCCC SISO decoder seen in Figure 4.14 then computes both the *a posteriori* bit probabilities $\underline{O}(U)$ and the *extrinsic* bit probabilities $\underline{E}(U)$ and $\underline{E}(W)$. The corresponding EXIT chart plots the *extrinsic* information I_E as a function of the *a priori* information I_A. In the context of SeCCC, I_A is the joint *a priori* information of U and W, and I_E is the joint *extrinsic* information of U and W.

The EXIT charts of self-concatenated codes are typically similar to those of the family of parallel concatenated TTCM schemes [199, 210], where an open EXIT tunnel exists, if the EXIT curve does not intersect with the straight line connecting the point ($I_A = 0$, $I_E = 0$) to the point ($I_A = 1$, $I_E = 1$) in the EXIT chart. In [208] EXIT charts were successfully used to compare the performance of non-binary SeCCC schemes by employing the same method. The various coding schemes considered in this section are characterised in Table 4.5. They are identified by the code rate (R_1), puncturing rate (R_2), overall code rate (R), code memory ν and bandwidth efficiency, expressed in bit/s/Hz, as η. The E_b/N_0 decoding convergence threshold, defined as the E_b/N_o value beyond which the EXIT tunnel becomes 'just' open is denoted by T_h, although this does not necessarily imply that the (I_A, I_E)=(1,1) point of 'perfect convergence' can be reached, because some of the decoding trajectories are curtailed owing to the limited interleaver length used. This is why the slightly different term, namely that of a tunnel T_l was introduced, which specifies the E_b/N_0 value where there is a more widely open EXIT tunnel definitely leading to the (1,1) point. Hence beyond the T_l threshold successful decoding convergence to an

SeCCC-ID Scheme	ν	η (bit/s /Hz)	AWGN Channel E_b/N_0 (dB)			Rayleigh Channel E_b/N_0 (dB)		
			T_h	$T-l$	ω	T_h	T_l	ω
R_1=1/2,R_2=3/4,	2	0.67	1.4	1.6	-0.6	2.6	2.8	1
R=1/3	3	0.67	0.7	0.8	-0.6	1.85	1.95	1
R_1=1/2,R_2=1/2,	2	1	2.3	2.4	0.19	4.6	4.75	1.83
R=1/2	3	1	1.55	1.6	0.19	3.6	3.7	1.83
R_1=1/2,R_2=1/3,	2	1.5	5.4	5.6	2	13.5	13.7	6
R=3/4	3	1.5	3.8	4.0	2	9.3	9.5	6
R_1=1/3,R_2=2/3,	3	0.5	0.4	0.5	-0.8	1.2	1.25	-0.2
R=1/4								
R_1=1/3,R_2=1/3,	3	1	1.5	1.6	0.19	3.6	3.7	1.83
R=1/2								
R_1=1/3,R_2=1/4,	3	1.33	2.7	2.8	1.5	6.5	6.7	3
R=2/3								

Table 4.5: Various SeCCC-ID schemes and their decoding convergence thresholds as well as EXIT tunnels.

infinitesimally low BER value can always be achieved, provided that both the interleaver length and the number of iterations is sufficiently high [116]. Furthermore, the channel capacity limit ω [147] is also expressed in dBs, as tabulated in Table 4.5. For R_1=1/2 and $\nu = 2$, the octally represented generator polynomial of $G = (7, 5)$ was used, whereas for $\nu = 3$, $G = (13, 15)$ was employed. For R_1=1/3 and $\nu = 3$, $G = (13, 15, 17)$ was used.

The EXIT charts recorded for the binary SeCCC-ID schemes characterized in Table 4.5 are shown in Figures 4.15 and 4.16. The two EXIT curves represent the two hypothetical decoder components of the SeCCC scheme, while the stair-case-shaped trajectories represent the iterations between them. Since these are identical components, we only have to compute the EXIT curve of one component and the other is its mirror image with respect to the diagonal line. The EXIT curves of the hypothetical decoder components are plotted within the same EXIT chart together with their corresponding decoding trajectory for the sake of visualizing the exchange of extrinsic information between the decoders. The EXIT curves of the proposed scheme exactly match the decoding trajectories computed from the bit-by-bit simulations.

The EXIT curves along with their corresponding Monte-Carlo simulation-based bit-by-bit decoding trajectory snap-shots recorded for the case of AWGN channels are shown in Figure 4.15 for a $\nu = 2$ RSC code. When employing the $\nu = 2$ RSC code We found that all SeCCC schemes exhibited EXIT curves having similar trends as those in Figure 4.15,

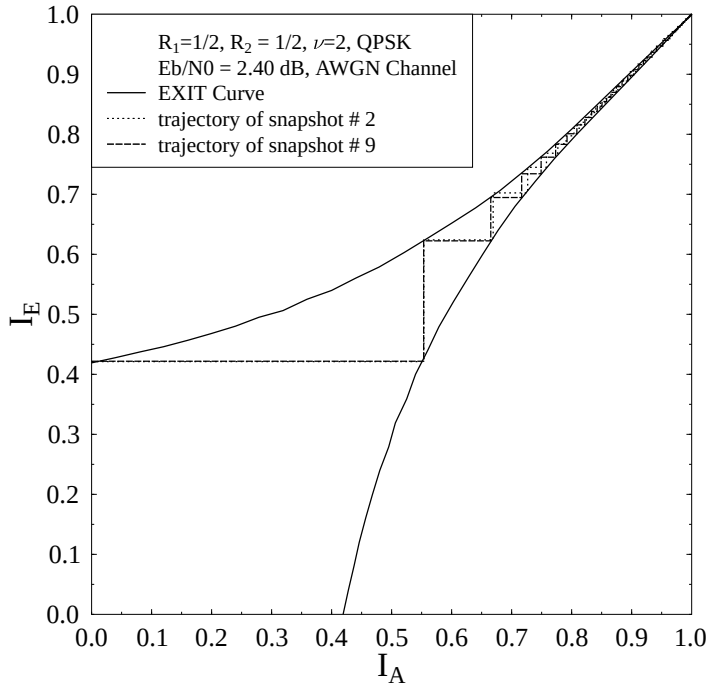

Figure 4.15: EXIT chart and two 'snap-shot' decoding trajectories for R_1=1/2 and R_2=1/2, QPSK-assisted SeCCC-ID, $\nu = 2$, $\eta = 1$ bit/s/Hz at $E_b/N_0 = 2.40$ dB, for transmission over an AWGN channel.

where the EXIT chart tunnel at the top-right corner becomes very narrow. Hence, a higher SNR was required for the decoding trajectory to pass through the marginally open, but narrow tunnel. As a result, their performance tends to be farther away from the channel capacity. For example, for $\nu = 2$, $R_1 = 1/2$ and $R_2 = 1/2$, an open EXIT tunnel emerges at E_b/N_0=2.40 dB. The above-mentioned threshold T_l is shown in Table 4.5 to be at E_b/N_0=2.30 dB, which is 2.11 dB away from capacity. The EXIT curves and the two distinct decoding trajectories were recorded for the best-performing binary SeCCC schemes operating closest to the Rayleigh channel's capacity, which are given in Figure 4.16. These were recorded by using 10^3 transmission frames, each consisting of 24×10^3 information bits for calculating the EXIT curve, and 10^3 frames each consisting of 120×10^3 information bits for calculating the decoding trajectories. The SeCCC scheme employing $R_1 = 1/3$, $R_2 = 2/3$, $\nu = 3$ starts to exhibit an open tunnel at E_b/N_0=1.25 dB, when communicating over uncorrelated Rayleigh fading channels, as shown in Figure 4.16. For this scheme the convergence threshold is at 1.2 dB according to Table 4.5, which is 1.4 dB away from capacity.

The employment of the interleaver, π_1 seen in Figure 4.13 and used in all of the schemes considered in Table 4.5 renders the information bits more-or-less uncorrelated. This is a necessary requirement for the employment of EXIT charts, because they require the LLRs

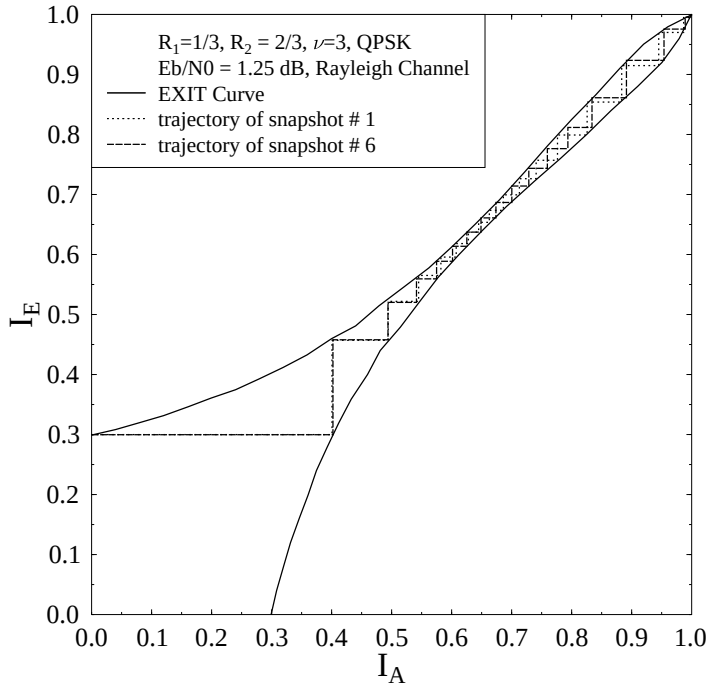

Figure 4.16: EXIT chart and two 'snap-shot' decoding trajectories for R_1=1/3 and R_2=2/3, QPSK-assisted SeCCC-ID, $\nu = 3$, $\eta = 0.5$ bit/s/Hz at $E_b/N_0 = 1.25$ dB, for transmission over a Rayleigh fading channel.

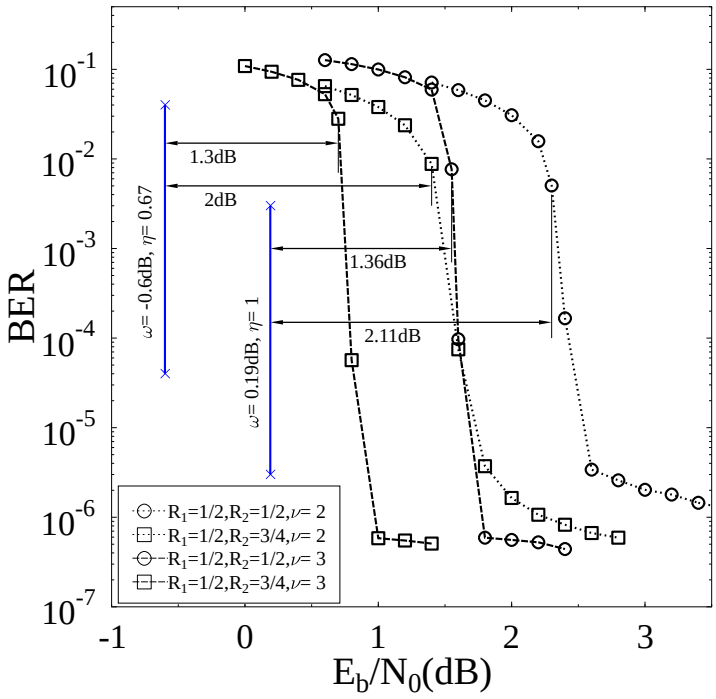

Figure 4.17: The BER versus E_b/N_0 performance of various QPSK-assisted SeCCC-ID schemes, $R_1 = 1/2$ and $I = 80$ decoding iterations for $\nu = 2$ and $I = 50$ decoding iterations for $\nu = 3$, operating over AWGN channel.

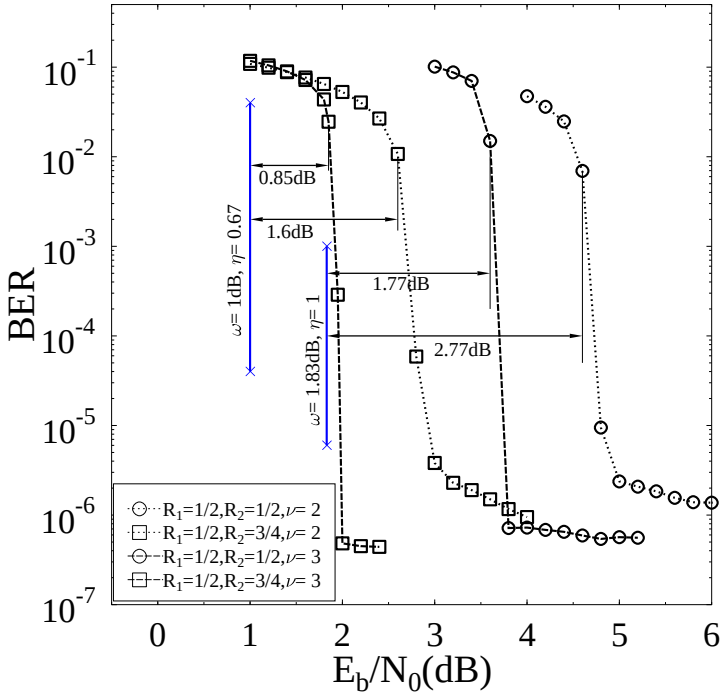

Figure 4.18: The BER versus E_b/N_0 performance of various QPSK-assisted SeCCC-ID schemes, $R_1 = 1/2$ and $I = 80$ decoding iterations for $\nu = 2$ and $I = 50$ decoding iterations for $\nu = 3$, operating over uncorrelated Rayleigh fading channel.

of the information bits to be Gaussian distributed. The interleaver used after the RSC encoder of Figure 4.13, namely π_2, randomises the coded bits before the puncturer.

EXIT charts were used to find the best SeCCC schemes for $\nu = \{2, 3\}$, when communicating over AWGN and uncorrelated Rayleigh fading channels. The convergence threshold predicted by the EXIT chart analysis closely matches the actual convergence threshold observed in the BER curve given by the specified E_b/N_0 value, where there is a sudden drop of the BER after a certain number of decoding iterations, as shown in Figures 4.17 and 4.18. Hence it becomes possible to attain an infinitesimally low BER beyond the convergence threshold, provided that the block length is sufficiently long and the number of decoding iterations is sufficiently high. Again, the BER versus E_b/N_0 performance curves of the various QPSK-assisted SeCCC-ID schemes recorded from our bit-by-bit simulations are shown in Figures 4.17 and 4.18. As mentioned, we considered an information block length of 120×10^3 bits per frame, transmitted 10^3 frames and the number of decoding iterations (I) was varied from 50 to 80. Figures 4.17 and 4.18 show the E_b/N_0 difference between the channel capacity and the above-mentioned convergence threshold T_l for the best SeCCC-ID schemes at a given code memory ν.

It can be observed from Figure 4.17 that by increasing the code memory ν from 2 to 3, in the case of $R_1 = 1/2$ and a higher puncturing rate of $R_2 = 3/4$, there is a 0.7 dB gain and 0.75 dB gain, when communicating over the AWGN and uncorrelated Rayleigh

fading channels, respectively. Similarly, observe from Figure 4.17, that upon increasing ν from 2 to 3, in the case of $R_1 = 1/2$ and $R_2 = 1/2$, there is a 0.75 dB gain and 1 dB gain, when communicating over AWGN and uncorrelated Rayleigh fading channel, respectively. Furthermore, as seen from Figures 4.17 and 4.18, the scheme using $R_1 = 1/2$, $R_2 = 1/2$ and $\nu = 3$ is operating within 1.36 dB and within 1.77 dB from the capacity in case of the AWGN and Rayleigh fading channels, respectively. As observed from Table 4.5, in the case of a lower puncturing rate of $R_2 = 1/3$ and $R_1 = 1/2$, the $\nu = 3$ code performs better compared to the $\nu = 2$ code. Under AWGN channel conditions the gain achieved is 1.6 dB, whereas under Rayleigh fading channel conditions it is 4.2 dB, but even this higher gain is insufficient to approach capacity. For the scheme considered the discrepancy with respect to the capacity of the $\nu = 3$ code is 1.8 dB and 3.3 dB in case of the AWGN and Rayleigh fading channels, respectively. This is due to the fact that the puncturing rate is low. The same trends were observed for lower puncturing rates, such as for example, $R_2 = 1/3$ and $1/4$ in conjunction with $R_1 = 1/3$.

As we can see by studying Table 4.5 and Figures 4.17 and 4.18, the actual BER convergence threshold is exactly the same as the convergence threshold predicted by the EXIT charts. Hence, the binary EXIT chart is useful for finding the best SeCCC-ID schemes for having a decoding convergence at the lowest possible E_b/N_0 value. The best-performing SeCCC schemes were characterized in Figures 4.17 and 4.18, which were found from our EXIT chart based design approach. These codes are summarised in Table 4.5. Observe from the table that they are capable of operating within about 1 dB of the AWGN channel's capacity. For the scheme employing $\nu = 3$, $R_1 = 1/2$ and $R_2 = 3/4$, the distance from capacity is 1.3 dB and 0.85 dB in case of the AWGN and Rayleigh fading channels, respectively. For a bandwidth efficiency of 0.67 bit/s/Hz, the capacity of this scheme was evaluated in [147], which is -0.6 dB and 1.0 dB for the QPSK-based discrete-input AWGN and Rayleigh fading channels, respectively.

4.4.3 Near-Capacity TH-UWB Using SeCCC

In this section, we will use the binary SeCCC scheme detailed in Section 4.4.1 to design a near-capacity TH-PPM based UWB Impulse Radio (IR) system. We contrive the iteratively detected SeCCC arrangements employing powerful design technique of EXIT charts. The Orthogonal Prolate Spheroidal Wave Function (OPSWF) based signalling pulse shapes discussed in Section 2.3.1 are used for the sake of minimizing the Multi-User Interference (MUI) and ISI. Recursive Systematic Convolutional (RSC) codes are employed as constituent codes combined with an interleaver for randomising the extrinsic information exchange between the constituent codes. Furthermore, a puncturer assists us in removing redundant bits, hence increasing the achievable bandwidth efficiency. Iterative decoding is invoked for exchanging extrinsic information between the hypothetical decoder components

at the receiver end. The convergence behaviour of the decoder is analysed with the aid of bit-based EXIT charts. Finally, we propose a novel TH-PPM-UWB-IR-SeCCC system configuration, which is capable of operating within about 0.9 dB of the information-theoretic limits.

Figure 4.19 shows the baseband model of the iteratively detected TH-PPM-UWB-IR-SeCCC system. We have used OPSWF signalling pulses and PPM for transmission over uncorrelated Nakagami-m fading channels. A rate $R = \frac{1}{2}$ SeCCC scheme is combined with the various system components of Figure 4.19. More explicitly, as shown in Figure 4.19, the input bit sequence $\{d_1\}$ of the self-concatenated encoder is interleaved for yielding the bit sequence $\{d_2\}$. The resultant bit sequences are parallel-to-serial converted and then fed to the RSC encoder using the generator polynomials of $(13, 15, 17)$ expressed in octal format and having a rate of $R_1 = \frac{1}{3}$ as well as a memory of $\varphi = 3$. As in the schematic of Figure 4.19 for every bit input to the SeCCC encoder there are six output bits generated by the RSC encoder. At the output of the encoder there is an interleaver and a rate-$R_2 = \frac{1}{3}$ puncturer, which punctures (i.e. obliterates) two bits out of three encoded bits. Hence, the overall code rate, R can be expressed based on [211] as:

$$R = \frac{R_1}{2 \times R_2} = \frac{1}{2}\left(\frac{1}{3\left(\frac{1}{3}\right)}\right) = \frac{1}{2}. \tag{4.19}$$

Therefore, at the output of the puncturer the number of encoded bits is reduced from six to two, namely to $(b_0 b_1)$. Again, puncturing is used in order to increase the achievable bandwidth efficiency η. Different coding schemes can be designed by changing R_1 and R_2 in order to achieve the best possible performance. The bits d seen in Figure 4.19 are then sent to the bit-to-symbol conversion buffer. The resultant symbols are then pulse position modulated, while obeying the OPSWF pulse shapes in order to minimize the effects of ISI and MUI. Finally, the TH-PPM-UWB-IR-SeCCC encoded transmitted signal is formed by invoking a PN generator for creating the required TH patterns obeying the corresponding PPM signalling delays, as shown in Figure 4.19. The resultant transmitted signal was characterized in Section 4.3.1.1.

After transmission over a non-dispersive Nakagami-m fading channel contaminated by AWGN having a variance of $\frac{N_0}{2}$ per dimension, the received signal y is fed into a pulse-position correlation detector, as shown in Figure 4.19. The closed-form matrix description of the receiver was detailed in Section 4.3.1.1. After the TH-UWB-PPM-IR detector of Figure 4.19 the signal $\hat{d}$ is then used by a soft demapper for calculating the conditional PDF of receiving y, when $e^{\{(k),(m)\}}$ was transmitted, where k is the number of users and the set $m \in \{0, 1, 2, 3\}$ represents the legitimate quarternary modulated symbols. Then, the resultant soft-values are passed to a soft depuncturer, which converts them to bit-based LLRs denoted by Λ in Figure 4.19 and zero LLRs are inserted at the punctured bit positions. These LLRs are then deinterleaved and fed to the self-concatenated SISO MAP

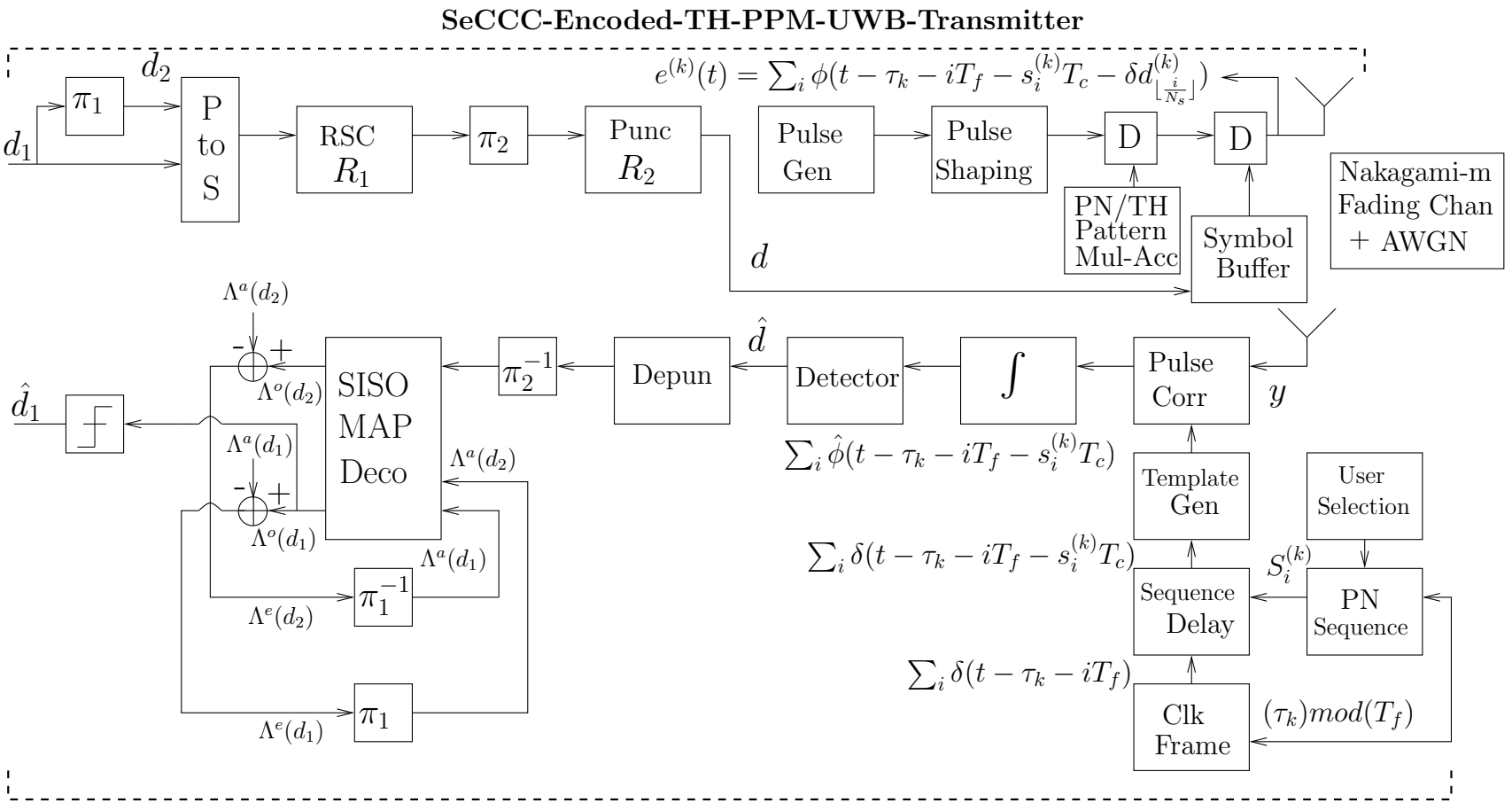

Figure 4.19: TH-PPM-UWB-IR-SeCCC system

decoder [212], which first calculates the extrinsic LLRs of the information bits, namely $\Lambda^e(d_1)$ and $\Lambda^e(d_2)$, that are then appropriately interleaved in order to generate the *a priori* LLRs of the information bits, namely $\Lambda^a(d_1)$ and $\Lambda^a(d_2)$, as shown in Figure 4.19. Self-concatenated decoding proceeds, until the affordable number of iterations is reached. Let us now analyze the performance of the iteratively detected TH-PPM-UWB-IR-SeCCC system of Figure 4.19 with the aid of EXIT charts.

4.4.3.1 EXIT Chart Based Performance Analysis

As detailed in Section 4.4.2, the EXIT charts of self-concatenated codes are typically similar to those of the parallel concatenated TTCM schemes [199, 210], where an open EXIT tunnel exists if the EXIT curve does not intersect the straight line connecting the point ($I_A = 0$, $I_E = 0$) to the point ($I_A = 1$, $I_E = 1$) in the EXIT chart. The various coding schemes considered in this section are characterised in Table 4.6. They are identified by the code rate (R_1), puncturing rate (R_2), overall code rate (R), code memory φ and bandwidth efficiency η expressed in bit/s/Hz. The $\frac{E_b}{N_o}$ decoding convergence threshold, beyond which the EXIT tunnel becomes "just" open is denoted by T_h, although this does not necessarily imply that the (I_A, I_E)=(1,1) point of 'perfect convergence' can be reached, because some of the decoding trajectories are curtailed owing to the limited interleaver length used. Again, this is why the slightly different term, tunnel T_l was introduced, which specifies the $\frac{E_b}{N_o}$ value, where there is a more widely open EXIT tunnel leading to the (1,1) point and where decoding convergence to an infinitesimally low BER value can always be achieved, provided that the interleaver length is large and the number of decoding iterations is sufficiently high [116]. Furthermore, the channel capacity limit ω is also expressed in dBs [147], as tabulated in Table 4.6. For R_1=1/2 and $\varphi = 2$, the octally represented generator polynomial of $G = (7, 5)$ is used, whereas for $\varphi = 3$, $G = (13, 15)$ is employed. For R_1=1/3 and $\varphi = 3$, $G = (13, 15, 17)$ is used.

The EXIT charts recorded for the TH-PPM-UWB-IR-SeCCC system of Table 4.6 are shown in Figure 4.20. The two EXIT curves represent the two hypothetical decoder components of the SeCCC scheme, while the stair-case-shaped trajectory "snap-shots" correspond to iterating between them. Since these are identical components, we only have to compute the EXIT curve of one component and the other is its mirror image with respect to the diagonal line. The EXIT curves of the hypothetical decoder components are plotted within the same EXIT chart together with their corresponding decoding trajectory for the sake of visualizing the transfer of extrinsic information between the decoders. The EXIT curves of the proposed scheme exactly match the decoding trajectories computed from the bit-by-bit simulations.

The EXIT curves and the two distinct decoding trajectories were recorded for the

TH-PPM-UWB-IR-SeCCC System	φ	η (bit/s /Hz)	Nakagami-m Channel E_b/N_0 (dB)		
			T_h	T_l	ω
R_1=1/2,R_2=3/4, R=1/3	2	0.67	2.5	2.7	1
	3	0.67	1.8	1.9	1
R_1=1/2,R_2=1/2, R=1/2	2	1	4.5	4.6	1.83
	3	1	3.5	3.6	1.83
R_1=1/2,R_2=1/3, R=3/4	2	1.5	13	13.6	6
	3	1.5	9.2	9.4	6
R_1=1/3,R_2=2/3, R=1/4	3	0.5	1.2	1.3	-0.2
R_1=1/3,R_2=1/3, R=1/2	3	1	3.5	3.6	1.83
R_1=1/3,R_2=1/4, R=2/3	3	1.33	6.4	6.6	3

Table 4.6: Various TH-PPM-UWB-IR-SeCCC system's decoding convergence thresholds and EXIT tunnels. φ:memory of SeCCC, η:bandwidth efficiency, ω:channel capacity limit and T_h,T_l:convergence threshold

best-performing TH-PPM-UWB-IR-SeCCC system operating closest to the Nakagami-m channel's capacity, which are given in Figure 4.20 for a specific bit-by-bit Monte-Carlo simulation. Similar decoding trajectory snapshots were found for all our simulations. These were recorded by using 10^3 transmission frames, each consisting of 24×10^3 information bits for calculating the EXIT curve, and 10^3 frames each consisting of 120×10^3 information bits for calculating the decoding trajectories, respectively.

In Figure 4.20, the scheme using $R_1 = 1/2$, $R_2 = 3/4$, $\varphi = 3$ succeeds in creating an open EXIT tunnel at $\frac{E_b}{N_o}$=1.9 dB, when communicating over an uncorrelated Nakagami-m fading channel. For this scheme the threshold T_h is reached at 1.8 dB according to Table 4.6, which is 0.8 dB away from capacity. The employment of the interleaver, π_1 seen in Figure 4.13 and used in all of the schemes considered in Table 4.6 renders the information bits more-or-less uncorrelated. This is a necessary condition for the employment of EXIT charts, because they require the LLRs of the information bits to be Gaussian distributed. The interleaver used after the RSC encoder of Figure 4.19, namely π_2, randomises the coded bits before the puncturer.

The EXIT charts of Figure 4.20 were used to find the best TH-PPM-UWB-IR-SeCCC system parameters for $\varphi = \{2, 3\}$, when communicating over uncorrelated Nakagami-m fading channels. The convergence threshold predicted by the EXIT chart analysis, as seen

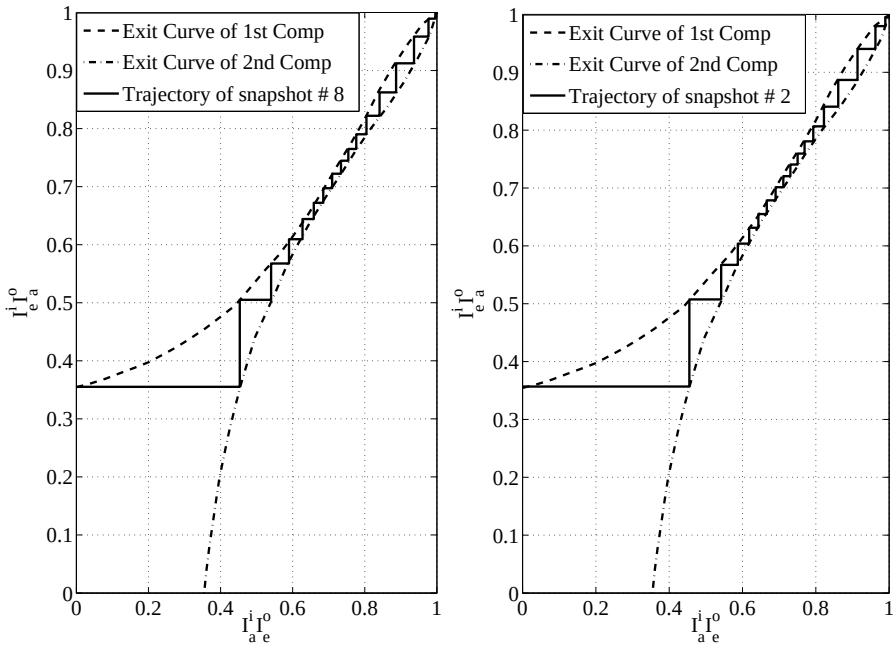

Figure 4.20: EXIT chart and decoding trajectories for R_1=1/2 and R_2=3/4, TH-PPM-UWB-IR-SeCCC, $\varphi = 3$, $\eta = 0.67$ bit/s/Hz at $\frac{E_b}{N_o} = 1.9$ dB, for transmission over a Nakagami-m fading channel.

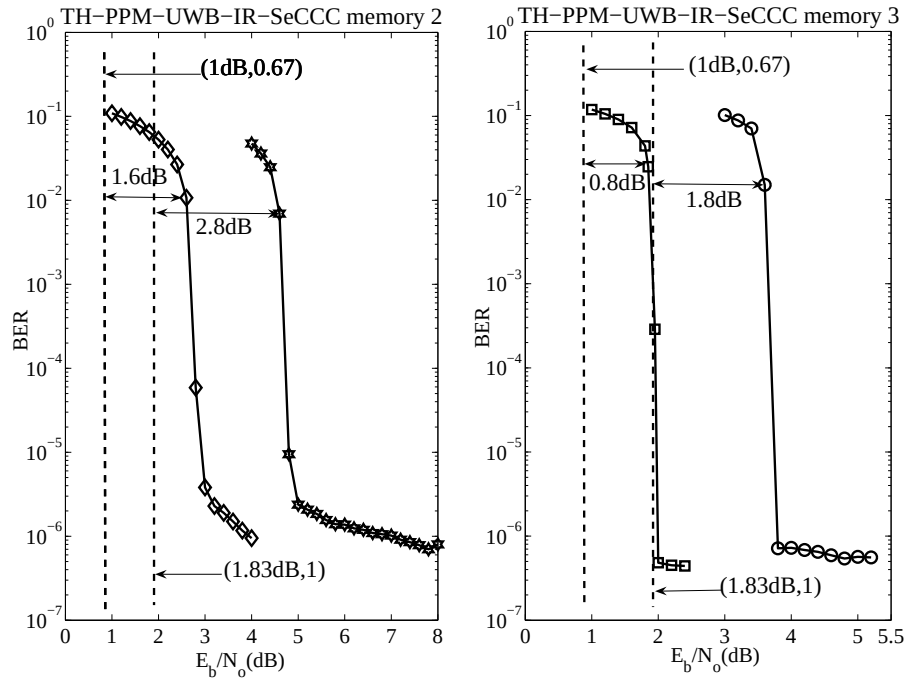

Figure 4.21: The BER versus E_b/N_0 performance of various TH-PPM-UWB-IR-SeCCC system, $R_1 = 1/2$, R_2=3/4 and $I = 80$ decoding iterations for $\varphi = 2$ and $I = 50$ decoding iterations for $\varphi = 3$, operating over uncorrelated Nakagami-m fading channel.

in Figure 4.20, closely matches the actual convergence threshold observed in the BER curve given by the specific $\frac{E_b}{N_o}$ value, where there is a sudden drop of the BER after a certain number of decoding iterations, as shown in Figure 4.21. Hence it becomes possible to attain an infinitesimally low BER beyond the convergence threshold T_h, provided that both the block length and the number of decoding iterations are sufficiently high.

The BER versus $\frac{E_b}{N_o}$ performance curves of the various TH-PPM-UWB-IR-SeCCC systems recorded from our bit-by-bit simulations are shown in Figure 4.21. As mentioned, we considered an information block length of 120×10^3 bits per frame, transmitted 10^3 frames and the number of decoding iterations (I) was varied from 50 to 80. Figure 4.21 shows the $\frac{E_b}{N_o}$ difference between the capacity and the convergence threshold T_h for the best TH-PPM-UWB-IR-SeCCC system at a given code memory φ. It can be observed from Figure 4.21 that the system using $R_1 = 1/2$, $R_2 = 3/4$ and $\varphi = 2$ is capable of operating within 1.6 dB and 2.8 dB of the Nakagami-m fading channel's capacity, respectively. As observed from Table 4.6, in the case of a lower puncturing rate yielding a code rate of $R_2 = 1/3$ and $R_1 = 1/2$, the memory $\varphi = 3$ code performs better compared to the $\varphi = 2$ code.

As we can see by studying Table 4.6 and Figure 4.21, the actual BER convergence threshold is exactly the same as the convergence threshold predicted by the EXIT charts. Hence, the binary EXIT chart is useful for finding the best TH-PPM-UWB-IR-SeCCC system parameter required for attaining a decoding convergence at the lowest possible $\frac{E_b}{N_o}$ value. The best-performing SeCCC schemes characterized in Figure 4.21 and found from the EXIT chart based design approach are summarised in Table 4.6, which are capable of operating within about 0.9 dB of the AWGN channel's capacity. For the scheme employing $\varphi = 3$, $R_1 = 1/2$ and $R_2 = 3/4$ and characterized in Table 4.6, the distance from capacity is 0.8 dB and 1.8 dB in case of Nakagami-m fading channels. For a bandwidth efficiency of 0.67 bit/s/Hz, the capacity of this scheme [147] is -0.6 dB and 1.0 dB for the quarternary discrete-input AWGN and Nakagami-m fading channels, respectively.

4.5 Chapter Conclusions

The conclusive findings of the chapter are:

- In Section 4.3.1 we conceived a two-stage iteratively detected IrVLC code design for UWB TH spread-spectrum impulse radio communicating over Nakagami-m fading channel. EXIT charts were used to analyse the serial concatenation of a unity rate decoder and the IrVLC outer decoder in order to achieve an improved performance at low SNR values.The IrVLC TH-PPM-UWB design provides an additional performance gain of up to 0.45dB over the regular VLC-based benchmark scheme, as detailed in Section 4.3.1.2.

- In addition to this two-stage scheme we have also investigated a three-stage concatenated of the TH-PPM-UWB arrangement constituted by a unity-rate decoder, the outer IrVLC decoder and an iterative zero forcing detector using 2-D EXIT charts in Section 4.3.2. We noted that the precoder-aided scheme yields a gain of about 6.9 dB over the system operating without a precoder, since an open EXIT chart tunnel may be created at low SNR values. Moreover, the three-stage scheme performs 2.9 dB better than the corresponding two-stage scheme, as quantified in Section 4.3.3.

- Finally, we have designed near-capacity SeCCC-ID schemes based on their decoding convergence analysis provided in Section 4.4. The SeCCC-ID schemes designed are capable of operating within about 1 dB from the AWGN as well as Rayleigh fading channel's capacity, as detailed in Section 4.4.2. Based on this design, a near-capacity TH-PPM-UWB-IR system was proposed in Section 4.4.3, which invoked iteratively detected SeCCCs and employed the powerful design technique of EXIT charts. The convergence behaviour of the decoder was analysed with the aid of bit-based EXIT charts. Finally, in Section 4.4.3.1 we proposed a novel TH-PPM-UWB-IR-SeCCC system configuration, which is capable of operating within about 0.9 dB of the information-theoretic limits.

4.6 Chapter Summary

in Section 4.3.1, an IrVLC scheme was designed for a serial concatenated two-stage and iteratively decoded TH-PPM UWB SS impulse radio system. The proposed design is capable of low-SNR operation in Nakagami-m fading channel's. A number of component VLC codebooks having different coding rates were invoked by the IrVLC scheme for encoding specific fractions of the input source symbol stream. EXIT charts were used to appropriately select these fractions in order to shape the inverted EXIT curve of IrVLC scheme according to the EXIT curve of the inner decoder.

In Section 4.3.2 we extended the concept of two-stage EI exchange between the unity-rate code's decoder and an IrVLC decoder to a three-stage scheme constituted by a unity-rate decoder, an IrVLC decoder and the TH-PPM-UWB detector. Again, EXIT charts were utilized to design the serial concatenation of the TH-PPM-UWB detector, unity-rate decoder and an IrVLC outer decoder in order to attain a better performance than the two-stage scheme of Section 4.3.1 as shown in Section 4.3.3. The practical rationale of the proposed system design procedure is that the three-stage IrVLC-aided TH-PPM-UWB scheme allows us to accurately shape the EXIT curves in order to create a marginally open EXIT tunnel, which facilitates near-capacity operation.

Furthermore, in Section 4.4.1 we invoked binary self-concatenated convolutional codes

employing iterative decoding for communicating over both uncorrelated Rayleigh fading and AWGN channels. Recursive systematic convolutional codes were selected as constituent codes and an interleaver was used for randomising the extrinsic information exchange of the constituent codes, while a puncturer assisted us in adjusting the bandwidth efficiency. At the receiver, self-iterative decoding was invoked for exchanging extrinsic information between the hypothetical decoder components. The convergence behaviour of the decoder was analysed with the aid of bit-based EXIT charts. Finally, we proposed an attractive system configuration, which is capable of operating within about 1 dB of the information-theoretic limits in Section 4.4.2.

Based on the design of the SeCCCs of Section 4.4.1, in Section 4.4.3 we constructed an iteratively decoded near-capacity TH-PPM-UWB-IR-SeCCC system using EXIT charts. More explicitly, the powerful tool of EXIT charts was used to appropriately select the coding rates of the SeCCCs in order to shape the inverted EXIT curve of the TH-PPM-UWB-IR-SeCCC system and hence to match it to that of the inner decoder for the sake of achieving an infinitesimally low BER at near-capacity SNR values. The associated iterative decoding convergence behaviour was characterized by EXIT charts. In Section 4.4.3.1 we demonstrated that the proposed TH-PPM-UWB-IR-SeCCC design became capable of performing within about 0.9 dB of the Nakagami-m fading channel's capacity.

Chapter 5

Conclusions and Future Research

In this concluding chapter, we will first provide our overall summary and conclusions in Section 5.1. Then a range of topics concerning potential future research ideas will be presented in Section 5.2.

5.1 Summary and Conclusions

In this thesis, we have provided detailed transceiver designs employing novel channel coding schemes for enhancing the achievable performance of UWB systems. After a brief historical perspective on UWB systems, we have commenced with the characterization of an uncoded UWB system benefiting from different diversity orders, as the first step in the evolutionary improvement of this model towards more sophisticated channel coded UWB systems in order to attain a near-capcity performance, as shown in Figure 1.7.

- **Chapter 1:** Chapter 1 has presented a brief historical and literature survey of UWB systems in Section 1.1. Then we have detailed the basic architecture of UWB transceivers in order to provide a rudimentary introduction to UWB transmission and detection in Section 1.2. Furthermore, multiple access techniques, which are frequently used in UWB systems were highlighted in Section 1.3. Finally, we have outlined the novelty and the structure of the thesis in Sections 1.4 and Section 1.5, respectively. Section 1.5 has also provided the road-map of the thesis, outlining the inter-dependencies of the chapters and their corresponding sections. Each chapter constitutes an evolutionary improvement of the previous chapter.

- **Chapter 2:** We have commenced in Chapter 2 with a detailed statistical characterization of UWB channels in Section 2.2 based on the past scientific advances presented

in Section 2.1. Then, we have used the UWB channel overview of Section 2.2 in order to present their generic z-domain DTTF estimation, which required no channel sounding sequence transmission and hence constituted a blind technique. This was achieved by estimating the CIR with the aid of the information signalling pulses and then equalizing the effects of the channel by the corresponding inverse system. Then we have presented the architecture of a memory-efficient equalizer based on the z-domain transfer function and difference equation presented in Section 2.3. The proposed equalizer attained exactly the same BER performance as the conventional equalizer, despite requiring only half the memory, as demonstrated against the benchmarker designs provided in [1], [77]. The background of Sections 2.2 and 2.3 was then used in order to provide a tangible quantitative characterization of the UWB channel's stability in Section 2.5. More explicitly, a general LTI-UWB-CIR model was investigated. Since the s-domain and z-domain transfer function corresponding to the UWB CIR has an extremely high number of singularities, it is not automatically guaranteed that none of the poles falls on the right-half of the s-plane or outside the unit-circle of the z-plane. Hence the stability analysis necessitates the exhaustive testing of this well-established stability criterion for a potentially excessive number of poles. We circumvented this arduous task by developing the closed-form time-domain response of the so-called homogenous, non-homogenous and vectorial LTI system, which directly demonstrated the potential instabilities. Furthermore, the normalized settling time of the step response was evaluated for diverse damping coefficients. In Section 2.5.4, a stability case-study was provided with the aid of Nichols charts. Finally, in the Section 2.6, we have provided a rigorous analysis and derived the expression of the MCB designed for UWB-TH-IR adaptive equalization. When the adaptive equalizer's step size parameter μ satisfied the *necessary and sufficient* convergence bound condition, no instabilities were observed. However, if μ exceeds the upper bound frequent, instabilities may be observed. The UWB channel model was then used by all the following chapters, when developing enhanced UWB systems.

- **Chapter 3:** Chapter 3 started with the implications of appropriate diversity order selection in an uncoded UWB system in Section 3.2. We quantified the effects of the UWB channel on an uncoded TH-IR system as a function of the diversity order. We have selected the L strongest MPCs from the N_r resolvable MPCs using MRC in order to achieve the maximum attainable performance gain in both single and full-load multiuser scenarios. Three classic detectors have being used, namely the correlation, the ZF and the MMSE detector. Our results suggested that the diversity order $L = 20$ achieved a gain of 18dB and 12dB in single and full-load $N_u = 63$ user scenarios, when

having a spreading factor of $N_s = 63$ over the no-diversity configuration. Hence, MPCs with delays higher than the TH chip time T_c were assumed to be resolved by the TD synchronization. However, as detailed in Section 3.3, the number of resolvable MPCs that can be utilized for diversity reception was limited by the affordable power consumption transceiver complexity [15, 39]. Therefore we are unable to increase the number of resolvable paths beyond a certain limit. Hence, we have provided an alternative solution for this problem by constructing a channel-coded UWB design, which invoked iterative detection to achieve an improved performance in comparison to that of the system detailed in Section 3.2.1. This was our first coded UWB model in the thesis, which was further improved in subsequent chapters in order to enhance the system's performance. More explicitly, a novel UWB-DS-CDMA aided system was designed for the IEEE 802.15.3a UWB channel specifications, which employed serially concatenated channel encoding combined with a URC. We compared the achievable performance of the iterative correlation and MMSE detectors that were capable of exchanging extrinsic information between the URC's decoder as well as the outer RSC code's decoder. Moreover, the iterative decoding convergence analysis of the proposed system was carried out with the aid of EXIT charts. As expected, the iteratively decoded fully-loaded system employing MMSE detection outperformed its counterpart employing the lower-complexity correlation detector. Explicitly, the UWB-DS-CDMA system using the MMSE detector attained a BER of 10^{-5} at $\frac{E_b}{N_o} = 2dB$, when supporting $N_u = 32$ users employing $i = 12$ decoding iterations, while the same system using the correlation detector operated at BER of 10^{-1}. Finally, a comprehensive comparative study of the DS-CDMA and TH-PPM UWB systems considered was presented in Section 3.4. A DS-CDMA and a TH-PPM UWB system were analyzed with the aid of EXIT charts using the same iterative detection scheme, as detailed in Section 3.3.2. Under the same user load, channel and diversity-order conditions, the performance of both systems was analyzed using the area properties of EXIT charts [107, 116, 129]. This analysis was important, since the best performing multiple access technique was used in the subsequent chapters for designing near-capacity UWB systems. In Section 3.4 the analysis of the decoding convergence of TH and DS-CDMA UWB systems communicating over multipath Nakagami channels was presented. The analysis was based on EXIT charts, where the UWB systems considered were either a serially concatenated pulse-position modulated TH or a code-synchronous DS-CDMA arrangement. It was shown by our EXIT chart analysis that the increased multipath diversity is capable of creating a larger area under the EXIT curve of the inner detector. This area is related to the achievable rate of the system and it can be exploited with the aid of iterative detection. The EXIT chart results of the iteratively detected TH and DS-CDMA UWB schemes were verified by the BER results. It was concluded that under the single-user senario, the scheme based

on the iterative TH-UWB system achieves a higher attainable rate than the iterative DS-UWB system. Explicitly, the areas under the EXIT chart curves of the TH-based detector and the DS-based detector were $A_E^{\mathrm{TH}} = 0.57$ and $A_E^{\mathrm{DS}} = 0.56$, respectively. Since we have $A_E^{\mathrm{TH}} > A_E^{\mathrm{DS}}$, the iterative TH-based system attained a convergence tunnel at a slightly lower SNR value.

- **Chapter 4:** Chapter 3 covered the basic structure of the channel coded UWB system model using regular FEC encoders with the aid of EXIT charts. Naturally, the coded UWB system provided a better performance than its uncoded counterpart but the inability of regular FEC encoders to arbitrarily approach the UWB system's capacity was also demonstrated. Chapter 4 addressed this problem by using IrVLCs [157, 158] in both two and three-stage concatenated iteratively detected UWB-TH-PPM-IR in order to approach the UWB system's capacity. The two-stage IrVLC scheme designed for our serially concatenated and iteratively decoded TH-PPM-UWB-SS-IR system was considered in Section 4.3.1. The proposed design was capable of low-SNR operation in Nakagami-m fading channels. A number of component VLC codebooks having different coding rates were utilized by the IrVLC scheme for encoding specific fractions of the input source symbol stream. EXIT charts were used to appropriately select these fractions in order to shape the inverted EXIT curve of the IrVLC scheme according to the EXIT curve of the inner decoder. The proposed scheme achieved a near-zero BER at low SNR values. This IrVLC based scheme provided a gain of up to 0.45 dB over the identical-rate single-class VLC based scheme. Then, in Section 4.3.2 we extended the concept of two-stage concatenation as outlined in Section 4.3.1. Hence the EI exchange between the URC's decoder and the IrVLC decoder was extended to a three-stage scheme constituted by a URC decoder, an IrVLC decoder and the TH-PPM-UWB detector. We contrasted the two-stage arrangement to the three-stage scheme and demonstrated that the three-stage scheme outperformed the two-stage arrangement. The practical rationale of the proposed system design procedure was that the three-stage IrVLC-aided TH-PPM-UWB scheme allows us to accurately shape the EXIT curves in order to create a marginally open EXIT tunnel, which facilitated near-capacity operation. Explicitly, the three-stage scheme performed 2.9 dB better than the corresponding two-stage scheme. Both the two and three-stage concatenated UWB systems have provided a near-capacity performance, however at the cost of an increased complexity and interleaver sizes. Hence in Section 4.4 we have constructed a reduced-complexity near-capacity TH-UWB system using SeCCCs, our novel TH-PPM-UWB-IR-SeCCC system configuration was capable of operating within about 0.9 dB of the information-theoretic limits.

5.2 Future Work

In this section, we briefly discuss a few future research ideas.

5.2.1 Multi-Stage Fast Frequency Hopping UWB Systems

Frequency hopping (FH) constitutes a powerful spread spectrum technique, which has historically been used for combatting intentional jamming or interference. In FH systems, the carrier frequency is hopped in a pseudo-random fashion across a large set of legitimate frequencies under the control of a random sequence generator. This perpetual hopping of the transmitted frequency renders the system robust against interference and jamming. In [213], an UWB system using multistage Fast Frequency Hopping (FFH) was proposed, where a high number of users was divided into a number of reduced-size subgroups. By virtue of allocating multiple users to small FH groups, the proposed system guaranteed reducing the interference among the various users and thus significantly improved the BER performance. We will investigate this novel alternative UWB [213] system in conjunction with various novel channel-coded schemes, in order to further enhance its performance and thus design a system capable of supporting a large number of users.

5.2.1.1 Successive Interference Cancellation in Multi-Stage Fast Frequency Hopping UWB Systems

A SISO decoding aided Successive Interference Cancellation (SIC) scheme will be considered in FFH UWB using Product Combining (PC), when operating in Multiple Access (MA) UWB channels. The M-ary source symbols of the users will be encoded using IrVLCs and the encoded symbols will be transmitted using FFH-MFSK modulation. A soft metric will be proposed for the IrVLC scheme. In the context of the proposed SIC scheme, the receiver will exploit the soft information fed back by the IrVLC decoder to the demodulator in order to cancel the interference imposed by the reliably detected symbols.

5.2.1.2 Iteratively Decoded FFH UWB Using LDPCs

Serially concatenated and iteratively decoded Low-density Parity Check Codes (IrVLC) combined with precoded FFH-UWB will be considered. The proposed channel coding scheme is expected to be capable of low-SNR operation in UWB channels contaminated by PBNJ. All user's M-ary source symbols will be encoded using non-binary LDPC codes and the encoded symbols will be transmitted using FFH-UWB modulation. The performance of the proposed schemes will be evaluated and compared to that of Fiebig's scheme, when the FFH-UWB system operates in a UWB channels.

5.2.1.3 Diversity Combining for FFH-UWB Subjected to UWB Channel Fading

The achievable performance of various diversity combining schemes used in FFH-UWB systems operating in a multiple access scenario subjected to UWB channel fading will be investigated. Specifically, linear, self-normalization based hard-limiting majority vote, soft limiting, product combining and order statistics-normalized envelope detection based diversity combining schemes will be considered. The comparison of various diversity combining schemes will be based on the achievable bit error rate versus the number of simultaneous users supported.

Appendix A

Karhunen-Loeve Transform

The Karhunen-Loeve Transform (KLT) (also known as Hotelling Transform and Eigenvector Transform) [49], which is closely related to the Principal Component Analysis (PCA) and widely used in data analysis in many fields. Let ϕ_k be the eigenvector corresponding to the kth eigenvalue λ_k of the covariance matrix $\mathbf{\Sigma}_g$, i.e.,

$$\mathbf{\Sigma}_g \phi_k = \lambda_k \phi_k \qquad (k = 0, \cdots, N-1). \tag{A.1}$$

As the covariance matrix $\mathbf{\Sigma}_g = \mathbf{\Sigma}_g^T$ is symmetric (Hermitian if $\mathbf{g}$ is complex), its eigenvector ϕ_i's are orthogonal. And we can construct an $N \times N$ orthogonal (unitary) matrix $\mathbf{\Phi}$ satisfying

$$\mathbf{\Phi}^T \mathbf{\Phi} = \mathbf{I} \quad \Longrightarrow \quad \mathbf{\Phi}^{-1} = \mathbf{\Phi}^T. \tag{A.2}$$

The N eigen equations above can be combined to be expressed as:

$$\mathbf{\Sigma}_g \mathbf{\Phi} = \mathbf{\Phi} \mathbf{\Lambda}, \tag{A.3}$$

where $\mathbf{\Lambda}$ is a diagonal matrix $\mathbf{\Lambda} = diag(\lambda_0, \cdots, \lambda_{N-1})$. Left multiplying $\mathbf{\Phi}^T = \mathbf{\Phi}^{-1}$ on both sides, the covariance matrix $\mathbf{\Sigma}_x$ can be diagonalized:

$$\mathbf{\Phi}^T \mathbf{\Sigma}_g \mathbf{\Phi} = \mathbf{\Phi}^{-1} \mathbf{\Sigma}_g \mathbf{\Phi} = \mathbf{\Phi}^{-1} \mathbf{\Phi} \mathbf{\Lambda} = \mathbf{\Lambda}. \tag{A.4}$$

Now, given a signal vector $\mathbf{g}$, we can define the orthogonal (unitary if $\mathbf{g}$ is complex) Karhunen-Loeve Transform of $\mathbf{g}$ as:

$$\mathbf{y} = \mathbf{\Phi}^T \mathbf{x}. \tag{A.5}$$

Appendix B

The Leibniz Integral *(General Form)*

Differentiation under the integral sign is a useful operation in the mathematical field of calculus [93]. Explicitly, when assuming

$$F(x) = \int_{a(x)}^{b(x)} f(x,t)\,dt, \quad \text{where } x_0 \le x \le x_1, \tag{B.1}$$

and that if $f(x,t)$, and $\frac{\partial}{\partial x}, f(x,t)$, are continuous in both t, and x, in some region of the (t,x), plane, including $a(x) \le t \le b(x)$, $x_0 \le x \le x_1$ and if $a(x)$, and $b(x)$, are continuous and have continuous derivatives for $x_0 \le x \le x_1$, then we have

$$\begin{aligned} \frac{d}{dx}F(x) &= \left(\frac{\partial F}{\partial b}\right)\frac{db}{dx} - \left(\frac{\partial F}{\partial a}\right)\frac{da}{dx} + \int_{a(x)}^{b(x)} \frac{\partial}{\partial x} f(x,t)dt \\ &= f(x,b(x))b'(x) - f(x,a(x))a'(x) + \int_{a(x)}^{b(x)} \frac{\partial}{\partial x} f(x,t)\,dt. \end{aligned} \tag{B.2}$$

for $x_0 \le x \le x_1$. This formula is the general form of the Leibniz integral rule and can be derived using the fundamental theorem of calculus. The fundamental theorem of calculus is just a particular case of the above formula, for $a(x) = a$, a constant, $b(x) = x$, and $f(x,t) = f(t)$.

Appendix C

Similarity Transformation

The term similarity transformation [85] is used either to refer to a geometric similarity, or to a matrix transformation that results in a similarity.

A similarity transformation is a conformal mapping whose transformation matrix $\mathbf{A}'$ can be written in the form

$$\mathbf{A}' \equiv \mathbf{BAB}^{-1}, \tag{C.1}$$

where $\mathbf{A}$ and $\mathbf{A}'$ are called similar matrices. Similarity transformations transform objects in space to similar objects. Similarity transformations and the concept of self-similarity are important foundations of fractals and iterated function systems.

The determinant of the similarity transformation of a matrix is equal to the determinant of the original matrix

$$\begin{aligned} |\, \mathbf{BAB}^{-1} \,| &= |\, \mathbf{B} \,||\, \mathbf{A} \,||\, \mathbf{B}^{-1} \,| \\ &= |\, \mathbf{B} \,||\, \mathbf{A} \,| \, \frac{1}{|\, \mathbf{B} \,|} \\ &= |\, \mathbf{A} \,| \,. \end{aligned} \tag{C.2}$$

The determinant of a similarity transformation minus a multiple of the unit matrix is given by

$$\begin{aligned} |\, \mathbf{B}^{-1}\mathbf{AB} - \lambda\mathbf{I} \,| &= |\, \mathbf{B}^{-1}\mathbf{AB} - \mathbf{B}^{-1}\lambda\mathbf{IB} \,| \\ &= |\, \mathbf{B}^{-1}(\mathbf{A} - \lambda\mathbf{I})\mathbf{B} \,| \\ &= |\, \mathbf{B}^{-1} \,||\, \mathbf{A} - \lambda\mathbf{I} \,||\, \mathbf{B} \,| \\ &= |\, \mathbf{A} - \lambda\mathbf{I} \,| \,. \end{aligned} \tag{C.3}$$

Glossary

ACL	Auto-CorreLation
AWGN	Additive White Gaussian Noise
BER	Bit Error Ratio
BICM	Bit Interleaved Coded Modulation
BLMS	Block Least Mean Square
BPAM	Binary Pulse Amplitude Modulation
BPE	Blind Polarimetric Equalization
BW	BandWidth
BWRC	Berkeley Wireless Research Center
CC	Concatenated Codes
CCL	Cross-CorreLation
CDMA	Code Division Multiple Access
CF	Characteristic Function
CIR	Channel Impulse Response
Corr	Correlation
CTF	Channel Transfer Function
DARPA	Defense Advanced Research Projects Agency
DFE	Decision Feedback Equalizer
DS	Direct Sequence

DSSS	Direct Sequence Spread Spectrum
DTTF	Discrete Time Transfer Function
EI	Extrinsic Information
EXIT	Extrinsic Information Transfer
FCC	Federal Communications Commission
FDCTF	Frequency Domain Channel Transfer Function
FEC	Forward Error Correction
FFH	Fast Frequency Hopping
FH	Frequency hopping
FIR	Finite Impulse Response
GF	Galois Field
GS	Gold Sequences
ID	Iterative Decoder
IF	Integrating Factor
IIR	Infinite Impulse Response
IR	Impulse Radio
IrCC	Irregular Convolutional Code
IrVLC	Irregular Variable Length Code
ISI	InterSymbol Interference
KLT	Karhunen-Loeve Transform
LDPC	Low-density Parity Check Codes
LFSR	Linear Feedback Shift Register
LLR	Logarithmic Likelihood Ratio
LMMSE	Linear Minimum Mean-Squared Error
LMS	Least Mean Square
LOS	Line Of Sight

LTI	Linear Time-Invariant
MA	Multiple Access
MAI	Multiple Access Interference
MCB	Mean Convergence Bound
MI	Mutual Information
MIMO	Multiple-Input Multiple-Output
MLS	Maximal-Length Sequences
MMSE	Minimum Mean Square Error
MP	Matching Pursuit
MPC	MultiPath Component
MRC	Maximal Ratio combining
MUI	Multi-User Interference
NLMS	Normalized Least Mean Square
NLOS	Non-Line Of Sight
OPSWF	Orthogonal Prolate Spheroidal Wave Function
OSD	Office of Secretary of Defense
PBNJ	Partial Band Noise Jamming
PC	Product Combining
PCA	Principal Component Analysis
PCCC	Parallel Concatenated Convolutional Codes
PDF	Probability Density Function
PDP	Power Delay Profile
PN	Pseudo-Noise
PPM	Pulse Position Modulation
PRF	Pulse Repetition Frequency
PSD	Power Spectral Density

PSWF	Prolate Spheroidal Wave Function
RF	Radio Frequency
RSC	Recursive Systematic Convolutional
RX	Receiver
SAR	Synthetic Aperture Radar
SCCC	Serially Concatenated Convolutional Codes
SeCCC	Self-Concatenated Convolutional Codes
SeCCC-ID	Self-Concatenated Convolutional Codes Iteratively-Decoded
SIC	Successive Interference Cancellation
SISO	Soft-Input Soft-Output
SJR	Signal-to-Jammer Ratio
SNR	Signal to Noise Ratio
SS	Spread-Spectrum
ST	Similarity Transformation
SV	Saleh-Valenzuela
TCM	Trellis Coded Modulation
TH	Time Hopping
TT	Tustin Transformation
TTCM	Turbo Trellis Coded Modulation
TX	Transmitter
URC	Unity Rate Code
UWB	Ultra-WideBand
VLC	Variable Length Coding
VLEC	Variable Length Error Correcting
WHS	Walsh Hadamard Sequences
WSS	Wide Sense Stationary

WSSUS	Wide Sense Stationary Uncorrelated Scattering
ZF	Zero Forcing
ZFD	Zero Forcing Detector

Bibliography

[1] R. A. Riaz, M. F. U. Butt, S. Chen, and L. Hanzo, "Generic z-domain discrete-time transfer function estimation for ultra-wideband systems," *Electronics Letters*, vol. 44, pp. 1491–1492, Dec 2008.

[2] R. A. Riaz, M. F. U. Butt, R. Maunder, S. X. Ng, S. Chen and L. Hanzo, "Optimized irregular variable length coding design for iteratively decoded ultraWideBand time-hopping spread-spectrum impulse radio," in *IEEE Vehicular Technology Conference (VTC2009-Spring)*, (Barcelona, Spain), pp. 1–5, Apr 2009.

[3] M. F. U. Butt, R. A. Riaz, S. X. Ng and L. Hanzo, "Near-capacity iteratively decoded binary self-concatenated code design using EXIT charts," in *IEEE Global Telecommunications Conference (GLOBCOM)*, (New Orleans, LO), pp. 1–5, Nov 2008.

[4] R. A. Riaz, M. El-Hajjar, Q. Z. Ahmed, S. X. Ng, S. Chen and L. Hanzo, "EXIT chart aided design of DS-CDMA ultraWideBand systems using iterative decoding," in *IEEE Vehicular Technology Conference (VTC2009-Fall)*, (Calgary, BC), pp. 1–5, Sep 2008.

[5] R. A. Riaz, M. El-Hajjar, Q. Z. Ahmed, S. X. Ng, S. Chen and L. Hanzo, "Convergence analysis of iteratively detected time hopping and DS-CDMA ultrawide bandwidth systems by EXIT charts," in *IEEE Vehicular Technology Conference (VTC2007-Spring)*, (Singapore), pp. 1127–1131, May 2008.

[6] R. A. Riaz, R. Maunder, M. F. U. Butt, S. X. Ng, S. Chen, L. Hanzo, "EXIT-Chart aided 3-Stage concatenated ultra-wideBand time-hopping spread-spectrum impulse radio design," *accepted for publication in IEEE Transactions on Vehicular Technology*, 2009.

[7] R. A. Riaz, M. F. U. Butt, S. Chen, and L. Hanzo, "Near-capacity UWB impulse radio using EXIT chart aided self-concatenated codes," in *accepted for publication in IEEE Vehicular Technology Conference*, (Alaska, USA), September 2009.

[8] M. F. U. Butt, R. A. Riaz, S. Chen, and L. Hanzo, "Distributed self-concatenated codes for low-complexity power-efficient cooperative communication," in *accepted for*

publication in IEEE Vehicular Technology Conference, (Alaska, USA), September 2009.

[9] R. A. Riaz, R. Maunder, M. F. U. Butt, S. X. Ng, S. Chen, L. Hanzo, "Three-stage concatenated ultra-Wide bandwidth time-hopping spread-spectrum impulse radio using iterative detection," in *IEEE International Conference on Communications ICC*, (Dresden), pp. 1–6, June 2009.

[10] S. B. T. Wang, A. M. Niknejad and R. W. Brodersen, "Design of a sub mW 960 MHz UWB CMOS LNA," in *IEEE Journal of Solid-State Circuits*, vol. 41, pp. 2449–2456, Nov 2006.

[11] L. Yang and G. B. Giannakis, "Ultra-wideband communications: an idea whose time has come," *IEEE Signal Processing Magazine*, vol. 21, pp. 26–54, Nov. 2004.

[12] M. Z. Win and R. A. Scholtz, "Impulse radio: how it works," *IEEE Communications Letters*, vol. 2, pp. 36–38, Feb 1998.

[13] Federal Communications Commission, "Revision of Part 15 of the Commission's rules regarding ultra-wideband transmission systems, First Report and Order," *FCC*, April 2002.

[14] M. Oner, "On the spectral correlation of UWB impulse radio signals," *IEEE Communications Letters*, vol. 12, pp. 714–716, Oct 2008.

[15] M. Z. Win and R. A. Scholtz, "On the energy capture of ultrawide bandwidth signals in dense multipath environments," *IEEE Communications Letters*, vol. 2, pp. 245–247, Sep. 1998.

[16] L. A. De Rosa, "Random impulse system," *U.S. Patent*, Mar 1954.

[17] G. F. Ross, "A time domain criterion for the design of wideband radiating elements," *IEEE Transactions on Antennas and Wireless Propagation*, vol. 16, pp. 335–338, Nov 1968.

[18] G. F. Ross, "Transmission and reception system for generating and receiving base-band pulse signals for short base-band pulse communication system.," *U.S. Patent*, Apr 1973.

[19] C. L. Bennett, G. F. Ross, "Time-domain electromagnetics and its applications," *Proceedings of the IEEE*, vol. 66, pp. 299–318, Mar 1978.

[20] H. F. Harmuth, "Synthetic aperture radar based on nonsinusoidal functions: VI-pulse position and pulse shape coding.," *IEEE Transactions Electromagnetic Compatibility*, vol. 3, pp. 93–106, Apr 1980.

[21] A. H. Kim, L. D. Didomenico, L. J. Jasper, R. J. Youmans and T. E. Koscica, "Ultrawideband high power photon triggered frequency independent radiator.," *U.S. Patent*, Jul 1993.

[22] R. Scholtz, "Multiple access with time-hopping impulse modulation," in *IEEE Military Communications Conference*, vol. 2, (Boston, MA), pp. 447–450, Oct 1993.

[23] M. Hamalainen, V. Hovinen, R. Tesi, J. H. J. Iinatti and M. Latva-Aho, "On the UWB system coexistence with GSM 900, UMTS/WCDMA, and GPS," *IEEE Journal on Selected Areas in Communications*, vol. 20, pp. 1712–1721, Dec 2002.

[24] A. F. Molisch, D. Cassioli, C. -C. Chong, S. Emami, A. Fort, B. Kannan, J. Karedal, J. Kunisch, H. G. Schantz, K. Siwiak and M. Z. Win, "A comprehensive standardized model for ultrawideband propagation channels," *IEEE Transactions on Antennas and Propagation*, vol. 54, pp. 3151–3166, Nov 2006.

[25] G. Bacci, M. Luise, H. V. Poor and A. M. Tulino, "Energy efficient power control in impulse radio UWB wireless networks," *IEEE Journal of Selected Topics in Signal Processing*, vol. 1, pp. 508–520, Oct 2007.

[26] S. Gezici and H. V. Poor, "Position estimation via ultra-wide-band signals," *Proceedings of the IEEE*, vol. 97, pp. 386–403, Feb 2009.

[27] M. Z. Win and R. A. Scholtz, "On the robustness of ultra-wide bandwidth signals in dense multipath environments," *IEEE Communications Letters*, vol. 2, pp. 51–53, Feb 1998.

[28] J. Foerster, E. Green, S. Somayazulu, D. Leeper, "Ultra-Wideband technology for short- or medium-range wireless communications," *Intel Technology Journal*, pp. 27–38, June 2001.

[29] S. Villarreal-Reyes and R. M. Edwards, "Analysis techniques for the power spectral density estimation of convolutionally coded impulse radio UWB signals subject to attenuation and timing jitter," *IEEE Transactions on Vehicular Technology*, vol. 58, pp. 1355–1374, Mar 2009.

[30] J. D. McKinney, I. S. Lin and A. M. Weiner, "Shaping the power spectrum of ultra-wideband radio-frequency signals," *IEEE Transactions on Microwave Theory and Techniques*, vol. 54, pp. 4247–4255, Dec 2006.

[31] Y. P. Nakache and A. F. Molisch, "Spectral shaping of UWB signals for time-hopping impulse radio," *IEEE Journal on Selected Areas in Communications*, vol. 24, pp. 738–744, Apr 2006.

[32] M. Chiani and A. Giorgetti, "Coexistence between UWB and narrow-Band wireless communication systems," *Proceedings of the IEEE*, vol. 97, pp. 231–254, Feb 2009.

[33] A. Mehbodniya and S. Aissa, "Ultra wideband technologies coexistence in Nakagami-m fading channels," *IET Communications*, vol. 3, pp. 1081–1088, Jul 2009.

[34] Z. Ahmadian and L. Lampe, "Performance analysis of the IEEE 802.15.4a UWB system," *IEEE Transactions on Communications*, vol. 57, pp. 1474–1485, May 2009.

[35] J. Ding, L. Zhao, S. R. Medidi and M. K. Sivalingam, "MAC protocols for ultra-wide-wand (UWB) wireless networks: impact of channel acquisition time," *Proceedings SPIE ITCOM*, pp. 5–10, Oct 2002.

[36] M.-I. Lai and S.-K. Jeng, "A microstrip three-port and four-channel multiplexer for WLAN and UWB coexistence," *IEEE Transactions on Microwave Theory and Techniques*, vol. 53, pp. 3244–3250, Oct 2005.

[37] N. Deparis, A. Bendjabballah, A. Boe, M. Fryziel, C. Loyez, L. Clavier, N. Rolland and P. A. Rolland, "Transposition of a baseband UWB signal at 60 GHz for high data rate indoor WLAN," *IEEE Microwave and Wireless Components Letters*, vol. 15, pp. 609–611, Oct 2005.

[38] C. R. Medeiros, J. R. Costa, C. A. Fernandes, "Compact tapered slot UWB antenna with WLAN band rejection," *IEEE Antennas and Wireless Propagation Letters*, vol. 8, pp. 661–664, Nov 2009.

[39] J.G. Proakis, *Digital communications*. McGraw-Hill, 2001.

[40] B. Razavi, *RF microelectronics*. Prentice Hall, 1998.

[41] T.M. Cover and J.A. Thomas, *Elements of information theory*. New York: Wiley, 1991.

[42] W. A. Kissik, "The temporal and spectral characteristics of ultrawideband signals," *U.S. Department of Commerce, NTIA Report 01-383*, 2001.

[43] S. Hara and R. Prasad, "Overview of multicarrier CDMA," *IEEE Communications Magazine*, vol. 35, pp. 126–133, December 1997.

[44] L.-L. Yang, and L. Hanzo, "Multicarrier DS-CDMA: a multiple access scheme for ubiquitous broadband wireless communications," *IEEE Communications Magazine*, vol. 41, pp. 116–124, Oct 2003.

[45] L.-L. Yang, and L. Hanzo, "Slow frequency-hopping multicarrier DS-CDMA for transmission over Nakagami multipath fading channels," *IEEE Journal on Selected Areas in Communications*, vol. 19, pp. 1211–1221, Jul 2001.

[46] L.-L. Yang, and L. Hanzo, "Performance of fractionally spread multicarrier CDMA in AWGN as well as slow and fast Nakagami-m fading channels," *IEEE Transactions on Vehicular Technology*, vol. 54, pp. 1817–1827, Sep 2005.

[47] L.-L. Yang, and L. Hanzo, "Blind joint soft-detection assisted slow frequency-hopping multicarrier DS-CDMA," *IEEE Transactions on Communications*, vol. 48, pp. 1520–1529, Sep 2000.

[48] S. W. Golomb, *Shift register sequences*. Aegean Park Press, 1992.

[49] L. Hanzo, L.-L. Yang, E.-L. Kuan and K. Yen, *Single and multi-carrier DS-CDMA: Multi-user detection, space-time spreading, synchronisation, networking and standards*. Chichester, England: John Wiley and Sons Ltd and IEEE Press, 2003.

[50] L.-L. Yang, *Multicarrier communications*. Wiley, 2009.

[51] S. Villarreal-Reyes, and R. M. Edwards, "Maximum free distance binary to M-ary convolutional codes for pseudo chaotic type time hopping PPM impulse radio UWB," *IEEE Microwave and Wireless Components Letters*, vol. 17, pp. 250–252, Apr 2007.

[52] S. Adlakha, R. K. Mallik, and A. Vazirani, "Multiuser detection techniques for TH-PPM systems," *IEEE Transactions on Vehicular Technology*, vol. 56, pp. 2915–2921, Sep 2007.

[53] A. K. Elhakeem, R. Di Girolamo, I. B. Bdira, and M. Talla, "Delay and throughput characteristics of TH, CDMA, TDMA, and hybrid networks for multipath faded data transmission channels," *IEEE Journal on Selected Areas in Communications*, vol. 12, pp. 622–637, May 1994.

[54] F. Ramirez-Mireles, "Performance of ultrawideband SSMA using time hopping and M-ary PPM," *IEEE Journal on Selected Areas in Communications*, vol. 19, pp. 1186–1196, June 2001.

[55] D. C. Laney, G. M. Maggio, F. Lehmann, and L. Larson, "Multiple access for UWB impulse radio with pseudochaotic time hopping," *IEEE Journal on Selected Areas in Communications*, vol. 20, pp. 1692–1700, Dec 2002.

[56] S. Benedetto, G. Montorsi, "Serial concatenation of block and convolutional codes," *Electronics Letters*, vol. 32, pp. 887–888, May 1996.

[57] S. Benedetto and G. Montorsi, "Iterative decoding of serially concatenated convolutional codes," *Electronics Letters*, vol. 32, pp. 1186–1188, June 1996.

[58] S. Benedetto, D. Divsalar, G. Montorsi, F. Pollara, "Self-concatenated trellis coded modulation with self-iterative decoding," in *IEEE Global Telecommunications Conference*, vol. 1, (Sydney, NSW, Australia), pp. 585–591, 1998.

[59] A. H. Loeliger, "New turbo-like codes," in *IEEE International Symposium on Information Theory*, (Ulm), p. 109, Jun 1997.

[60] Y. P. Zhang and Y. Hwang, "Measurements of the characteristics of indoor penetration loss," in *IEEE 44th Vehicular Technology Conference*, (Stockholm, Sweden), pp. 1741–1744, Apr 1994.

[61] G. Durgin, T. S. Rappaport, and H. Xu, "Measurements and models for radio path loss and penetration loss in and around homes and trees at 5.85 GHzM," *IEEE Transactions on Communications*, vol. 46, pp. 1484–1496, Nov 1998.

[62] C. R. Anderson, T. S. Rappaport, K. Bae, A. Verstak, N. Ramakrishnan, W. Tranter, C. Shaffer and L. Watson, "In-building wideband multipath characteristics at 2.5 and 60 GHz," in *IEEE 56th Vehicular Technology Conference*, pp. 97–101, May 2002.

[63] Y. H. Chang, S. H. Tsai, X. Yu and C. J. Kuo, "Ultrawideband transceiver design using channel phase precoding," *IEEE Transactions on Signal Processing*, vol. 55, pp. 3807–3822, Jul 2007.

[64] A. F. Molisch, J. R. Foerster and M. Pendergrass, "Channel models for ultrawideband personal area networks," *IEEE Wireless Communications*, vol. 10, pp. 14–21, Dec 2003.

[65] H. Hashemi, "The indoor radio propagation channel," *Proceedings of the IEEE*, vol. 81, pp. 943–968, Jul 1993.

[66] A. F. de Toledo and A. M. D. Turkmani, "Propagation into and within buildings at 900, 1800, and 2300 MHz," in *IEEE 42nd Vehicular Technology Conference*, pp. 633–636, May 1992.

[67] A. F. de Toledo and A. M. D. Turkmani, "In-situ characterization of building mateirals," in *11th International Conference on Antennas and Propagation*, pp. 269–274, Apr 2001.

[68] A. Saleh and R. Valenzuela, "A statistical model for indoor multipath propagation," *IEEE Journal on Selected Areas in Communications*, vol. 5, pp. 128–137, Feb 1987.

[69] J. M. Cramer, R. A. Scholtz and M. Z. Win, "On the analysis of UWB communication channels," in *IEEE Military Communications Conference Proceedings, MILCOM*, vol. 2, (Atlantic City, NJ), pp. 1191–1195, Oct 1999.

[70] J. R. Foerster, "The effects of multipath interference on the performance of UWB systems in an indoor wireless channel," in *IEEE 53rd Vehicular Technology Conference, VTC Spring*, vol. 2, (Rhodes), pp. 1176–1180, May 2001.

[71] R.J.-M. Cramer, R. A. Scholtz and M. Z. Win, "Evaluation of an ultra-wide-band propagation channel," *IEEE Transactions on Antennas and Propagation*, vol. 50, pp. 561–570, May 2002.

[72] H. Hashemi, "Impulse response modeling of indoor propagation channels," *IEEE Journal on Selected Areas in Communications*, vol. 11, pp. 128–137, Sep 1993.

[73] G. D. Durgin, and T. S. Rappaport, "Theory of multipath shape factors for small-scale fading wireless channels," *IEEE Transactions on Antennas and Wireless Propagation*, vol. 48, pp. 682–693, May 2000.

[74] T. S. Rappaport, "Characterization of UHF multipath radio channels in factory buildings," *IEEE Transactions on Antennas and Wireless Propagation*, vol. 37, pp. 1058–1069, Aug 1989.

[75] T. S. Rappaport and D. A. Hawbaker, "Wide band microwave propagation parameters using circular and linear polarization antennas for indoor wireless channels," *IEEE Transactions on Antennas and Wireless Propagation*, vol. 40, pp. 1–6, Feb 1992.

[76] T. S. Rappaport, *Wireless communications: Principles and practice.* Prentice Hall, 1996.

[77] R. Dilmaghani, M. Ghavami and H. Aghvami, "Channel estimation technique for ultra-wideband pulse transmitters," *IET Electronics Letters*, vol. 40, pp. 1348–1350, 2004.

[78] A. F. Molisch, "Ultrawideband propagation channels theory, measurement, and modeling," *IEEE Transactions on Vehicular Technology*, vol. 54, pp. 1528–1545, Sep 2005.

[79] L. Correia, *Wireless Flexible Personalized Communications.* Wiley, New York, 2001.

[80] C.-C. Chong and S. K. Yong, "A generic statistical-based UWB channel model for high-rise apartments," *IEEE Transactions on Antennas and Propagation*, vol. 53, pp. 2389–2399, Aug 2005.

[81] M. D. Yacoub, J. E. V. Bautistu and L. Guedes, "On higher order statistics of the Nakagami-m distribution," *IEEE Transactions on Vehicular Technology*, vol. 48, pp. 790–794, May 1999.

[82] R. S. Dilmaghani, M. Ghavami, B. Allen and H. Aghvami, "Novel UWB pulse shaping using prolate spheroidal wave functions," in *IEEE 14th Proceedings on Personal, Indoor and Mobile Radio Communications, PIMRC*, vol. 1, pp. 602–606, Sep 2003.

[83] D. Slepian, "Prolate spheroidal wave functions, Fourier analysis and uncertainty V: The discrete case," *Bell Systems Technical Journal*, vol. 57, pp. 103–110, Apr 1978.

[84] C. Flammer, *Spheroidal wave functions.* Stanford University Press, 1957.

[85] G. Arfken, *Mathematical methods for physicists.* Academic Press, 1985.

[86] M. Ghavami, L. B. Michael and R. Kohno, *Ultra Wideband signals and systems in communication engineering.* Wiley, 2007.

[87] B. Parr, C. ByungLok, K. Wallace and Z. Ding, "A novel ultra-wideband pulse design algorithm," *IEEE Communications Letters*, vol. 7, pp. 219–221, May 2003.

[88] H. Tingshu and L. Zongli, "Absolute stability analysis of discrete-time systems with composite quadratic Lyapunov functions," *IEEE Transactions on Automatic Control*, vol. 50, pp. 781–797, Jun 2005.

[89] C. Barquinero, A. Suarez, A. Herrera, J. L. Garcia, "Complete Stability Analysis of Multifunction MMIC Circuits," *IEEE Transactions on Microwave Theory and Techniques*, vol. 55, pp. 2024–2033, oct 2007.

[90] N. E. Barabanov and D. V. Prokhorov, "Stability analysis of discrete-time recurrent neural networks," *IEEE Transactions on Neural Networks*, vol. 13, pp. 292–303, Mar 2002.

[91] N. Olgac and R. Sipahi, "An exact method for the stability analysis of time-delayed linear time-invariant LTI systems," *IEEE Transactions on Automatic Control*, vol. 47, pp. 793–797, May 2002.

[92] R. Hu and J. Li, "Exploiting Slepian-Wolf codes in wireless user cooperation," in *IEEE 6th Workshop on Signal Processing Advances in Wireless Communications*, pp. 275–279, June 2005.

[93] H. Flanders, "Differentiation under the integral sign," *American Mathematical Monthly*, vol. 80, pp. 615–627, Jun 1973.

[94] A. A. Goulianos and S. Stavrou, "UWB path arrival times in body area networks," *IEEE Antennas and Wireless Propagation Letters*, vol. 6, pp. 223–226, 2007.

[95] F. M. Gardner, *Phaselock techniques*. Wiley, 2005.

[96] A. G. Showman and J. H. McClellan, "Blind polarimetric equalization of UWB SAR imagery," in *IEEE International Conference on Image Processing*, vol. 1, (Vancouver, BC), pp. 673–676, Sep 2000.

[97] G. A. Showman and J. H. McClellan, "Filters for polarimetric calibration of UWB SAR imagery," in *IEEE Radar Conference*, (Atlanta, GA), pp. 432–437, May 2001.

[98] V. S. Somayazulu, J. R. Foerster and S. Roy, "Design challenges for very high data rate UWB systems," in *Conference Record of the Thirty-Sixth Asilomar Conference on Signals, Systems and Computers*, vol. 1, pp. 717–721, Nov 2002.

[99] A. G. Klein and C. R. Johnson, "MMSE decision feedback equalization of pulse position modulated signals," in *IEEE International Conference on Communications ICC*, vol. 5, pp. 2648–2652, Jun 2004.

[100] L. Zhiwei, A. B. Premkumar and A. S. Madhukumar, "Matching pursuit-based tap selection technique for UWB channel equalization," *IEEE Communications Letters*, vol. 9, pp. 835–837, Sep 2005.

[101] Y. Wang and X. Dong, "Frequency-domain channel estimation for SC-FDE in UWB communications," *IEEE Transactions on Communications*, vol. 54, pp. 2155–2163, Dec 2006.

[102] A. Parihar, L. Lampe, R. Schober and C. Leung, "Equalization for DS-UWB systems—Part II: 4BOK modulation," *IEEE Transactions on Communications*, vol. 55, pp. 1525–1535, Aug 2007.

[103] D. Wang, L. Jiang and H. Chen, "Robust noise variance and channel estimation for SC-FDE UWB systems under narrowband interference," *IEEE Transactions on Wireless Communications*, vol. 8, pp. 3249–3259, Jun 2009.

[104] P. S. R. Diniz and L. W. P. Biscainho, "Optimal variable step size for the LMS/Newton algorithm with application to subband adaptive filtering," *IEEE Transaction of Signal Processing*, vol. 40, pp. 2825–2829, Nov 1992.

[105] J. T. Cilke and D. M. Etter, "A new adaptive algorithm to reduce weight fluctuations caused by high variance data," *IEEE Transaction of Signal Processing*, vol. 40, pp. 2324–2327, Sep 1992.

[106] S. Haykin, *Adaptive filter theory.* Prentice Hall, 2001.

[107] S. ten Brink, "Designing iterative decoding schemes with the extrinsic information transfer chart," *AEÜ International Journal of Electronics and Communications*, vol. 54, pp. 389–398, November 2000.

[108] F. Brännström, L.K. Rasmussen and A.J. Grant, "Convergence analysis and optimal scheduling for multiple concatenated codes," *IEEE Transactions on Information Theory*, vol. 51, no. 9, pp. 3354–3364, 2005.

[109] E. Fishler and H. V. Poor, "Low-complexity multiuser detectors for time-hopping impulse-radio systems," *IEEE Transactions on Signal Processing*, vol. 52, pp. 2561–2571, Sep 2004.

[110] J. Fiorina and W. Hachem, "On the asymptotic distribution of the correlation receiver output for time-hopped UWB signals," *IEEE Transactions on Signal Processing*, vol. 54, pp. 2529–2545, Jul 2006.

[111] S. R. Aedudodla, S. Vijayakumaran, and T. F. Wong, "Ultra-wideband signal acquisition with hybrid DS-TH spreading," *IEEE Transactions on Wireless Communications*, vol. 5, pp. 2504–2515, Sep 2006.

[112] X. Chu and R. D. Murch, "The effect of NBI on UWB time-hopping systems," *IEEE Transactions on Wireless Communications*, vol. 3, pp. 1431–1436, Sep 2004.

[113] S. S. Tan, A. Nallanathan and B. Kannan, "Performance of DS-UWB multiple-access systems with diversity reception in dense multipath environments," *IEEE Transactions on Vehicular Technology*, vol. 55, pp. 1269–1280, Jul 2006.

[114] N. Boubaker and K. B. Letaief, "Performance analysis of DS-UWB multiple access under imperfect power control," *IEEE Transactions on Communications*, vol. 52, pp. 1459–1463, Sep 2004.

[115] W. Cao, A. Nallanathan, and C. C. Chai, "Performance analysis of prerake DS UWB multiple access system under imperfect channel estimation," *IEEE Transactions on Wireless Communications*, vol. 6, pp. 3892–3896, Nov 2007.

[116] S. ten Brink, "Convergence behavior of iteratively decoded parallel concatenated codes," *IEEE Transactions on Communications*, vol. 49, no. 10, pp. 1727–1737, 2001.

[117] S. X. Ng, O. R. Alamri, Y. Li, J. Kliewer and L. Hanzo, "Near-capacity turbo trellis coded modulation design based on EXIT charts and union bounds," *IEEE Transactions on Communications*, vol. 56, pp. 2030–2039, Dec 2008.

[118] L. Kai and X. Wang, "EXIT chart analysis of turbo multiuser detection," *IEEE Transactions on Wireless Communications*, vol. 4, pp. 300–311, Jan 2005.

[119] A. Q. Pham, L.-L. Yang, N. S. Othman and L. Hanzo, "EXIT chart optimized block codes for wireless video telephony," *IEEE Transactions on Circuits and Systems for Video Technology*, vol. 18, pp. 1671–1680, Dec 2008.

[120] M. Ardakani, T. H. Chan and F. R. Kschischang, "EXIT-chart properties of the highest-rate LDPC code with desired convergence behavior," *IEEE Communications Letters*, vol. 9, pp. 52–54, Jan 2005.

[121] R. Tee, R. G. Maunder and L. Hanzo, "EXIT-chart aided near-capacity irregular bit-interleaved coded modulation design," *IEEE Transactions on Wireless Communications*, vol. 8, pp. 32–37, Jan 2009.

[122] L. Hanzo, O. Alamri, M. El-Hajjar and N. Wu, *Near-Capacity Multi-Functional MIMO Systems: Sphere-Packing, Iterative Detection and Cooperation*. Wiley, 2009.

[123] T.J. Richardson and R. Urbanke, "The capacity of low-density parity-check codes under message-passing decoding," *IEEE Transactions on Information Theory*, vol. 47, pp. 599–618, February 2001.

[124] T.J. Richardson, A. Shokrollahi and R. Urbanke, "Design of capacity-approaching low-density parity-check codes," *IEEE Transactions on Information Theory*, vol. 47, pp. 619–637, February 2001.

[125] S.Y. Chung, G.D. Forney, T.J. Richardson and R. Urbanke, "On the design of low-density parity-check codes within 0.0045 dB of the Shannon limit," *IEEE Communication Letter*, vol. 5, pp. 58–60, February 2001.

[126] H. El Gamal and A.R. Hammons, "Analyzing the turbo decoder using the Gaussian approximation," *IEEE Journal on Selected Areas in Communications*, vol. 47, pp. 671–686, February 2001.

[127] D. Divsalar, S. Dolinar and F. Pollara, "Low complexity turbo-like codes," in *2nd International Symposium on Turbo Codes and Related Topics*, (Brest, France), pp. 73–80, September 2000.

[128] M. Peleg, I. Sason, S. Shamai and A. Elia, "On interleaved differentially encoded convolutional codes," *IEEE Transactions on Information Theory*, vol. 45, pp. 2572–2582, November 1999.

[129] J. Hagenauer, "The EXIT chart - Introduction to extrinsic information transfer in iterative processing," in *European Signal Processing Conference*, (Vienna, Austria), pp. 1541–1548, September 2004.

[130] M. Tüchler, S. ten Brink and J. Hagenauer, "Measures for tracing convergence of iterative decoding algorithms," in *Proceedings of the 4th International ITG Conference on Source and Channel Coding*, (Berlin, Germany), pp. 53–60, January 2002.

[131] O. Alamri, B.L. Yeap and L. Hanzo, "A turbo detection and sphere-packing-modulation-aided space-time coding scheme," *IEEE Transactions on Vehicular Technology*, vol. 56, pp. 575–582, March 2007.

[132] S. W. Kim, "Adaptive orthogonal signaling with diversity in a frequency-nonselective Rayleigh fading channel," *IEEE Transactions on Communications*, vol. 48, pp. 1865–1870, Nov 2000.

[133] S. X. Ng and L. Hanzo, "Space-time IQ-interleaved TCM and TTCM for AWGN and Rayleigh fading channels," *Electronics Letters*, vol. 38, pp. 1553–1555, Nov 2002.

[134] Z. Chen, J. Yuan, B. Vucetic and Z. Zhou, "Performance of Alamouti scheme with transmit antenna selection," *Electronics Letters*, vol. 39, pp. 1666–1668, Nov 2003.

[135] N. Prasad and M. K. Varanasi, "Analysis of decision feedback detection for MIMO Rayleigh-fading channels and the optimization of power and rate allocations," *IEEE Transactions on Information Theory*, vol. 50, pp. 1009–1025, Jun 2004.

[136] E. Sengul, E. Akay and E. Ayanoglu, "Diversity analysis of single and multiple beamforming," *IEEE Transactions on Communications*, vol. 54, pp. 990–993, Jun 2006.

[137] Y. S. Chan, P. C. Cosman and L. B. Milstein, "A multiple description coding and delivery scheme for motion-compensated fine granularity scalable video," *IEEE Transactions on Image Processing*, vol. 17, pp. 1353–1367, Aug 2008.

[138] R. N. McDonough and A. D. Whalen, *Detection of Signals in Noise*. Academic Press, 1995.

[139] A. Klein, G. Kaleh and P. W. Baier, "Zero forcing and minimum mean-square-error equalization formultiuser detection in code-division multiple-access channels," *IEEE Transactions on Vehicular Technology*, vol. 45, pp. 276–287, May 1996.

[140] D. F. Mix, *Random signal processing*. Prentice Hall, 1995.

[141] G. M. Maggio, N. Rulkov and L. Reggiani, "Pseudo-chaotic time hopping for UWB impulse radio," *IEEE Transactions on Circuits and Systems I: Fundamental Theory and Applications*, vol. 48, pp. 1424–1435, Dec 2001.

[142] E. Baccarelli and M. Biagi, "A simple adaptive coding scheme for multiuser interference suppression in ultra-wideband radio transmissions," *IEEE Transactions on Communications*, vol. 53, pp. 1283–1287, Aug 2004.

[143] X. Cheng and W. Zhu, "A subspace detection method of analog space-time codes for multiantenna ultra-wideband transmissions," *IEEE Communications Letters*, vol. 9, pp. 493–495, Jun 2005.

[144] B. U. Riaz, M. Pun and C. C. Kuo, "Performance analysis of single-user Ultra-Wide band impulse radio with super-orthogonal turbo codes," *IEEE Transactions on Wireless Communications*, vol. 6, pp. 4534–4545, Dec 2006.

[145] J. I. Jamp and L. E. Larson, "A coding technique for the spectral shaping of ultra-wideband time-hopping signals," *IEEE Transactions on Vehicular Technology*, vol. 56, pp. 1671–1682, Jul 2007.

[146] D. Kim, "Multiuser performance of M-ary orthogonal coded/balanced UWB transmitted-reference systems," *IEEE Transactions on Communications*, vol. 57, pp. 1013–1024, Apr 2009.

[147] L. Hanzo, S.X. Ng, T. Keller and W. Webb, *Quadrature amplitude modulation: From basics to adaptive trellis-coded, turbo equalised and space-time coded OFDM, CDMA and MC-CDMA systems, 2nd Edition.* Chichester, England: John Wiley and Sons Ltd and IEEE Press, 2004.

[148] D. Divsalar, S. Dolinar and F. Pollara, "Serial concatenated trellis coded modulation with rate-1 inner code," in *IEEE Global Telecommunications Conference (GLOBECOM)*, vol. 2, (San Francisco, CA), pp. 777–782, 2000.

[149] M. Tüchler and J. Hagenauer, "EXIT charts of irregular codes," in *Conference on Information Science and Systems*, (Princtone, NJ), pp. 748–753, March 2002.

[150] S. ten Brink, "Convergence of iterative decoding," *Electronics Letters*, vol. 35, no. 13, pp. 1117–1119, 1999.

[151] K. Hao and J. A. Gubner, "The distribution of sums of path gains in the IEEE 802.15.3a UWB channel model," *IEEE Transactions on Wireless Communications*, vol. 6, pp. 811–816, Mar 2007.

[152] T. Sakamoto, and T. Sato, "Code-Division multiple transmission for high-speed UWB radar imaging with an antenna array," *IEEE Transactions on Geoscience and Remote Sensing*, vol. 47, pp. 1179–1186, Apr 2009.

[153] L. Jofre, A. P. Toda, J. Montana, P. C. Carrascosa, J. Romeu, S. Blanch, and A. Cardama, "UWB short-range bifocusing tomographic imaging," *IEEE Transactions on Instrumentation and Measurement*, vol. 57, pp. 2414–2420, Nov 2008.

[154] V. Venkatasubramanian, H. Leung and L. Xiaoxiang, "Chaos UWB radar for through-the-wall imaging," *IEEE Transactions on Image Processing*, vol. 18, pp. 1255–1265, Jun 2009.

[155] H. Sato and T. Ohtsuki, "Frequency domain channel estimation and equalisation for direct sequence ultra wideband DS-UWB system," *IEE Proceedings Communications*, vol. 153, pp. 93–98, Feb 2006.

[156] L.M.A. Jalloul, K. Rohani, K. Kuchi and J. Chen, "Performance analysis of CDMA transmit diversity methods," in *IEEE Vehicular Technology Conference*, vol. 3, (Amsterdam), pp. 1326–1330, 1999.

[157] M. El-Hajjar, R. G. Maunder, O. Alamri, S. X. Ng and L. Hanzo, "Iteratively detected irregular variable length coding and sphere packing modulation aided differential space-time spreading," in *IEEE 66th Vehicular Technology Conference*, (Baltimore, MD, USA), pp. 1238–1242, September 2007.

[158] R.G. Maunder, J. Wang, S.X. Ng, L.-L. Yang and L. Hanzo, "On the performance and complexity of irregular variable length codes for near-capacity joint source and channel coding," *IEEE Transactions on Wireless Communications*, vol. 7, pp. 1338–1347, April 2008.

[159] S. Benedetto, D. Divsalar, G. Montorsi and F. Pollara, "Analysis, design and iterative decoding of double serially concatenated codes with interleavers," *IEEE Journal on Selected Areas in Communications*, vol. 16, pp. 231–244, February 1998.

[160] A. Ashikhmin, G. Kramer and S. ten Brink, "Extrinsic information transfer functions: model and erasure channel properties," *IEEE Transactions on Information Theory*, vol. 50, no. 11, pp. 2657–2673, 2004.

[161] M. Tüchler, "Design of serially concatenated systems depending on the block length," *IEEE Transactions on Communications*, vol. 52, no. 2, pp. 209–218, 2004.

[162] J. Wang, S.X. Ng, A. Wolfgang, L.-L. Yang, S. Chen and L. Hanzo, "Near-capacity three-stage MMSE turbo equalisation using irregular convolutional codes," in *International Symposium on Turbo Codes*, (Munich, Germany), April 2006.

[163] A. Q. Pham, J. Wang, L.-L. Yang and L. Hanzo, "An iterative detection aided unequal error protection wavelet video scheme using irregular convolutional codes," in *IEEE 63rd Vehicular Technology Conference, VTC Spring*, vol. 5, (Melbourne, Vic.), pp. 2484–2488, May 2006.

[164] O. Alamri, J. Wang, S. X. Ng, L.-L. Yang, and L. Hanzo, "Near-capacity transceiver design using Exit-curve fitting: three-stage turbo detection of irregular convolutional coded joint sphere-packing modulation and space-time coding," in *IEEE International Conference on Communications, ICC*, (Glasgow), pp. 4028–4033, Jun 2007.

[165] J. Wang, N. S. Othman, J. Kliewer, L.-L. Yang and L. Hanzo, "Turbo-detected unequal error protection irregular convolutional codes designed for the wideband advanced multirate speech codec," in *IEEE 62nd Vehicular Technology Conference, VTC Fall*, vol. 2, pp. 927–931, Sep 2005.

[166] G. Forney, *Concatenated codes*. MIT Press, Cambridge, MA, 1966.

[167] C. Berrou, A. Glavieux, "Near optimum error correcting coding and decoding: turbo-codes," *IEEE Transactions on Communications*, vol. 44, pp. 1261–1271, October 1996.

[168] C. E. Shannon, "A mathematical theory of communication," *Bell Systems Technical Journal*, vol. 27, pp. 623–656, October 1948.

[169] S. Le Goff, A. Glavieux and C. Berrou, "Turbo-codes and high spectral efficiency modulation," in *IEEE International Conference on Communications*, (New Orleans, LA), pp. 645–649, 1994.

[170] S. Benedetto, D. Divsalar, G. Montorsi and F. Pollara, "Bandwidth efficient parallel concatenated coding schemes," *Electronics Letters*, vol. 31, pp. 2067–2069, Nov 1995.

[171] P. Robertson and T. Worz, "Coded modulation scheme employing turbo codes," *Electronics Letters*, vol. 31, pp. 1546–1547, Aug 1995.

[172] S. Benedetto, D. Divsalar, G. Montorsi, and F. Pollara, "Serial concatenated trellis coded modulation with iterative decoding," in *IEEE International Symposium on Information Theory*, (Ulm), p. 8, Jun 1997.

[173] G. Forney, *Concatenated codes*. Cambridge: MIT Press, 1966.

[174] C. Berrou, A. Glavieux and P. Thitimajshima, "Near Shannon limit error-correcting coding and decoding: Turbo-codes. 1," in *IEEE International Conference on Communications*, vol. 2, (Geneva), pp. 1064–1070, May 1993.

[175] D. Divsalar and F. Pollara, "Multiple turbo codes for deep-space communications," Telecommunications and Data Acquisition Progress Report 42-121, Jet Propulsion Laboratory, Pasadena, CA, May 1995.

[176] D. Raphaeli and Y. Zarai, "Combined turbo equalization and turbo decoding," in *Proceedings of IEEE Global Telecommunications Conference (GLOBECOM)*, vol. 2, (Phoenix, AZ), pp. 639–643, November 1997.

[177] D. Raphaeli and Y. Zarai, "Combined turbo equalization and turbo decoding," *IEEE Communications Letters*, vol. 2, pp. 107–109, April 1998.

[178] M. Toegel, W. Pusch and H. Weinrichter, "Combined serially concatenated codes and turbo-equalization," in *2nd International Symposium on Turbo Codes*, (Brest, France), pp. 375–378, September 2000.

[179] R. Ramamurthy and W.E. Ryan, "Convolutional double accumulate codes (or double turbo DPSK)," *IEEE Communications Letters*, vol. 5, pp. 157–159, April 2001.

[180] C. Douillard, M. Jezequel, C. Berrou, A. Picart, P. Didier and A. Glavieux, "Iterative correction of intersymbol interference: turbo equalization," *European Transaction on Telecommunications*, vol. 6, pp. 507–511, September/October 1995.

[181] S. Benedetto, D. Divsalar, G. Montorsi and F. Pollara, "A soft-input soft-output APP module for iterative decoding of concatenated codes," *IEEE Communications Letters*, vol. 1, pp. 22–24, January 1997.

[182] G. Caire, G. Taricco and E. Biglieri, "Bit-interleaved coded modulation," in *Proceedings of IEEE International Symposium on Information Theory (ISIT)*, (Ulm, Germany), p. 96, June/July 1997.

[183] G. Caire, G. Taricco and E. Biglieri, "Bit-interleaved coded modulation," *IEEE Transactions on Information Theory*, vol. 44, pp. 927–946, May 1998.

[184] S. ten Brink, J. Speidel and R.-H. Yan, "Iterative demapping and decoding for multilevel modulation," in *IEEE Global Telecommunications Conference (GLOBCOM)*, vol. 1, (Sydney,NSW), pp. 579–584, 1998.

[185] X. Li and J. A. Ritcey, "Bit-interleaved coded modulation with iterative decoding," *IEEE Communications Letters*, vol. 1, pp. 169–171, November 1997.

[186] X. Li and J. A. Ritcey, "Bit-interleaved coded modulation with iterative decoding using soft feedback," *IEE Electronics Letters*, vol. 34, pp. 942–943, May 1998.

[187] X. Li and J. A. Ritcey, "Trellis-coded modulation with bit interleaving and iterative decoding," *IEEE Journal on Selected Areas in Communications*, vol. 17, pp. 715–724, April 1999.

[188] X. Wang and H. V. Poor, "Iterative (turbo) soft interference cancellation and decoding for coded CDMA," *IEEE Transactions on Communications*, vol. 47, pp. 1046–1061, July 1999.

[189] A. Sezgin, D. Wuebben and V. Kuehn, "Analysis of mapping strategies for turbo-coded space-time block codes," in *Proceedings of IEEE Information Theory Workshop*, (Paris, France), pp. 103–106, March/April 2003.

[190] L. Bahl, J. Cocke, F. Jelinek and J. Raviv, "Optimal decoding of linear codes for minimizing symbol error rate," *IEEE Transactions on Information Theory*, vol. 20, no. 2, pp. 284–287, 1974.

[191] P. Robertson, E. Villebrun and P. Hoeher, "A comparison of optimal and sub-optimal MAP decoding algorithms operating in the Log domain," in *Proceedings of International Conference on Communications*, (Seattle, USA), pp. 1009–1013, June 1995.

[192] S. Benedetto, D. Divsalar, G. Montorsi and F. Pollara, "Serial concatenation of interleaved codes: performance analysis, design and iterative decoding," *IEEE Transactions on Information Theory*, vol. 44, pp. 909–926, May 1998.

[193] I. Lee, "The effect of a precoder on serially concatenated coding systems with an ISI channel," *IEEE Transactions on Communications*, vol. 49, pp. 1168–1175, July 2001.

[194] S. ten Brink, "Convergence of multidimensional iterative decoding schemes," in *Conference Record of the Thirty-Fifth Asilomar Conference on Signals, Systems and Computers*, vol. 1, (Pacific Grove, CA, USA), pp. 270–274, 2001.

[195] M. Tüchler, "Convergence prediction for iterative decoding of threefold concatenated systems," in *IEEE Global Telecommunications Conference (GLOBECOM)*, vol. 2, pp. 1358–1362, November 2002.

[196] L. Lifang, D. Divsalar and S. Dolinar, "Iterative demodulation, demapping and decoding of coded non-square QAM," in *IEEE Transactions on Communications*, vol. 53, pp. 16–19, January 2005.

[197] S. Benedetto, D. Divsalar, G. Montorsi and F. Pollara, "Serial concatenation of interleaved codes: performance analysis, design and iterative decoding," *IEEE Transactions on Information Theory*, vol. 44, pp. 909–926, May 1998.

[198] K.R. Narayanan, "Effect of precoding on the convergence of turbo equalization for partial response channels," *IEEE Journal on Selected Areas in Communications*, vol. 19, pp. 686–698, April 2001.

[199] J. Kliewer, S. X. Ng and L. Hanzo, "Efficient computation of EXIT functions for nonbinary iterative decoding," *IEEE Transactions on Communications*, vol. 54, pp. 2133–2136, Dec 2006.

[200] M. Luby, M. Mitzenmacher, A. Shokrollahi, D. Spielman, and V. Stemann, "Practical loss-resilient codes," in *ACM Symposium on Theory of Computing*, (Beijing, China), pp. 775–779, May 1997.

[201] R. G. Gallager, "Low-density parity-check codes," *IRE Transactions on Information Theory*, vol. 8, pp. 21–28, Jan 1962.

[202] R. Tanner, "A recursive approach to low complexity codes," *IEEE Transactions on Information theory*, vol. 27, pp. 533–547, September 1981.

[203] V. Buttigieg and P. G. Farrell, "Variable-length error-correcting codes," *IEE Proceedings on Communications*, vol. 147, pp. 211–215, Aug 2000.

[204] R. Y. S. Tee and S. X. Ng and L. Hanzo, "Precoder-aided iterative detection assisted multilevel coding and three-dimensional EXIT-chart analysis," in *IEEE Wireless Communications and Networking Conference, 2006. WCNC 2006*, vol. 3, (Las Vegas, NV), pp. 1322–1326, Apr 2006.

[205] L. Hanzo, P.J. Cherriman and J. Streit, *Wireless video communications: second to third generation and beyond*. IEEE Press-John Wiley & Sons, 2001.

[206] L. Hanzo, T.H. Liew and B.L. Yeap, *Turbo coding, turbo equalisation and space time coding for transmission over fading channels*. Chichester, UK: Wiley: IEEE Press, 2002.

[207] P. C. P. Liang and W. E. Stark, "Algorithm for joint decoding of turbo codes and M-ary orthogonal modulation," in *IEEE International Symposium on Information Theory*, p. 191, Jun 2000.

[208] M. F. U. Butt, S. X. Ng and L. Hanzo, "EXIT Chart Aided Design of Near-Capacity Self-Concatenated Trellis Coded Modulation Using Iterative Decoding," in *67th IEEE Vehicular Technology Conference. VTC-'08 Spring.*, (Marina Bay, Singapore), pp. 1–5, May 2008.

[209] A. Grant, "Convergence of non-binary iterative decoding," in *IEEE Global Telecommunications Conference*, vol. 2, (San Antonio, TX, USA), pp. 1058–1062, Nov 2001.

[210] H. Chen and A. Haimovich, "EXIT charts for turbo trellis-coded modulation," *IEEE Communications Letters*, vol. 8, pp. 668–670, Nov 2004.

[211] J. Hagenauer, "Rate-compatible punctured convolutional codes (RCPC codes) and their applications," *IEEE Transactions on Communications*, vol. 36, pp. 389–400, Apr 1988.

[212] S. Benedetto, D. Divsalar, G. Motorsi and F. Pollara, "A soft-input soft-output APP module for iterative decoding of concatenated codes," *IEEE Communications Letter*, vol. 1, pp. 22–24, January 1997.

[213] L.-L. Yang and L. Hanzo, "Residue number system assisted fast frequency-hopped synchronous utlra-wideband spread-spectrum mutiple-access: a design alternative to impulse radio," *IEEE Journal on Selected Areas of Communications*, vol. 20, pp. 1652–1663, December 2002.

Index

Author Index

C

D

E

F

G

H

I

J

K

L

M

N

O

P

R

S

T

U

V

W

X

Y

Z